uOttawa

L'Université canadienne
Canada's university

FACULTÉ DES ÉTUDES SUPÉRIEURES ET POSTOCTORALES

uOttawa

L'Université canadienne
Canada's university

FACULTY OF GRADUATE AND POSDOCTORAL STUDIES

R. James Evans

AUTEUR DE LA THÈSE / AUTHOR OF THESIS

Ph.D. (Physics)

GRADE / DEGREE

Department of Physics

FACULTÉ, ÉCOLE, DÉPARTEMENT / FACULTY, SCHOOL, DEPARTMENT

Mössbauer Hyperfine Parameters in Oxygen-coordinated Octahedral Fe2+ from Electric Structure Calculations

TITRE DE LA THÈSE / TITLE OF THESIS

Denis Rancourt

DIRECTEUR (DIRECTRICE) DE LA THÈSE / THESIS SUPERVISOR

CO-DIRECTEUR (CO-DIRECTRICE) DE LA THÈSE / THESIS CO-SUPERVISOR

EXAMINATEURS (EXAMINATRICES) DE LA THÈSE / THESIS EXAMINERS

Madhu Dixit

Zbigniew Stadniuk

Paul Finnie

James Rustad

Gary W. Slater

Le Doyen de la Faculté des études supérieures et postdoctorales / Dean of the Faculty of Graduate and Postdoctoral Studies

Mössbauer Hyperfine Parameters in Oxygen-Coordinated Octahedral Fe^{2+} from Electronic Structure Calculations

R. James Evans

Department of Physics
University of Ottawa
Ottawa, Ontario
September 21, 2005

Your file Votre référence
ISBN: 978-0-494-25869-9
Our file Notre référence
ISBN: 978-0-494-25869-9

Abstract

Ab initio electronic structure calculations are reported which directly relate local chemical and distortion environments of oxygen-coordinated octahedral Fe^{2+} to corresponding hyperfine parameter distributions in Mössbauer spectroscopy. Changes in the quadrupole splitting (QS) and other properties of the electric field gradient (EFG) with various distortions were investigated on model clusters including the bare octahedra FeO_6^{10-} and $Fe(OH)_6^{4-}$, and various seven-octahedra sections of an octahedral sheet, through self-consistent charge (SCC) Xα ab initio calculations. The percent change in the EFG over the range of distortion parameters found in trioctahedral micas is greatest with flattening for the clusters compared, suggesting that flattening is the most important structural distortion in determining the EFG. The independent parameters of the EFG tensor - particularly the principal value V_{ZZ}, the asymmetry parameter η, and the direction of the principal axis with regards to the octahedral sheet - are examined in detail as functions of octahedral flattening for each of the thirteen possible configurations of Mg^{2+} and Al^{3+} cations in the first nearest neighbour octahedra of a Fe^{2+}-centred seven-octahedra cluster. It is demonstrated that the argument that the EFG tensor at a particular site is largely determined by the point group symmetry of the corresponding crystallographic site is not correct. Averages and distributions of η, principal axis angles and quadrupole splittings are simulated by taking EFG tensor results from all seven-octahedra clusters, and using probabilities for the occurrence of each possible cation configuration in a chemically disordered octahedral sheet of a given bulk composition. Simulations of all hyperfine parameter distributions, including the isomer shift (IS) and the hyperfine magnetic field, were performed using ensembles of $Fe(OH)_6^{4-}$ octahedra generated by applying random distortions to the average structure. Distributions of the QS at 0 and 300 K agree well with experimental results, possessing a low QS tail and a sharp edge at high QS values. This high edge is due to a universal upper bound on the QS, corresponding to the maximum of the QS versus flattening curve. The width-to-mean ratio of the distribution of the nuclear electron spin polarization, the dominant contribution to the hyperfine magnetic field, is large compared to that of the other parameter distributions. The variation of the spin polarization due to local structural variation alone is found to be sufficient to account for the widths and intensities of lines in magnetic hyperfine spectra. The widths of most distributions increase monotonically with the static disorder parameter, and are universal functions of one another, providing a useful constraint in fitting Mössbauer spectra. The correlations between hyperfine parameters are non-linear and considerably more complicated than those supposed in current spectral fitting

models. The correlation between QS and isomer shift increases with the amount of disorder in the material. Isomer shift and spin polarization have a strong non-linear correlation. The complexity of the correlations between hyperfine parameters, together with the fact that optimal fits of Mössbauer spectra are not unique, strongly implies that fits to spectra require supporting electronic structure calculations and crystal chemical models of the measured materials for a correct interpretation. It is also shown that published mathematical models of electric field gradient tensor distributions in amorphous materials, derived assuming an isotropic solid, do not describe the distributions in $^{[6]}Fe^{2+}$ sites in disordered materials, except under special symmetry conditions.

Statement of Originality / Contributions of Co-Authors

The three papers comprising this thesis present original electronic structure calculations of Mössbauer hyperfine parameters performed by R. James Evans, under the supervision of D. G. Rancourt. All calculations were performed using the SCC Xα code written by M. Grodzicki of the University of Salzburg. The first paper, "Hyperfine electric field gradients and local distortion environments of octahedrally coordinated Fe^{2+}", presents the first systematic calculations of quadrupole splitting and electric field gradient tensor properties in $Fe^{2+}O_6$-centred clusters as functions of progressive distortion from octahedral symmetry. The second paper, "Hyperfine electric field gradient tensors at Fe^{2+} sites in octahedral layers: Towards understanding oriented single-crystal Mössbauer spectroscopy measurements of micas", presents the systematic study of the complete electric field gradient tensor as a function of progressive flattening of the Fe^{2+} site, with applications towards oriented single-crystal Mössbauer spectroscopy. The first two papers have been previously published in American Mineralogist (see Introduction, references). The final paper, "Simulated quadrupole splitting, isomer shift and hyperfine field distributions of octahedral Fe^{2+} in Mössbauer spectroscopy from electronic structure calculations", presents the first simulations of hyperfine parameter distributions using electronic structure calculations of large numbers of randomly distorted octahedra, and has yet to be published.

All calculations, original mathematical derivations and analyses were performed by R. James Evans. D.G Rancourt provided supervision, comments and editorial suggestions. M. Grodzicki designed and provided the SCC Xα code, as well as comments on the manuscripts.

Acknowledgements

I would like to thank my supervisor, Dr. Denis Rancourt, for his help and encouragement in preparing this work. Many thanks also to Dr. Michael Grodzicki, for supplying the SCC Xα code and for his useful suggestions, and to Dr. Patrick Mercier for many insightful discussions.

I would also like to thank my colleagues Jean-Paul Prevost, Iana Tsandev and Connie Sutherland for their assistance and support.

Table of Contents

The most incomprehensible thing about the Universe is that it is comprehensible.

– Albert Einstein, attributed

A story that is simple enough for an overdeveloped ape brain to understand is unlikely to be the whole story.

– Ian Stewart, What Shape is a Snowflake? Weidenfeld and Nicholson, U.K. (2001)

Introduction

Mössbauer spectroscopy is a very precise method of characterization of materials in the solid state, based upon the Mössbauer effect, where a nucleus in a solid absorbs a gamma ray photon without recoil. The most common isotope for Mössbauer spectroscopy by a very wide margin is ^{57}Fe. Iron is the most common transition metal in the earth, present in a large number of common minerals and sediments, and plays an important role in many environmental systems as well as being technologically important. The combination of iron's importance and the relative ease of performing Mössbauer spectroscopy with ^{57}Fe compared to most other nuclei is responsible for the dominance of iron Mössbauer spectroscopy.

The greatest obstacle in Mössbauer spectroscopy is that while performing the measurement is relatively easy, fitting the resulting spectrum so as to extract useful information from it is difficult, and actually interpreting the fitted spectrum is even harder. There is a great need for theory in the Mössbauer field (Rancourt 1998, Stadnik 1994) to overcome this barrier by providing models, based in the relationship between mineral structure and Mössbauer hyperfine parameters, for interpreting spectra. The ab initio electronic structure methods of quantum chemistry are the best tools for exploring this relationship.

In ^{57}Fe Mössbauer spectroscopy, absorption of a photon with an energy of 14.41 keV excites the ^{57}Fe nucleus from its I = 1/2 ground state to an I = 3/2 excited state. Hyperfine interactions, the interactions of electrons with the ^{57}Fe nucleus, lift the degeneracy of the nuclear states and alter the resulting Mössbauer spectrum (figure 1, from Rancourt 1998). Interaction between the electron density at the nucleus and the nuclear charge shifts the nuclear energy levels at the absorber (^{57}Fe) with respect to the source, producing the isomer shift, the main component of the centre shift of the spectrum, measured relative to metallic α-Fe at room temperature (figure 1, part A). Interaction between the electric field gradient at the nucleus, due to the non-spherical distribution of electrons, and the nuclear quadrupole moment of the I = 3/2 state, splits the excited state into $m_I = \pm 1/2$ and $m_I = \pm 3/2$ states, splitting the single line spectrum into a doublet (figure 1 , part B). The separation between the two lines is the quadrupole splitting, proportional to one of the matrix invariants of the electric field gradient. Finally, a non-zero magnetic field at the nucleus, some components of which are due to local electronic properties (see paper 3), lifts all degeneracy between mI levels of the nuclear states, resulting in a sextet in the limit of low electric field gradient (figure 1, part C), or an octet in the most general case.

The properties of the Mössbauer spectrum are the result of the local electronic structure of the ^{57}Fe nucleus. The electronic structure of the atom, in turn, is a result of the local chemical and structural environment of the iron atom, up to the first and second nearest neighbours at least. Therefore, the values of the hyperfine parameters of an experimental Mössbauer spectrum contain information about the local environment of iron in the sample measured. Most minerals contain some chemical and/or structural disorder, which leads to a distribution of local environments for each class of crystallographic site. This leads to distributions of all the hyperfine parameters, and to Mössbauer spectra with lines broader than the elemental Lorentzian Heisenberg line-width. The hyperfine parameter distributions, in the absence of dynamical line-shape effects, represent the greatest amount of information that can be extracted from the Mössbauer spectrum. Electronic structure calculations are needed to make the link between local structure and the hyperfine parameters, and between experimentally extracted hyperfine parameter distributions and information about the distribution of local environments in the sample.

This thesis is composed of three papers applying electronic structure calculations of hyperfine parameters to oxygen-coordinated octahedral Fe^{2+}. Most mineralized iron apart from the iron oxides is in the form of Fe^{2+}, and octahedral oxygen-coordination is the most common local environment of Fe^{2+}. Most of the present work was done assuming that the Fe^{2+} octahedron is part of a brucite-like octahedral sheet in a layer silicate, specifically in a 1M trioctahedral mica. Micas are very common minerals and many different cations are found in their octahedral sites; thus Fe^{2+} has a particularly wide distribution of local environments in the micas' octahedral sheets, and it provides a good test material for exploring the links between local environment and hyperfine parameter distributions. Model clusters used that are larger than a single octahedron are surrounded by six edge-sharing neighbour octahedra, and OH groups in $Fe(OH)_6^{4-}$ and larger clusters were aligned normal to the hypothetical sheet. However, $Fe^{2+}O_6$ octahedra are common in a large number of minerals (often edge-sharing in sheet-like structures), and form a fundamental part of the Earth's geochemistry (Putnis 1992); so while this work is particularly applicable to micas and other layer silicates, it is also applicable to any $Fe^{2+}O_6$-bearing mineral, particularly the results of papers 1 and 3.

Each of the three papers includes its own introduction, theoretical background, and review of past work, thus, this material will not be covered in detail here. All electronic structure calculations are performed in the local density approximation with the spin-polarized self-consistent charge $X\alpha$ (SCC $X\alpha$)

method, described in Grodzicki (1980) and Grodzicki et al. (1987), and summarized in the introduction to paper 1.

The first paper, "Hyperfine electric field gradients and local distortion environments of octahedrally coordinated Fe^{2+}" (Evans et al. 2005a), takes the elementary approach of calculating the quadrupole splitting V^* for various model clusters (FeO_6^{10-}, $Fe(OH)_6^{4-}$, and $Fe^{2+}O_6$-centred clusters of seven octahedra) while progressively distorting the cluster. That is, V^* is calculated as a function of a distortion parameter for an otherwise undistorted octahedron, and also for combinations of key distortions. This differs from the usual approach of electronic structure calculations, where a specific structure is imposed from a real material or from structural optimization. A similar approach was taken in my Master's thesis (Evans 2001, see below). If the effects of different distortions on the electric field gradient (EFG) were linear, then calculating the EFG as a function of the most important distortions in a particular material would be all that is required. However, in examining combinations of distortions, it was found that their effects do not combine linearly, particularly at finite temperatures where thermal population of the predominantly-Fe(3d) valence orbitals reduces the magnitude of V^*.

The main distortions examined in paper 1 are flattening of the octahedron, measured by the flattening angle ψ; uniform scaling of the Fe-O bond length, d; and counter-rotation of the top and bottom faces of the octahedron, measured by the angle δ. These three distortions together allow up to three distinct sites in an octahedral sheet (Evans 2001, Mercier et al. 2005). In examining the individual modes of distortion, the percent change in V^* over physically realistic ranges of the distortion in micas are compared to determine which distortion, if any, is the most important in determining the quadrupole splitting. This was found to be flattening, followed by chemical substitution in the neighbouring sites.

In addition to structural or geometric distortions, the effects of chemical disorder in neighbouring octahedral sites was also investigated. Paper 1 discusses exclusively the EFG invariant V^* which is proportional to the quadrupole splitting. Paper 2, "Hyperfine electric field gradient tensors at Fe^{2+} sites in octahedral layers: Towards understanding oriented single-crystal Mössbauer spectroscopy measurements of micas" (Evans et al. 2005b), expands the discussion for seven-octahedra clusters to other EFG tensor properties - the principal value V_{ZZ}, the asymmetry parameter η, and the Euler angles of the principal axes. These quantities are trivial in FeO_6^{10-} and $Fe(OH)_6^{4-}$ clusters - $\eta = 0$ and $V^* = -V_{ZZ}$ for distortions with

trigonal point-group symmetry, and the principal axes correspond to the crystallographic axes of the hypothetical octahedral sheet. In the larger seven-octahedra clusters with general formula $Fe(OH)_6(MgF_2OH_2)_n(AlF_2OH_2)_{6-n}^{(2-n)+}$, however, flattened clusters may be triclinic or monoclinic as well as trigonal, depending on how the neighbour sites are populated, so that all the EFG tensor components change with distortion. These other EFG parameters may be measured with oriented single-crystal Mössbauer spectroscopy.

In paper 2, the effects of flattening on the EFG tensor are investigated for the thirteen unique configurations obtained by populating the first nearest neighbour sites with combinations of Al^{3+} and Mg^{2+}, common cations of their respective valences in trioctahedral micas. Assuming complete chemical disorder in the hypothetical octahedral sheet, and that the fraction of Fe^{2+} sites is much smaller than the fractions of Mg^{2+} and Al^{3+} sites, it is a simple matter to calculate the populations of each of the unique configurations in the sheet. This allows the calculation of average EFG parameters given the overall ratio of Mg to Al content in the sheet, as well distributions of the EFG parameters due to chemical disorder. Paper 2 is thus a transition work between paper 1, which focuses on hyperfine parameters of single clusters as a function of specific distortions, and paper 3, which deals with means and distributions of hyperfine parameters for disordered ensembles of clusters.

Paper 3, "Simulated quadrupole splitting, isomer shift and hyperfine field distributions of octahedrally coordinated Fe^{2+} in Mössbauer spectroscopy from electronic structure calculations" (Evans et al. 2005c), abandons almost completely the attempt to find hyperfine parameters as simple functions of only a few distortion parameters. As a result, a far deeper understanding of the hyperfine parameters is achieved. Isomer shifts and hyperfine fields (as spin polarization of electrons at the nucleus) are calculated as well as quadrupole splitting and other EFG parameters. Ensembles of 1000 perturbed octahedra are generated by adding Gaussian-distributed random distortions to a starting $Fe(OH)_6^{4-}$ cluster of a given geometry. An electronic structure calculation is performed on each cluster to obtain the hyperfine parameters, and then distributions are calculated from the set of calculated parameters.

The effects on the hyperfine parameter distributions of different flattening angles, Fe-O bond lengths, and OH bond orientations for the starting $Fe(OH)_6^{4-}$ cluster are investigated, along with the changes in the distribution shapes, means and widths with increasing static disorder. The results of the

simulations are compared with models of hyperfine parameter distributions in disordered materials. Paper 3 also investigates the correlation between hyperfine parameters, and between the hyperfine parameters and different structural parameters. Finally, sample Mössbauer spectra, both doublets and generalized magnetic octets, are calculated and compared with analogous experimental spectra.

These three papers comprise the most complete theoretical exploration of the link between local structure and hyperfine parameters to date. Previous hyperfine parameter calculations using electronic structure methods (e.g. Blaha et al. 1992, Ellis et al. 1992, Terra and Ellis 1997, Terra and Ellis 1998, Guenzberger et al. 1998, Petrilli et al. 1998, Blaha et al. 2000, Neese 2002, Lougear et al. 2000, Lottermoser et al. 2002) have focused on hyperfine parameters in specific molecules or mineral sites, rather than the hyperfine parameters as functions of geometric distortions, without taking into account the effects of structural disorder. Simulations of hyperfine parameter distributions and the effects of static (Pustówka et al. 1973, Stöckmann 1981, Domes et al. 1986, Dengler et al. 1991) and/or chemical disorder (Billard et al. 1984, Dainyak and Drits 1987, Dainyak et al. 1992, Dainyak et al. 2004) have not thus far taken advantage of full electronic structure calculations, relying instead on point charge models and/or crystal field theory. There have been investigations of the correlation between hyperfine parameters and average distortion (Zhe and De Grave 1995, Zhe and De Grave 1998) but these likewise have not until now taken advantage of full electronic structure calculations. Models of the EFG tensor distributions have been derived from models of disordered materials (Varret and Henry 1980, Czjzek et al. 1981, Le Caer and Brand 1998), but these are only generally applicable to Fe^{3+} materials, as they deal only with the EFG due to point charges around the iron site, ignoring the EFG due to the anisotropy of the valence orbitals which is the dominant effect in Fe^{2+}.

Similar material to paper 1, together with crystal field theory and point charge calculations of EFGs and a first attempt at simulating quadrupole splitting distributions analytically, was presented in Evans (2001). The bulk of the electronic structure calculations in Evans (2001) were performed using a different electronic structure code, less suited to hyperfine parameter calculations.

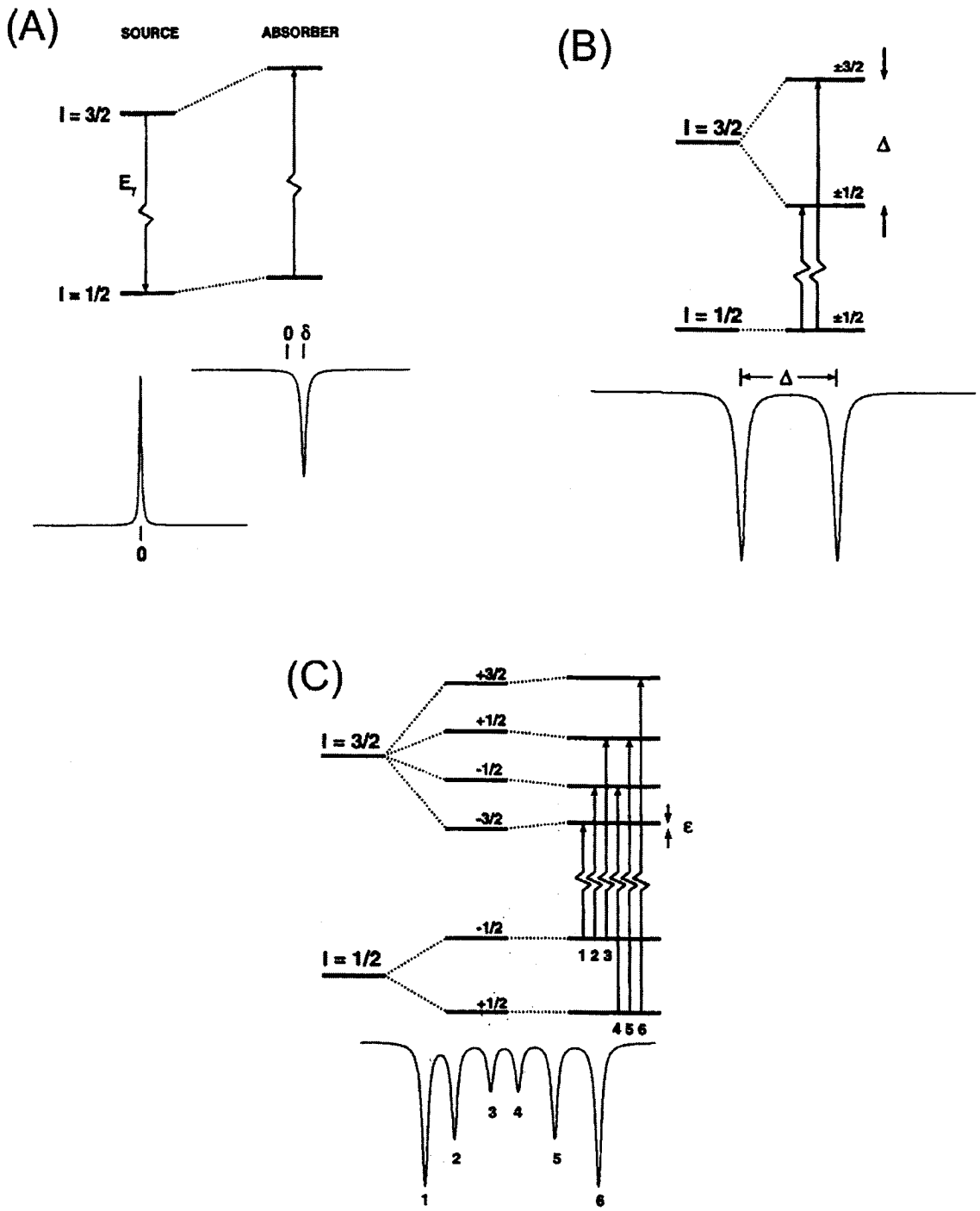

Figure 1. How different hyperfine interactions affect the ^{57}Fe nuclear ground (I = 1/2) and excited (I = 3/2) states, resulting in the hyperfine parameters of the Mössbauer spectrum: (A) centre shift, (B) quadrupole splitting, and (C) hyperfine field. From Rancourt (1998).

References

Blaha, P., Singh, D.J., Sorantin, P.I. and Scwarz, K. (1992) Electric-field gradient calculations for systems with large extended-core-state contributions. Physical Review B **46**, 1321-1325.

Blaha, P., Schwarz, K., Faber, W., and Luitz, J. (2000) Calculations of electric field gradients in solids: How theory can complement experiment. Hyperfine Interactions **126**, 389-395.

Czjzek, G., Fink, J., Götz, F., Schmidt, H., Coey, J. M. D., and Rebouillat, J.-P. (1981) Atomic coordination and the distribution of electric field gradients in amorphous solids. Physical Review B **23**, 2513-2529.

Dainyak, L.G., and Drits, V.A. (1987) Interpretation of Mössbauer spectra of nontronite, celadonite and galuconite. Clay and Clay Minerals **35**, 363-372.

Dainyak, L.G., Drits, V.A., and Heifitz, L.M. (1992) Computer simulation of cation distribution in dioctahedral 2:1 layer silicates using IR-data: Application to Mössbauer spectroscopy of a glauconite sample. Clay and Clay Minerals **40**, 470-479.

Dainyak, L.G., Drits, V.A., and Lindgreen, H.. (2004) Computer simulation of octahedral cation distribution an interpretation of the Mössbauer Fe^{2+} in dioctahedral trans-vacant micas. European Journal of Mineralogy **16**, 451-468.

Dengler, H., Leupold, O., Nagy, D. L., Ritter, G., Aubertin, F., Limbach, C. T., and Gonser, U. (1991) Distribution of hyperfine fields of $^{57}Fe^{2+}$ in amorphous $LiNbO_3$: Mössbauer study at low temperature in high magnetic fields. Hyperfine Interactions **69**, 667-672.

Domes, H., Leupold, O., Nagy, D. L., Ritter, G., Spiering, H., Molnár, B., and Szücs, I. S. (1986) Mössbauer study of short range order in frozen aqueous solutions of $Fe(ClO_4)_2$. Journal of Chemical Physics **85**, 7294-7300.

Ellis, D.E., Baggio Saitovitch, E., and Lam, D.J. (1992) Hyperfine interactions in iron substituted high-T_c superconducting oxides. Physica C **198**, 57-69

Evans, R. J., Rancourt, D. G., and Grodzicki, M. (2005a) Hyperfine electric field gradients and local distortion environments of octahedrally co-coordinated Fe^{2+}. American Mineralogist **90**, 187-198.

Evans, R. J., Rancourt, D. G., and Grodzicki, M. (2005b) Hyperfine electric field gradient tensors at Fe^{2+} sites in octahedral layers: Towards understanding oriented single-crystal Mössbauer spectroscopy measurements of micas. American Mineralogist **90**, 1540-1555.

Evans, R. J., Rancourt, D. G., and Grodzicki, M. (2005c) Simulated quadrupole splitting, isomer shift and hyperfine field distributions of octahedrally coordinated Fe^{2+} in Mössbauer spectroscopy from electronic structure calculations. In preparation for submission to Physics and Chemistry of Minerals.

Evans, R.J. (2001) The electric field gradient of octahedral Fe^{2+} in layer silicates. M.Sc. Thesis, University of Ottawa, Ottawa, Ontario, Canada.

Grodzicki, M. (1980) A self-consistent charge Xα method I. Theory. Journal of Physics B: Atomic and Molecular Physics 13, 2683-2691

Grodzicki, M., Männing, V., Trautwein, A.X., and Friedt, J.M. (1987) Calibration of isomer shift and quadrupole coupling for ^{119}Sn, ^{127}I and ^{129}I as derived from self-consistent charge Xα calculations and Mössbauer measurements. Journal of Physics B: Atomic and Molecular Physics 20, 5595-5625

Guenzberger, D., Ellis, D.E., and Zeng, Z. (1998) First principles calculations of Mössbauer parameters for

solids and large molecules. Hyperfine Interactions **113**, 25-36.

Le Caer, G. and Brand, R. A. (1998) General models for the distributions of electric field gradients in disordered solids. Journal of Physics: Condensed Matter **10**, 10715-10774.

Lottermoser, W., Steiner, K., Grodzicki, M., Jiang, K., Scharfetter, G., Bats, J.W., Redhammer, G., Teutmann, W., Hosoya, S., Amthauer, G. (2002) The electric field gradient in synthetic fayalite α-Fe_2SiO_4 at moderate temperatures. Physics and Chemistry of Minerals 29, 112-121

Lougear, A., Grodzicki, M., Bertoldi, C., Trautwein, A.X., Steiner, K., Amthauer, G.(2000) Mössbauer and molecular orbital study of chlorites. Physics and Chemistry of Minerals 27, 258-269

Mercier, P.H.J., Evans, R. J., and Rancourt, D. G. (2005) Geometric crystal chemical models for structural analysis of micas and their stacking polytypes. American Mineralogist **90**, 392-398.

Pustówka, A. J., Sawicka, B. D., and Sawicki, J. A. (1973) Electric field gradients in charge-perturbed lattices. Physica Status Solidi B **57**, 783-791.

Putnis, A. (1992) Introducton to Mineral Sciences, Cambridge University Press, Cambridge, U.K.

Rancourt, D.G. (1998) Mössbauer spectroscopy in clay science. Hyperfine Interactions **117**, 3-38.

Stadnik, Z. M. (1994) Mössbauer spectroscopy of quasicrystals. Hyperfine Interactions **90**, 215-227.

Stöckmann, H. (1981) Electric field gradients resulting from randomly distributed unscreened point charges. Journal of Magnetic Resonance **44**, 145-158.

Terra, J. and Ellis, D.E. (1997) Electronic structure, chemical bonding, and hyperfine parameters in layered silicates. Physical Review B 56, 1834-1847

Terra, J. and Ellis, D.E. (1998) Hyperfine interactions of *cis* and *trans* octahedral Fe^{2+} sites in the layered silicate annite. Journal of the American Ceramic Society 81, 465-468

Varret, F. and Henry, M. (1980) Amorphes ioniques: caractères spécifiques d'une étude Mössbauer (isotope ^{57}Fe). Revue de Physique Appliquée **15**, 1057-1061.

Zhe, L. and De Grave, E. (1995) Correlation of Fe^{2+} isomer shifts with bond lengths and bond strengths in neso- and sorosilicates. Science in China B **38**, 478-483.

Zhe, L. and De Grave, E. (1998) The Fe^{2+} quadrupole splitting at octahedral sites in chain silicates: correlations with the site-distortion parameters. Hyperfine Interactions **116**, 173-178.

Hyperfine electric field gradients and local distortion environments of octahedrally coordinated Fe^{2+}

R. James Evans[1], Denis G. Rancourt[1], and Michael Grodzicki[2]
[1] Department of Physics, University of Ottawa, Ottawa, Ontario, Canada K1N 6N5
[2]Institute of Mineralogy, University of Salzburg, A-5020 Salzburg

Abstract

We report ab initio electronic structure calculations that directly relate given local chemical and distortion environments to corresponding hyperfine electric field gradients (EFGs) in ^{57}Fe Mössbauer spectroscopy, thereby giving needed interpretive power to the technique in characterizing $^{[6]}Fe^{2+}$ environments in minerals. Changes of the EFG with various distortions were investigated on model clusters, including the bare octahedra FeO_6^{10-} and $Fe(OH)_6^{4-}$, and various seven-octahedra sections of an octahedral sheet, through self-consistent charge $X\alpha$ ab initio calculations. Distortions examined for all clusters were flattening, counter-rotation and bond scaling, as well as changes in neighbor bond lengths and the identity and ordering of neighbor cations for the seven-octahedra clusters. The evolution of the EFG with distortion was derived at $T = 0$ K and $T = 300$ K as a function of the distortion parameters. We find that the percent change in the EFG over the range of distortion parameters found in 1M trioctahedral micas is greatest with flattening for the clusters compared, suggesting that flattening is the most important structural distortion in determining the EFG. The EFGs for the seven-octahedra cluster as a function of flattening were compared for thirteen configurations of Mg^{2+} and Al^{3+} cations in the first nearest neighbor octahedra. The percent change in the EFG for flattening and cation substitution was found to be of similar magnitude. In comparing EFG vs. flattening curves with measured quadrupole splitting distributions (QSDs), the magnitudes of the theoretical curves agree well with experiment. The sharp high quadrupole splitting edge is explained by the presence of a maximum in the EFG vs. flattening curve. These model calculations are a necessary first step in establishing a firmer link between local structural distortions in minerals and measured QSDs.

Introduction

The ^{57}Fe Mössbauer spectra of minerals contain a great deal of information about chemical and physical structure in the form of distributions of hyperfine parameters. However, a major barrier to the wider use of Mössbauer spectroscopy in the Earth sciences is uncertainty in how to interpret these distributions (Rancourt 1998). The quadrupole splitting (QS) is a key local hyperfine parameter that has such a distribution of values for a give sample. It is a splitting of nuclear energy levels due to the interaction of the ^{57}Fe nuclear quadrupole moment with the electric field gradient (EFG) at the nucleus. The EFG is a property of the iron's electronic structure, which is highly sensitive to the local distortion environments of the iron atom. Chemical and structural disorder leads to distributions of local environments for the ^{57}Fe atom, which is why the Mössbauer spectrum of a given sample must be described not by a single quadrupole splitting, but by a distribution. In order to interpret quadrupole splitting distributions (QSDs), electronic structure calculations are needed to determine how specific local distortion environments affect the EFG (Rancourt 1998; Rancourt et al. 1994), and this has not previously been attempted by ab initio methods.

The $^{[6]}Fe^{2+}$ coordination polyhedra occur in many different types of crystal structure (c.f., Mottanna et al. 2002, Bailey 1984, Bailey 1988, Veblen 1981, Prewitt 1980, Ribbe 1980, Burns 1993, Anthony et al. 1995). Often the main distortions found in the octahedra are determined by how they are connected within the overall structure. An important class of local distortions are those that are uniform (i.e., each Fe-O bond is affected in the same way) and trigonally symmetric (i.e., one of the octahedron's C_3 axes is preserved). Three of these are considered here - flattening, counter-rotation, and bond scaling. The motivation for studying these particular distortions is that they are important in layer silicates, where they are required to fit octahedra of different sizes into a sheet of uniform thickness (Evans 2001). The change in the EFG is investigated as these distortions are applied systematically. Previous studies have used electronic structure methods to calculate hyperfine parameters in octahedrally coordinated Fe^{2+} (e.g., Terra and Ellis 1997, Terra and Ellis 1998, Ellis et al. 1992, Lougear et al. 2000, Lottermoser et al. 2002), but this is the first to use systematically distorted model clusters to investigate how specific distortions affect the EFG. Our goal is to use these artificial model clusters to establish a specific link between geometric distortions of an octahedral Fe^{2+} site and the EFG, which will then allow future studies to better explain and interpret QSDs.

One of the main questions in this investigation is whether there is one distortion more than any others that determines the magnitude of the EFG. Changes in EFG over the range of parameters seen in real materials are compared with each other for several different model clusters. Small octahedral clusters FeO_6^{10-} and $Fe(OH)_6^{4-}$ represent bare octahedra. The effects of near neighbor sites are also important, and differ from crystal structure to crystal structure, however many interesting features can be discerned through the abstraction of bare octahedra. As an example of near neighbor effects, seven-octahedra clusters representing sections of a brucite-like octahedral sheet are examined, both with the trigonal structural distortions and cation substitutions in sites adjacent to the central Fe^{2+} octahedron.

Although it may seem academic to investigate single octahedra, we find that the EFGs in these simpler systems are sufficiently similar to those in larger, more realistic systems that studying these small clusters, and comparing them with calculations on larger clusters, can reveal important features. Moreover, results on single octahedra can (to a good first approximation) be widely applied to many systems, to octahedra in sheets, in chains or in other structures, provided the limitations of the small clusters are kept in mind.

Theory

Definition of distortions and sheet geometry

Bond scaling is simply a uniform change in all six Fe-O bond lengths, from d to $d + \Delta d$. The other two distortions, flattening and counter-rotation, leave the bond lengths constant and only change the bond angles and octahedral edge lengths.

Let the z-axis correspond to one of the C_3-axes of symmetry of the undistorted octahedron, a line running through the midpoint of two opposite faces (called the top and bottom faces) and the geometric center of the octahedron. Flattening is the distortion where the thickness of the octahedron along the z-axis is reduced while the top and bottom faces expand (figure 1a and 1b). In an octahedral sheet, this corresponds to a reduction in the thickness of the sheet accompanied by a lateral expansion. The flattening angle ψ, first defined by Donnay et al. (1964) and Hazen and Wones (1972), is defined as the angle between one of the bonds and the normal to the top and bottom faces (i.e., the z-axis), and for an undistorted octahedron $\psi_{ideal} = \tan^{-1}\sqrt{2} \approx 54.74°$. The thickness of a flattened octahedron with bond length d and flattening angle ψ is $2d\cos\psi$. In a flattened octahedron, the edges forming the top and bottom faces

(the unshared edges in a sheet) and the edges connecting the top to the bottom face (shared edges in a sheet) are no longer equal, but there is only one unshared edge length and one shared edge length.

Counter-rotation involves rotating the upper and lower faces in opposite directions, each in their respective planes (figure 1c). Each face is rotated by an amount δ, the counter-rotation angle. This definition of the counter-rotation angle differs by a factor of two from the angle defined elsewhere (Weiss et al. 1985, 1992), as it is more convenient mathematically, eliminating a factor of 1/2 in many equations. Introducing counter-rotation produces two unequal shared edge lengths, but the unshared edge lengths are unchanged.

The result of two different shared edge lengths is that, with flattening and counter-rotation, three unique sites can be fit into an octahedral sheet of constant thickness, each with a unique bond length d_i, flattening angle ψ_i and counter-rotation δ_i. The three bond lengths d_1, d_2, d_3, and one flattening angle are sufficient to determine all other parameters in the sheet; the relations are derived in Evans (2001).

Following Weiss et al. (1985) and Mercier (2003), we shall refer to octahedral sheets where d_1, d_2 and d_3 are all distinct as geometric hetero-octahedral, sheets where only two of d_1, d_2 and d_3 are unique as geometric meso-octahedral, and sheets where $d_1 = d_2 = d_3$ as geometric homo-octahedral. In geometric hetero-octahedral sheets, the ψ_i are also all distinct and none of the δ_i are zero. In geometric meso-octahedral sheets, if we take $d_1 = d_2 \neq d_3$ then $\psi_1 = \psi_2 \neq \psi_3$, $\delta_1 = -\delta_2$ and $\delta_3 = 0°$. In geometric homo-octahedral sheets, all ψ_i are equal and all δ_i are zero.

Calculation methods and model clusters

Electronic structure calculations were performed in the local density approximation with the spin-polarized self-consistent charge Xα (SCC Xα) method. The method is described in detail in Grodzicki (1980) and Grodzicki et al. (1987), and has proven to give reliable hyperfine parameters and magnetic properties for a wide variety of large and small transition metal complexes (Lougear et al. 2000; Lottermoser et al. 2002; Grodzicki et al. 2001; Grodzicki and Amthauer 2000).

In SCC Xα, the molecular potential is factored into a radial function and a series of spherical harmonics, allowing analytical integration of the angular parts of all Hamiltonian matrix elements. The respective integrals are separated into one-, two- and three-center integrals. The one-center and multi-center

integrals are treated with different levels of accuracy. One-center integrals require high accuracy, and are derived numerically from all-electron, relativistic atomic calculations with a semi-local (gradient corrected) exchange correlation functional (Becke 1988) and a local correlation functional (Vosko et al. 1980). The two- and three-center integrals are evaluated with small basis sets (2s, 2p for O and F; 3s and 3p for Mg and Al; 3d, 4s and 4p for Fe) and the Slater Xα potential with $\alpha = 0.7$ for the valence electrons; core electrons are treated with simple pseudopotentials that are also derived from relativistic atomic calculations and are kept frozen during the iteration process.

The one-center integrals are calculated beforehand and entered as atom-specific parameters in subsequent calculations. Thus only the small, fast calculations need to be done anew each time, so that the calculation of large clusters (or very many small clusters) is very efficient, while still being ab initio in that there are no adjustable parameters.

The electric field gradient elements with the Mössbauer atom at the origin are

$$V_{ij} = \left. \frac{\partial^2 V(\mathbf{r})}{\partial x_i \partial x_j} \right|_{\mathbf{r}=\mathbf{0}}, \tag{1}$$

where $V(\mathbf{r})$ is the electrostatic potential. The eigenvalues of V_{ij} are denoted V_{XX}, V_{YY} and V_{ZZ} in order of increasing absolute magnitude. The direction of the eigenvector associated with V_{ZZ} is called the principal direction of the EFG. The asymmetry parameter η is given by

$$\eta = \frac{V_{XX} - V_{YY}}{V_{ZZ}}. \tag{2}$$

Finally, we define

$$V^* = |V_{ZZ}| \sqrt{1 + \frac{\eta^2}{3}}. \tag{3}$$

The quadrupole splitting is then $\Delta = (1/2)e^2 Q V^*$ (where Q is the nuclear quadrupole moment of the first excited state of the ^{57}Fe nucleus). EFGs are reported in atomic units (au), which are converted to the usual units of mm/s used in Mössbauer spectroscopy by the conversion 1 au = $10.11Q$ mm/s; using the value of Q = 0.16 barn given in Dufek et al. (1995) means multiplying the atomic units by 1.62 gives the value in mm/s. The sign of V_{ZZ} in equation 3 is ignored, since this sign does not affect the experimentally measured quadrupole splitting or quadrupole splitting distributions in most (i.e., random powder absorber) Mössbauer

spectroscopy measurements. The sign of V_{ZZ} can be determined by oriented single crystal or oriented mosaic Mössbauer experiments, that we discuss in a forthcoming paper.

In the SCC-Xα code, the EFG is calculated from integrating the charge density multiplied by the tensor operator

$$V_{ij}(r) = \left(\frac{1-\gamma(r)}{r^3}\right)\left(\frac{3x_i x_j - r^2\delta_{ij}}{r^2}\right), \tag{4}$$

where γ(r) is the Sternheimer shielding function, arising from the polarization of the core Fe electrons by charges outside the core. It is derived from atomic self-consistent first order perturbation calculations (Lauer et al. 1979). The calculation of hyperfine parameters within the framework of a valence electron-only molecular orbital method has been described in detail previously (Grodzicki et al. 1987, Grodzicki and Amthauer 2000). In particular, the EFG is decomposed into valence, covalence and ligand contributions, corresponding to the Fe(3d) anisotropy, cation-ligand integrals and ligand-ligand integrals of atomic orbitals. In high spin Fe^{2+}, the valence contribution dominates the EFG by about an order of magnitude. For example, the room-temperature V_{ZZ} calculated for the cluster $Fe(OH)_6^{4-} \bullet 6(MgF_2OH_2)$ with a flattening angle of 58° is -1.422 au (-2.304 mm/s); the valence component of V_{ZZ} in this case is -1.548 au (-2.508 mm/s), the ligand component is +0.097 au (+0.157 mm/s), and the covalence component is +0.029 au (+0.047 mm/s).

Room temperature EFGs were approximated by first performing zero-temperature calculations to determine the relative orbital energies E_i; these energies were used to calculate thermal average populations n_i for each orbital thermodynamically:

$$n_i = \frac{\exp(-E_i/kT)}{\sum_j \exp(-E_j/kT)}. \tag{5}$$

In practice this was only done for the spin-down t_{2g} Fe(3d) orbitals (see discussion below), the lowest energy of which is the highest fully occupied molecular orbital. Those orbitals below these three remain fully occupied at finite temperatures, and the last two unoccupied spin-down orbitals, the e_g*-like orbitals, are high enough above the t_{2g} in energy that their occupation at T = 300 K is negligible (with occupation numbers less than 10^{-7}). The SCC Xα calculation is then repeated with the spin-down t_{2g} orbitals given

their thermal average populations. The orbital energies of the second calculation are generally shifted only a few meV from those of the zero-temperature calculations.

Thermal population of molecular orbitals is only one effect temperature has on electronic structure; changes in atomic positions themselves may be equally important. These include, thermal vibration of atoms about an equilibrium position and changes in the equilibrium positions themselves (e.g., through thermal expansion). The time scale of Mössbauer spectroscopy, dictated by the nuclear transition of the ^{57}Fe (Rancourt 1998), is normally much longer than that of thermal vibration. Mössbauer spectroscopy therefore usually only sees the atoms' equilibrium positions. As for changes in the crystal structure with temperature, the current study is not intended to simulate the actual room temperature structure or EFG of any particular material; rather, given a particular structure at T = 0 K or 300 K, we are asking what the resulting hyperfine parameters would be.

Distortions were applied to three types of model clusters - FeO_6^{10-} ; $Fe(OH)_6^{4-}$, where the OH bonds are normal to the top and bottom faces of the octahedron; and $Fe(OH)_6^{4-} \bullet n[MgF_2OH_2] \bullet (6 - n)[AlF_2OH_2^+]$ for n from 0 to 6 (see figure 2). This latter cluster represents a seven octahedron section of a brucite-like octahedral sheet. The center octahedron is occupied by an Fe^{2+} cation, and the six nearest neighbor octahedra are occupied by either Mg^{2+} or Al^{3+}, chosen as simple (i.e. d-orbital free) representative cations of their respective valences common in layer silicates. The six OH bonds on the central octahedron are normal to the sheet. A mixture of F^- and OH_2 ligands terminates the edge of the cluster. It has been found (Lougear et al. 2000) that using incompletely terminated oxygen atoms at the cluster edge can lead to convergence problems due to unsaturated O(2p) lone pairs in the same energy range as the Fe(3d) orbitals. Replacing OH^- with F^- at the corners and waters at the bridging positions eliminates the problem by bringing the edge ligand 2p energies down to their expected levels. It additionally helps to reduce the overall cluster charge. This is desirable both for the technical reason that calculations for clusters with small charges tend to converge more easily, and in that it is closer to reality in that molecules and most crystal unit cells are electrically neutral.

Results from crystal field theory

From crystal field (Burns 1993) and simple molecular orbital models (Burdett 1980), the five highest occupied molecular orbitals in the FeO_6-centred clusters are primarily Fe(3d) in character. Ferrous iron is generally high-spin in minerals, with the five Fe(3d)-like spin-up molecular orbitals fully occupied whereas the remaining sixth d-electron occupies the lowest d-like spin-down molecular orbital. Since spin-up and spin-down electrons experience different exchange potentials, this occupation scheme results in a considerable splitting between spin-up and spin-down orbitals in the range between 2 and 3 eV ("exchange splitting"). Consequently, the occupied spin-up orbitals are in the same energy range as the ligand p-orbitals and both are strongly mixed. On the other hand, the (partially occupied) spin-down 3d-like orbitals are well above all the occupied molecular orbitals and are almost pure Fe(3d)-orbitals. The character of the occupied spin-down 3d-orbital then determines the sign of V_{ZZ} and the principal direction of the EFG.

In an octahedral crystal field, the five d-orbitals are split into triply-degenerate t_{2g} (approximately non-bonding) and doubly-degenerate e_g* (anti-bonding) orbitals. For the trigonally distorted octahedron, the t_{2g} orbitals are split into a single a_{1g} and doubly degenerate e_g orbitals. In FeO_6, the a_{1g} orbital, which is primarily of 3d z^2 character, is the lowest in energy when $\psi > 54.74°$ and $|\delta| > 0°$; in this state V_{ZZ} is negative. When $\psi < 54.74°$, the two e_g orbitals are lowest in energy and there is a degenerate ground state; in this state, V_{ZZ} is positive and smaller in magnitude. (In fact, $V_{ZZ}(\psi_{ideal} + d\psi) = -\frac{1}{2}V_{ZZ}(\psi_{ideal} - d\psi)$ as $d\psi$ approaches zero.) In both cases, $\eta = 0$, since $V_{XX} = V_{YY} = -\frac{1}{2}V_{ZZ}$, and the EFG principal direction is along the z-axis. The asymmetry parameter η is non-zero and the principal direction begins to tilt away from the z-axis when FeO_6 is distorted away from trigonal symmetry. When $\psi = \psi_{ideal}$, the EFG is identically zero. This latter effect is specifically an artifact of the ideal octahedral symmetry of the undressed FeO_6 cluster, and does not occur for larger clusters (see below).

From crystal field calculations using point charges, V_{ZZ} for an octahedron with bond length d, flattening angle ψ and counter-rotation δ at $T = 0$ is

$$V_{ZZ} = -A_{val} + \frac{B_{lat}}{d^3}\left(\frac{1-3\cos^2\psi}{2}\right). \qquad (6)$$

The coefficients A_{val} and B_{lat} contain the Sternheimer factors, and B_{lat} is a positive constant. The first term in equation 6 is the valence term, analogous to the SCC-Xα valence contribution described above, and the

second term is the lattice term, analogous to the SCC-Xα ligand contribution. (The covalence contribution is ignored in this simple approximation.) In the point charge approximation, the valence term is constant with respect to all distortions, and the sign and magnitude of A_{val} depends only on the electronic ground state of the cluster. The lattice term is an electrostatic sum due to the point charge near-neighbors of the Fe^{2+} cation, and is small compared to the valence term. In this approximation the EFG is independent of counter-rotation.

Taking Taylor expansions of equation 6 about $\psi = \psi_0$ and $d = d_0$,

$$V_{ZZ}(d_0,\psi) = V_{ZZ}(d_0,\psi_0) + \frac{3}{2}\frac{B_{lat}}{d_0^3}(\sin 2\psi_0)\Delta\psi + O(\Delta\psi^2) \tag{7}$$

and

$$V_{ZZ}(d,\psi_0) = V_{ZZ}(d_0,\psi_0) - 3\frac{B_{lat}}{d_0^3}\left(\frac{1-3\cos^2\psi_0}{2}\right)\frac{\Delta d}{d_0} + O\left(\frac{\Delta d^2}{d_0^2}\right), \tag{8}$$

where $\Delta d = d - d_0$ and $\Delta\psi = \psi - \psi_0$. For small deviations Δd and $\Delta\psi$, V_{ZZ} is linear with a positive slope versus $\Delta\psi$ (for all ψ_0) and a negative slope versus Δd (for $\psi_0 \geq 54.74°$). Then from equation 2, we expect zero temperature graphs of V^* vs. ψ to be negatively sloped at all bond lengths, and V^* vs. d to be positively sloped for $\psi \geq 54.74°$, over small ranges of d and ψ. As shown below, these conclusions are supported by the calculated EFGs at T = 0 K.

Results and Discussion

Flattening alone

Figure 3 shows V^* vs. ψ calculated for three different clusters - FeO_6^{10-}, $Fe(OH)_6^{4-}$ and $Fe(OH)_6^{4-} \bullet 6(MgF_2OH_2)$ (henceforth abbreviated as 7-oct.), all with Fe-O bond length d = 2.11 Å and $\delta = 0°$. In the 7-oct. cluster, the Mg-O and Mg-F bond lengths were also 2.11 Å; when flattening angle is reported for any seven-octahedra cluster, it is the flattening angle of the central Fe^{2+} that is given. Figure 3a shows V^* at T = 0 K. With the exception of jump discontinuities in two of the curves, V^* is linear with respect to ψ with negative slope as predicted in equation 6 for each cluster, thus the change in the EFG's valence term with flattening is small compared to the change in the lattice term. The curve for FeO_6^{10-} (squares) is

discontinuous at $\psi_{ideal} = 54.74°$, being zero at ψ_{ideal}, when the octahedron is undistorted, and around 2 au above ψ_{ideal}. Below ψ_{ideal} (not shown), V^* for FeO_6^{10-} takes values around 1 au. The corresponding values of V_{ZZ} (also not shown) are positive below ψ_{ideal} and negative above. At ψ_{ideal}, the three spin-down t_{2g} orbitals are degenerate, and the cluster's lone spin-down d-electron is shared between them. When ψ does not equal ψ_{ideal}, the degeneracy of the t_{2g} orbitals is partially lifted, and we are left with a doubly degenerate e_g orbital and an a_{1g} orbital, the z^2 orbital. Above ψ_{ideal} , the a_{1g} orbital is lowest in energy, and thus occupied by the spin-down d-electron. Below ψ_{ideal}, the e_g orbitals are lowest in energy, so the ground state is again degenerate and the spin-down d-electron is shared between them. This is how the electron ground state and the EFG change with flattening for a bare, undistorted octahedron with no additional groups attached, with ψ_{ideal} being the critical angle flattening angle for the change in V_{ZZ}, V^* and the order of the spin-down d-orbitals.

Larger clusters, such as $Fe(OH)_6^{4-}$ and 7-oct., that are more than a single, bare octahedron do not show such discontinuities at ψ_{ideal}. In the curve for $Fe(OH)_6^{4-}$ (circles), there is no discontinuity in V^*, which is around 2 au for all ψ shown, and V_{ZZ} is strictly negative. The presence of the OH bonds, which break the cluster's ideal octahedral symmetry at ψ_{ideal}, has shifted the critical flattening angle to some ψ below ψ_{ideal}. The OH bonds lie parallel to the z-axis, and so stabilize the z^2 (a_{1g}) d-orbital with respect to the e_g orbitals, which lie more in the xy-plane.

In the curve for the 7-oct. cluster (triangles), for $\psi \leq 56°$, V^* is about 1 au and V_{ZZ} is positive. Past 56°, V^* jumps to around 2 au and V_{ZZ} becomes negative. Here the six near-neighbor octahedra, which have the cluster as a whole lying more in the xy-plane, have stabilized the d-orbitals in the opposite way as happened in $Fe(OH)_6^{4-}$, and the critical flattening angle has been pushed above ψ_{ideal} to about 56°.

In figure 3b we see how V^* changes with flattening at room temperature ($T = 300$ K). When moving from zero to finite temperature, discontinuities such as those in figure 3a are replaced by continuous curves. As ψ increases, V_{ZZ} (not shown) changes continuously from positive to negative values, reaching a maximum in absolute value and then approaching the zero temperature curve at high flattening angles. Since all three clusters are trigonally symmetric, $\eta = 0$ and so V^* is just the modulus of V_{ZZ}. So at room temperature, V^* decreases from about 1 au at low ψ to zero in a cusp-like minimum (a result of ignoring

the sign) then increases steeply to a maximum value (at ~58° for $Fe(OH)_6^{4-}$, ~61° for FeO_6^{10-} and 7-oct.), after which it decreases and approaches the zero temperature curve (near 2 au) at high ψ. All three V^* curves in figure 3b show this behavior, though only the 7-oct. curve has a critical flattening angle high enough that we see the low ψ decreasing section and the cusp minimum.

In order to determine whether one particular distortion affects the EFG more than others, it is necessary to estimate the range of values the distortion parameter typically assumes. Mercier (2003) has compiled a database of 170 structural X-ray diffraction refinements of 1M trioctahedral micas. From this data we have taken minimum and maximum values for the flattening angle ψ, the counter-rotation angle δ and the bond length d, given in table 1. A range of 57° to 61° covers the flattening angles found in micas. The samples with lowest flattening angles are several Mn-bearing biotites (Knurr and Bailey 1986, Kato et al. 1979) and a norrishite (Tyrna and Guggenheim, 1991), and those with highest flattening angles are samples with germanium in their tetrahedral sheets (Toraya et al. 1978, Toraya and Maramo 1981), and an iron-rich biotite (Tepikin et al. 1969), although this latter sample appears highly flattened (59.6°) compared with most biotites (which generally fall between 58° and 59.5°). The change in V^* over the range ψ = 57° to 61° for each of the three clusters is given in table 2. The percent change in V^* over the domain is calculated as

$$\frac{\left|V^*(\max) - V^*(\min)\right|}{V^*(\psi = 58°)} \times 100\% . \tag{9a}$$

If an intermediate extremum (maximum or minimum) occurs between the two endpoints, the location of the extremum is given followed by the approximate value of V^* at that point, and the percent change is calculated as

$$\frac{\left|V^*(\max) - V^*(IE)\right| + \left|V^*(IE) - V^*(\min)\right|}{V^*(\psi = 58°)} \times 100\% . \tag{9b}$$

The results from table 2 are that the change in V^* with flattening is an order of magnitude less in the domain of 57° to 61° for the $Fe(OH)_6^{4-}$ cluster (5.6%) than for the FeO_6 and 7-oct. clusters (50% and 68% respectively). This is because the shift of the T = 0 K discontinuity to ψ < 54.74° also shifts the region of the sharp increase in V^* out of the range of observed flattening angles.

The cluster energy calculated in the SCC-Xα code is the total atomization energy, the energy required to separate the cluster into its component ions at infinity. Graphs of calculated energies versus flattening angle for the three clusters are shown in figure 4, relative to the undistorted cluster ($\psi = 54.74°$). Two of the energy curves show a minimum: FeO_6^{10-} at $\psi_{ideal} = 54.74°$ and $Fe(OH)_6^{4-}$ at about 57°. This suggests that the flattening angles seen in layer silicates are at least partly due to bonding effects, and not solely determined by fitting requirements between octahedral and tetrahedral sheets. Peterson et al. (1979) previously studied total energies versus flattening for clusters of three Mg-centered octahedra and two Al-centered octahedra using CNDO/2 molecular orbital calculations, and found minimum energies at 59.7° (based on Mg-O bond length and shared edge length) and 57.1° (based on Al-O bond length and octahedral thickness) for the two clusters. The energy curve for the 7-oct cluster has a discontinuity at about 56.5°, the origin of which is not clear, but which may be a cluster artifact, meaning that we expect it to disappear for larger, more complete clusters.

Bond length scaling

Figures 5a, 5b and 5c show V^* vs. d curves for FeO_6^{10-}, $Fe(OH)_6^{4-}$ and 7-oct respectively at $T = 0$ K, at two different flattening angles ($\psi = 58°$ and $\psi = 60°$). In the 7-oct cluster, bond lengths in all octahedra are scaled. In each case V^* increases with d as predicted in equation 8, with the $\psi = 58°$ curve lying above the $\psi = 60°$ curve. Again this implies that changes in the valence term of the EFG with bond length are small compared to changes in the lattice term. Figure 6 shows V^* vs. d curves at $T = 300$ K. How V^* varies with d at room temperature depends strongly on both the flattening angle and the cluster.

Two different ranges for bond length found in micas are given in table 1. The average metal-oxygen bond length of all cation sites in the octahedral sheet is labeled d_{sheet}. By taking the minimum and maximum average bond lengths in the population studied by Mercier (2003), we have a range of 2.01 Å to 2.13 Å. However, we are only interested in the range of possible $^{[6]}Fe^{2+}$-O bond lengths. Unless there is strict ordering of cations among crystallographically distinct sites, which is not usually the case, average bond lengths from structural X-ray diffraction refinements are not useful for determining ranges for specific metal-oxygen bond lengths. Additionally, in many materials, including 1M micas, there frequently are more cations present than there are distinct octahedral sites.

Mercier (2003) also performed a detailed analysis on $^{[6]}$M-O bond lengths for several cations, using data reported for various micas and olivines. An average $^{[6]}Fe^{2+}$-O bond length of 2.126(11) Å was found, slightly higher than the base value of 2.11 Å used for most of this work, taken from Weiss et al. (1985). The range of values assumed by $d_{Fe}2+$ was about 2.10 Å to 2.16 Å. Despite the upper limit being higher than that observed for d_{sheet}, this was taken as the range of possible values for d within the central FeO_6 octahedra of all of our clusters.

The variation of the EFG as d varied from 2.10 Å to 2.16 Å at constant flattening angle is given in table 3. The percent change in EFG was calculated as in equation 9, except $V^*(\psi = 60°)$ was used in the denominator for clusters where $\psi = 60°$. There is considerable variation with the percent change as the constant flattening angle is changed, the most extreme being a drop from 20% at $\psi = 58°$ to only 0.49% at $\psi = 60°$ for the 7-oct. cluster. Comparing these changes with those in table 2, we see that the percent change with bond scaling is considerably smaller than that with flattening for each cluster: 4.0% vs. 50% for FeO_6^{10-}, 1.8% vs. 5.6% for $Fe(OH)_6^{4-}$, and 20% vs. 68% for 7-oct. This result is not surprising since the EFG is determined by the anisotropy of the Fe 3d-shell, which generally exhibits only minor variations if all bond lengths are changed by an equal amount. Such a behavior has earlier been obtained for a series of iron-bearing clinozoisites (Grodzicki et al. 2001).

Figure 7 shows V^* vs. ψ curves for FeO_6^{10-}, $Fe(OH)_6^{4-}$ and 7-oct clusters of different bond lengths at T = 300 K. The flattening/EFG curves at higher and lower bond lengths are qualitatively the same as at d = 2.11 Å. An increase in bond length causes the maximum to shift to higher ψ. At low ψ, $d_1 < d_2$ implies $V^*_1 > V^*_2$; at high ψ, $d_1 < d_2$ implies $V^*_1 < V^*_2$.

In figure 7c, flattening/EFG curves for 7-oct. clusters with $d_{Fe} = d_{Mg}$ = 2.06 Å and 2.11 Å (i.e., all seven octahedra have the equal bond lengths) are plotted along with one where d_{Fe} = 2.11 Å and d_{Mg} = 2.06 Å (i.e., d = 2.11 Å for the central octahedron and d = 2.06 Å for the six neighboring octahedra). This latter cluster corresponds to a section of a geometric meso-octahedral sheet where one third of the sites are occupied by Fe^{2+} and two thirds by the smaller Mg^{2+} cation. In this cluster, the six neighbor octahedra have non-zero counter-rotation angles. At T = 0 K (not shown, see supplementary figure S1), V^* is nearly equal in the geometric meso-octahedral cluster and the d = 2.11 Å 7-oct. cluster after the discontinuity (as should be expected, since both clusters have an identical central octahedron), but the discontinuity is shifted to a

higher flattening angle. As a result, the maximum in the T = 300 K curve is also shifted to higher ψ, and V^* at low ψ is considerably lower in magnitude for the geometric meso-octahedral cluster than for the two geometric homo-octahedral 7-oct. clusters.

Counter-rotation and near-neighbor bond length

Graphs of V^* as a function of counter-rotation angle are given in figure 8 for FeO_6^{10-} and $Fe(OH)_6^{4-}$ at $T = 0$ K and 300 K. In an octahedral sheet, counter-rotation of the central octahedron is not possible without distorting the six neighbor octahedra as well, so in order to study the effects of counter-rotation alone, we only consider the two clusters of bare octahedra.

In each case V^* increases non-linearly with $\delta > 0°$, having a minimum at $\delta = 0°$. For a bare octahedron, a cluster with counter-rotation $\delta > 0$ is a mirror image of one with counter-rotation $-\delta$ and so by symmetry V^* will be equal. In table 1, we find that $|\delta|$ ranges from near 0° to 3.5° in 1M micas; the calculated percent change in V^* from equation 9 is 11% for FeO_6^{10-} and 1.4% for $Fe(OH)_6^{4-}$ (see table 4).

Figure 9 shows V^* vs. ψ for FeO_6^{10-} and $Fe(OH)_6^{4-}$ for several constant counter-rotations at T = 300 K. The main effect of increasing counter-rotation is to translate the curve to higher V^* values by a small amount.

In the octahedral sheet, counter-rotation occurs when neighboring octahedra have different bond lengths. In figure 2, let the central Fe^{2+} octahedron have bond length d_1, sites M2, M4 and M6 have bond length d_2 and sites M1, M3 and M5 have bond length d_3. In a geometric meso-octahedral sheet, two of d_1, d_2 and d_3 will be equal. If we keep d_1 fixed at 2.11 Å as we have been doing, there are two ways to accomplish this. In cluster NCR, d_1 is held constant and $d_2 = d_3 \neq d_1$ is varied, and the Fe^{2+} octahedron has zero counter-rotation. In cluster CR, d_1 and d_2 are held constant and equal, $d_3 \neq d_1$ alone is varied, and the counter-rotation of the Fe^{2+} octahedron, δ_1, varies with d_3. This counter-rotation is positive when $d_3 > d_1$ and negative when $d_3 < d_1$.

Figure 10 shows V^* as a function of the neighbor bond length d_3 for both clusters. The EFG increases with d_3 at 0 K and 300 K more steeply for NCR than for CR. When $d_3 < d_1$, V^*(NCR) < V^*(CR), and when $d_3 > d_1$, V^*(NCR) > V^*(CR). In NCR, the Fe^{2+} octahedron in the middle remains unchanged as we change d_3, so changes in the EFG are purely due to effects of the neighbor octahedra. However in cluster CR, the

EFG is due to the combined effects of counter-rotation of the Fe^{2+} octahedron as well as the neighbor octahedra. From equation 6, the EFG due to the counter-rotation has no lattice point-charge component, and is purely due to covalent bonding and the spatial extension of the cluster's electron clouds. The near-neighbor octahedra contribution, however, is predominantly a point charge one proportional to $1/\rho^3$, where ρ is the cation-cation distance; there is very little electron density along the Fe^{2+}-Mg^{2+} lines.

From the maximum and minimum values of d_{sheet} in table 1, we suppose that the near-neighbor octahedral bond lengths range from about 2.01 Å to about 2.13 Å. The variation of V^* over this domain is given in table 5; the percent change in V* was calculated using equation 9, where $V^*(\psi = 60°)$ was used in the denominator when $\psi = 60°$. The greatest percent change was for the NCR cluster at both $\psi = 58°$ (23% for NCR vs. 5.6% for CR) and $\psi = 60°$ (6.6% for NCR vs. 2.2% for CR).

Comparing distortions

Given the range of values of the various distortion parameters in table 1, we can now estimate the degree to which each distortion influences the EFG. Table 6 summarizes the percent change in the EFG over the domain of the distortion parameter observed in 1M tri-octahedral micas from tables 2-5. For each of the three clusters, the EFG change produced by flattening is significantly larger than the changes due to any other distortion. We conclude that, of the purely geometric local distortions (i.e. those that do not include a local change in chemistry), flattening is the most important in determining the EFG, and hence the quadrupole splitting.

Chemical effects of neighbor cations in an octahedral sheet

The purely chemical effects of cations adjacent to the Fe^{2+} octahedron will vary depending on how the octahedron is connected within the crystal structure. To illustrate how chemical effects can influence the EFG and its response to trigonal distortions, we will continue to use the seven-octahedra section of a trioctahedral sheet as an example.

Various combinations of Mg^{2+} and Al^{3+} cations were substituted into the six M*i* octahedra of figure 2. As noted above, Mg^{2+} and Al^{3+} were chosen as common cations of their respective valences found in micas and other layer silicates. The metal-anion bond lengths in the near-neighbor octahedra were kept at 2.11 Å,

rather than allow the octahedra to take the cation-specific bond lengths, for two reasons: first, in order to investigate the effects on the EFG of chemical substitution alone, without any other associated local distortions, and second, because in cases where the substituted cluster is not trigonally symmetric (e.g. AAAMMM or AMMMMM), it is not immediately apparent how these cation-specific bond lengths could be accommodated without performing some kind of structural optimization. Figure 7c shows an example of a trigonally symmetric cluster where the six near-neighbor octahedra, in this case all occupied with Mg^{2+}, have different bond lengths and local distortions than the central Fe^{2+} octahedron (d_{Fe} = 2.11 Å and d_{Mg} = 2.06 Å). The curve is not very different qualitatively from the clusters where all metal-anion bond lengths are the same. We do not expect that allowing the near-neighbor octahedra to assume cation-specific bond lengths will substantially affect the way the EFG responds to other distortions.

There are 13 possible symmetry-unique ways to populate the six neighbor octahedra with Mg or Al cations - one each with all Mg, all Al, Mg_5Al_1 and Mg_1Al_5; and three each with Mg_2Al_4, Mg_3Al_3 and Mg_4Al_2. The different configurations are labeled as $X_1X_2X_3X_4X_5X_6$, where X_i = 'M' if site Mi (see figure 2) contains an Mg^{2+} cation and 'A' if it contains Al^{3+}. Thus the one Mg_5Al_1 configuration is AMMMMM, the three Mg_4Al_2 configurations are {AAMMMM, AMAMMM, AMMAMM}, and so forth.

Only three configurations maintain trigonal symmetry - AAAAAA, AMAMAM and MMMMMM. These configurations correspond to sections of geometric hetero-octahedral (AMAMAM) and geometric meso-octahedral sheets. All other configurations have monoclinic point group symmetry except for AAMAMM, which is triclinic. These non-trigonal clusters have EFGs with non-zero η values, and as a result, V^* is no longer simply the modulus of V_{ZZ} for these clusters. The evolution of elements of the EFG tensor other than V^*, such as η, the EFG eigenvectors, and the sign of V_{ZZ}, will be discussed in a future paper.

Flattening curves for the different configurations are shown in figure 11 at 0 K and 300 K. The three trigonally-symmetric clusters (MMMMMM, AAAAAA, and AMAMAM) have V^* vs. ψ curves that behave as discussed above (cluster MMMMMM is the 7-oct. cluster). At T = 0 K there is a discontinuity, occurring at about 56° for all three curves, where the e_g and a_{1g} d-orbitals cross in energy and the cluster's ground state changes. After the discontinuity, V^* is about 2 au and decreases linearly with ψ. At T = 300 K, V^* rises sharply after ψ = 56° to a maximum and approaches the T = 0 K curve at high ψ. The non-trigonal

clusters tend to have non-linear flattening curves at 0 K; their behavior tends to approach that of the trigonal clusters at high ψ. At room temperature, most of the non-trigonal clusters have curves which seem to be gentler versions of the trigonal clusters, with the cusp-like minimum of the latter due to ignoring the sign of V_{ZZ} replaced with a true minimum. Clusters MAAMAA and AMMAMM are exceptions, having very flat curves.

When the cluster is no longer trigonally symmetric, the degeneracy in the e_g levels is lifted. Moreover, there is more mixing between the atomic Fe(3d) orbitals in the corresponding molecular orbitals, so that, for example, the orbital labeled a_{1g} is no longer purely the Fe^{2+} 3d z^2 orbital. As a result, the EFG's principal direction is no longer strictly along the z-axis and the EFG asymmetry parameter η is no longer identically zero. In clusters MAAAAA, AMAMMM and AAAMMM, one of the former e_g orbitals is lower in energy than the a_{1g} at low flattening angles. At slightly higher flattening, the a_{1g} drops below this other d-orbital, resulting in the discontinuities in those clusters' $T = 0$ K curves, near 55.0° for MAAAAA, 55.5° for AMAMMM, and 56.5° for AAAMMM. The discontinuity of cluster AAAMMM also shows up in the 300 K curve, because not only do the spin-down d-orbitals change energetic order at this flattening angle, but the admixture between Fe(3d) orbitals in the molecular orbitals is also changing very rapidly with flattening in this region. This is probably a result of the very lopsided distribution of charge in this cluster (all the 3+ cations are on one side, all the 2+ cations on the other).

Taking all thirteen configurations together, figure 11 shows that V^* (and hence the Mössbauer quadrupole splitting) evolves in an essentially similar way with flattening regardless of what cations occupy the first nearest neighbor octahedra. In an octahedral sheet containing chemical disorder, the effect of adding additional shells of neighboring octahedra would tend to smooth out the differences due to the Fe^{2+} octahedron's immediate neighbors.

It was established from table 6 that, of the purely structural distortions, flattening produces the greatest percent change in V^*. The percent changes in V^* over the range of flattening angles found in 1M trioctahedral micas for the different configurations, as calculated with equation 9, are given in table 7. The percent change varies greatly from cluster to cluster, from 2.7% for the relatively flat MAAMAA curve to nearly 110% for the AAAMMM curve, the latter a result of relatively low V^* with large changes over the range of flattening angles. Size of the percent change seems to be partly correlated with symmetry - three of

the four largest values belong to the trigonally symmetric configurations - but not completely - the MAAAAA and AMMMMM clusters are of the same symmetry but have significantly different percent changes. Figure 12 shows the maximum percent change with chemistry as a function of flattening angle, calculated as

$$\frac{\max_{C}\{V^*(\psi)\} - \min_{C}\{V^*(\psi)\}}{\frac{1}{13}\sum_{C} V^*(\psi)} \times 100\%, \qquad (10)$$

where C is the set of all thirteen possible configurations of near-neighbor cations. There is a clear and significant decrease in the effects of the near-neighbor cations as the flattening angle increases, reflecting that the flattening curves tend to all become very similar at high flattening angles. The effects of flattening and chemistry (i.e., identity of cations without regard to changes in bond length) cannot be easily separated; both seem to be equally significant in determining the EFG when geometric and chemical variation occur together.

Comparison with Experiment

Figure 13 compares the magnitudes of various measured quadrupole splittings with the previously shown (figure 3) flattening curves for the FeO_6^{10-}, $Fe(OH)_6^{4-}$ and 7-oct. clusters, in this case with V^* expressed in mm/s. Thickness-corrected quadrupole splitting distributions (QSDs) for a natural annite and a natural phlogopite (Rancourt et al. 1994) are plotted against the left-hand axis, while flattening angles for the three theoretical curves (present work) and sheet average flattening angles versus average quadrupole splitting for twenty natural biotite samples (Shabani 1998) are plotted against the right-hand axis.

The theoretically calculated quadrupole splittings agree well in magnitude with the experimental data. The 7-oct. curve shows the best agreement with the experimental values, as is expected since it is the cluster which best approximates the octahedral sheet of the three. The 7-oct. curve assumes the same quadrupole splitting values as the two experimental QSDs over a realistic range of flattening angles (56° to 61°, c.f. table 1) and reaches a maximum quadrupole splitting (~2.9 mm/s) in good agreement with the upper edge of the distributions (~2.8 mm/s for the annite and ~2.9 mm/s for the phlogopite). Above we concluded that at constant chemical composition, the value of the EFG is most affected by flattening, and knowing this, the sharp edge in the QSDs at high quadrupole splittings can be explained by the maximum

in the flattening curve. This is true irrespective of local chemical effects (i.e. cation substitutions) because such effects are small at high flattening angles (figure 12), where the EFG vs. flattening maxima occur.

The points representing the average quadrupole splittings of the natural biotite samples show a fair agreement with the theoretical curves. Both the experimental points and theoretical curves of FeO_6^{10-} and 7-oct. in this region show a positive correlation between QS and flattening angle. A line fit by least squares to the plot of quadrupole splitting versus flattening angle for the natural biotite samples has a slope 0.16(2) mm/s per degree. Fitting the regions from 58° to 60° for the three theoretical curves, the 7-oct. line has a slope of 0.34(5) mm/s per degree, the FeO_6^{10-} line has a slope of 0.21(5) mm/s per degree and the $Fe(OH)_6^{4-}$ line has a slope of –0.037(9) mm/s per degree. The value for $Fe(OH)_6$ is a reflection of the "flatness" of its EFG vs. flattening curve, a result of the ground state change from e_g to a_{1g} being shifted to $\psi < 54.74°$ by the perpendicular OH bonds, as discussed above. The slopes of the 7-oct. and FeO_6^{10-} curves are of the same order of magnitude as that of the best fit line through the experimental points. This is the first time that measured average QS vs. ψ data are explained based on ab initio electronic structure calculations, and that a fundamental explanation is given for the high QS edge in the QSDs of $^{[6]}Fe^{2+}$-bearing minerals.

Acknowledgements

We would like to thank Dr. John Tse, Steacie Institute for Molecular Sciences, National Research Council, Canada, for being involved as co-supervisor in the first stages of this work and for his help and encouragement. We would also like to thank Patrick Mercier for helpful discussions. We acknowledge financial support from the Natural Sciences and Engineering Research Council of Canada, in the form of a Discoveries Grant to DGR.

Table 1. Ranges take by distortion parameters in 1M trioctahedral micas*

	Minimum	Maximum	Average	Standard deviation
ψ (°)	57.15	60.97	58.88	0.44
$\|\delta\|$ (°)	0.005	3.442	0.284	0.535
d_{sheet} (Å)	2.0109	2.1294	2.0750	0.0212
$d_{Fe^{2+}}$ (Å)	2.100	2.155	2.126(11)	–

*values for flattening angle (ψ), counter-rotation angle (δ) and total octahedral sheet-average bond length (d_{sheet}) taken 170 samples from the database described in (Mercier 2003); Fe^{2+}-specific bond length ($d_{Fe}2+$) minimum, maximum and average taken over biotites and olivines in Mercier 2003 (see table 6.6 and figure 6.74).

Table 2. EFG changes due to flattening at 300K (all d = 2.11 Å, δ = 0°)

Cluster	V^* at ψ_{min} = 57° (au)	V^* at ψ_{max} = 61° (au)	ψ of IE†	V^* at IE† (au)	% Change
FeO_6^{10-}	0.85	1.42	–	–	50
$Fe(OH)_6^{4-}$	1.92	1.87	58°	1.95	5.6
7-oct.	0.89	1.86	–	–	68

†IE = intermediate extremum

Table 3. EFG changes due to bond length scaling at 300K (all δ = 0°)

Cluster	V^* at d_{min} = 2.10 Å (au)	V^* at d_{max} = 2.16 Å (au)	d of IE† (Å)	V^* at IE† (au)	% Change
FeO_6^{10-}, ψ = 58°	1.143	1.097	–	–	4.0
FeO_6^{10-}, ψ = 60°	1.396	1.382	–	–	1.0
$Fe(OH)_6^{4-}$, ψ = 58°	1.954	1.948	2.11	1.955	0.41
$Fe(OH)_6^{4-}$, ψ = 60°	1.815	1.923	–	–	1.8
7-oct., ψ = 58°	1.46	1.18	–	–	20
7-oct., ψ = 60°	1.832	1.823	–	–	0.49

†IE = intermediate extremum

Table 4. EFG changes due to counter-rotation at 300K (all ψ = 58°, d = 2.11 Å)

Cluster	V^* at δ_{min} = 0° (au)	V^* at δ_{max} = 3.5° (au)	% Change
FeO_6^{10-}	1.13	1.26	11
$Fe(OH)_6^{4-}$	1.955	1.982	1.4

Table 5. EFG changes due to changes in M-O bond length in neighbour octahedra (all d_1 = 2.11 Å)

Cluster	V^* at $d_{3,min}$ = 2.01 Å (au)	V^* at $d_{3,max}$ = 2.13 Å (au)	% Change
NCR, ψ = 58°	1.14	1.48	23
NCR, ψ = 60°	1.72	1.84	6.6
CR, ψ = 58°	1.36	1.44	5.6
CR, ψ = 60°	1.79	1.83	2.2

Table 6. Comparison of EFG changes with distortion†

Distortion	% Change in V^*		
	FeO_6^{10-}	$Fe(OH)_6^{4-}$	7-oct.
Flattening	50	5.6	68
Bond scaling	4.0, 1.0	0.41, 1.8	20, 0.49
Counter-rotation (at ψ = 58°)	11	1.4	–
Neighbour bond scaling (NCR)	–	–	23, 6.6
Neighbour bond scaling (CR)	–	–	5.6, 2.2

† for distortions other than flattening - when two values are given, the first is for ψ = 58° and the second is for ψ = 60°; when one value is given, it is for ψ = 58°.

Table 7. Comparison of EFG changes with flattening in seven-octahedral clusters.

Configurations		% change in V^* over ψ = 57° to 61°
All Mg	MMMMMM	68
Mg_5Al_1	AMMMMM	33
Mg_4Al_2	AMAMMM	60
	AAMMMM	48
	AMMAMM	4.7
Mg_3Al_3	AMAMAM	103
	AAAMMM	110
	AAMAMM	19
Mg_2Al_4	MAMAAA	46
	MMAAAA	45
	MAAMAA	2.7
Mg_1Al_5	MAAAAA	58
All Al	AAAAAA	90

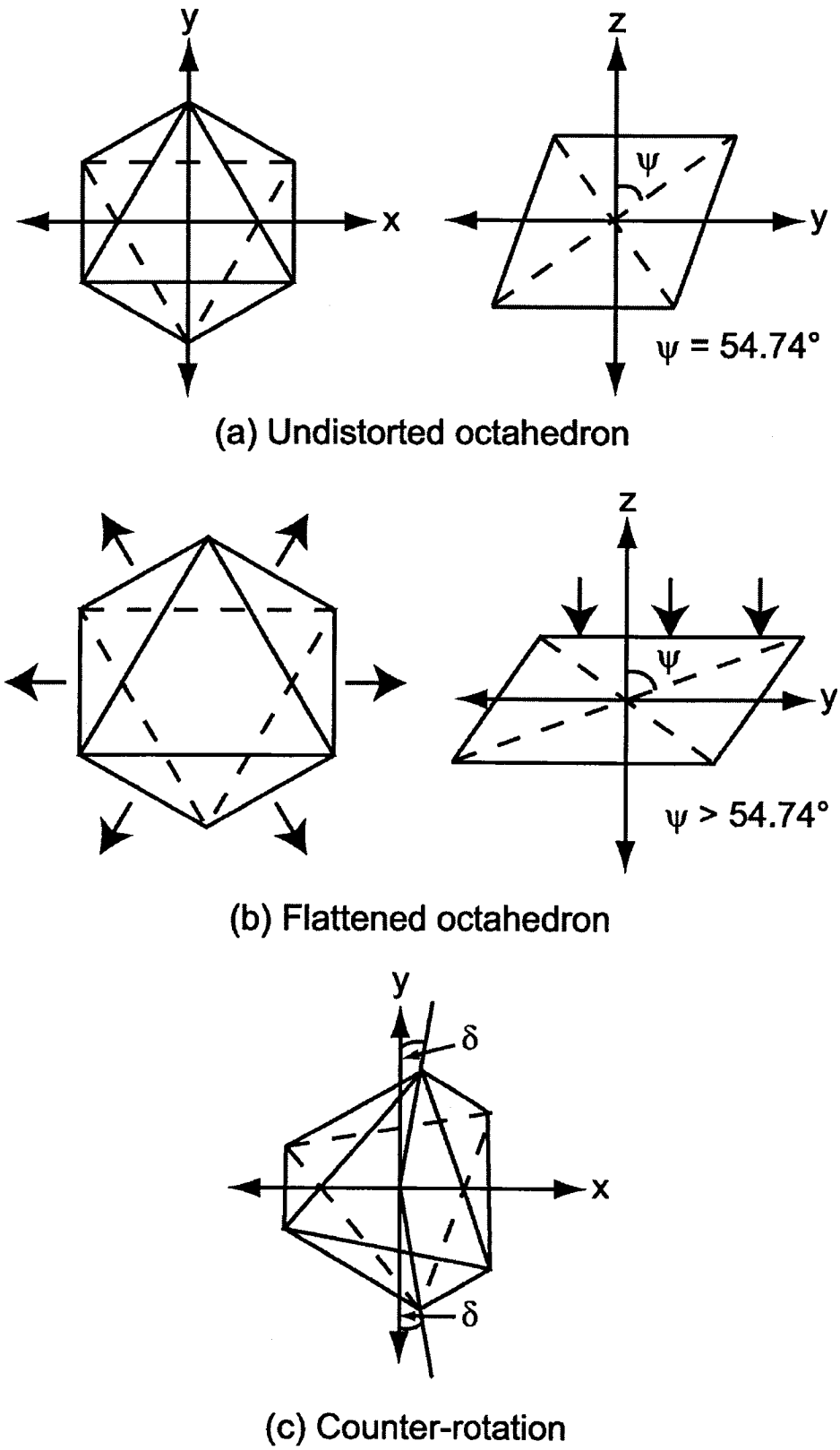

Figure 1 - Schematics illustrating flattening and counter-rotation.

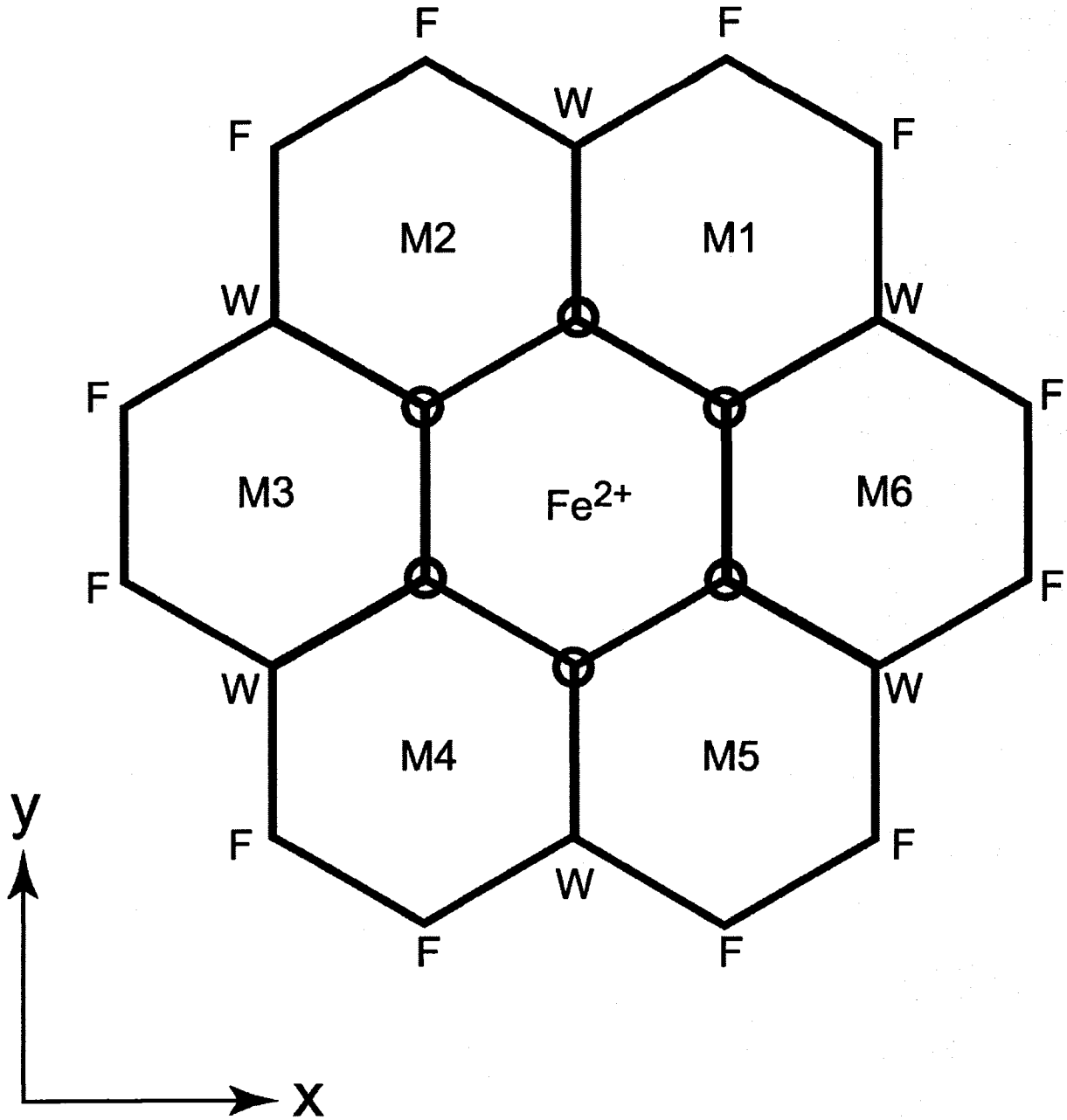

Figure 2. Schematic of the seven-octahedra cluster, showing positions of OH groups (circles), water groups (W), fluorine anions (F), and cations (Fe^{2+} and M*i*). Neighbor cations (M*i*, i = 1 to 6) were either Mg^{2+} or Al^{3+}.

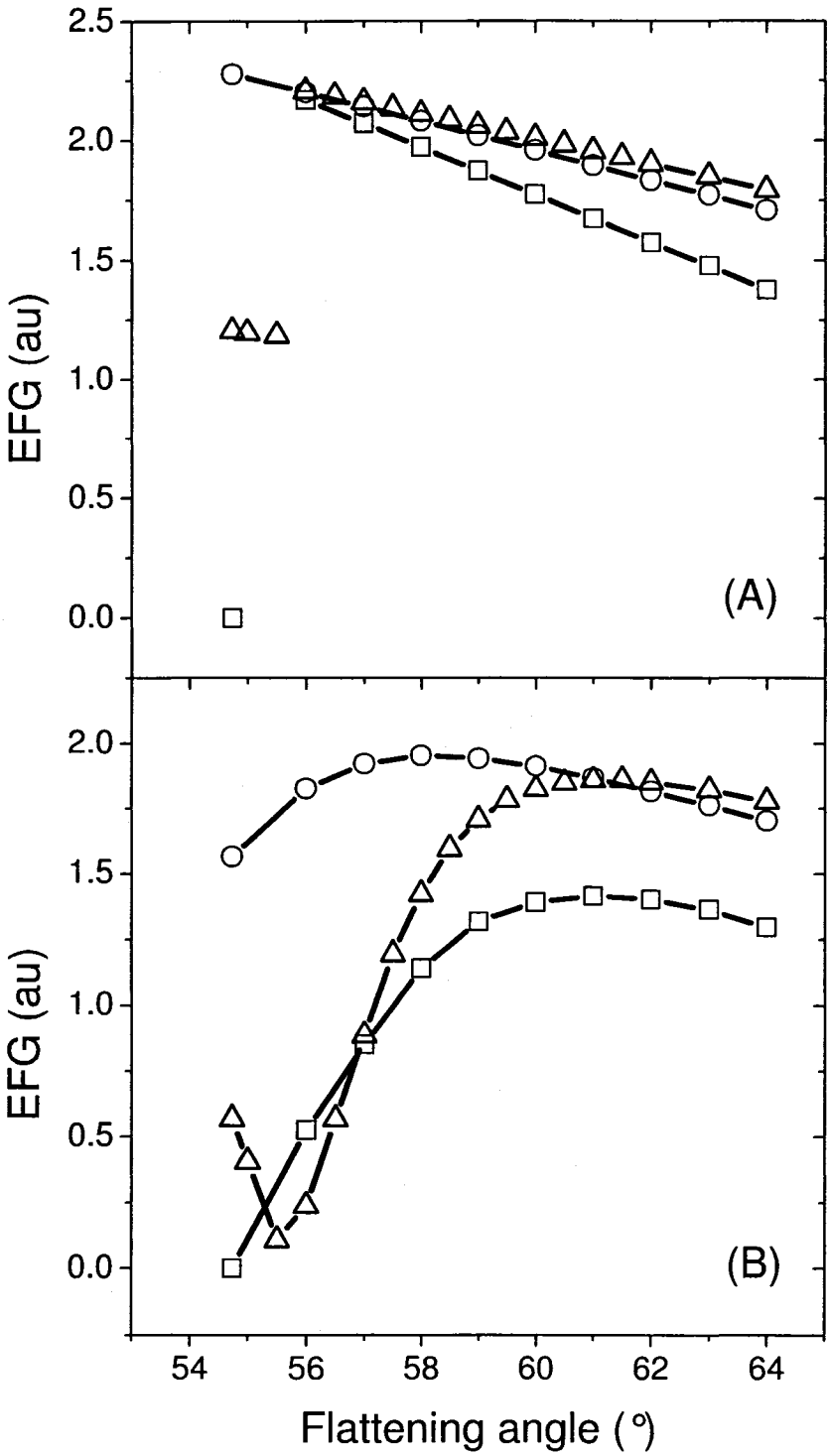

Figure 3. Comparison of EFG V^* vs. flattening angle for FeO_6^{10-} (squares), $Fe(OH)_6^{4-}$ (circles) and 7-oct. (triangles) clusters at (a) $T = 0$ K and (b) $T = 300$ K; $d = 2{:}11$ Å and $\delta = 0°$ for all.

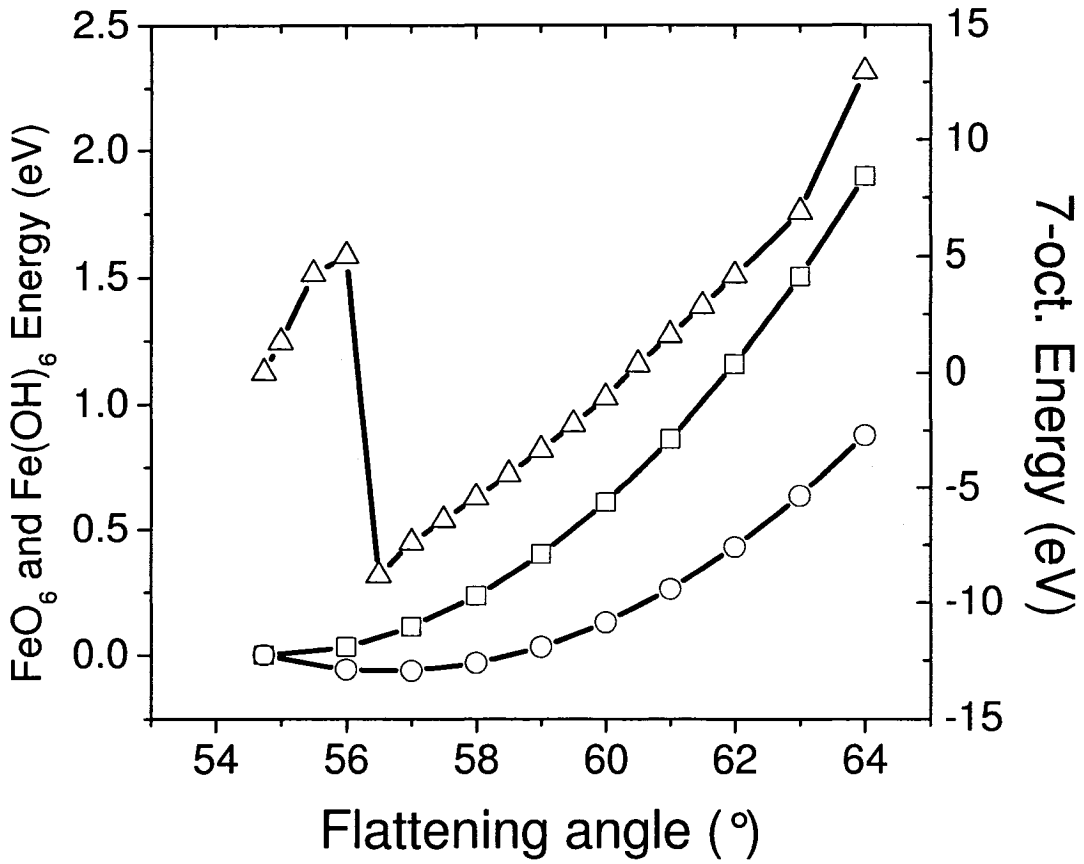

Figure 4. Total atomization energies calculated by SCC-Xα, relative to ψ = 54.74°, as a function of flattening angle ψ for FeO_6^{10-} (squares), $Fe(OH)_6^{4-}$ (circles) and 7-oct. (triangles) clusters.

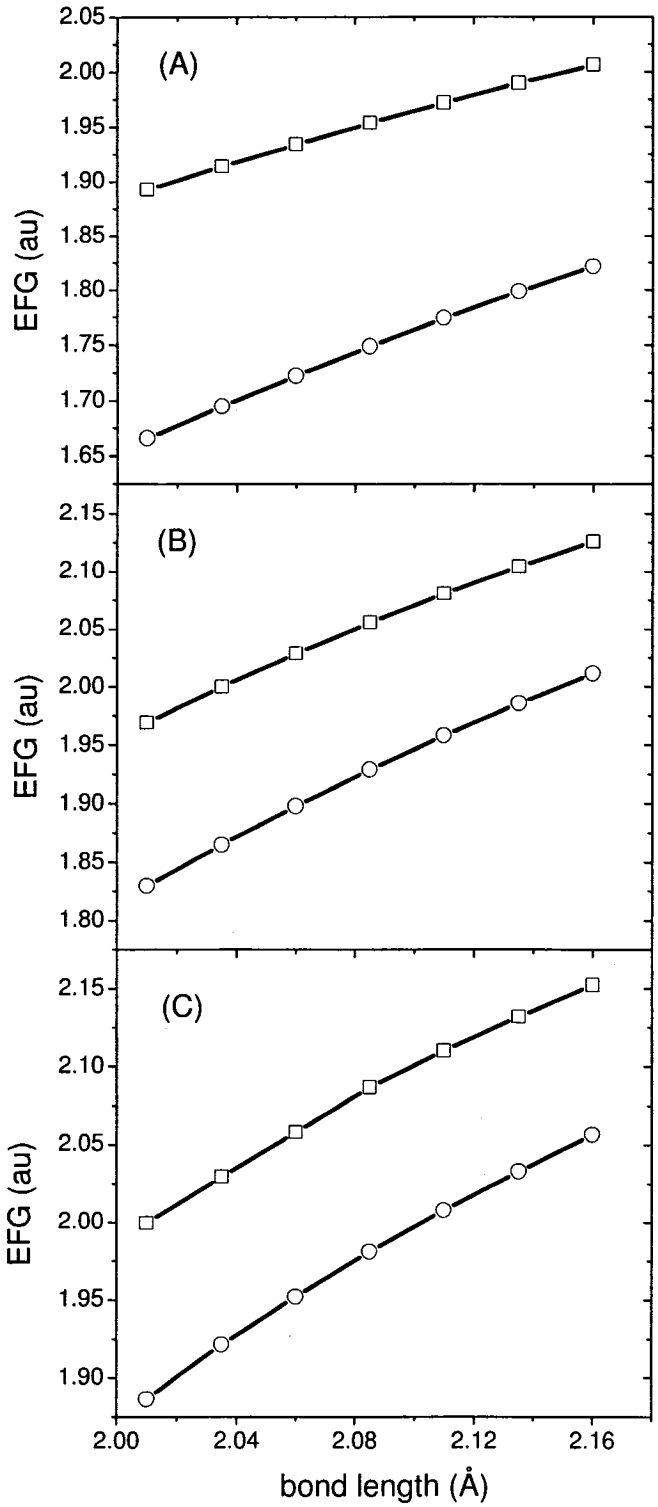

Figure 5. EFG V^* versus bond length d at $T = 0$ K for (a) FeO_6^{10-}, (b) $Fe(OH)_6^{4-}$, (c) 7-oct. clusters at $\psi = 58°$ (squares) and $\psi = 60°$ (circles).

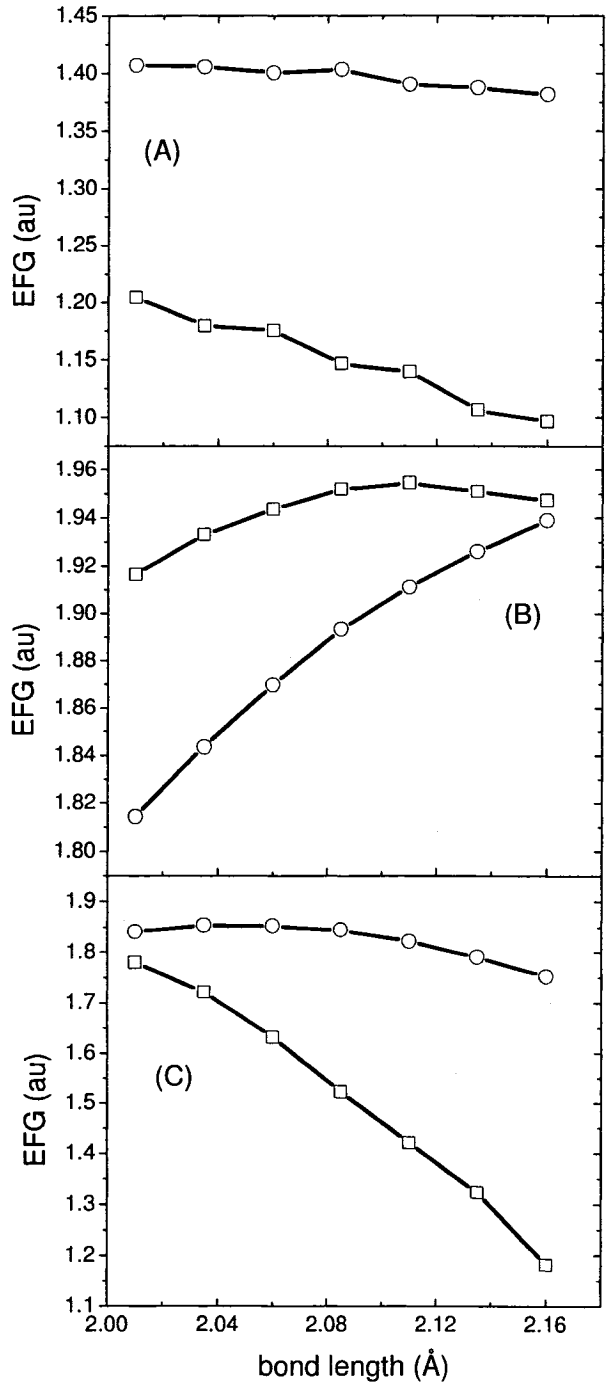

Figure 6. EFG V^* versus bond length d at $T = 300$ K for (a) FeO_6^{10-}, (b) $Fe(OH)_6^{4-}$, (c) 7-oct. clusters at $\psi = 58°$ (squares) and $\psi = 60°$ (circles).

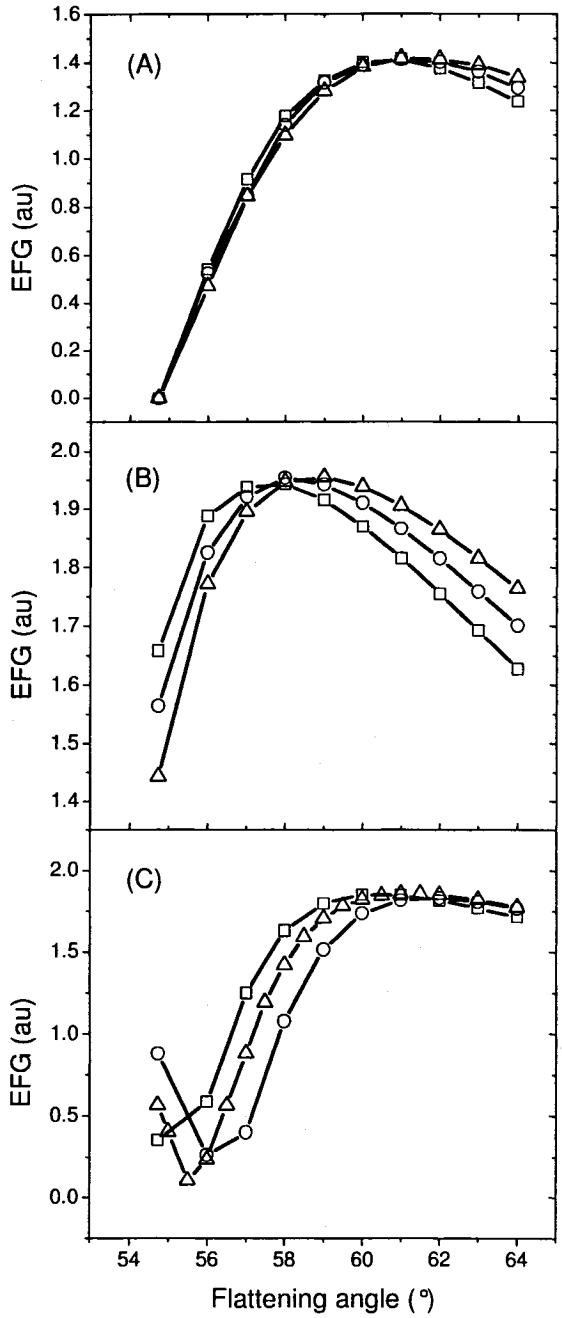

Figure 7. EFG V^* versus flattening angle for different bond lengths at T=300 K for different clusters. (a) FeO_6^{10-}, squares, d = 2.06 Å; circles, d = 2.11 Å; triangles, d = 2.16 Å; (b) $Fe(OH)_6^{4-}$, squares, d = 2.06 Å; circles, d = 2.11 Å; triangles, d = 2.16 Å; (c) 7-oct., squares, $d_{Fe} = d_{Mg}$ = 2.06 Å; circles, $d_{Fe} = d_{Mg}$ = 2.11 Å; triangles, d_{Fe} = 2.11 Å and d_{Mg} = 2.06 Å.

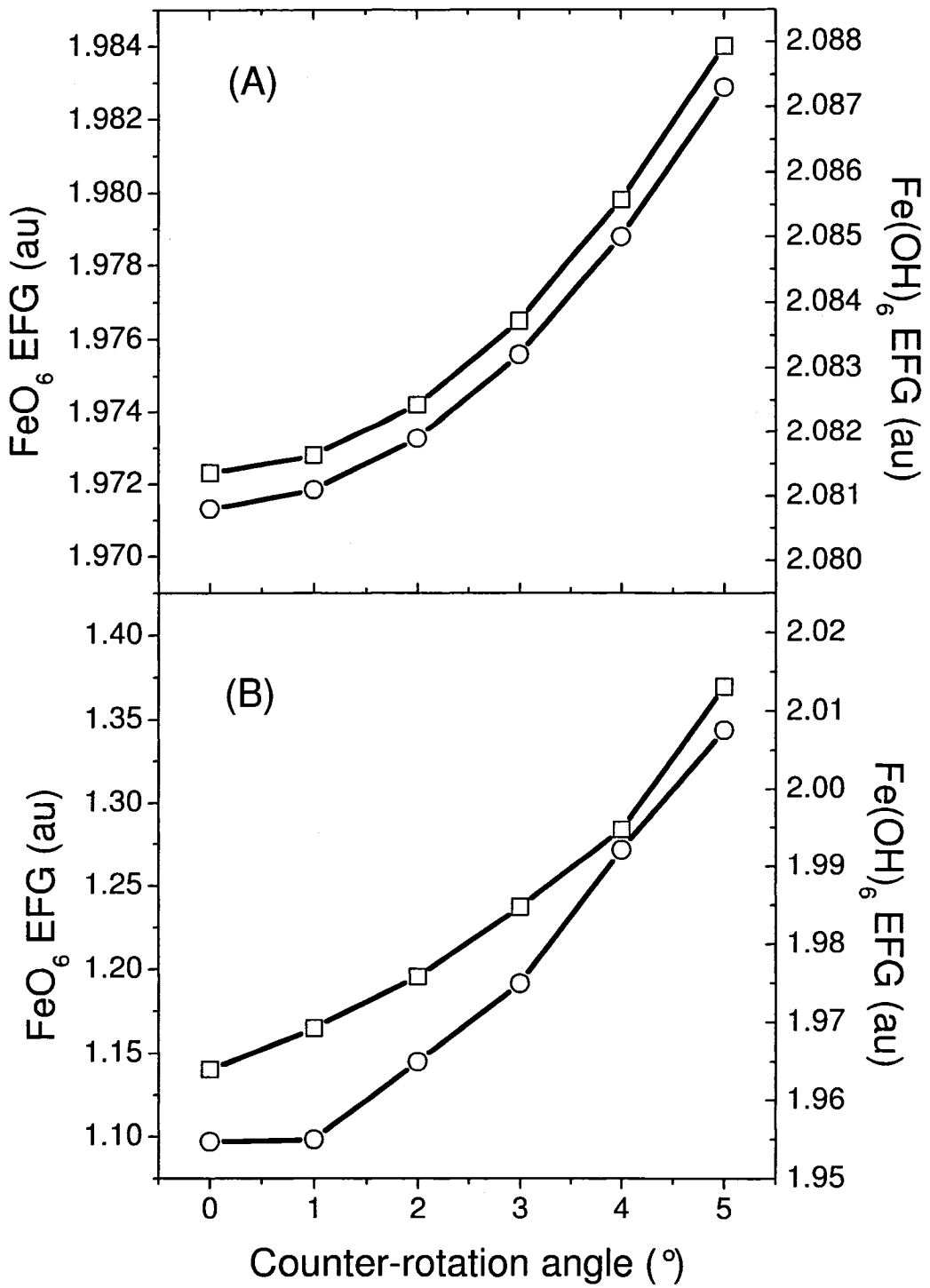

Figure 8. EFG V^* versus counter-rotation δ with $\psi = 58°$ and $d = 2.11$ Å for the clusters FeO_6^{10-} (squares) and $Fe(OH)_6^{4-}$ (circles) at (a) $T = 0$ K and (b) $T = 300$ K.

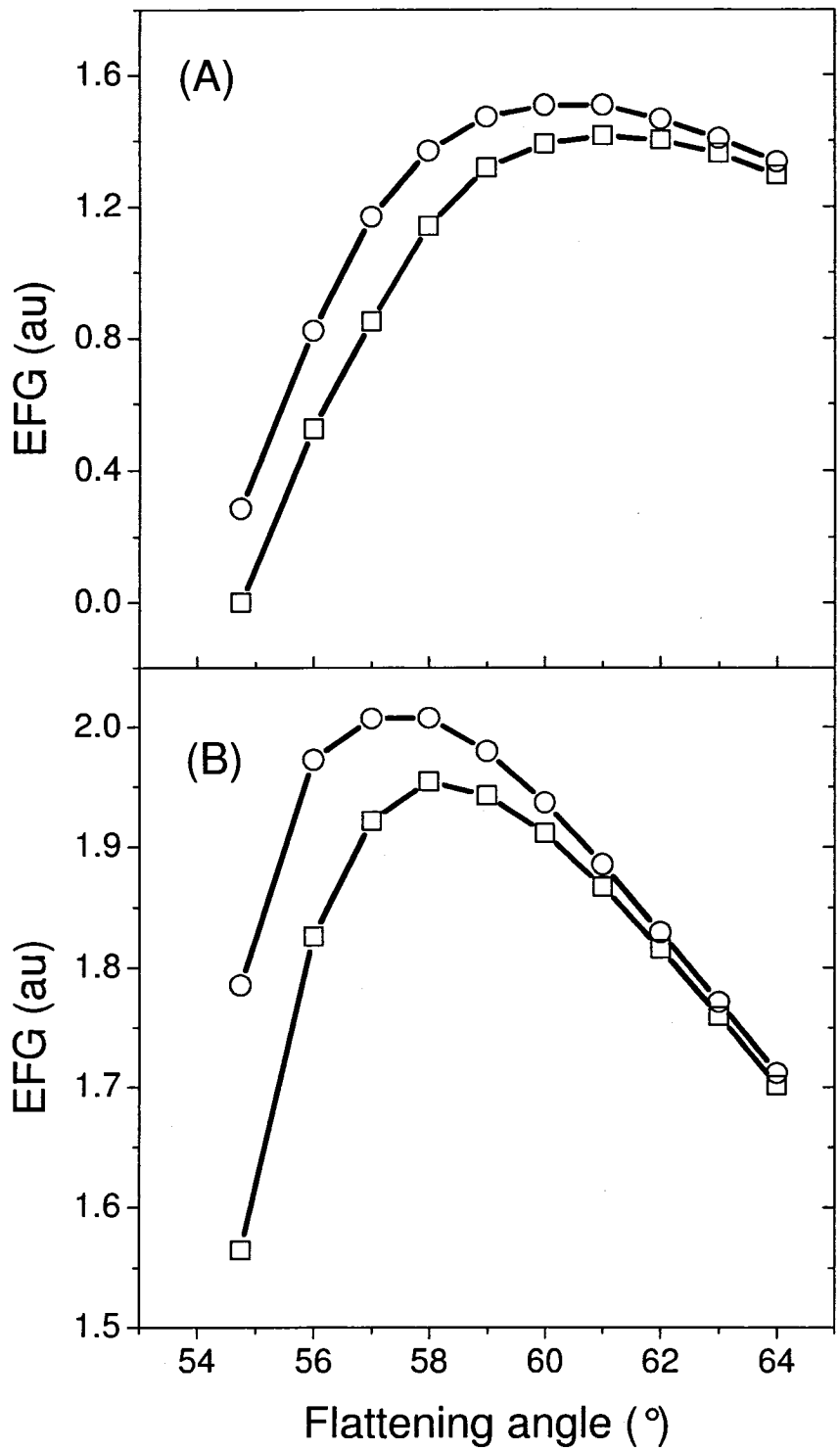

Figure 9. EFG V^* versus flattening angle ψ at different counter-rotation angles δ at $T = 300$ K for (a) FeO_6^{10-} and (b) $Fe(OH)_6^{4-}$ clusters at $\psi = 58°$ (squares) and $\psi = 60°$ (circles).

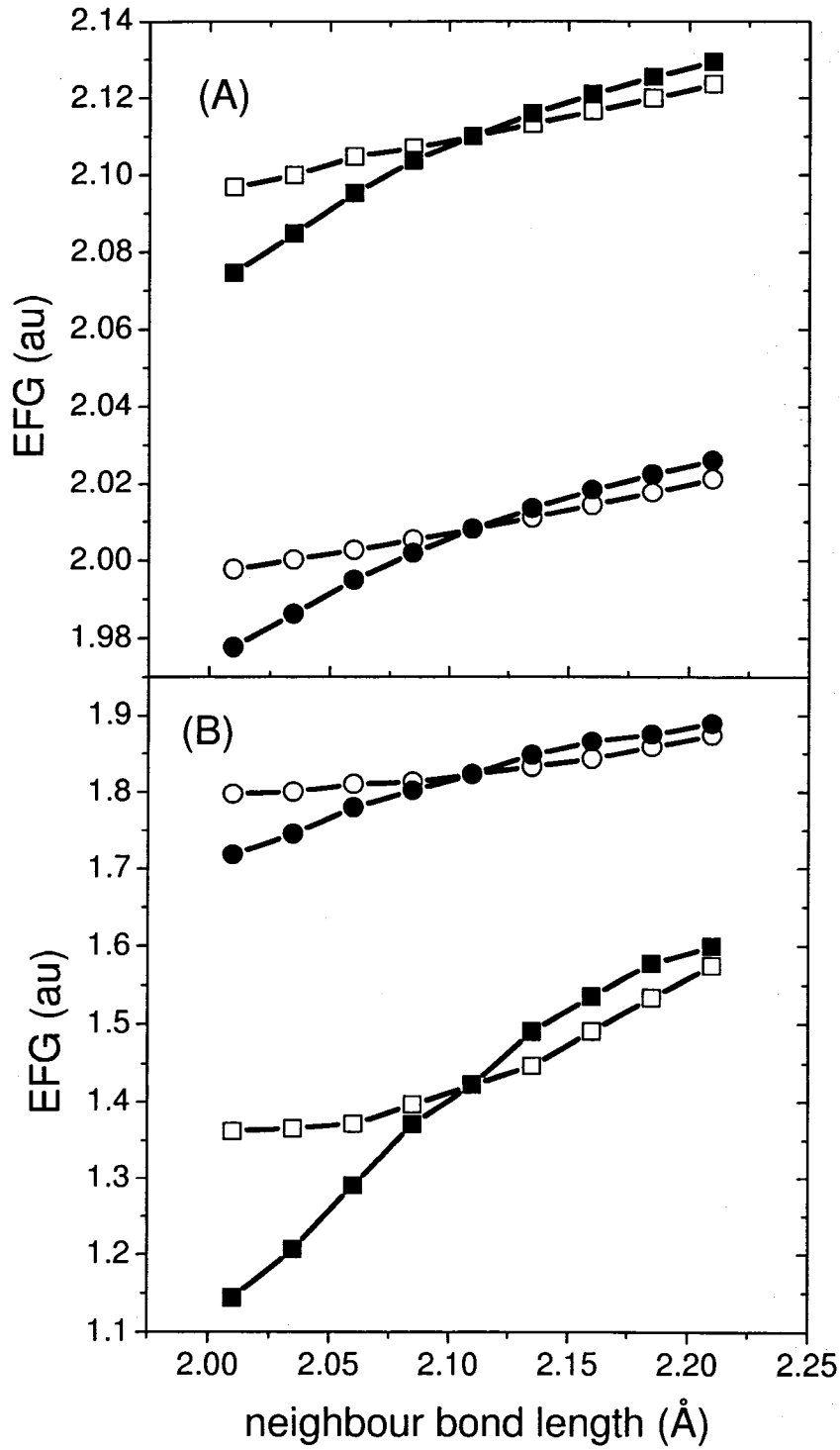

Figure 10. EFG V^* vs. neighbor bond length d_3 for counter-rotated (CR, open squares are $\psi_1 = 58°$ and open circles are $\psi_1 = 60°$) and non-counter-rotated (NCR, filled squares are $\psi_1 = 58°$ and filled circles are $\psi_1 = 60°$) 7-oct. clusters at (a) $T = 0$ K and (b) $T = 300$ K.

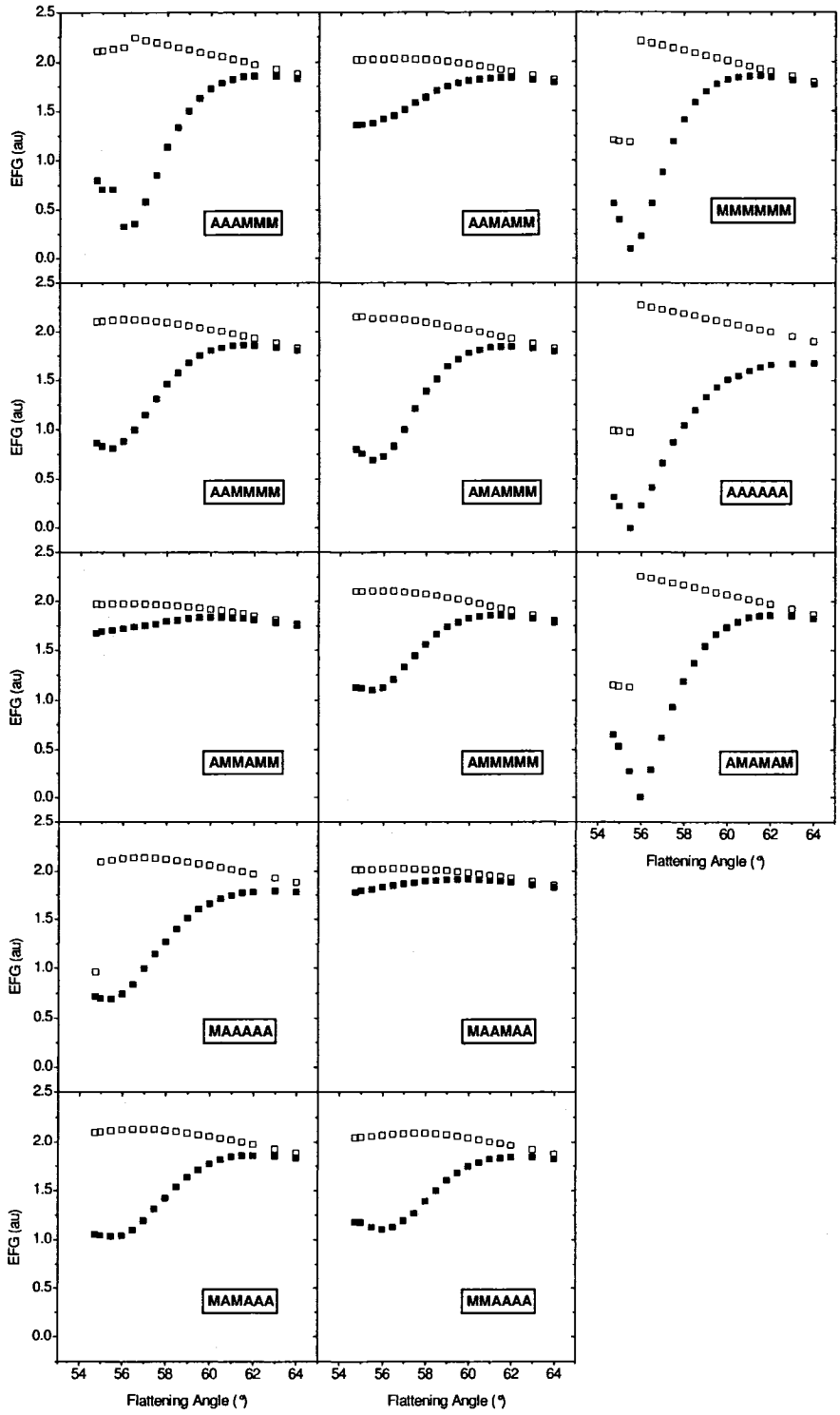

Figure 11: EFG V^* versus flattening angle ψ for all seven-octahedra clusters at $T = 0$ K (open squares) and $T =$ 300 K (filled squares).

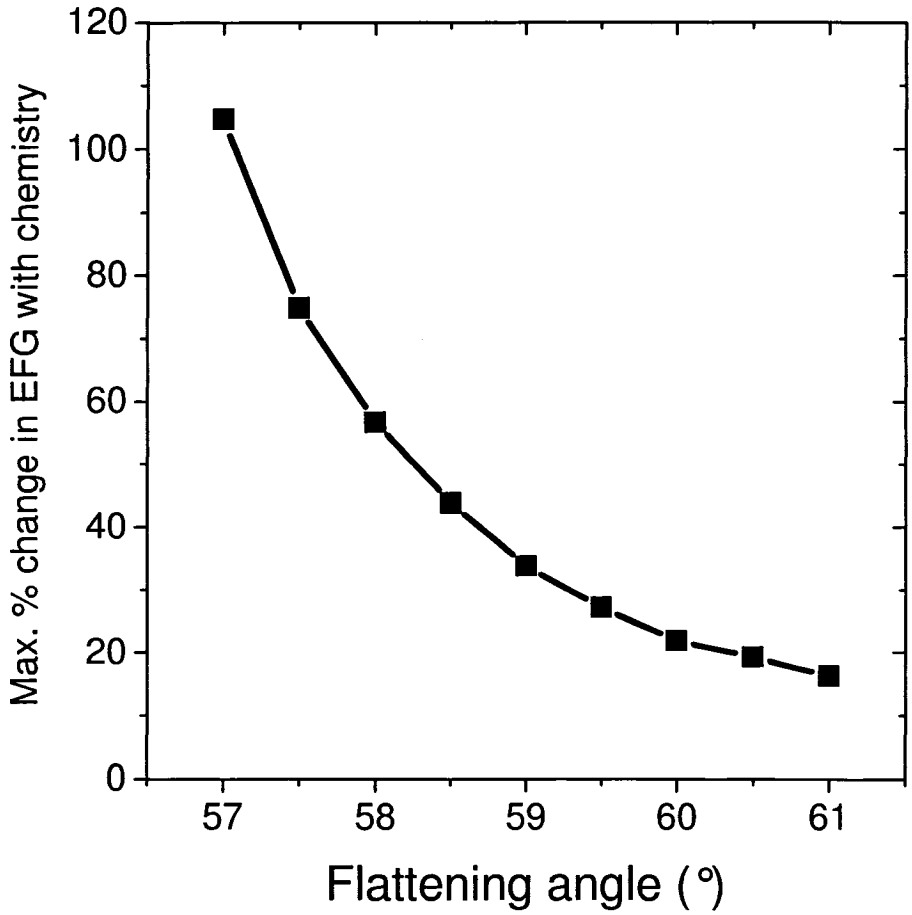

Figure 12. The maximum percent change in EFG on changing the configuration of neighbour cations, as a function of flattening.

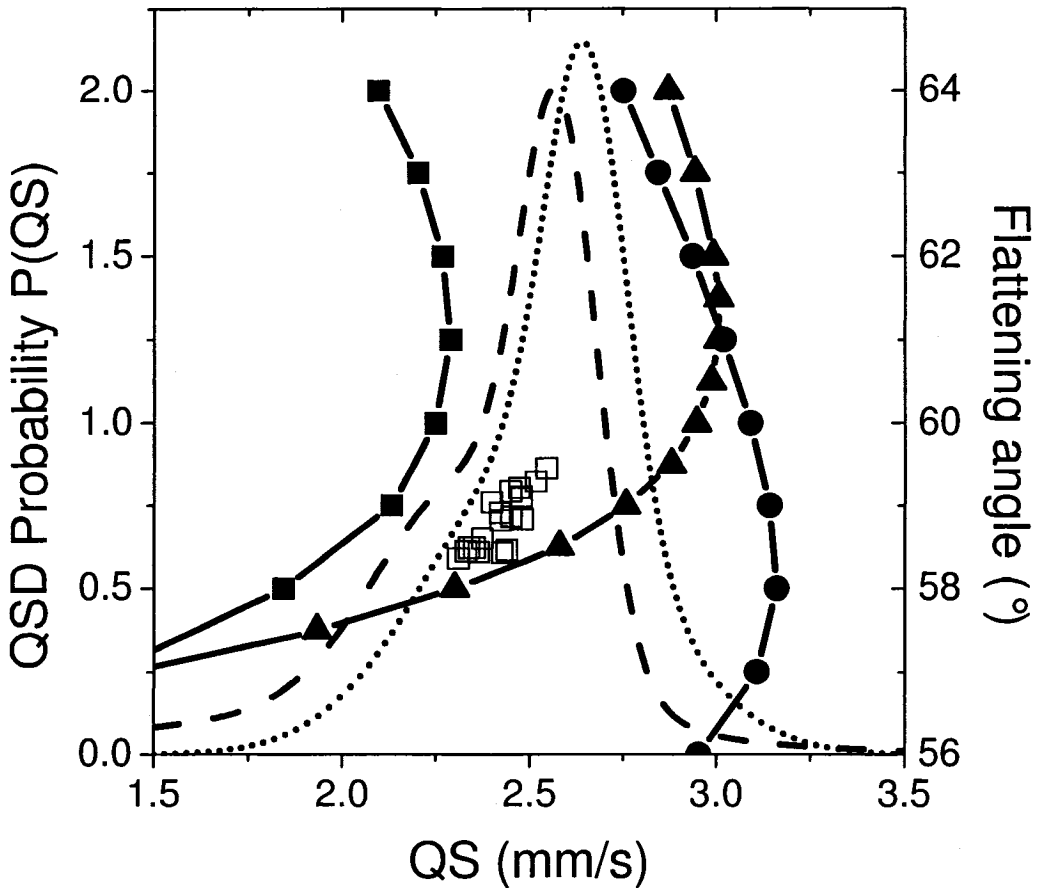

Figure 13. Experimental quadrupole splitting distributions from Rancourt et al. (1994) of natural annite (dashed line) and natural phlogopite (dotted line) plotted against the left-hand axis, compared with theoretical flattening curves for FeO_6^{10-} (solid squares), $Fe(OH)_6^{4-}$ (solid circles) and 7-oct. clusters (solid triangles) taken from figure 3, and average quadrupole splittings versus average flattening angles for several biotite samples from Shabani (1999) (open squares), plotted against the right-hand axis.

References

Anthony, J.W., Bideaux, R.A., Bladh, K.W., and Nicols, M.C. (1995) Handbook of Mineralogy, Volume II: Silicates. Mineral Data Publishing

Bailey, S., Ed. (1984) Micas. Reviews in Mineralogy & Geochemistry 13

Bailey, S., Ed. (1988) Hydrous Phyllosilicates. Reviews in Mineralogy & Geochemistry 19

Burdett, J. (1980) Molecular Shapes. John Wiley & Sons, Inc., New York

Burke, A.D. (1988) Density-functional energy-exchange approximation with correct asymptotic behavior. Physical Review A 58, 3098-3100

Burns, R.G. (1993) Mineralogical Applications of Crystal Field Theory, 2nd Ed. Cambridge University Press

Donnay, G., Donnay, J.D.H., and Takeda, H. (1964) Trioctahedral one-layer micas II. Prediction of the structure from composition and cell dimensions. Acta Crystallographica 17, 1371-1381

Dufek, P., Blaha, P., Schwarz, K. (1995) Determination of the nuclear-quadrupole moment of Fe-57. Physical Review Letters 75, 3545-3548

Ellis, D.E., Baggio Saitovitch, E., and Lam, D.J. (1992) Hyperfine interactions in iron substituted high-T_c superconducting oxides. Physica C 198, 57-69

Evans, R.J. (2001) Electric Field Gradient of Octahedral Fe^{2+} in Layer Silicates. M.Sc. Thesis, University of Ottawa, Ottawa, Ontario, Canada

Grodzicki, M. (1980) A self-consistent charge Xα method I. Theory. Journal of Physics B: Atomic and Molecular Physics 13, 2683-2691

Grodzicki, M. and Amthauer, G. (2000) Electronic and magnetic structure of vivianite: cluster molecular orbital calculations. Physics and Chemistry of Minerals 27, 694-702

Grodzicki, M., Heuss-Assbichler, S., Amthauer, G. (2001) Mössbauer investigations and molecular orbital calculations on epidote. Physics and Chemistry of Minerals 28, 675-681

Grodzicki, M., Männing, V., Trautwein, A.X., and Friedt, J.M. (1987) Calibration of isomer shift and quadrupole coupling for ^{119}Sn, ^{127}I and ^{129}I as derived from self-consistent charge Xα calculations and Mössbauer measurements. Journal of Physics B: Atomic and Molecular Physics 20, 5595-5625

Hazen, R.M., and Wones, D.R. (1972) The effect of cation substitution on the physical properties of trioctahedral micas. American Mineralogist 57, 103-129

Knurr, R.A., and Bailey, S.W. (1986) Refinement of Mn-substituted muscovite and phlogopite. Clays and Clay Minerals 34, 7-16

Kato, T., Miura, Y., Yoshii, M., and Maeda, K. (1979) The crystal structures of 1M-kinoshitalite, a new barium brittle mica and 1M-manganese trioctahedral micas. Mineralogical Journal 9, 392-408

Lauer, S., Marathe, V.R., and Trautwein, A. (1979) Sternheimer shielding using various approximations. Physical Review A 19, 1852-1861

Lottermoser, W., Steiner, K., Grodzicki, M., Jiang, K., Scharfetter, G., Bats, J.W., Redhammer, G., Teutmann, W., Hosoya, S., Amthauer, G. (2002) The electric field gradient in synthetic fayalite α-Fe_2SiO_4 at moderate temperatures. Physics and Chemistry of Minerals 29, 112-121

Lougear, A., Grodzicki, M., Bertoldi, C., Trautwein, A.X., Steiner, K., Amthauer, G. (2000) Mössbauer and molecular orbital study of chlorites. Physics and Chemistry of Minerals 27, 258-269

Mercier, P.H.J. (2003) Crystal chemistry of trioctahedral 2:1 layer silicates: Testing the limits of simple geometrical models. Ph.D. thesis, University of Ottawa, Ottawa, Ontario, Canada

Mottana, A., Sassi, F.P., Thompson, J.B., and Guggenheim, S., Eds. (2002) Micas: Crystal Chemistry and Metamorphic Petrology. Reviews in Mineralogy & Geochemistry 46

Peterson, R.C., Hill, R.J., and Gibbs, G.V. (1979) A molecular-orbital study of distortions in the layer structures brucite, gibbsite and serpentine. Canadian Mineralogist 17, 703-711

Prewitt, C.T., Ed. (1980) Pyroxenes. Reviews in Mineralogy & Geochemistry 7

Rancourt, D.G. (1998) Mössbauer spectroscopy in clay science. Hyperfine Interactions 117, 3-38

Rancourt, D.G., Ping, J.Y., and Berman, R.G. (1994) Mössbauer spectroscopy of minerals, III. Octahedral-site Fe^{2+} quadrupole splitting distributions in the phlogopite-annite series. Physics and Chemistry of Minerals 21, 258-267

Ribbe, P.H., Ed. (1980) Orthosilicates. Reviews in Mineralogy & Geochemistry 5

Shabani, A.A.T. (1998) Mineral chemistry and Mössbauer spectroscopy of micas from granitic rocks of the Canadian Appalachians. Ph.D. thesis, University of Ottawa, Ottawa, Ontario, Canada

Tepikin, E.V., Drits, V.A. and Alexandrova, V.A. (1969) Crystal structure of iron biotite and construction of structural models for trioctahedral micas. Proceedings of the 4th International Clay Conference, Tokyo, 43-49

Terra, J. and Ellis, D.E. (1997) Electronic structure, chemical bonding, and hyperfine parameters in layered silicates. Physical Review B 56, 1834-1847

Terra, J. and Ellis, D.E. (1998) Hyperfine interactions of *cis* and *trans* octahedral Fe^{2+} sites in the layered silicate annite. Journal of the American Ceramic Society 81, 465-468

Toraya, H., Iwai, S., Marumo, F., and Hirao, M. (1978) The crystal structures of germanate micas, $KMg_{2.5}Ge_4O_{10}F_2$ and $KLiMg_2Ge_4O_{10}F_2$. Zeitshrift fur Kristallographie 148, 65-81

Toraya, H., and Marumo, F. (1981) Structure ariation with octahedral cation substitution in the system of germanate micas, $KMg_{[3-x]}Mn_{[x]}Ge_3AlO_{10}F_2$. Mineralogical Journal 11, 222-231

Tyrna, P.L., and Guggenheim, S. (1991) The crystal structure of norrishite, $KLiMn_2^{3+}Si_4O_{12}$: An oxygen-rich mica. American Mineralogist 76, 266-271

Veblen, D.R., Ed. (1981) Amphiboles and other hydrous pyriboles - Mineralogy. Reviews in Mineralogy & Geochemistry 9A

Vosko, S.H., Wilk, L., and Nusair, M. (1980) Accurate spin-dependent electron liquid correlation energies for local spin-density calculations: a critical analysis. Canadian Journal of Physics 58, 1200-1211

Weiss, Z., Rieder, M., and Chmielová, M. (1992) Deformation of coordination polyhedra and their sheets in phyllosilicates. European Journal of Mineralogy 4, 665-682

Weiss, Z., Rieder, M., Chmielová, M., and Krajìček, J. (1985) Geometry of the octahedral coordination in micas: a review of refined structures. American Minerologist 70, 747-757

Hyperfine electric field gradient tensors at Fe^{2+} sites in octahedral layers: Towards understanding oriented single-crystal Mössbauer spectroscopy measurements of micas

R. James Evans[1], Denis G. Rancourt[1] , and Michael Grodzicki[2]
[1] Department of Physics, University of Ottawa, Ottawa, Ontario, Canada K1N 6N5
[2]Institute of Mineralogy, University of Salzburg, A-5020 Salzburg

Abstract

In this first systematic, theoretical study of the complete electric field gradient (EFG) tensor of ^{57}Fe Mössbauer spectroscopy as a function of chemistry and local structural distortion using electronic structure calculations, local EFG tensors were calculated at the central Fe^{2+} sites in clusters of seven octahedra, where the neighbor octahedra were populated with a mixture of Mg^{2+} and Al^{3+} cations. The independent parameters of the EFG tensor - particularly the principal value V_{ZZ}, the asymmetry parameter η, and the direction of the principal axis with regards to the octahedral sheet - were examined in detail as functions of octahedral flattening for each of the thirteen possible configurations of cations. We demonstrate that the argument that the EFG tensor at a particular site is largely determined by the point group symmetry of the corresponding crystallographic site is not correct. We find that in clusters with monoclinic or triclinic local point group symmetry, the value of V_{ZZ} changes discontinuously from positive to negative as flattening increases. The principal axis changes from being in the plane of the octahedral sheet to being normal to it at this discontinuity, and the value of η reaches a maximum and begins to decline. This discontinuous behavior is caused by the continuous change of the EFG eigenvalues as the Fe(3d) character of the highest occupied spin-down orbital evolves with flattening. Taking EFG tensor results from all clusters, and using probabilities for the occurrence of each possible cation configuration in a chemically disordered octahedral sheet of a given bulk composition, we simulate averages and distributions of η, principal axis angles and quadrupole splittings. While the value of η is broadly distributed from zero to one at all flattening angles and bulk compositions, there are two distinct populations of principal axes, normal to and in-plane with the octahedral sheet, as has been observed experimentally. We find these in-plane and normal populations of principal axes correspond exactly to populations with positive and negative values of V_{ZZ}, respectively. Histograms representing quadrupole splitting distributions (QSDs) show features found in experimental

QSDs, such as a constant high edge, a variable low edge and a QSD width that changes dramatically with flattening. These results represent the first predictions relating average structural parameters, that would be obtained by X-ray diffraction, to characteristics of the Fe^{2+} QSD, as obtained by ^{57}Fe Mössbauer spectroscopy, in a chemically disordered material.

Introduction

Structural and chemical information can only be extracted from Mössbauer spectra to the extent that the measured hyperfine parameters can be linked to corresponding crystal chemical features by relations such as those obtained through ab initio electronic structure calculations. The indirect nature of any such hyperfine method, where crystal chemical features affect the measured nuclear resonances only through the local electronic structure, is probably the greatest barrier to a more widespread use of ^{57}Fe Mössbauer spectroscopy in materials science and mineralogy (Rancourt, 1998). The present paper is part of a continuing effort (Evans 2001, Evans et al. 2005) to bridge the gap between the measurement of hyperfine parameters and the determination of the corresponding crystal chemical features of a mineral.

We feel it is essential to acknowledge and treat a particular sample's intrinsic disorder, rather than to only calculate the electronic structure corresponding to the average unit cell, as is generally done (e.g., Tossell et al. 1974, Terra and Ellis 1997, Terra and Ellis 1998, Lougear et al. 2000). Only in this way can the distributions of hyperfine parameters measured using Mössbauer spectroscopy be properly interpreted and exploited (Rancourt 1994, Rancourt et al. 1994). This is the first study that explicitly considers how different local distortion environments produce different kinds of EFG tensors.

In a previous paper (Evans et al. 2005) we presented the results of hyperfine electric field gradient calculations at the Fe^{2+} nucleus in FeO_6^{10-}-centered clusters, focusing primarily on that component of the electric field gradient (EFG) tensor which is proportional to the quadrupole splitting observed in random powder absorber Mössbauer spectroscopy. The current work focuses on the other independent components of the EFG tensor, which can be determined through oriented single-crystal Mössbauer spectroscopy - the asymmetry parameter η, and the directions of the EFG eigenvectors.

Mössbauer spectroscopy is generally carried out on random orientation powder samples. Layer silicates are popular choices for oriented single-crystal Mössbauer spectroscopy (Annerston 1975, Chandra and Lokanathan 1977, Ballet et al. 1979, Ballet and Coey 1982, Ballet et al. 1985, Townsend and Longworth 1985, Ballet and Amthauer 1986, Aldridge et al. 1987, Aldridge et al. 1991, Hargraves et al. 1990, Tennant et al. 1992) as they often occur in large, thin lamellae parallel to their *ab*-plane. The ratio of intensities of the high and low energy lines in the Mössbauer spectra is fit as a function of the orientation of the γ-ray beam to the sample, and from this function the elements of the EFG tensor are calculated subject

to certain mathematical constraints on the tensor (Zory 1965, Zimmermann 1975, Ballet and Amthauer 1986). The fit is not unique (Ballet and Amthauer 1986, Aldridge et al. 1987) and as such requires some assumptions to be made regarding one or more of the EFG tensor properties, e.g., that the tensor has axial symmetry ($\eta \sim 0$) or that the principal axis lies in a particular direction. The result also depends on what model is assumed for the underlying distribution of local EFG tensors for the given sample.

There are two commonly used models of EFG tensor distributions. In one model, one can take the Fe^{2+} sites in the material's crystallographic unit cell, as determined by X-ray diffraction measurements, to define classes of Fe^{2+}sites in the material, and then assume that all sites of a particular class have identical EFG tensors. This is the model implicitly assumed in much of the literature on Mössbauer spectroscopy, equivalent to assuming that all sites of a particular class are identical throughout the crystal, or in other words that the crystal consists of perfect repetitions of the average crystallographic unit cell. This is not an accurate representation of a real mineral, and is not supported by Mössbauer spectroscopy measurements (Hargraves et al. 1990, Rancourt et al. 1994).

An alternative model is to assume a continuous distribution of EFG tensors within the sample, with families of EFGs that may (or may not) correspond to different classes of Fe^{2+} sites. The unit cell determined by X-ray diffraction represents an average over the measured sample. In a real crystal, factors such as chemical disorder ensure that a given crystallographic site will have a distribution of local environments throughout the material which are distorted from the average. The local distortion environment of the Fe^{2+} cation alters the EFG tensor at the nucleus, and so a distribution of environments gives rise to the quadrupole splitting distribution (QSD) measured by Mössbauer spectroscopy, as well as to distributions of the asymmetry parameter and EFG principal axis directions. That entire distributions of EFG tensor parameters arising from local distortion environments of the probe nucleus must exist has previously been pointed out by Hargraves et al. (1990), and Ballet and Amthauer (1986) stressed that fitting spectra with Lorenztian doublets associated with sites in the average unit cell can at most yield information only on macroscopic EFG tensors (that is, as averaged over the whole octahedral sheet).

Previous experimental studies of oriented single-crystal Mössbauer spectroscopy have reported different values of the average EFG asymmetry parameter (η) and average principal axis directions. Some studies find principal axis directions normal or nearly normal to the octahedral sheet (e.g. Chandra and

Lokanathan 1977, Ballet and Coey 1982, Ballet et al. 1985, Townsend and Longworth 1985) while others find principal axes normal to the plane at some sites and in-plane at other sites (e.g. Aldridge et al. 1987, Hargraves et al. 1990, Aldridge et al. 1991, Tennant et al. 1992). Reported values of the asymmetry parameter have varied considerably, from near zero (Ballet et al. 1985) to near one (Aldridge et al. 1987).

Aldridge et al. (1991) stressed that the point group symmetry of the crystallographic site has a powerful influence on the EFG tensor, demanding that at a site in the unit cell with monoclinic point group symmetry, one EFG eigenvector must lie along the crystallographic **b** axis, and the other two must lie in the *ac*-plane. The authors also emphasized that it is not possible to say a priori which of the three eigenvectors will be the principal (V_{ZZ}) axis, and that there is no reason to expect the normal to the plane (the crystallographic **c*** axis) to coincide with any of the EFG eigenvectors. The existence of a distribution of local distortion environments in a real mineral, however, means that the ideal symmetry implied by the average unite cell does not actually exist. At best we can define a local point group symmetry, based on a spherical region centered at the ^{57}Fe site, encompassing a certain number of neighboring atoms. As a result, we show here that the approach of Aldridge et al. (1991) is incorrect.

In the current work, we expand on the results in Evans et al. (2005) to show how distortions of the Fe^{2+} environment in an octahedral sheet change the EFG tensor. Specifically, we investigate how flattening, shown in the above paper to be the most important structural distortion in determining the EFG, combined with chemical disorder in near-neighbor octahedra, affects the EFG asymmetry parameter and principal axis. These results are then used to calculate model distributions of EFG tensor parameters, assuming an octahedral sheet with no chemical order. These results on simple model clusters have a direct relevance for oriented single-crystal Mössbauer spectroscopy measurements, by illustrating features that a realistic fitting model for the EFG tensor parameter distribution requires.

Theory

Electric field gradient definitions

The EFG tensor with the Mössbauer atom at the origin has elements

$$V_{ij} = \left. \frac{\partial^2 V(\mathbf{r})}{\partial x_i \partial x_j} \right|_{\mathbf{r}=0}, \qquad (1)$$

where $V(\mathbf{r})$ is the electrostatic potential. It is a real symmetric tensor, therefore its eigenvectors are mutually orthogonal. The eigenvalues are traditionally labeled V_{XX}, V_{YY} and V_{ZZ} such that

$$|V_{XX}| \le |V_{YY}| \le |V_{ZZ}| . \tag{2}$$

The corresponding unit eigenvectors will be labeled $\mathbf{e}_{XX}$, $\mathbf{e}_{YY}$ and $\mathbf{e}_{ZZ}$. When referring to unordered eigenvalues, we shall label them V_1, V_2 and V_3 and the eigenvectors $\mathbf{e}_1$, $\mathbf{e}_2$ and $\mathbf{e}_3$. The asymmetry parameter η is defined as

$$\eta = \frac{V_{XX} - V_{YY}}{V_{ZZ}} . \tag{3}$$

and takes values between 0 and +1. The eigenvector $\mathbf{e}_{ZZ}$ is referred to as the principal direction or axis of the EFG, and V_{ZZ} as the principal eigenvalue. The three EFG unit eigenvectors can be uniquely specified with respect to the crystallographic {**a**, **b**, **c***} basis (where **a** and **b** lie in the plane of the octahedral sheet and **c*** is normal to the plane) by the Euler angles ϕ, θ and ζ; where ϕ is the angle between $\mathbf{e}_{ZZ}$ and **c***, θ is between the projection of $\mathbf{e}_{ZZ}$ in the *ab*-plane and **b**, and ζ is between the projection of **c*** in the $\mathbf{e}_{XX}\mathbf{e}_{YY}$-plane and $\mathbf{e}_{XX}$ (see figure 1).

Since the EFG tensor is traceless, and has mutually orthogonal eigenvectors, five parameters are sufficient to determine it in a given coordinate system, viz. V_{ZZ}, η, ϕ, θ and ζ.

If we define V^* as

$$V^* = |V_{ZZ}| \sqrt{1 + \frac{\eta^2}{3}} , \tag{4}$$

then the Mössbauer quadrupole splitting is

$$\Delta = \tfrac{1}{2} e Q V^* \tag{5}$$

where e is the charge of the electron, Q is the nuclear quadrupole moment of the first excited state of the ^{57}Fe nucleus. The EFG is calculated in atomic units (au). With $Q = 0.16$ barn (Dufek et al. 1995), 1 au = $10.11Q$ mm/s = 1.62 mm/s in the usual units of ^{57}Fe Mössbauer spectroscopy.

Calculation methods

All electronic structure calculations were performed in the local density approximation with the spin-polarized self-consistent charge Xα (SCC Xα) method (Grodzicki 1980, Grodzicki et al. 1987). In this treatment, the molecular potential is factored into a radial function and a series of spherical harmonics (allowing analytical integration of the angular parts of all Hamiltonian matrix elements), and separated into one-, two- and three-center integrals. One-center integrals require high accuracy, and are derived numerically from all-electron, relativistic atomic calculations with semi-local (gradient corrected) exchange correlation functionals. The two- and three-center integrals are evaluated with small basis sets (2s and 2p for O and F; 3s and 3p for Mg and Al; 3d, 4s and 4p for Fe) and the Slater Xα potential with $\alpha = 0.7$ for the valence electrons (Grodzicki 1980, Baerends and Ros 1973); core electrons are treated with simple pseudopotentials that are also derived from relativistic atomic calculations and are kept frozen during the iteration process.

The EFG is calculated by integrating the electron charge density multiplied by the tensor operator

$$V_{ij}(r) = \left(\frac{1-\gamma(r)}{r^3}\right)\left(\frac{3x_i x_j - r^2\delta_{ij}}{r^2}\right), \tag{6}$$

where $\delta_{ij} = 1$ when $i = j$ and 0 otherwise, and $\gamma(r)$ is the Sternheimer shielding function which arises from the polarization of the core Fe electrons by charges outside the core. It is derived from atomic self-consistent first order perturbation calculations (Lauer et al. 1979). The EFG can be broken up into valence, covalence and ligand contributions. For high-spin Fe^{2+}, the total EFG is dominated by the valence contribution, which is roughly proportional to the Fe(3d) and Fe(4p) shell anisotropies,

$$\Delta n_d = n_{x^2-y^2} + n_{xy} - n_{z^2} - \tfrac{1}{2}(n_{xz} + n_{yz}) \tag{7a}$$

$$\Delta n_p = \tfrac{1}{2}(n_x + n_y) - n_z \tag{7b}$$

where n_i is the occupation of the $3d_i$ or $4p_i$ atomic orbital, respectively. The Fe(3d) anisotropy dominates the valence EFG. The covalence EFG contribution results from anisotropy of the bonding electrons between the iron atom and its surrounding ligands, and the ligand EFG from the ion cores and the valence electrons of the ligands. The covalence and ligand EFGs together are about 5% of the total in the cases considered.

Non-zero temperature EFGs were approximated by first performing zero-temperature calculations to determine the relative orbital energies E_i, and then these energies were used to calculate thermal average populations n_i for each orbital thermodynamically:

$$n_i = \frac{\exp(-E_i/kT)}{\sum_j \exp(-E_j/kT)}, \tag{8}$$

where T is temperature and k is the Boltzmann constant. In practice this was only done for the spin-down t_{2g} Fe(3d) orbitals, the lowest energy of which is the highest fully occupied molecular orbital. Those orbitals below these three remain fully occupied at finite temperatures, and the last two unoccupied spin-down orbitals the e_g anti-bonding orbitals are high enough above the t_{2g} in energy that their occupation at 300 K is negligible (with calculated occupation numbers less than 10^{-7}). The SCC Xα calculation is then repeated with the spin-down t_{2g} orbitals given their thermal average populations. The orbital energies of the second calculation are generally shifted only a few meV from those of the zero-temperature calculations.

Temperature effects other than the thermal population of molecular orbitals were neglected in the 300 K calculations. The time scale of Mössbauer spectroscopy, dictated by the nuclear transition of the ^{57}Fe nucleus (Rancourt 1998), is normally much longer than that of thermal vibration, thus Mössbauer spectroscopy generally sees only the atoms' equilibrium positions. Therefore effects of thermal vibration were not included in the calculation. We have also neglected any changes in bond lengths or flattening angles with temperature. The current study is not intended to simulate the actual mica structure or EFG at low or high temperatures, rather, we are asking what the resulting EFG tensor would be given a particular structure at 0 K or 300 K.

Model clusters

Calculations were carried out using seven-octahedra clusters of the form $Fe(OH)_6^{4-} \bullet n[MgF_2OH_2] \bullet (6 - n)[AlF_2OH_2^+]$ (see figure 2). The center octahedron is occupied by an Fe^{2+} cation. Its six nearest neighbor octahedra may be occupied by either Mg^{2+} or Al^{3+} cations, chosen as simple (i.e. d-orbital free) representative cations of their respective valences common in layer silicates.

There are thirteen unique ways to populate the six neighbor octahedra with two types of cations. Referring to figure 2, these configurations are labeled $X_1X_2X_3X_4X_5X_6$, where X_i = 'M' if cation i is Mg^{2+}

and 'A' if it is Al^{3+}. Three of these configurations have trigonal symmetry (MMMMMM, AAAAAA and AMAMAM). Of the ten non-trigonal configurations, nine are monoclinic and one is triclinic (AAMAMM). Clusters were oriented in the calculations such that the *z*-axis is normal to the plane of the cluster (the **c*** axis) and the *x*-axis corresponds to either a 2-fold rotational axis or the normal to a mirror plane (the **b** axis). The triclinic cluster was oriented so that in figure 2, the *x*-axis ran through site 3, the central site and site 6; sites 1, 2 and 4 contained Al^{3+} and sites 3, 5 and 6 contained Mg^{2+}.

All metal-ligand bond lengths were set at 2.110 Å, the average Fe-O bond length in micas found by Weiss et al. (1992), and geometrical distortions due to differences in cation sizes were not taken into account. This was done to separate chemical and geometrical influences on the EFG.

The six OH bonds on the central octahedron are normal to the sheet. The O-H bond length was taken as 0.958 Å. A mixture of F^- and OH_2 ligands terminate the edge of the cluster. It has been found (Lougear et al. 2000) that using incompletely terminated oxygen atoms at the cluster edge can lead to convergence problems due to unsaturated O(2p) lone pairs in the same energy range as the Fe(3d) orbitals. Replacing OH^- with F^- at the corners and waters at the bridging positions eliminates the problem by bringing the edge ligand 2p energies down to their expected levels, as well as helping to reduce the overall cluster charge. The latter is desirable both for the technical reason that calculations for clusters with small charges tend to converge more easily, and in that it is closer to reality in that molecules and most crystal unit cells are electrically neutral.

Electric field gradients were calculated as a function of the flattening angle of the central Fe^{2+} octahedron. Flattening is an important crystallographic feature in micas and was first defined by Donnay et al. (1964). It is an octahedral distortion where the perpendicular distance between the octahedron's top and bottom faces (i.e. the thickness of the octahedron) is reduced, while the Fe-O bond length remains constant. The top and bottom faces expand while remaining equilateral. The flattening angle ψ is defined as the angle between one of the bonds and the normal to the top and bottom faces (i.e. the *z*-axis), and for an undistorted octahedron $\psi_{ideal} = \tan^{-1}(2^{1/2}) \approx 54.74°$. Flattening is largely determined by the composition of the octahedral sheet (Mercier et al. 2005).

Since the metal-oxygen (M-O) bond length in each octahedron is the same, and the cluster is of uniform thickness, the flattening angle is the same in all seven octahedra. The EFG invariant V^* as a

function of flattening for these clusters was previously discussed in Evans et al. (2005), where it was shown that flattening is a dominant distortion in determining V^*.

In real micas, Fe^{2+}-Mg^{2+} and Fe^{2+}-Al^{3+} are only two of many possible near-neighbour combinations involving Fe^{2+}; others of interest include Fe^{2+}-Fe^{2+} and Fe^{2+}-Fe^{3+}. However, we believe that the present clusters illustrate many of the important effects of local crystal chemical environments on the EFG tensor.

Results and Discussion

EFG tensor properties of individual clusters, and their origins in electronic structure

In this section, we discuss the calculated EFG tensors for the thirteen clusters and their variation with flattening, and how changes in the Fe(3d) orbitals produce the EFG tensor's observed behavior. These results will be used to discuss average (macroscopic) EFG tensors, and the distribution of local EFG tensors for a given sample, in the following section. Understanding the behavior of the EFG tensor at the level of the individual Fe^{2+} sites enhances the understanding of the averages and distributions of the tensor in an octahedral sheet, the properties that are measurable by Mössbauer spectroscopy.

The variation of V_{ZZ} with flattening angle at 0 K and 300 K is shown in figure 3, with the three trigonal clusters on the far right. For these three high-symmetry clusters, V_{ZZ} is the EFG tensor's only independent parameter. The trigonal space group imposes that $V_{XX} = V_{YY} = -(1/2)V_{ZZ}$, so that $\eta = 0$, and $\mathbf{e}_{ZZ}$ is always along the z-axis (i.e., $\mathbf{e}_{ZZ} = \mathbf{c}^*$). The two other eigenvectors correspond to **a** and **b**.

The V_{ZZ} curves for the three trigonal clusters at 0 K are essentially the same, showing a positive V_{ZZ} around +1 au below 56°, and a negative V_{ZZ} around –2 au increasing slowly after 56°. The discontinuity is due to a change in ground state.

From crystal field theory (Bleany and Stevens, 1953), the Fe(3d) orbitals of an undistorted octahedral cluster in the {**a**, **b**, **c***} coordinate system are

$$\begin{aligned} |t_{2g}^0\rangle &= |z^2\rangle, \quad |t_{2g}^1\rangle = \sqrt{\frac{2}{3}}|x^2-y^2\rangle + \sqrt{\frac{1}{3}}|yz\rangle, \quad |t_{2g}^2\rangle = \sqrt{\frac{2}{3}}|xy\rangle + \sqrt{\frac{1}{3}}|xz\rangle \\ |e_g^1\rangle &= \sqrt{\frac{1}{3}}|x^2-y^2\rangle - \sqrt{\frac{2}{3}}|yz\rangle, \quad |e_g^2\rangle = \sqrt{\frac{1}{3}}|xy\rangle - \sqrt{\frac{2}{3}}|xz\rangle. \end{aligned} \tag{9}$$

Note that the t_{2g} and e_g orbitals are written differently in this system of coordinates than if the *xyz*-axes lay along the axes of the octahedron, in which case one has the more familiar |*xy*>, |*xz*> and |*yz*> for the t_{2g} and

$|x^2-y^2\rangle$ and $|z^2\rangle$ for the e_g orbitals. The difference is purely due to the coordinate system used. Flattening or counter-rotating the octahedron creates a splitting between the t_{2g}^0 and $t_{2g}^{1,2}$ orbitals, and between the e_g^1 and e_g^2 orbitals. Orbitals t_{2g}^1 and t_{2g}^2 remain degenerate. The coefficients $\sqrt{2/3}$ and $\sqrt{1/3}$ in equation 9 are replaced by cos(ω) and sin(ω), respectively, where ω is a function of the flattening and counter-rotation angles.

In the seven-octahedra clusters, the highest occupied and four lowest unoccupied molecular orbitals are predominantly of Fe(3d) character (95% or more for the t_{2g} orbitals, about 90% for the e_g orbitals), so to a close approximation they may be considered d-orbitals. For high-spin Fe^{2+} only one of the spin-down d-orbitals is occupied, and it is the character of this occupied orbital that determines the valence EFG. At low ψ, the energy of the z^2 (t_{2g}^0) orbital is higher than the energy of the $t_{2g}^{1,2}$ orbitals, so the spin-down electron is shared between the two $t_{2g}^{1,2}$ orbitals and the ground state is degenerate. At high ψ, z^2 is lower in energy than $t_{2g}^{1,2}$ and so the spin-down electron occupies the z^2 orbital. The principal value V_{ZZ} is positive in the $t_{2g}^{1,2}$-occupied ground state and negative in the z^2-occupied ground state.

In a bare FeO_6^{10-} octahedron the change in ground state occurs exactly at $\psi_{ideal} = 54.74°$ (Evans et al. 2005). In $Fe(OH)_6^{4-}$, the addition of OH bonds perpendicular to the plane, biasing somewhat the electron density at the iron nucleus along the z-axis, pushes the transition back to flattening angles lower than ψ_{ideal}. Adding the six neighbor octahedra in the seven-octahedra cluster shifts the bias on the electron density into the *xy*-plane, and then the transition occurs at flattening angles higher than ψ_{ideal}.

The remaining ten plots in figure 3 show V_{ZZ} as a function of flattening for the non-trigonal clusters. At 0 K, all V_{ZZ} curves show a sign change discontinuity, with $V_{ZZ} > 0$ at low ψ and $V_{ZZ} < 0$ at high ψ. Cluster AAMMMM shows two sign change discontinuities, switching from $V_{ZZ} < 0$ below 55.5° to $V_{ZZ} > 0$, then back to $V_{ZZ} < 0$ above 59.0°. Cluster AMAMMM shows a discontinuity without a change of sign at about 55° (arrow; the discontinuity is more clearly seen in the EFG eigenvalues, figure 4) in addition to a sign change around 58.5°. The magnitude of V_{ZZ} in all of these clusters regardless of sign is about 2 au (or 3.24 mm/s).

The principal EFG eigenvalue V_{ZZ} is a difficult parameter to discuss on its own, because it is not really one parameter but three, two of which are independent. V_{ZZ} is the EFG eigenvalue of maximum

magnitude, and when another eigenvalue exceeds it in magnitude as the tensor evolves with distortion, then that eigenvalue becomes the new V_{ZZ}. A discontinuity in V_{ZZ} (and parameters tied to it, like the angle ϕ) can result from continuously varying EFG eigenvalues V_1, V_2 and V_3.

It can easily be seen that when none of the eigenvalues are zero, V_{XX} and V_{YY} will have the opposite sign to V_{ZZ}, a result of the eigenvalues summing to zero. Unless V_1, V_2 and V_3 are themselves discontinuous (as can happen when energy levels cross, see below), the identity of V_{ZZ} changes when two of the eigenvalues are equal and opposite and the third passes through zero, e.g. $V_1 = -V_3$ and $V_2 = 0$. (Note that at this point, $\eta = 1$, and while V^* and $|V_{ZZ}|$ are defined, the sign of V_{ZZ} is not.) When V_{ZZ} changes identity at $V_1 = -V_3$, say from V_1 to V_3, it must change sign.

Figure 4 shows the EFG eigenvalues at 0 K for the non-trigonal clusters. Clusters AAAMMM and AMAMMM both have discontinuities in their eigenvalue curves due to a crossing of t_{2g} orbital energies, which also correspond to discontinuities in their V_{ZZ} curves. All other V_{ZZ} sign discontinuities occur when one of a cluster's EFG eigenvalues crosses through zero.

It can be seen in figure 4 that three distinct patterns of EFG eigenvalue behavior occur as flattening increases. The non-trigonal clusters may be sorted into three classes based on this behavior:

class I: AMMAMM, AMMMMM, MAMAAA, MMAAAA, AAMAMM

class II: MAAMAA, MAAAAA, AMAMMM, AAMMMM

class III: AAAMMM

(The discontinuity in eigenvalues of cluster AMAMMM at $\psi = 55.5°$ is ignored in this classification; see the discussion below and the Appendix.) Classes I and II differ mainly at low flattening angles; both have a strictly positive eigenvalue (V_1), an eigenvalue that crosses zero (V_2), and a strictly negative eigenvalue (V_3). At low ψ, V_1 is relatively flat in class I and concave down in class II. The other eigenvalues are nearly equal and again relatively flat in class I, before V_2 rises towards zero. In class II, V_1 and V_2 are widely separated at low ψ, with V_2 near or just above zero (the latter in cluster AAMMMM, responsible for its first discontinuity in V_{ZZ}); they meet and repel each other after which V_2 rises back towards zero. In class I, the eigenvector $\mathbf{e}_1$ associated with V_1 approaches **a** as ψ increases, $\mathbf{e}_3$ approaches **c***, and $\mathbf{e}_2$ is identically equal to **b** for all ψ. In class II, the $\mathbf{e}_1$ is identically **b**, $\mathbf{e}_2$ approaches **a** and V_3 approaches **c***.

Class III contains only cluster AAAMMM. Apart from the region immediately after the discontinuity, V_{XX} and V_{YY} are nearly equal. The EFG of AAAMMM resembles the trigonal clusters more than any of the other monoclinic clusters.

The classification of clusters by their EFG behavior does not appear to follow either chemistry (i.e., Al/Mg content) or local point group symmetry. The monoclinic clusters, however, do show an interesting "chemical inversion" property. Replacing Al^{3+} with Mg^{2+} and vice-versa in each of the group II clusters produces a monoclinic group I cluster. Cluster AAAMMM is transformed into itself under this operation, and is in a class by itself. Cluster AAMAMM likewise is transformed into itself, but it is triclinic, so apparently the "chemical inversion rule" does not apply.

The distinction between the three classes arises from differences in the ordering and evolution of the t_{2g} d-orbitals. When a trigonal cluster is reduced to monoclinic symmetry, additional mixing occurs between the $t_{2g}{}^0$ (z^2) and $t_{2g}{}^1$ orbitals of equation 9:

$$\begin{aligned}
\left|t_{2g}^{A}\right\rangle &= \cos(\chi)\left|t_{2g}^{0}\right\rangle + \sin(\chi)\left|t_{2g}^{1}\right\rangle \\
&= \cos(\chi)\left|z^2\right\rangle + \sin(\chi)\cos(\omega)\left|x^2-y^2\right\rangle + \sin(\chi)\sin(\omega)\left|yz\right\rangle \\
\left|t_{2g}^{B}\right\rangle &= -\sin(\chi)\left|t_{2g}^{0}\right\rangle + \cos(\chi)\left|t_{2g}^{1}\right\rangle \\
&= -\sin(\chi)\left|z^2\right\rangle + \cos(\chi)\cos(\omega)\left|x^2-y^2\right\rangle + \cos(\chi)\sin(\omega)\left|yz\right\rangle
\end{aligned} \tag{10}$$

where χ varies with flattening. The third t_{2g} orbital, $t_{2g}{}^2$, remains unchanged from that in equation 9. In class I clusters, $t_{2g}{}^B$ is the lowest in energy, while in class II $t_{2g}{}^A$ is lowest. In both classes, the coefficient of z^2 increases in magnitude as flattening increases, that is, the lowest energy d-orbital approaches a pure z^2 orbital as the cluster becomes more flattened. The discontinuity in V_{ZZ} comes not from a change in the ground state, but a continuous evolution of the lowest energy spin-down d-orbital. A crystal-field-based derivation of how these orbitals give rise to the observed EFG tensors is given in the Appendix.

In cluster AMAMMM, orbital $t_{2g}{}^2$ is lowest in energy below 55.5°, afterwards it is $t_{2g}{}^A$ as for the other class II clusters. Cluster AAMAMM, despite its triclinic point group symmetry, has essentially the same t_{2g} orbitals as in equation 10, with only small amounts of xy and xz mixed into $t_{2g}{}^A$ and $t_{2g}{}^B$, and of z^2, x^2-y^2 and yz in $t_{2g}{}^2$. Thus its V_{ZZ}, η and EFG eigenvalue curves are the same as the monoclinic class I clusters.

Cluster AAAMMM (class III) is again a strange exception. The lowest energy orbital at all flattening angles is t_{2g}^{A}. At low flattening, $\chi \approx 90°$ so that t_{2g}^{A} is nearly pure t_{2g}^{1} and t_{2g}^{B} is nearly pure z^2. As flattening increases, the two orbitals approach one another in energy, and at around $\psi = 55.7°$ there is a weakly avoided crossing (c.f. Albright et al., 1985) and χ drops rapidly but continuously to zero. After the avoided crossing, t_{2g}^{A} is nearly pure z^2 and t_{2g}^{B} is nearly pure t_{2g}^{1}. This is why AAAMMM shows behavior so similar to the trigonal clusters, because except for near the avoided crossing, its orbitals are the same as those of the trigonal clusters (equation 9). It is not clear why this behavior occurs in this cluster, but it may be a polarization effect due to the very lopsided distribution of 2+ and 3+ cations.

At 300 K, the discontinuity in the V_{ZZ} curve for the three trigonal clusters disappears for non-zero temperature, as the occupations of the t_{2g} orbitals become continuous rather than step functions when orbital energies cross. Those discontinuities in the non-trigonal clusters remain which are due to reordering of the EFG eigenvalues as the t_{2g} orbitals evolve. (V^* is continuous for all clusters at 300 K (Evans et al. 2005)). Curves for the class I non-trigonal clusters are about the same qualitatively as at zero temperature, despite a change in curvature at low ψ. Class II clusters change significantly at low ψ; three of the four show a low ψ sign change from negative to positive at 300 K (AAMMMM, AMAMMM and MAAAAA) compared to only one at 0 K (AAMMMM). This is a result of thermally reduced z^2 occupation due to the three t_{2g} orbitals being close in energy at low ψ (see Appendix). Cluster AAAMMM (class III) continues to resemble the trigonal clusters, except for those points near the weakly avoided crossing where there is greater mixing between the d-orbitals.

In general, the EFG tensor at 300 K differs from the EFG at 0 K only at low flattening angles. This is because in all clusters, the gap between the lowest energy t_{2g} d-orbital from the other two increases with flattening angle and therefore the occupation of the lowest energy d-orbital approaches one.

Like V_{ZZ}, η is a parameter derived from the EFG eigenvalues. Figure 5 shows η for the non-trigonal clusters at 0 K and 300 K. The curves rise to one where V_{ZZ} changes sign (figure 3) and eigenvalue V_2 crosses zero (figure 4), and then decrease as the cluster is flattened further. Class II clusters have high η (> 0.4) at low ψ, indicating an additional maximum, due to the wide spread between V_2 and V_3 in that region. Class I clusters correspondingly have a low η (< 0.2) at low ψ. Cluster AAAMMM has a

discontinuous η curve. There is not a lot of change in the η curves on changing temperature from 0 K to 300 K. At 300 K, class I asymmetries are higher at low flattening angles than at 0 K. Class II and class III asymmetry curves also have additional activity at low flattening angles, including extra peaks (c.f. MAAAAA).

Figure 6 shows the variation of ϕ (the angle between $\mathbf{e}_{ZZ}$, the EFG principal axis, and **c***, the normal to the octahedral sheet) with flattening for the ten non-trigonal clusters. The sheet structure makes **c*** quite distinct from **a** and **b**, and so ϕ is the most physically interesting of the three Euler angles which define the EFG eigenvectors. In the EFG tensor of the monoclinic clusters, V_{ac} is the only off-diagonal component that is non-zero. Therefore one of the eigenvectors will always be **b**, and the other two will lie in the *ac*-plane at 90° to one another. This leaves the following possibilities for ϕ, θ and ζ:

ϕ free, $\theta = 0°$, $\zeta = 0°$;

ϕ free, $\theta = 0°$, $\zeta = 90°$;

ϕ free, $\theta = 180°$, $\zeta = 90°$;

ϕ free, $\theta = 180°$, $\zeta = 180°$;

or $\phi = 90°$, $\theta = 90°$, ζ free.

The first four possibilities have $\mathbf{e}_{ZZ}$ in the *ac*-plane and the last has $\mathbf{e}_{ZZ} = \mathbf{b}$. Of course, in the triclinic case, all three angles are free.

All clusters in figure 6 have $\mathbf{e}_{ZZ}$ close to the *ab*-plane (the octahedral sheet) at low ψ and close to **c*** at high ψ, the transition occurring at the V_{ZZ} sign change (compare figure 3). Class II has ϕ identically 90° at low ψ, corresponding to $\mathbf{e}_{ZZ} = \mathbf{b}$, while for class I, ϕ rises from about 45° at ψ_{ideal} to about 80-85° before the transition. Class III has ϕ about 30-35° before the transition. At 300 K, Class I ϕ curves change very little from their 0 K behavior. Class II ϕ curves, except for cluster MAAMAA, have an added segment at low ψ where ϕ is about 70-80° and steeply decreasing, corresponding to the negative segment in their 300 K V_{ZZ} curves. Class III has an extra peak of high ϕ near its weakly avoided crossing, where orbital energies are close and there is the greatest difference from 0 K occupation.

The prominent coupling of the EFG principal direction and the sign of V_{ZZ} (figures 3 and 6) is a result that has immediate experimental implications. These calculations indicate that for samples with a low

average flattening, the measured average quadrupole splitting should be positive and the average principal direction should be within the *ab*-plane (large average ϕ), and for samples with a high average flattening, the measured average quadrupole splitting should be negative and the average principal direction should be normal to the *ab*-plane (small average ϕ). Samples with a bimodal distribution of EFG directions, as observed by Hargraves et al. (1990), should have their high-ϕ populations corresponding to positive values of V_{ZZ} and their low-ϕ populations corresponding to negative values of V_{ZZ}. Significant populations of sites where the local EFG tensors follow a contrary trend (i.e. negative V_{ZZ} and in-plane principal directions, or positive V_{ZZ} and normal principal directions) should not occur. In addition, these results (figures 3 and 6) show that different samples, with either large or small flattening angles (on the scale of ψ values in the figures and observed in layer silicates), would have dramatically different oriented single crystal Mössbauer spectroscopy behaviours, as could be tested experimentally.

Figure 7 shows the EFG directional angles θ and ζ as functions of flattening for the triclinic cluster AAMAMM. Both angles show a discontinuity where V_{ZZ} changes sign, as does ϕ, which is not unexpected since we have relabeled the EFG axes at this point, and therefore essentially changed the definition of the angles. Except for the discontinuity, θ is approximately constant, so that with regards to figure 2, the ab-plane component of $\mathbf{e}_{ZZ}$ points roughly towards site 2 before the sign change, and towards site 5 afterwards. The angle ζ changes rapidly at low flattening angles, and in different ways at zero and room tmperatures, then like θ becomes approximately constant. This suggests that when θ and ζ are not fixed by point group symmetry, the orientation of the EFG principal direction within the *ab*-plane is constant, except when V_{ZZ} changes sign.

We have examined the EFG tensors of all possible seven-octahedra clusters, given a central Fe^{2+} site and neighbour sites occupied by either Mg^{2+} or Al^{3+}, and their variation with flattening, a key local structual distortion in octahedral sheets. Though the behaviour of the EFG tensor parameters with changing flattening shows similarities among all clusters, we find that there are also differences, some based on local point group symmetry (i.e., the differences between mono- or triclinic clusters and the trigonally symmetric clusters) but others are based on no obvious combinations of local symmetry and chemistry (i.e., the differences between the groups of clusters we have labeled class I, II and III). In larger clusters, additional chemical disorder will lower the point group symmetry of the Fe^{2+} site, and as a result somewhat perturb

the EFGs away from those we have calculated. Nonetheless, it should be clear that since, in a given sample that is not perfectly chemically ordered, many or all of these seven-octahedra configurations will occur within the octahedral sheet, it is not the point group symmetry of the Fe^{2+} site in the refined structure, that is, the *average* Fe^{2+} site, that determines the local EFG, but rather the *local* point group symmetry, that is, the local structural distortions and chemical disorder, that is important. It is the population of these local distortion environments that gives rise to the QSD that is measured by ^{57}Fe Mössbauer spectroscopy.

Distributions of EFG tensor properties in an octahedral sheet, and implications for experimental measurements

It is useful to explain the behavior of EFG properties for individual model clusters, but perhaps more useful is the ability to predict how these properties will be distributed in the bulk material. As an example, we assume an octahedral sheet where the octahedral sites are occupied by Mg^{2+}, Al^{3+} and a very small fraction of Fe^{2+}, small enough that every iron cation is surrounded entirely by a mixture of Mg^{2+} and Al^{3+}. Thus the first nearest neighbor coordination sphere of every possible Mössbauer center looks like one of our thirteen sample clusters.

Assuming no chemical order, the probability of an Fe^{2+} cation in the sheet being in an environment like cluster C is given by

$$P(C;p,q) = \frac{1}{K_n}\frac{720}{n!(6-n)!}p^n q^{6-n}, \tag{11}$$

where n is the number of Mg^{2+} cations adjacent to Fe^{2+} in cluster C (between 0 and 6), K_n is the number of clusters with n Mg^{2+} cations adjacent to Fe^{2+} (equal to 3 for n = 2, 3, 4 and 1 for n = 0, 1, 5, and 6), p is the fraction of Mg^{2+} sites in the sheet, and $q = 1 - p$ is the fraction of Al^{3+} sites. The average value of a particular EFG property W in a sheet of composition (p, q) is then

$$\langle W \rangle_{\text{sheet}} = \sum_C W(C)P(C;p,q). \tag{12}$$

Figure 8 shows average values of V^*, η and ϕ at 300 K as a function of Mg^{2+} content at constant flattening, as calculated with equation 10. The flattening angles shown, 58-60°, are in the range of flattening angles observed in layer silicates (e.g. Hazen and Wones 1972, Weiss et al. 1985, Mercier 2003, Piilonen et al. 2003). Figure 8a shows that when all M-O bond lengths are the same, $<V^*>$ and therefore the

average Mössbauer quadrupole splitting increases with both increasing flattening and increasing Mg^{2+} content (decreasing Al^{3+} content) in this region of flattening angles. At $\psi = 58°$ and 59°, the maximum $\langle V^* \rangle$ occurs slightly before the 100% Mg^{2+} end point, at about 80% and 90% Mg^{2+} respectively.

Parts b and c of figure 8 show average asymmetry parameter $\langle \eta \rangle$, and average principal axis angle $\langle \phi \rangle$, respectively, and convey similar information. Both η and ϕ are, in a sense, a measure of disorder in the environment around the iron nucleus, taking values of zero at the 100% Mg^{2+} and 100% Al^{3+} endpoints and rising to maxima at mixed compositions. Neither parameter rises to its theoretical maxima of 1 for η and 90° for ϕ at any flattening or composition. This is partly because the trigonal clusters make no contribution to either parameter average, so that those environments that do contribute do not add up to 100% of the total; and partly because at no flattening angle do either of the parameters reach their theoretical maxima for all clusters simultaneously. Both graphs also show a significant difference between the $\psi = 58°$ curve and the two higher flattening curves. This is because most of the non-trigonal clusters (AAAMMM and MAAMAA being the exceptions) have their V_{ZZ} sign change discontinuity, and the accompanying discontinuity in ϕ and maximum in η, at ψ between 58° and 59°. Thus, in figure 8b, $\langle \eta \rangle$ increases from $\psi = 58°$ to $\psi = 59°$, then decreases from $\psi = 59°$ to $\psi = 60°$; and in figure 8c, $\langle \phi \rangle$ is high for $\psi = 58°$ and low for $\psi = 59°$ and $\psi = 60°$.

Figure 8 helps to illustrate how fitting oriented single-crystal Mössbauer data with a single EFG tensor rather than a distribution can be misleading. The best that a fit using a single EFG tensor can do is to give the average values of the tensor parameters. At significantly mixed compositions (e.g., Mg/(Mg+Al) ~ 50%), $\langle \phi \rangle$ takes an intermediate value (that is, the principal axes is neither in the *ab*-plane nor normal to it) and $\langle \eta \rangle$ is in the range 0.5-0.6. This is clearly inconsistent with an axial model of the EFG (i.e., $\eta = 0$ and $\phi = 0°$), which is often assumed for fitting purposes. Also, if the average flattening angle of the Fe^{2+} site is high (i.e., greater than 59°), then figures 5 and 6 indicate these values of $\langle \phi \rangle$ and $\langle \eta \rangle$ are not consistent with the local geometry. Moreover, if the sample contains populations of EFGs with both positive and negative values of V_{ZZ}, then attempting to assign a sign to the average quadrupole splitting is questionable.

Figure 9 shows details of the distribution of η and ϕ at constant flattening and bulk composition through bubble graphs. Points (η, ϕ) are plotted for the thirteen clusters, and the area of the bubble is

proportional to the probability $P(C; p, q)$ of equation 11. Points that are closer together than 0.02 in η and 2° in ϕ are combined for clarity (e.g., the three trigonal clusters at (0, 0°)), with the center of the combined bubble located at the average position. All compositions and flattening angles have significant probability density in both high and low η regions, and in both normal ($\phi = 0°$) and in-plane ($\phi = 90°$) principal axis directions. As the flattening angle increases, most probability density shifts from in-plane to normal principal axis directions. The asymmetry parameter values remain broadly distributed between low and high values as both flattening and composition change.

The most important result shown by these bubble plots is that at all flattening angles for non-end-point compositions, there exist populations of sites with near-normal and near-planar EFG principal axes, and with low and high asymmetry parameters, in the same octahedral sheet. This is consistent with the findings of Hargraves et al. (1990), who found that the room temperature spectra of phlogopite was consistent with two populations of sites, one with EFG directions in the *ab*-plane and the other with EFG directions normal to the plane.

Figure 10 shows a series of probability histograms for V^* at 300 K, where V^* is the EFG component proportional to the quadrupole splitting measured in Mössbauer spectroscopy, defined in equation 4. The probabilities associated with each seven-octahedra cluster, as calculated with equation 11 for a constant bulk composition, are binned according to V^* at a particular flattening angle. At every composition and flattening angle studied, the extreme high V^* value (the high edge of the distribution) is from cluster MAAMAA, and the extreme low value (the low edge of the distribution) is from cluster AAAMMM; these values are shown as vertical dotted lines in the figure. As flattening increases, the peak of the distribution moves towards higher values of V^*, and the width or standard deviation of the distribution decreases dramatically. The low edge increases significantly from 1.04 to 1.51 au (1.68 to 2.45 mm/s) as flattening increases from 58° to 60°, while the high edge remains relatively constant, increasing only from 1.89 to 1.91 au (3.06 to 3.09 mm/s). This can also be seen by comparing the V_{ZZ} curves for the two clusters in figure 3; cluster MAAMAA is high and relatively constant in the region 58-60°, while the magnitude of V_{ZZ} for cluster AAAMMM is low and steeply increasing.

This kind of behavior, a constant high edge and a variable width and low edge, is seen in many experimental QSDs of layer silicates (e.g., Rancourt et al. 1994, Shabani 1999, Piilonen et al. 2004). In

Evans et al. (2005), it was shown that the maximum in 300 K V^* vs. ψ curves coincided closely with the high edge of experimental QSDs for micas, and that V^* changes most rapidly with flattening when compared with other octahedral distortions. Together these results suggest that the maximum in the V^* vs. ψ curves is largely responsible for the constant high edge observed in experimental QSDs. Figure 10 adds to this result, showing that when the local geometry (flattening, bond length, etc.) is held constant, chemical disorder in the first nearest-neighbor octahedra also produces a maximum EFG resulting in a constant high edge. The chemical high edge (about 1.9 au or 3.1 mm/s) is similar in magnitude to the value of the maximum due to flattening (about 2.9 mm/s, Evans et al. 2005), which is in good agreement with experiment. These results represent the first predictions relating average structural parameters to characteristics of the Fe^{2+} QSD in a solid solution material. This high edge value of about 3 mm/s seems to be the maximum quadrupole splitting value due to different local chemical and distortion environments of Fe^{2+} in an octahedral sheet, at least in trioctahedral sheets and in the absence of anionic substitutions such as F^- or Cl^- for OH^-. We do not expect that allowing neighboring sites to take their own cation-specific bond lengths and corresponding local distortions in a more realistic seven octahedra calculation, or including additional shells of neighbor octahedra or groups in adjacent tetrahedral sheets, would change this conclusion or the value of the high edge significantly.

Figure 10 shows changes in the QSD histograms with both flattening angle and bulk composition, as if the composition and geometry of the octahedral sheet were mutually independent. This is not the case in real minerals. Additionally, in these seven octahedra clusters we have artificially constrained the M-O bond length at all sites to be 2.110 Å. In reality, Mg^{2+} is a larger cation than Al^{3+} (Shannon 1976, Weiss et al. 1992, Mercier 2003), so that the average M-O bond length will decrease from sample to sample as the fraction of Al^{3+}, Al/(Mg+Al), increases. Many studies have investigated the interrelation of flattening angle, chemical composition, M-O bond length and QSD properties in micas (for example, Hazen and Wones 1972, Rancourt et al. 1994, Redhammer 1998, Shabani 1999, Redhammer et al. 2000, Redhammer and Roth 2002, Mercier 2003). Experimentally it is found that as a larger cation is substituted into the octahedral sheet, average and peak quadrupole splittings decrease, average flattening angle decreases, and average M-O bond length increases; as a smaller cation is substituted, average and peak quadrupole splittings increase, average flattening angle increases and average M-O bond length decreases. This occurs

both when substituting divalent cations for other divalent cations, as in the annite-phlogopite solid solution (e.g., Hazen and Wones 1972, Rancourt et al. 1994, Redhammer 1998, Redhammer and Roth 2002), and when substituting Al^{3+} for divalent cations, as in the annite-siderophyllite solid solution (e.g., Redhammer 1998, Redhammer et al. 2000, Redhammer and Roth 2002). Therefore, we expect the "correct" sequence of QSD histograms in a mica solid solution series where Mg^{2+} is progressively replaced by Al^{3+} to be graphs 10g, 10e and 10c. In this sequence, the distribution narrows and the peak value increases as the fraction of Al^{3+} increases and the octahedral flattening angle decreases. This is typical of QSDs in solid solution series of layer silicates.

In summary, we have succeeded in producing two significant features of mica hyperfine EFG tensors: the two distinct populations of EFG principal axis directions, normal to and in plane with the octahedral sheet, as observed by Hargraves et al. (1990), and a sequence of QSD histograms that alter their shape with the chemical composition of the octahedral sheet in a good approximation to observed QSDs in solid solution series, as first observed by Rancourt et al. (1994). On the other hand, in relation to a real mica octahedral sheet, our model calculations still contain several limitations, including the lack of realistic M-O bond lengths in the Mg- and Al-substituted octahedra, the lack of adjoining tetrahedra, a stoichiometry which does not actually represent any real mica species, the limited cluster size, and our assumption of perfectly random chemical disorder in calculating the EFG parameter averages and histograms. Despite these assumptions, this work is an important step towards understanding the origins of hyperfine EFG tensor distributions in the variation of local chemical and distortion environments, and in connecting the features of measured hyperfine EFG distributions to crystal chemical properties of the sample. We have examined how a key octahedral distortion in layer silicates, flattening, in combination with the cation population of near-neighbor sites, affects the elements of the EFG tensor (V_{ZZ} and its sign, V^*, principal direction and the asymmetry parameter) and how this can lead to distributions of these parameters in the bulk mineral. This is important both in the basic understanding of mineral EFG tensors and in the interpretation of oriented single-crystal Mössbauer data and extracted QSDs.

Acknowledgements

We acknowledge financial support from the Natural Sciences and Engineering Research Council of Canada, in the form of a Discoveries Grant to DGR.

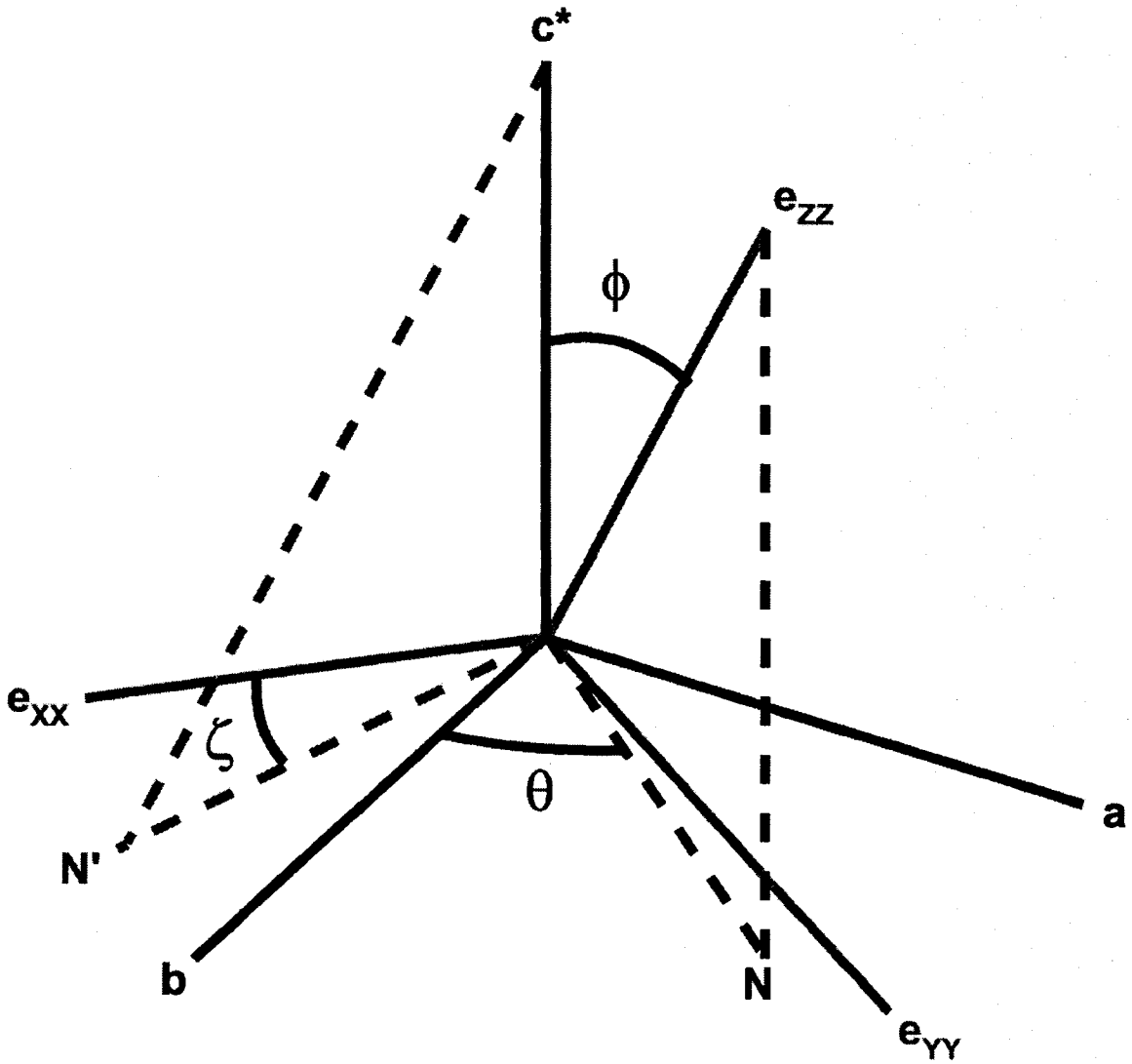

Figure 1. Directional angles of the EFG eigenvectors (grey lines) with respect to the crystallographic axes (black lines). **N** is the projection of $\mathbf{e_{ZZ}}$ in the *ab*-plane, and **N'** is the projection of **c*** in the plane of $\mathbf{e_{XX}}$ and $\mathbf{e_{YY}}$.

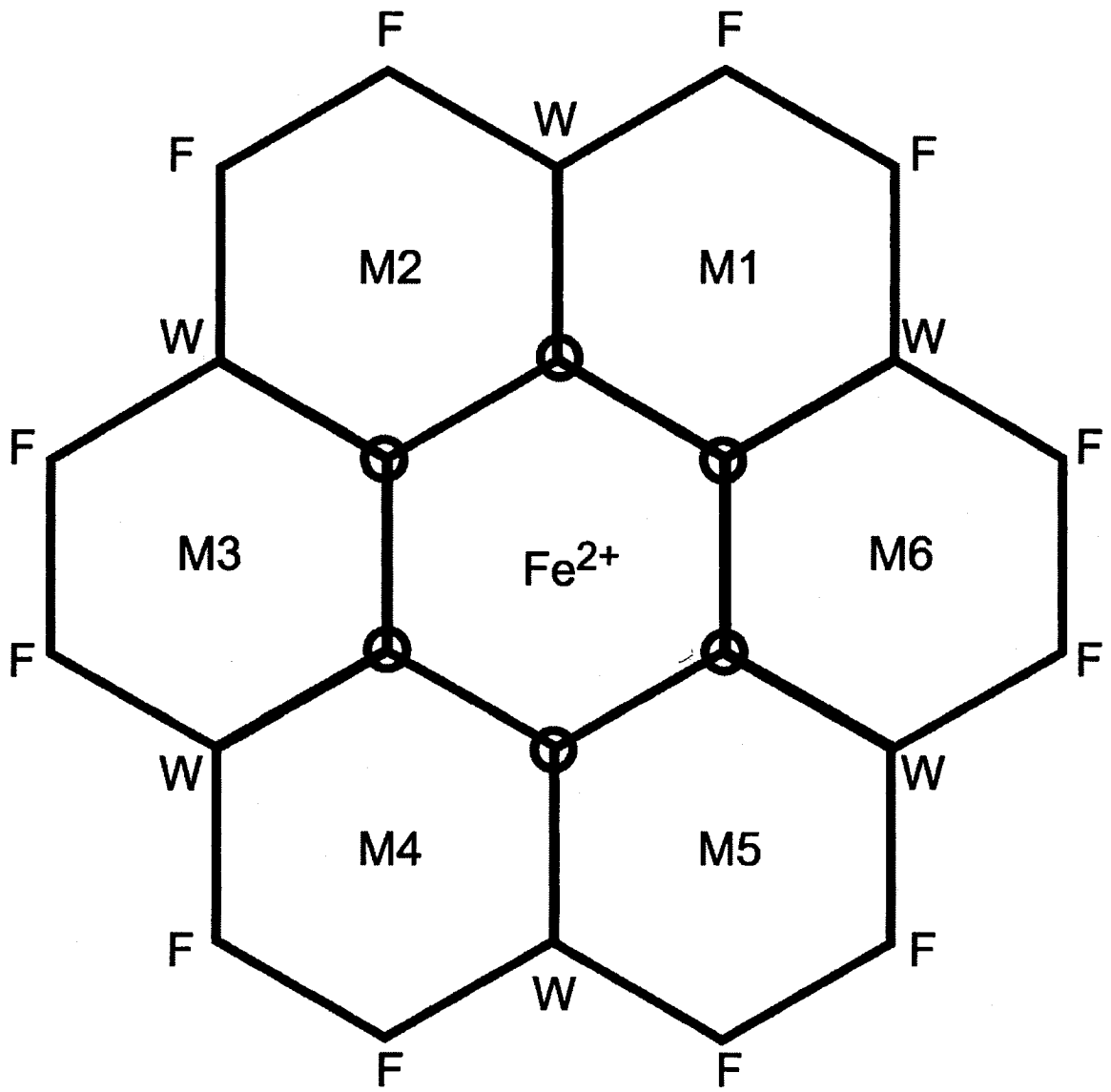

Figure 2. Schematic of the model cluster, showing positions of OH groups (circles), water groups (W), fluorine anions (F), and cations (Fe^{2+} and integers 1 to 6). Neighbor cations C_i were either Mg^{2+} or Al^{3+}. Clusters are labelled $X_1X_2X_3X_4X_5X_6$, where X_i = 'M' if cation i is Mg^{2+} and 'A' if it is Al^{3+}.

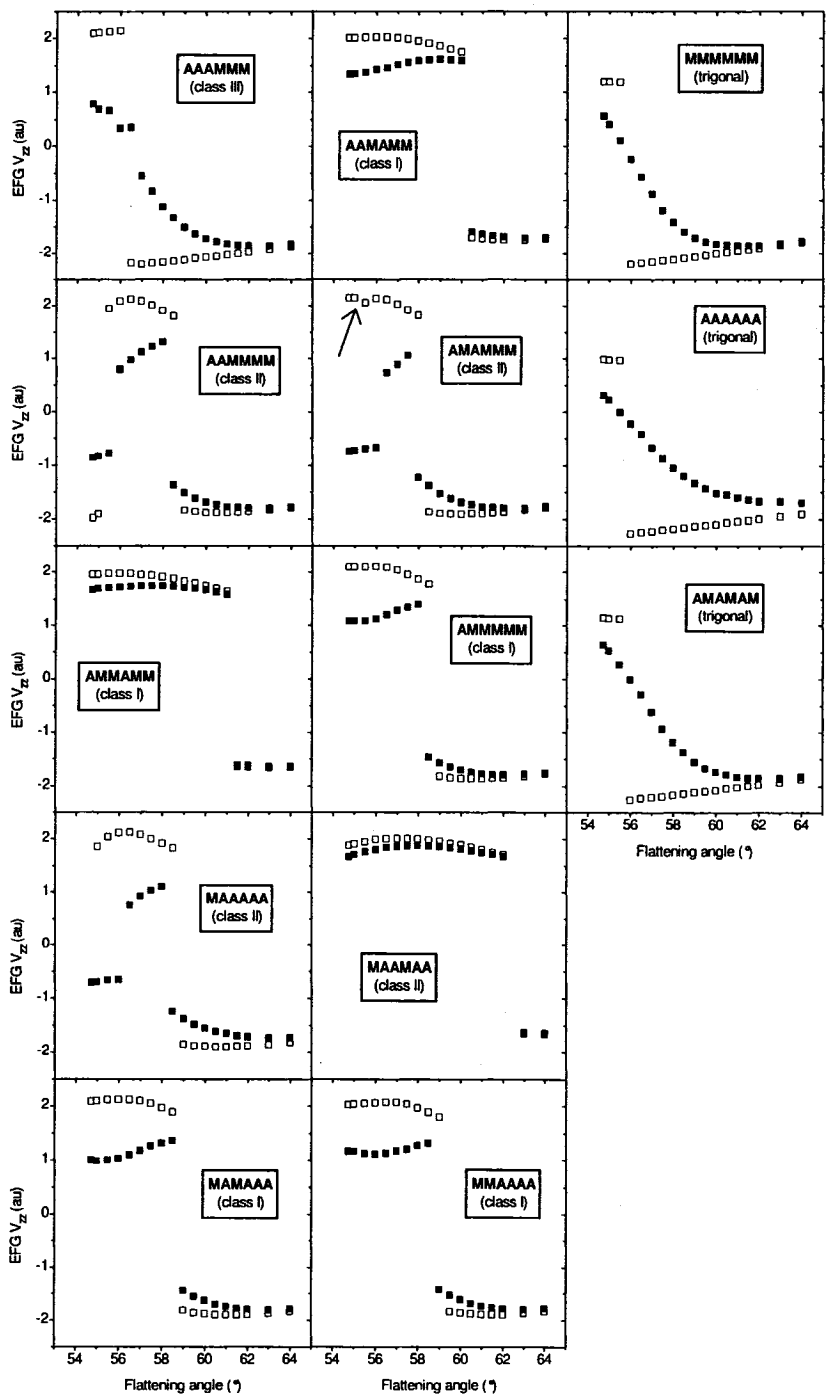

Figure 3. EFG principal eigenvalue V_{ZZ} as a function of flattening angle ψ at 0 K (open squares) and 300 K (filled squares) for all configurations. The arrow on AMAMMM shows a discontinuity in the curve.

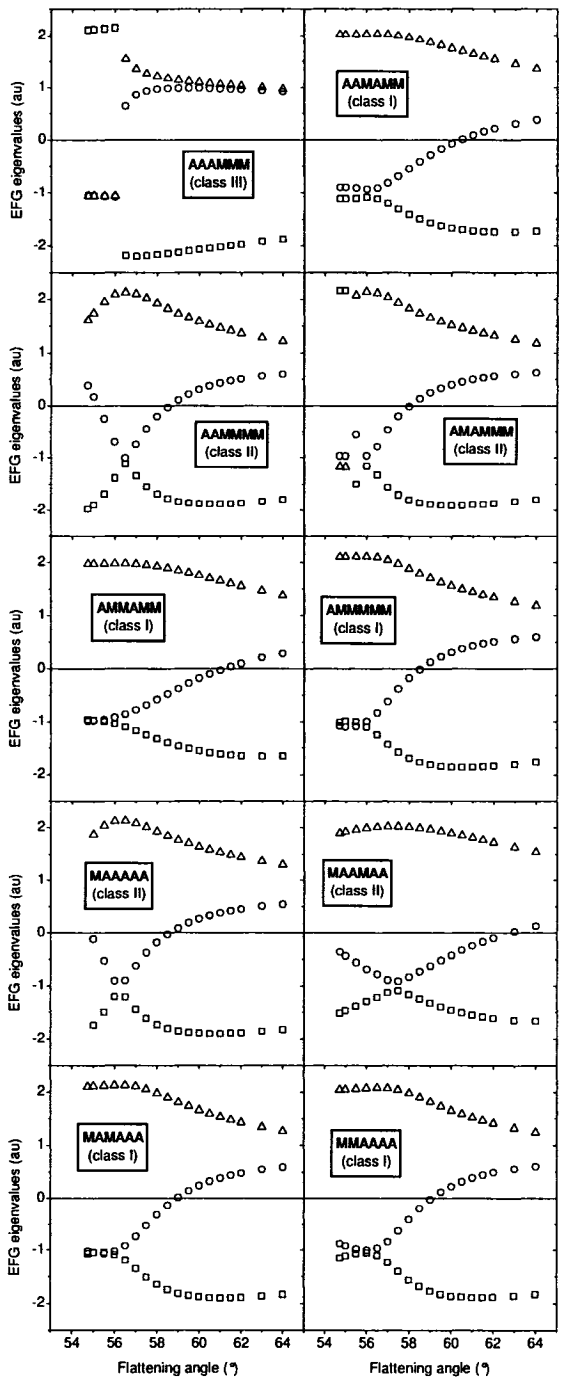

Figure 4. EFG eigenvalues V_1 (triangles), V_2 (circles) and V_3 (squares) as a function of flattening angle ψ at 0 K for all configurations.

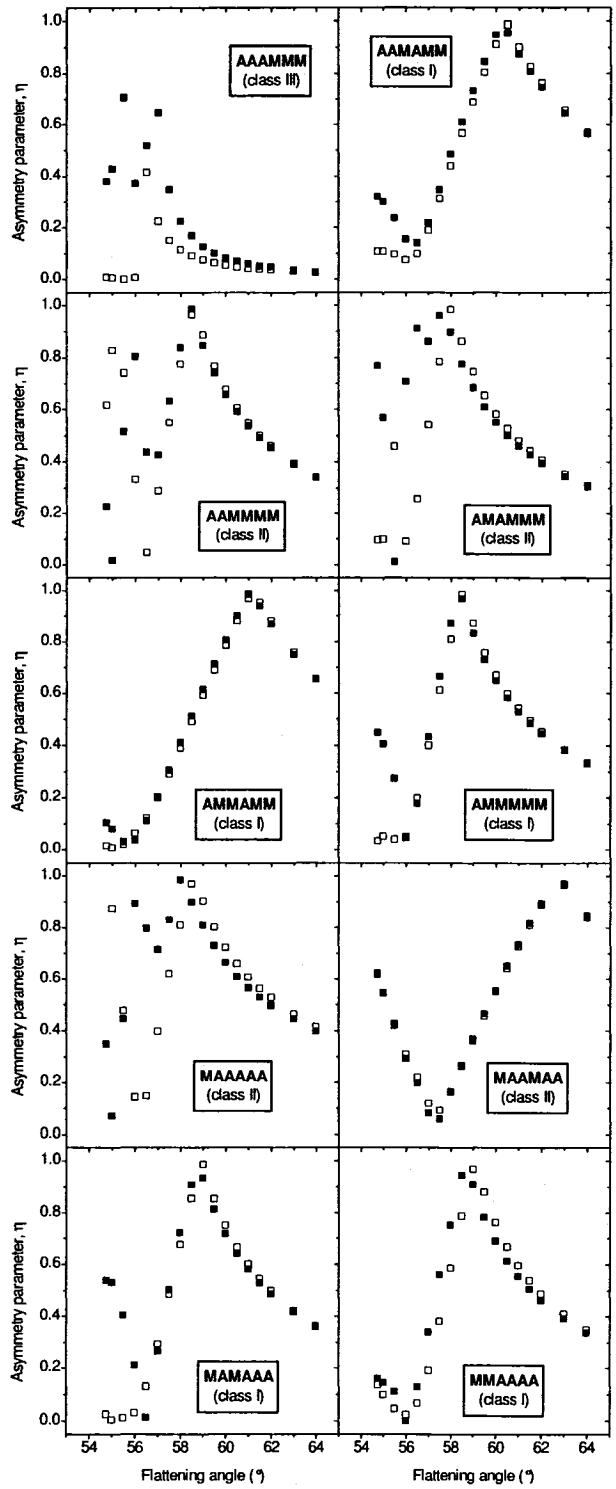

Figure 5. Asymmetry parameter η as a function of flattening angle ψ for the non-trigonal configurations at 0 K (open squares) and 300 K (filled squares).

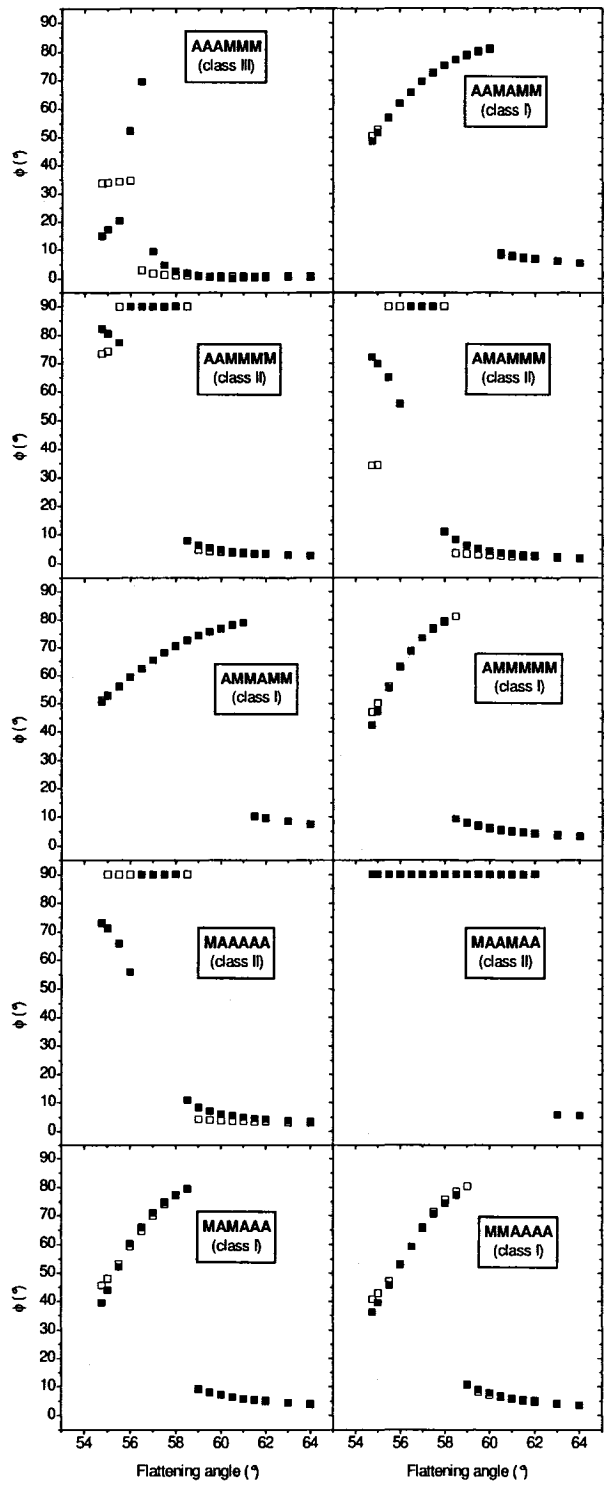

Figure 6. EFG directional angle ϕ as a function of flattening angle ψ for the non-trigonal configurations at 0 K (open squares) and 300 K (filled squares).

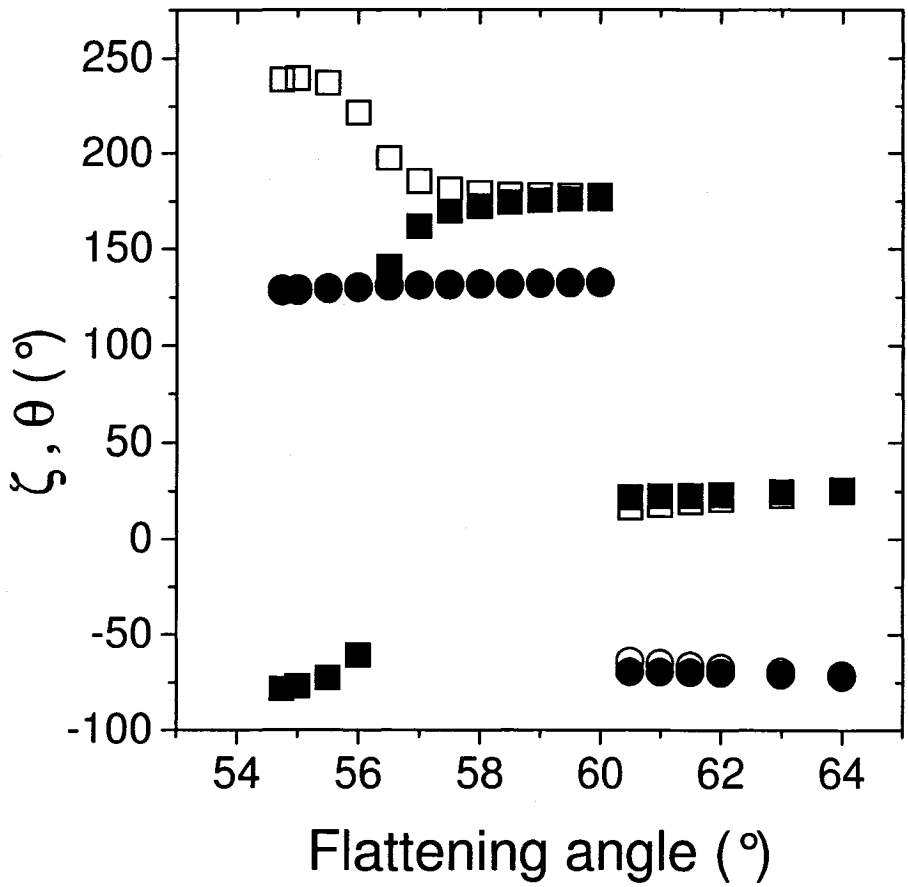

Figure 7. EFG directional angles ζ (squares) and θ (circles) as a function of flattening angle ψ for the triclinic configuration AAMAMM at 0 K (open symbols) and 300 K (filled symbols).

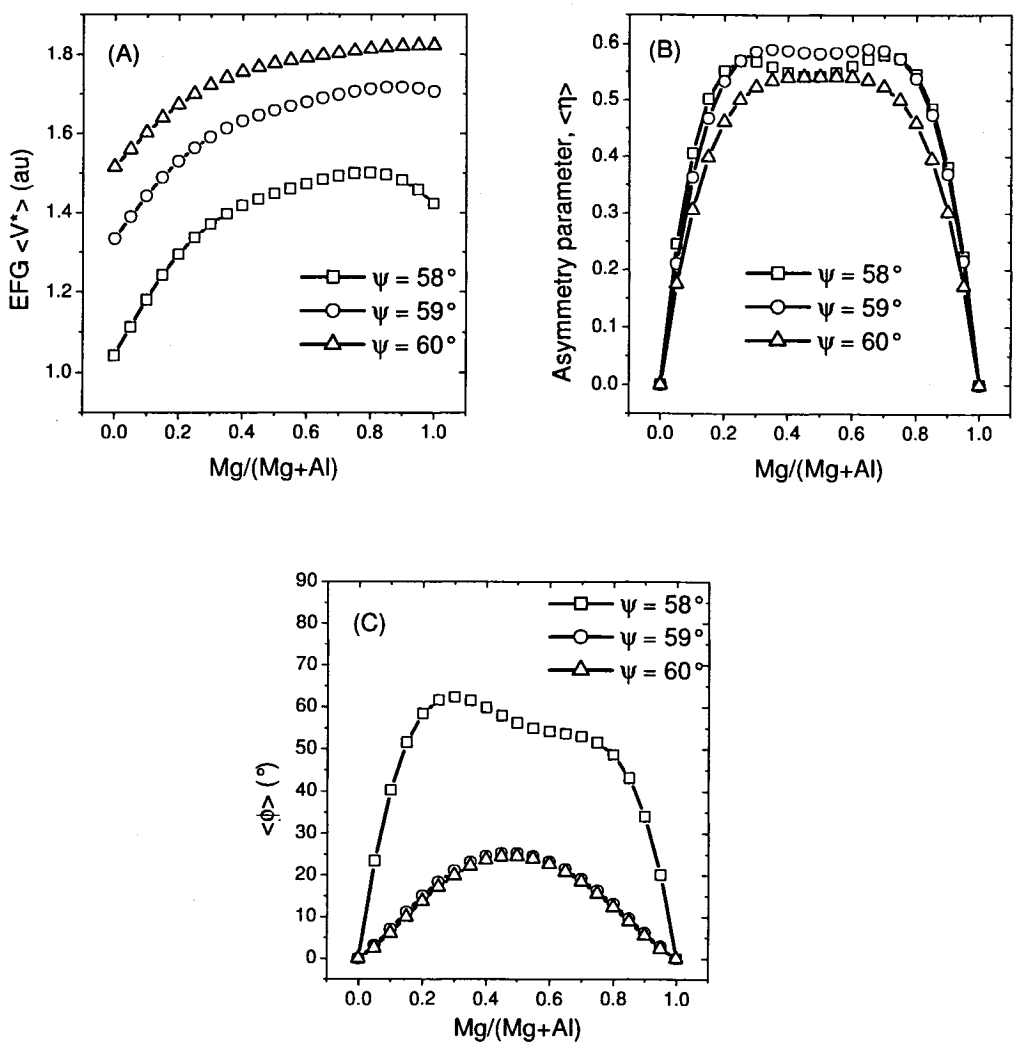

Figure 8. Contour plots of EFG properties with Mg^{2+} content at constant flattening at 300 K, averaged over a chemically disordered octahedral sheet (averaging is indicated by angle brackets). (a) EFG component proportional to the quadrupole splitting, $V^* = |V_{ZZ}|(1+\eta^2/3)^{1/2}$, (b) asymmetry parameter η, (c) angle of EFG principal axis with the normal to the octahedral sheet, ϕ.

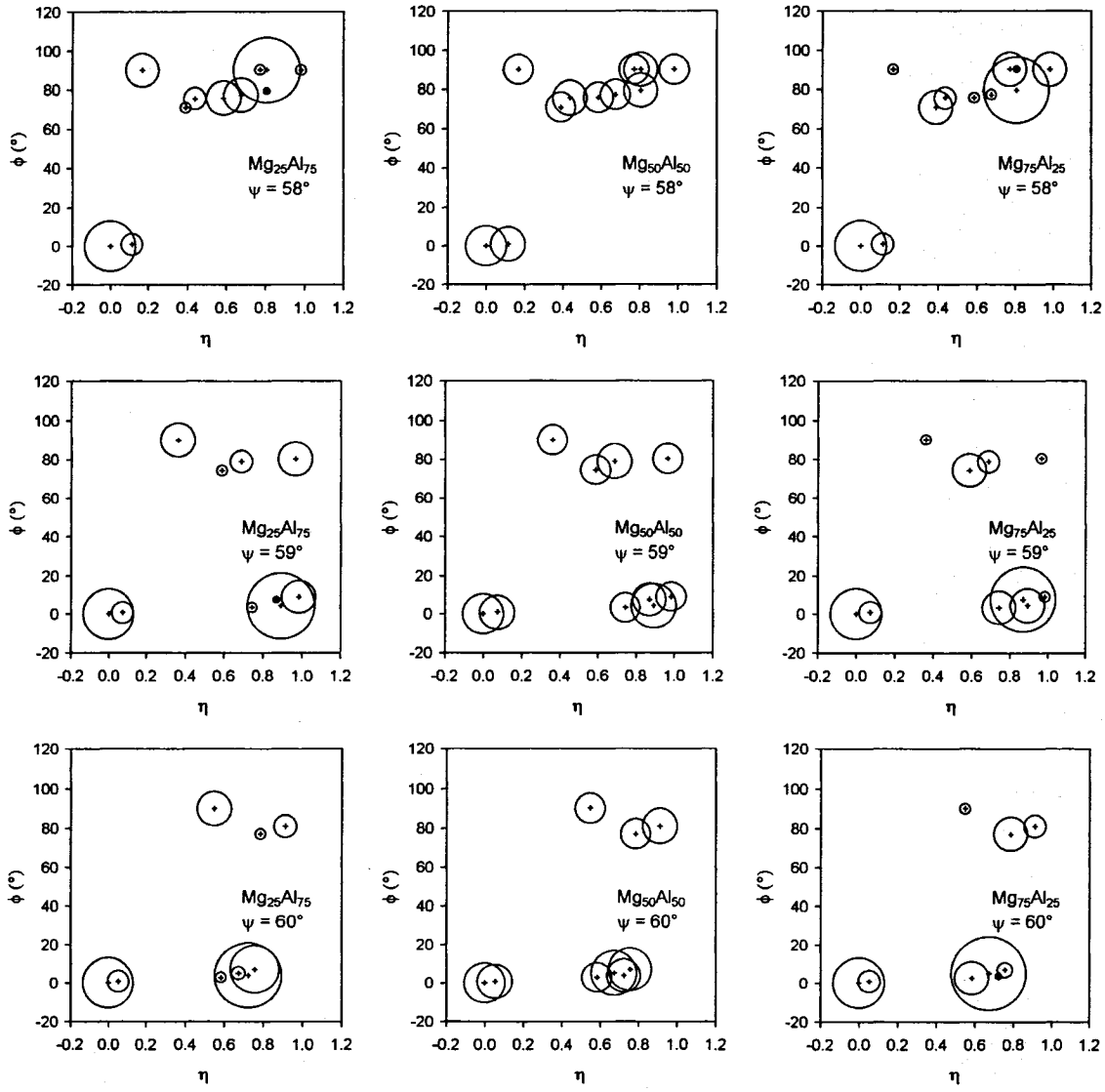

Figure 9. Bubble graphs illustrating distributions of the asymmetry parameter η and the EFG directional angle ϕ in octahedral sheets of constant composition and flattening at 300 K. The centres of the bubbles (small crosses) correspond to η and ϕ values of the seven-octahedra clusters, and area of the bubbles are proportonal to the number of those clusters present in the sheet. Bubbles with centres closer than $\Delta\eta = 0.02$ and $\Delta\phi = 2°$ are combined for clarity.

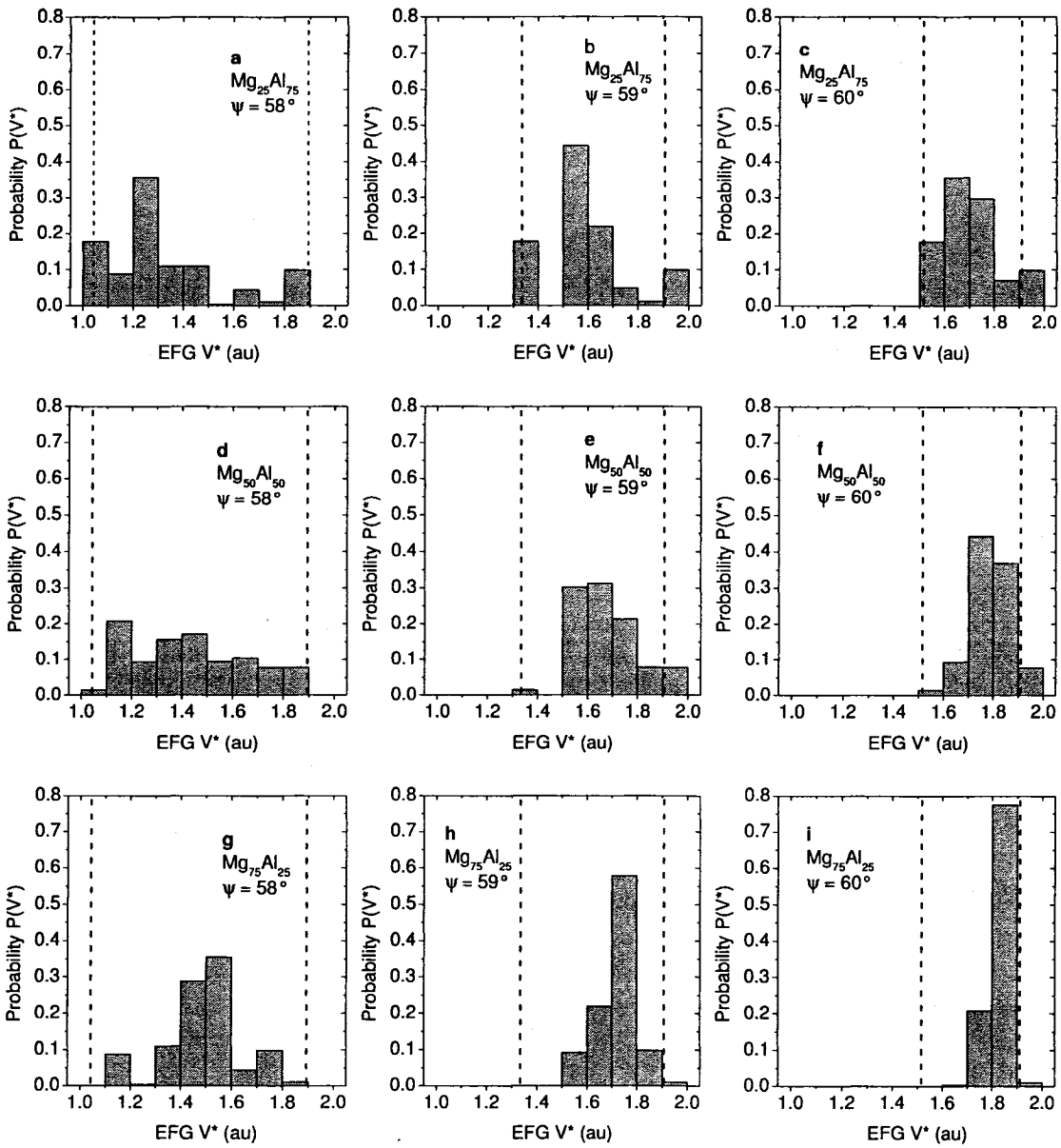

Figure 10. Probability histograms of the EFG V^* at 300 K, simulating quadrupole splitting distributions, in octahedral sheets of constant composition and flattening, based on the calculated proportion of the thirteen clusters examined present in the sheet. Dashed vertical lines represent the extreme low and high values for a particular flattening angle.

Appendix

An analytic approximation of the d-orbitals of a cluster, and the EFG tensor arising from its electronic structure, can be derived using crystal field theory and a point charge model of the octahedron (Bleany and Stevens 1953, Ingalls 1964, Evans 2001). This sort of model is a limited but useful qualitative tool for understanding the origins and behavior of EFGs. In this appendix we use the techniques of crystal field theory together with arguments based on orbital symmetry to derive the mathematical basis for the discussion of the EFG tensors of group I, II and III clusters above, showing how differences in the order and evolution of the spin-down d-orbitals gives rise to differences in the evolution of the EFG.

Operators for the valence EFG can be constructed from angular momentum operators using the partial matrix-elements approach of Bleany and Stevens (1953):

$$\mathbf{V}_{ii} = \frac{2}{21}\left(3\mathbf{L}_i^2 - \mathbf{L}^2\right)\left\langle r^{-3}\right\rangle, \text{ for } i = x, y, z, \tag{A1a}$$

$$\mathbf{V}_{ij} = \frac{1}{7}\left(\mathbf{L}_i\mathbf{L}_j + \mathbf{L}_j\mathbf{L}_i\right)\left\langle r^{-3}\right\rangle, \text{ for } i \neq j. \tag{A1b}$$

where $\mathbf{L}^2$ and $\mathbf{L}_i$ are orbital angular momentum operators, and $\langle r^{-3}\rangle$ is averaged over the radial 3d wave-function. The valence EFG tensor is then given by

$$V_{ij} = \sum_{\nu} n(d_\nu)\left\langle d_\nu \left| \mathbf{V}_{ij} \right| d_\nu \right\rangle \tag{A2}$$

where $n(d_\nu)$ is the occupation of the νth spin-down 3d-orbital. (The spin-up d-orbitals are completely filled, so there is no contribution to the EFG.) We ignore the small 4p-contribution. Equation A2 is straight forward to evaluate analytically since the d-orbital eigenvectors are linear combinations of the $\ell = 2$ orbital angular momentum eigenvectors.

For the monoclinic clusters, suppose that the lowest energy spin-down d-orbital has the form

$$\left|d_\alpha\right\rangle = \alpha\left|z^2\right\rangle + \beta\left|x^2 - y^2\right\rangle + \gamma\left|yz\right\rangle, \tag{A3}$$

where α, β and γ are real and $\alpha^2 + \beta^2 + \gamma^2 = 1$. Without loss of generality, we can also assume that β and γ are both positive, and α may be positive or negative. Furthermore, we suppose that at T = 0 K, $n(d_\alpha) = 1$ and all other $n = 0$. This situation represents the general case for all nine monoclinic clusters. From equations A1 and A2, the non-zero components of the EFG tensor are:

$$
\begin{aligned}
V_{xx} &= \tfrac{2}{7}\left\langle r^{-3}\right\rangle\left(\alpha^2 - \beta^2 + 2\gamma^2 + \sqrt{12}\alpha\beta\right) \\
V_{yy} &= \tfrac{2}{7}\left\langle r^{-3}\right\rangle\left(\alpha^2 - \beta^2 - \gamma^2 - \sqrt{12}\alpha\beta\right) \\
V_{zz} &= \tfrac{2}{7}\left\langle r^{-3}\right\rangle\left(-2\alpha^2 + 2\beta^2 - \gamma^2\right) \\
V_{yz} &= \tfrac{2}{7}\left\langle r^{-3}\right\rangle\left(3\beta\gamma - \sqrt{3}\alpha\gamma\right).
\end{aligned}
\tag{A4}
$$

Rewriting these in terms of the occupations of orbitals z^2, $x^2 - y^2$ and yz, and ignoring the factor of $\frac{2}{7}\left\langle r^{-3}\right\rangle$:

$$
\begin{aligned}
V_{xx} &\propto n(z^2) - n(x^2 - y^2) + 2n(yz) \pm \left[12n(z^2)\cdot n(x^2 - y^2)\right]^{1/2} \\
V_{yy} &\propto n(z^2) - n(x^2 - y^2) - n(yz) \mp \left[12n(z^2)\cdot n(x^2 - y^2)\right]^{1/2} \\
V_{zz} &\propto -2n(z^2) + 2n(x^2 - y^2) - n(yz) \\
V_{yz} &\propto 3\left[n(x^2 - y^2)\cdot n(yz)\right]^{1/2} \mp \left[3n(z^2)\cdot n(yz)\right]^{1/2}.
\end{aligned}
\tag{A5}
$$

where $n(z^2) + n(x^2 - y^2) + n(yz) = 1$. The top sign is taken when $\alpha > 0$ and the bottom when $\alpha < 0$. The EFG eigenvalues and eigenvectors will be

$$
V^0 = V_{xx}\,,\ \mathbf{e}^0 = \mathbf{x} \tag{A6a}
$$

$$
\begin{aligned}
V^{\pm} &= -\tfrac{1}{2}V_{xx} \pm \tfrac{1}{2}\sqrt{\left(V_{yy} - V_{zz}\right)^2 + 4V_{yz}^2}\,, \\
\mathbf{e}^{\pm} &\propto \left(\tfrac{1}{2}\left(V_{yy} - V_{zz}\right) \pm \tfrac{1}{2}\sqrt{\left(V_{yy} - V_{zz}\right)^2 + 4V_{yz}^2}\right)\mathbf{y} + V_{yz}\mathbf{z}\,.
\end{aligned}
\tag{A6b}
$$

where **x**, **y**, and **z** are unit vectors along the x, y and z axes; and in the last expression, the eigenvectors are not normalized.

Next, we make the assumption, based on equation 9 for an undistorted octahedron, that

$$
\begin{aligned}
n(x^2 - y^2) &= \frac{2}{3}\left(1 - n(z^2)\right), \\
n(yz) &= \frac{1}{3}\left(1 - n(z^2)\right).
\end{aligned}
\tag{A7}
$$

Substituting equation A7 into A5, and the result into equation A6, the EFG eigenvalues and eigenvectors, and therefore any parameter of the EFG tensor, can be calculated as a function of $n(z^2)$. Figure A1 shows that the spin-down z^2 occupation for the monoclinic clusters at $T = 0$ K, and all clusters at $T = 300$ K, is an increases with flattening. Since $n(z^2)$ is a monotonically increasing function of flattening, curves of the EFG as a function of $n(z^2)$ should behave similarly to curves of the EFG as a function of ψ.

Figures A2, A3, A4 and A5 show the EFG eigenvalues, V_{ZZ}, η and ϕ as functions of $n(z^2)$ for the cases of α positive and negative. Comparisons with figures 3 - 6 clearly show that $\alpha > 0$ behaves as the group II clusters, and $\alpha < 0$ as the group I clusters. Examination of the SCC-Xα orbital wave-functions for the group I and II clusters shows that, in fact, the coefficient of the spin-down 3d z^2 component is of opposite sign to the $x^2 - y^2$ and yz coefficients in group I clusters, and of the same sign in group II clusters. Comparing the hypothetical orbital d_α of equation A3 with the monoclinic orbitals given in equation 10, we conclude that the group I clusters have the orbital t_{2g}^{B} as the lowest in energy, while group II clusters have t_{2g}^{A} as the lowest.

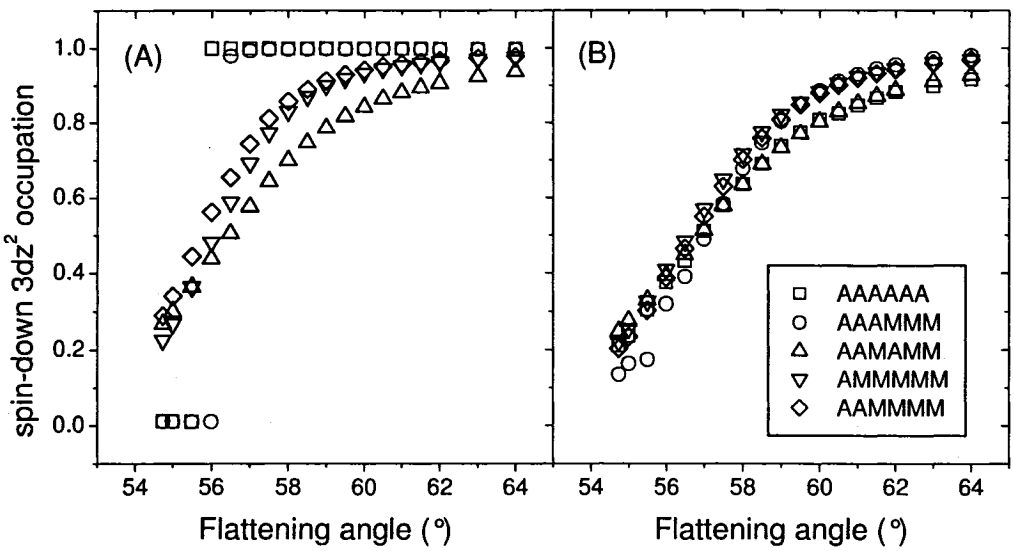

Figure A1. Occupation of the spin-down z^2 3d-orbital is an increasing function of flattening. Representative clusters of monoclinic group I (AMMMMM), triclinic group I (AAMAMM), group II (AAMMMM), group III (AAAMMM) and trigonal clusters (AAAAAA) are shown at (a) $T = 0$ K and (b) $T = 300$ K.

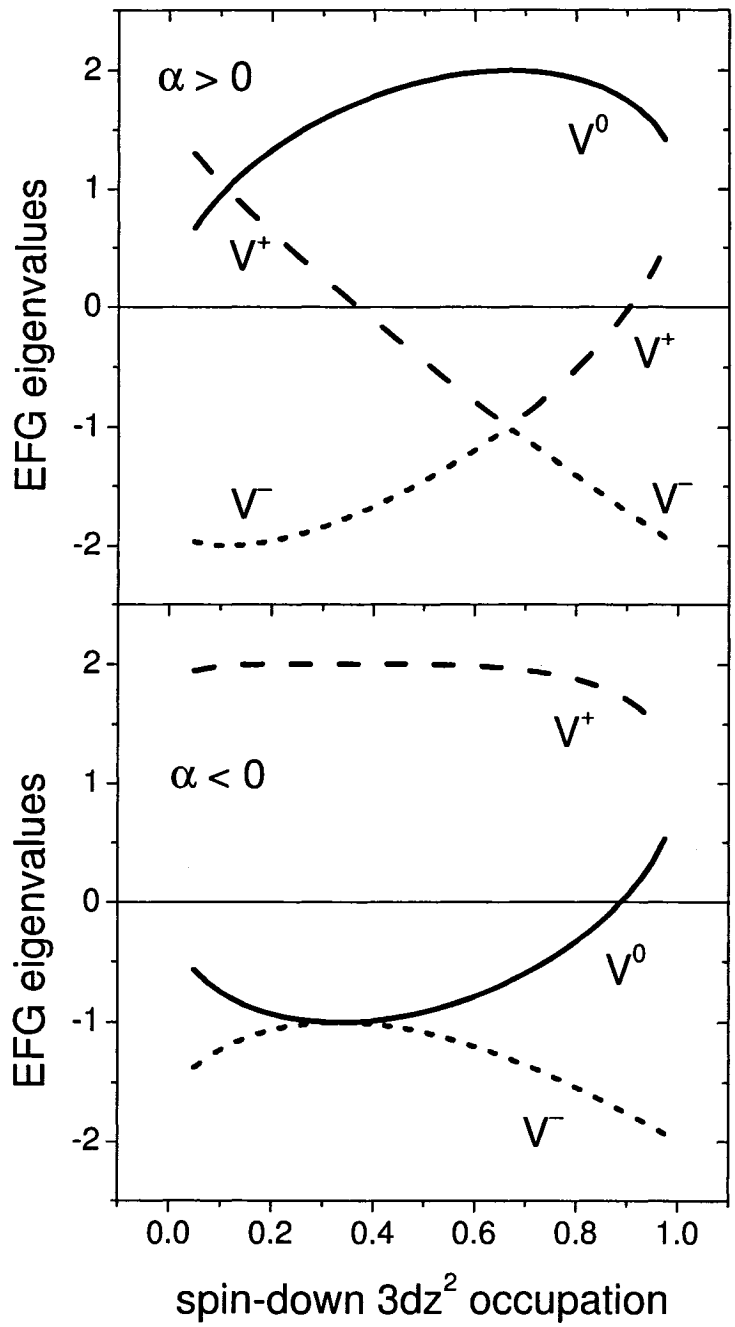

Figure A2. Analytic EFG eigenvalue for group I ($\alpha < 0$) and group II ($\alpha > 0$) clusters.

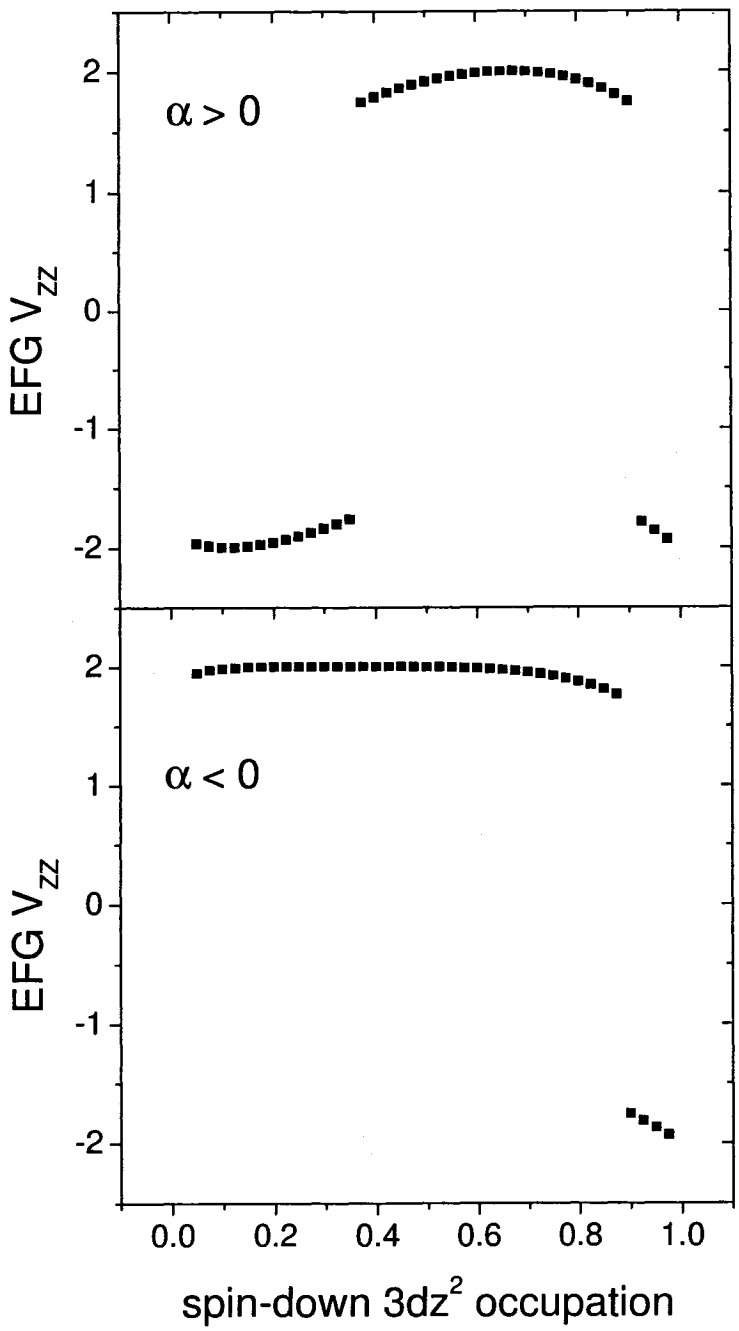

Figure A3. Analytic EFG principal eigenvalue V_{ZZ} curves for group I ($\alpha < 0$) and group II ($\alpha > 0$) clusters.

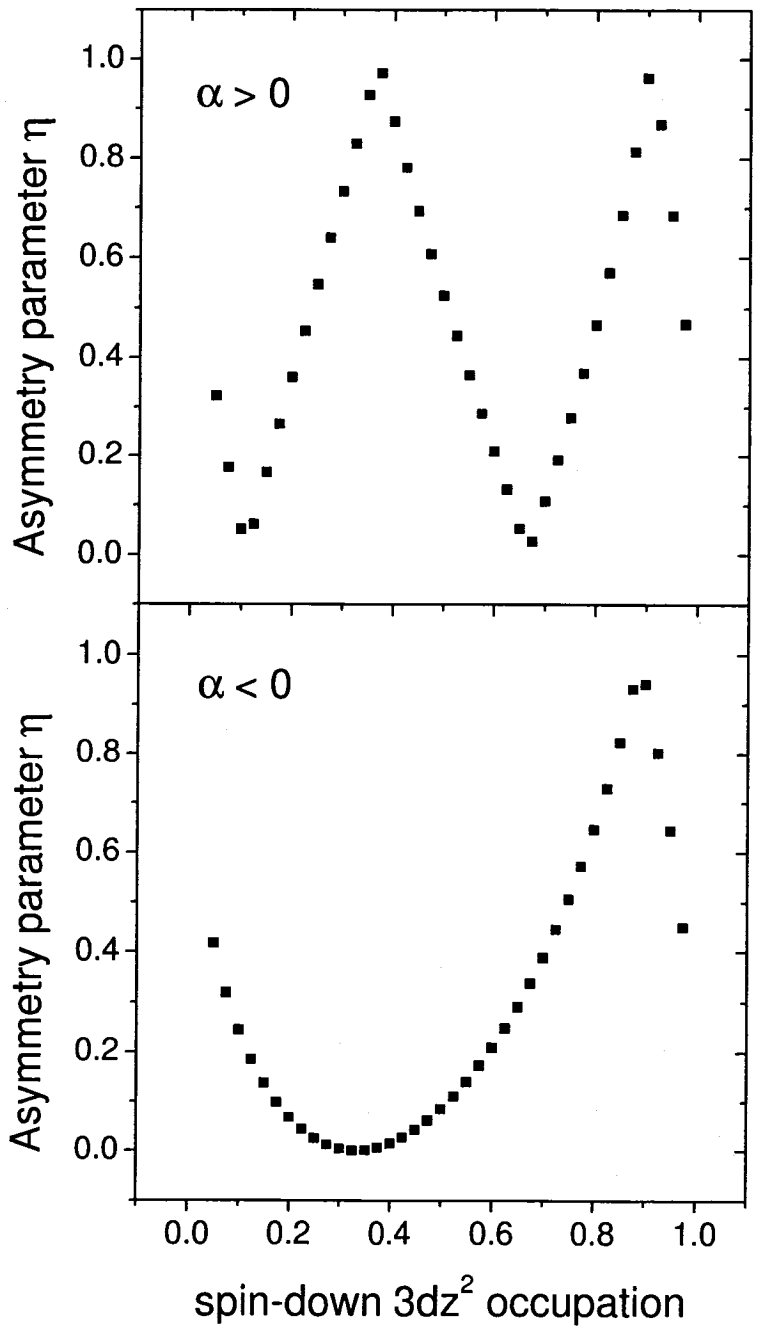

Figure A4. Analytic asymmetry parameter η for group I (α < 0) and group II (α > 0) clusters.

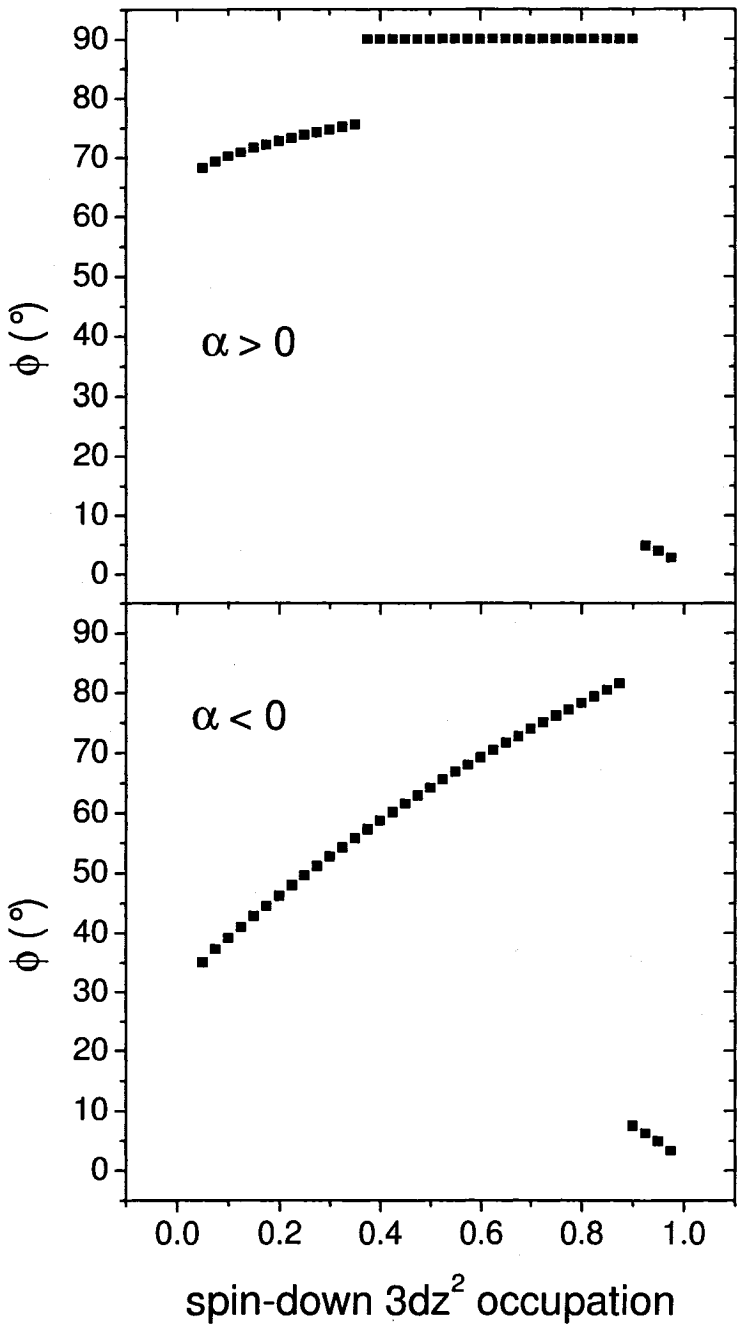

Figure A5. Analytic EFG directional angle ϕ for group I ($\alpha < 0$) and group II ($\alpha > 0$) clusters.

References

Albright, T.A., Burdett, J.K., and Whangbo, M.H. (1985) Orbital Interactions in Chemistry, John Wiley and Sons, New York

Aldridge, L.P., Finch, J., Gainsford, A.R., Tennant, W.C., and Childs, C.W. (1987) Electric field gradient in muscovites. American Mineralogist 72, 528-536

Aldridge, L.P., Finch, J., Gainsford, G.J., Patterson, K.H., and Tennant, W.C. (1991) Single crystal Mössbauer studies of 1M biotite. Physics and Chemistry of Minerals 17, 583-590

Annersten, H. (1975), Mossbauer study of iron in natural and synthetic biotites. Fortschritte der mineralogie 52, 583-590

Baerends, E.J., and Ros, P. (1973), Self-consistent molecular Hartree-Fock-Slater calculations II. The effect of exchange scaling in some small molecules. Chemical Physics 2, 52-59

Ballet, O., Coey, J.M.D. and Massenet, O. (1979) Electric field gradient at Fe^{2+} sites in trioctahedral layer silicates. Journal de Physique Colloque 40, C2-283-C2-285

Ballet, O. and Amthauer, G. (1986) Room-temperature Mössbauer study of the EFG tensor at the iron sites in sheet silicates. Journal of Physics C: Solid State Physics 19, 7099-7112

Ballet, O. and Coey, J.M.D. (1982) Magnetic properties of sheet silicates; 2:1 layer minerals. Physics and Chemistry of Minerals 8, 218-229

Ballet, O., Coey, J.M.D, and Burke, K.J. (1985) Magnetic properties of sheet silicates; 2:1:1 layer minerals. Physics and Chemistry of Minerals 12, 370-378

Bleany, B., and Stevens, K.W.H. (1953) Paramagnetic Resonance, Reports on the Progress of Physics 16, 108-157

Chandra, R. and Lokanathan, S. (1977) Electric field gradient in biotite mica. Physica Status Solidi B 83, 273-280

Coey, J.M.D., Ballet, O., Moukarika, A., and Soubeyroux, J.L. (1981) Magnetic properties of sheet silicates; 1:1 layer minerals. Physics and Chemistry of Minerals 7, 141-148

Donnay, G., Donnay, J.D.H., and Takeda, H. (1964) Trioctahedral one-layer micas II. Prediction of the structure from composition and cell deimensions. Acta Crystallographica 17, 1371-1381

Dufek, P., Blaha, P., and Schwarz, K. (1995) Determination of the nuclear-quadrupole moment of Fe-57, Physical Review Letters 75, 3545-3548

Evans, R.J. (2001) Electric Field Gradient of Octahedral Fe^{2+} in Layer Silicates, M.Sc. Thesis, University of Ottawa, Ottawa, Ontario, Canada

Evans, R. J., Rancourt, D. G., and Grodzicki, M. (2005) Hyperfine electric field gradients and local distortion environments of octahedrally co-coordinated Fe^{2+}, American Mineralogist 90, 187-198

Grodzicki, M. (1980) A self-consistent charge Xα method I. Theory, Journal of Physics B: Atomic and Molecular Physics 13, 2683-2691

Grodzicki, M., Männing, V., Trautwein, A.X., and Friedt, J.M. (1987) Calibration of isomer shift and quadrupole coupling for ^{119}Sn, ^{127}I and ^{129}I as derived from self-consistent charge Xα calculations and

Mössbauer measurements, Journal of Physics B: Atomic and Molecular Physics 20, 5595-5625

Hargraves, P., Rancourt, D.G. and Lalonde, A.E. (1990) Single-crystal Mössbauer study of phlogopite mica. Canadian Journal of Physics 68, 128-144

Hazen, R.M., and Wones, D.R. (1972) The effect of cation substitution on the physical properties of trioctahedral micas. American Mineralogist 57, 103-129

Ingalls, R. (1964) Electric-field gradient tensor in ferrous compounds, Physical Review 133, 787-795

Lauer, S., Marathe, V.R., and Trautwein, A. (1979) Sternheimer shielding using various approximations, Physical Review A 19, 1852-1861

Lougear, A., Grodzicki, M., Bertoldi, C., Trautwein, A.X., Steiner, K., Amthauer, G. (2000) Mössbauer and molecular orbital study of chlorites, Physics and Chemistry of Minerals 27, 258-269

Mercier, P.H.J. (2003) Crystal chemistry of trioctahedral 2:1 layer silicates: Testing the limits of simple geometrical models, Ph.D. thesis, University of Ottawa, Ottawa, Ontario, Canada

Mercier, P.H.J., R. James Evans, and D.G. Rancourt (2005) Geometric crystal chemical models for structural analysis of micas and their stacking polytypes, American Mineralogist 90, 382-410

Piilonen, P.C., McDonald, A.M., Lalonde, A.E. (2003) Insights into astrophyllite-group minerals. II. Crystal chemistry, Canadian Mineralogist 41, 27-54

Piilonen, P.C., Rancourt, D.G., Lalonde, A.E., Evans, R.J., McDonald, A.M. (2004) Insights into astrophyllite-group minerals. III. Relationship between crystal-chemical and hyperfine parameters: a combined ^{57}Fe Mössbauer spectroscopy and single-crystal X-ray diffraction study, European Journal of Mineralogy 16, 989-1002

Rancourt, D.G. (1994) Mössbauer spectroscopy of minerals, II. Problem of resolving cis and trans octahedral Fe^{2+} sites, Physics and Chemistry of Minerals 21, 250-257

Rancourt, D.G., Ping, J.Y., and Berman, R.G. (1994) Mössbauer spectroscopy of minerals, III. Octahedral-site Fe^{2+} quadrupole splitting distributions in the phlogopite-annite series, Physics and Chemistry of Minerals 21, 258-267

Rancourt, D.G. (1998) Mössbauer spectroscopy in clay science, Hyperfine Interactions 117, 3-38

Redhammer, G. J. (1998) Characterisation of synthetic trioctahedral micas by Mössbauer spectroscopy. Hyperfine Interactions 117, 85-115

Redhammer, G. J., Beran, A., Schneider, J., Amthauer, G., and Lottermoser, W. (2000) Spectroscopic and structural properties of synthetic micas on the annite-siderophyllite binary: Synthesis, crystal structure refinement, Mössbauer, and infrared spectroscopy, American Mineralogist 85, 449-465

Redhammer, G. J. and Roth, G. (2002) Single-crystal structure refinements and crystal chemistry of synthetic trioctahedral micas $KM_3(Al^{3+},Si^{4+})_4O_{10}(OH)_2$, where M = Ni^{2+}, Mg^{2+}, Co^{2+}, Fe^{2+}, or Al^{3+}, American Mineralogist 87, 1464-1476. 2002

Shabani, A.A.T. (1999) Mineral chemistry and Mössbauer spectroscopy of micas from granitic rocks of the Canadian Appalacians, Ph.D. thesis, University of Ottawa, Ottawa, Ontario, Canada

Shannon, R.D. (1976) Revised effective ionic radii and systematic studies of interatomic distances in halides and chalcogenides, Acta Crystalographica A 32, 751

Tennant, W.C., Finch, J., Aldridge, L.P., and Gainsford, G.J. (1992) The electric field gradient and mean squared displacement tensor in 1M biotites investigated by Mössbauer spectroscopy. Journal of Physics: Condensed Matter 4 , 5447-5459

Terra, J. and Ellis, D.E. (1997) Electronic structure, chemical bonding and hypefine parameters in layered silicates. Physical Review B 56, 1834-1847

Terra, J. and Ellis, D.E. (1998) Hyperfine interactions of *cis* and *trans* octahedral Fe^{2+} sites in the layered silicate annite. Journal of the American Ceramic Society 81, 465-468

Tossell, J.A., Vaughn, D.J., and Johnson, K.H. (1974) The electronic structure of rutile, wustite and hematite from molecular orbital calculations. American Mineralogist 59, 319-334

Townsend, M.G., and Longworth, G. (1985) Sign of the magnetic coupling of Fe^{2+} and Fe^{3+} in biotite. Physics and Chemistry of Minerals 12, 141-144

Weiss, Z., Rieder, M., Chmielová, M and Krajíček, J. (1985) Geometry of the octahedral coordination in micas: a review of refined structures, American Mineralogist 70, 747-757

Weiss, Z., Rieder, M., and Chmielová, M. (1992) Deformation of coordination polyhedra and their sheets in phyllosilicates, European Journal of Mineralogy 4, 665-682

Zimmerman, R. (1975) A method for evaluation of single crystal ^{57}Fe Mössbauer spectra ($FeCl_2 \cdot 4H_2O$), Nuclear Instruments and Methods 128, 537-543

Zory, P. (1965) Nuclear EFG determination utilizing the Mössbauer effect (Fe^{57}), Physical Review A 140, 1401-1407

Simulated quadrupole splitting, isomer shift and hyperfine field distributions of octahedral Fe^{2+} in Mössbauer spectroscopy from electronic structure calculations

R. James Evans[1], Denis G. Rancourt[1] , and Michael Grodzicki[2]
[1] Department of Physics, University of Ottawa, Ottawa, Ontario, Canada K1N 6N5
[2]Institute of Mineralogy, University of Salzburg, A-5020 Salzburg

Abstract

We have simulated hyperfine parameter distributions in $^{[6]}Fe^{2+}$-bearing minerals with structural and/or chemical disorder, by calculating the isomer shift, quadrupole splitting/electric field gradient tensor, and the hyperfine magnetic field with electronic structure calculations for ensembles of $Fe(OH)_6^{4-}$ octahedra generated by applying random distortions to the average structure. Quadrupole splitting (QS) distributions at 0 and 300 K agree well with experimental results, possessing a low QS tail and a sharp edge at high QS values. This high edge is due to a universal upper bound on the QS. The width-to-mean ratio of the nuclear electron spin polarization, the dominant contribution to the hyperfine magnetic field, is large compared to that of the other parameter distributions. The variation of the spin polarization due to local structural variation alone is found to be sufficient to account for the widths and intensities of lines in magnetic hyperfine spectra. The widths of most distributions increase monotonically with the static disorder parameter, and are universal functions of one another, providing a useful constraint in fitting Mössbauer spectra. The correlations between hyperfine parameters are non-linear and considerably more complicated than those supposed in current spectral fitting models. The correlation between quadrupole splitting and isomer shift increases with the amount of disorder in the material. Isomer shift and spin polarization have a strong non-linear correlation. The complexity of the correlations between hyperfine parameters, together with the fact that optimal fits of Mössbauer spectra are not unique, strongly implies that fits to spectra without supporting electronic structure calculations and crystal chemical models of the measured materials are meaningless. We also show that published mathematical models of electric field gradient tensor distributions in amorphous materials, derived assuming an isotropic solid, do not describe the distributions in $^{[6]}Fe^{2+}$ sites in disordered materials, except under special symmetry conditions.

Introduction

Mössbauer spectra of materials with chemical or structural disorder are best described not by single sets of hyperfine parameters – quadrupole splitting (QS), isomer shift (IS) and hyperfine field (HF) – but by distributions of hyperfine parameters (Rancourt 1994a and 1994b, Rancourt et al. 1994). Chemical and structural disorder give rise to distributions of local distortion environments. All Mössbauer hyperfine parameters are affected by the local structural environment of the absorber atom (in our case, iron). Thus the only way to extract truly useful structural information from Mössbauer spectra is through hyperfine parameter distributions. It is not adequate to fit the spectra with sums of Lorentzian lines corresponding to average crystallographic iron sites, because the true distribution of hyperfine parameters may be quite different from what one might be led to believe from the average structure.

There is therefore a considerable need for theoretical calculations to link experimentally extracted hyperfine parameter distributions with distributions of local distortion environments. We have taken preliminary steps in this direction for octahedrally-oxygen-coordinated Fe^{2+}, first by performing electronic structure calculations determining how specific common distortions to octahedral symmetry affect the quadrupole splitting (Evans et al 2005a), and then through calculations of other electric field gradient (EFG) tensor parameters measurable through oriented single crystal Mössbauer spectrometry and of limited QS distributions due to chemical disorder in first-nearest-neighbour sites (Evans et al 2005b). We now attempt the broader step of simulating full hyperfine parameter distributions through a statistical simulation. These are the first full electronic structure calculations simulating hyperfine parameter distributions by a distribution of local distortion environments.

Definitions

The EFG tensor **V** is defined with components

$$V_{ij} = \left. \frac{\partial^2 V(\mathbf{r})}{\partial x_i \partial x_j} \right|_{\mathbf{r}=0} , \tag{1}$$

where $V(\mathbf{r})$ is the electrostatic potential and the Fe atom is located at the origin. The eigenvalues are labelled V_{XX}, V_{YY} and V_{ZZ} such that

$$|V_{XX}| \leq |V_{YY}| \leq |V_{ZZ}| , \tag{2}$$

and the asymmetry parameter η is defined as

$$\eta = \frac{V_{XX} - V_{YY}}{V_{ZZ}}. \tag{3}$$

If we define V^* as

$$V^* = |V_{ZZ}|\sqrt{1+\frac{\eta^2}{3}}, \tag{4}$$

then the Mössbauer quadrupole splitting is $\Delta = \frac{1}{2}eQV^*$, where e is the charge of the electron and Q is the nuclear quadrupole moment of the first excited state of the ^{57}Fe nucleus. We shall regard the factor $\frac{1}{2}eQ$ as a merely a conversion factor between EFG units and QS units, and treat the QS and V^* as interchangeable.

The centre shift is the sum of the isomer shift (IS) and the second order Doppler shift. The latter contribution is due to the atomic vibrations and is generally calculable from simple models; it is usually proportional to k_BT at high temperatures (where k_B is the Boltzmann constant and T is temperature). The IS is a function of electron densities at the ^{57}Fe nucleus:

$$\text{IS} \propto \Delta R\left(\left[\rho_{\uparrow}^{a}(0)+\rho_{\downarrow}^{a}(0)\right]-\rho^{s}(0)\right) \tag{5}$$

where $\rho_{\uparrow}^{a}(0)$ and $\rho_{\downarrow}^{a}(0)$ are the spin-up and spin-down electron densities at the absorber (Fe) nucleus, $\rho^{s}(0)$ is the total electron density at the source nucleus, and ΔR is the difference in the ^{57}Fe nuclear radius between the excited and ground states. The difference ΔR is negative, so an increase in electron density at the Fe nucleus leads to a decrease in IS.

The hyperfine field is more complex than the QS or IS in that it has several sources (Rancourt 1998, Greenwood and Gibb 1971):

$$\text{HF} = H_{\text{ext}} + H_{\text{SP}} + H_{\text{L}} + H_{\text{D}} + H_{\text{demag}}, \tag{6}$$

where each component is actually a vector contributing to the total hyperfine magnetic field. H_{ext} is the applied external field; H_{demag} is the demagnetizing field in magnetic materials; H_{D} is due to the dipole interaction of the nucleus with the spin moment of the atom, and is proportional to the QS; H_{L} is due to the orbital magnetic moment of the Fe atom, and is also coupled to the QS since both are proportional to the radial expectation value $\langle r^{-3} \rangle$ of the valence orbitals. Finally, H_{SP} is the Fermi contact term (Fermi 1930),

which depends on the electron spin polarization (SP) of electrons at the nucleus,

$$H_{SP} = \frac{8\pi}{3} g_e \mu_B \left[\rho^a_\uparrow(0) - \rho^a_\downarrow(0)\right], \tag{7}$$

where g_e is the electron g-factor, μ_B is the Bohr magneton and $\rho^a_\uparrow(0)$ and $\rho^a_\downarrow(0)$ are the spin up and spin down electron densities at the nucleus, as in equation 5. Since both the IS and SP are linear functions of $\rho^a_\uparrow(0)$ and $\rho^a_\downarrow(0)$, we expect some correlation between the two parameters. H_{SP} is generally the largest magnitude term of the HF in magnetic materials (Guenzberger et al. 1998, Rancourt 1998), although in Fe^{2+} it may be cancelled out by the other contributions (Greenwood and Gibb 1971, Watson and Freeman 1961, Trautwein and Zimmermann 1976). We shall examine this term exclusively. In the figures, SP is given in terms of the resulting H_{SP} field, in kilogauss (kG).

When discussing the moments of distributions of parameters, we shall denote the mean of X as $\langle X \rangle$, where angular brackets denote an ensemble average, and the width or standard deviation as $s(X) = \langle (X - \langle X \rangle)^2 \rangle^{1/2}$, reserving the symbol σ for the static disorder parameter used in our simulations.

Theoretical Review

We are concerned with two distinct theoretical aspects of hyperfine parameter distributions – firstly, deriving mathematically or simulating computationally the distributions, mostly the QS distribution, from a statistical and physical model; and secondly, the representation and use of distributions in fitting experimental spectra. We shall briefly review both aspects, as we shall use the following models and equations in discussing the results of the current simulations.

Hyperfine parameter distributions in fitting spectra

Fitting of a Mössbauer spectrum involves solving the integral equation

$$Y(v) = \int L(v \mid \mathbf{h}, \Gamma)\, P(\mathbf{h})\, d\mathbf{h} \tag{8}$$

where v is Doppler velocity, $Y(v)$ is the artefact-corrected experimental Mössbauer spectrum, $L(v \mid \mathbf{h}, \Gamma)$ is the elemental spectrum (Lorentzian multiplet) with Lorentzian line-width Γ, and $\mathbf{h}$ is the full set of

hyperfine parameters. In general the elemental spectrum will be an octet (Blaes et al. 1985) but in common limiting cases may be a doublet or a sextet composed of Lorentzian lines. The full set of hyperfine parameters in the most general case consists of four components of the EFG tensor (e.g. the principal eigenvalue V_{ZZ}, the asymmetry parameter η, and two Euler angles describing the direction of the HF field in the EFG principal axes frame), the centre shift, and three components of the magnetic HF vector.

The function $P(\mathbf{h})$ is the joint distribution of all hyperfine parameters in the sample. In practice, $L(v \mid \mathbf{h}, \Gamma)$ is often independent of many of these parameters. If the HF is zero, the spectrum is a doublet and the distribution of all but one component of the EFG (the QS) is irrelevant, and so a joint centre shift-QS distribution is sufficient. When the quadrupole *shift* (a function of several EFG tensor parameters, distinct from the quadrupole *splitting*) is small in comparison to the HF, the spectrum is a sextet and a joint distribution of only the quadrupole shift, centre shift, and HF are required. Often one or more of the remaining parameters is either assumed constant or coupled to other parameters, further reducing the degrees of freedom of the fitting problem. A functional form with adjustable parameters is then assumed for $P(\mathbf{h})$ (e.g. a sum of Gaussians or step-functions, or some more specific function from a statistical model) and the integral deconvoluted numerically.

There have been several comprehensive reviews of different Mössbauer fitting methods using distributions (Campbell and Aubertin 1989, Nagy and Rölich 1991, Le Caer and Brand 1992, Vandenberghe et al. 1994) and another is not necessary for our purposes, except insofar as the majority of theoretical work concerning hyperfine parameter distributions has been in this area. More recent methods include those of Rancourt and Ping (1991) and Lagarec and Rancourt (1997 & 1998), discussed below.

If the measured Mössbauer spectrum is noisy, which it always is, then the inversion of the integral in equation 8 is an ill-posed problem. This means it is not always possible to find a mathematically unique solution for $P(\mathbf{h})$, and small changes in $Y(v)$ may lead to large changes in $P(\mathbf{h})$ (Odintsov and Pushkarev 1990, Le Caer and Brand 1992, Ping and Rancourt 1994). Nagy and Rölich (1991) provide a good discussion of equation 8 and the inversion problem, and ways around it, while Le Caer and Brand (1998) discussed the mathematical conditions under which two joint distributions of hyperfine parameters give rise to the same spectra.

The general Mössbauer spectrum requires a multidimensional probability distribution in all the relevant hyperfine parameters. In the case of a quadrupole doublet, this is a two-dimensional distribution

P(QS, IS); in the case of a powder-averaged sextet with weak quadrupole interactions, this is a three-dimensional distribution $P(\varepsilon, \mathrm{IS}, \mathrm{HF})$, where ε is the quadrupole shift. The hyperfine parameters are all dependent on local structure, and so are not truly independent, so that $P(\mathbf{h})$ is not simply the product of individual parameter distributions. Linear dependence between parameters is often assumed during fitting. For doublets,

$$\mathrm{IS} = b_0 + a_0\,\mathrm{QS} \tag{9}$$

and for sextets,

$$\mathrm{IS} = b_1 + a_1\,\mathrm{HF},\ \varepsilon = b_2 + a_2\,\mathrm{HF}. \tag{10}$$

This effectively turns the joint distribution $P(\mathbf{h})$ into a one-dimensional distribution. An example is the Voigt-based fitting (VBF) approach (Rancourt and Ping 1991), where the distribution of the independent variable is fit as a sum of Gaussian functions.

An even more simplistic assumption is to assume that only one of the relevant parameters has a non-negligible distribution. Ignoring the distribution of one or more hyperfine parameters has been shown to introduce spurious features into the distribution of the independent parameter (Turek 1990, Ping and Rancourt 1994). The linearly-dependent approximations (equations 9 and 10) do better than neglecting distributions altogether, but are still not realistic. All hyperfine parameters are complex functions of local environment and electronic structure, and the relations between them may not even be expressible by a functional relationship.

A more realistic approach is that employed in extended Voigt-based fitting (xVBF) (Lagarec and Rancourt 1998, 1999), where each hyperfine parameter distribution is fitted independently with linear correlations between each. For example, a doublet is fit as a sum of functions (δ = IS),

$$P(V^*,\delta)=\sum_i\sum_j \frac{P_{ij}}{2\pi w_i^{\mathrm{QS}} w_j^{\mathrm{IS}}\sqrt{1-\rho^2}} \exp\left[\frac{1}{2(1-\rho^2)}\left(\left(\frac{V^*-V_i}{w_i^{\mathrm{QS}}}\right)^2+\left(\frac{\delta-\delta_j}{w_j^{\mathrm{IS}}}\right)^2-2\rho\left(\frac{V^*-V_i}{w_i^{\mathrm{QS}}}\right)\left(\frac{\delta-\delta_j}{w_j^{\mathrm{IS}}}\right)\right)\right] \tag{11}$$

where $\{P_{ij}, w_i^{\mathrm{QS}}, w_j^{\mathrm{IS}}, V_i, \delta_j, \rho\}$ are all adjustable parameters ($\Sigma_i\Sigma_j P_{ij} = 1$), and ρ is the correlation parameter, $-1 \le \rho \le +1$, between the IS and QS distributions.

Statistical derivations and simulations of quadrupole splitting distributions

Statistical treatments of the EFG tensor in the context of nuclear magnetic resonance line-shapes

(Cohen and Reif 1957) pre-date the discovery of the Mössbauer effect (Mössbauer 1958). Point charge or hard-sphere model simulations of QS and EFG tensor distributions in the context of Mössbauer spectroscopy have been common for a long time for amorphous materials (Lines 1979, Lines 1981, Varret and Henry 1980, Grenèche et al. 1987, Bureau et al. 2000) as well as for crystalline materials with high concentrations of defects (Pustówka 1973, Stöckmann 1981) or chemical disorder (Billard et al. 1984).

The most mathematically complete theoretical model of EFG distributions is termed the Gaussian Isotropic Model, summarized in Le Caer and Brand (1998), which developed from the so-called "shell model" of Czjzek et al. (1981). Because it is traceless, the EFG tensor can be represented by five linearly independent components,

$$\begin{aligned} &U_1 = \tfrac{1}{2}V_{zz}, \quad U_2 = \tfrac{1}{\sqrt{3}}V_{xz}, \quad U_3 = \tfrac{1}{\sqrt{3}}V_{yz}, \\ &U_4 = \tfrac{1}{\sqrt{3}}V_{xy}, \text{ and } U_5 = \tfrac{1}{2\sqrt{3}}\left(V_{xx} - V_{yy}\right), \end{aligned} \tag{12}$$

where V_{xx}, V_{yy}, V_{zz}, V_{xy}, V_{xz} and V_{yz} are the components of the EFG tensor **V** in coordinates $\{x, y, z\}$. The joint distribution $P(V_{ZZ}, \eta)$ is related to the joint distribution $P(U_1, ..., U_5)$ as

$$P(V_{ZZ},\eta) = 2V_{ZZ}^4\eta\left(1-\eta^2/9\right)\int d\phi \int d\theta \int d\zeta(\sin\theta)P(U_1, ..., U_5) \tag{13}$$

where ϕ, θ, and ζ are the Euler angles of the EFG's principal axes. Equation 13 is completely general for any EFG; it merely changes the representation of the EFG from $\{U_1, ..., U_5\}$ to $\{V_{ZZ}, \eta, \phi, \theta, \zeta\}$, producing the Jacobian in front of the integral, and then integrates over the Euler angles for a distribution in V_{ZZ} and η alone. Czjzek et al. (1981) assumed an isotropic amorphous solid such that, by the central limit theorem, $P(U_1, ..., U_5)$ may be approximated by a five-dimensional Gaussian function. This agrees with the result of Cohen and Reif (1957), who found that each U_i was normally distributed in the limit of high defect concentrations in imperfect cubic crystals. The integral in equation 13 then evaluates to

$$P(V_{ZZ},\eta) = \frac{1}{\sqrt{2\pi}}\frac{V_{ZZ}^4}{w^5}\eta\left(1-\eta^2/9\right)\exp\left[-V_{ZZ}^2\left(1+\eta^2/3\right)/\left(2w^2\right)\right], \tag{14}$$

where w is the Gaussian width of each U_i distribution. Note that the distribution is zero for both $V_{ZZ} = 0$ and $\eta = 0$. The marginal distribution of η (which we shall refer to as the Czjzek η distribution), i.e. the distribution of η alone formed by integrating equation 14 over V_{ZZ}, is

$$P(\eta) = \frac{3\eta\left(1-\eta^2/9\right)}{\left(1+\eta^2/3\right)^{5/2}}, \tag{15}$$

a completely parameter-free distribution with mean $\langle\eta\rangle = 0.6089$ and standard deviation $s(\eta) = 0.2427$. The marginal distribution of the QS, V^*, is

$$P(V^*) = \frac{1}{3}\sqrt{\frac{2}{\pi}}\frac{(V^*)^4}{w^5}\exp\left(-\frac{(V^*)^2}{2w^2}\right) \tag{16}$$

which we shall refer to as the Czjzek QS distribution. The marginal distribution of V_{ZZ} is symmetric with respect to sign (i.e. $P(V_{ZZ} = +v_{zz}) = P(V_{ZZ} = -v_{zz})$) and goes to zero for $V_{ZZ} = 0$.

Although Czjzek et al. derived the joint distribution in equation 14 assuming an isotropic amorphous solid, they and other authors have found it valid for a wide range of Fe^{3+}-bearing solids. Cohen and Reif (1957) showed that the individual $P(U_i)$ distributions were Gaussian in the limit of large concentrations of defects in imperfect cubic solids. Pustówka et al. (1973) performed point-charge EFG simulations for iron in various cubic and hexagonal lattices, showing that the distribution of V_{ZZ} changed from narrow peaks centred on zero, or at a negative value for the hexagonal lattice, to the sign-symmetric V_{ZZ} distribution predicted by equation 14 as defect concentration increased. Stöckmann (1981) derived the same results as Czjzek et al. (1981) independently, for cubic lattices with large concentrations of defects. Billard et al. (1984) simulated EFG distributions of binary alloys, and found that EFG contributions from both purely structural and purely chemical disorder followed equation 14 well. Brand et al. (1990) showed that the Czjzek QS distribution applied to quasicrystalline as well as amorphous systems.

In Le Caer et al. (1984b) and subsequent papers (Le Caer et al. 1985, Le Caer and Dubois 1987, Le Caer and Brand 1992, Le Caer and Brand 1998), the authors demonstrated that the Czjzek model is a consequence of two assumptions: (1) the solid is isotropic on average, that is, the EFG tensor $\mathbf{V}$ is statistically invariant under any transformation $\mathbf{V} \rightarrow \mathbf{V}' = \mathbf{M}^{\dagger}\mathbf{V}\mathbf{M}$ (where $\mathbf{M}$ is an orthogonal matrix), and (2) the distribution of each linearly independent U_i is normal. This is referred to as the Gaussian Isotropic Model. The first hypothesis requires that

$$\langle U_i \rangle = 0, \langle U_i U_j \rangle = 0 \text{ when } i \neq j, \text{ and } \langle U_i^2 \rangle = \tfrac{1}{5}\left\langle (V^*)^2 \right\rangle. \tag{17}$$

Le Caer et al. (1985) also remark that a Gaussian centre shift distribution, distributed independently of V_{ZZ} and η, is a natural consequence of the Gaussian Isotropic Model, although they do not prove this or argue it in any detail. Le Caer and Brand (1998) contains the most complete summary of the Gaussian Isotropic Model and related models.

Various extensions of the Gaussian Isotropic Model have been explored (Czjzek et al. 1981, Czjzek 1982, Le Caer et al. 1984, Le Caer et al. 1985, Maurer 1986, Le Caer and Brand 1998) suspending either of its two assumptions, but a general theory of EFG distributions, particularly in the wider case where the amount of disorder is small, as in mineral samples, is still lacking. A drawback to the Gaussian Isotropic Model and its extensions is that they all implicitly assume that the iron is in the high spin Fe^{3+} state, that is, that the electronic structure is nearly spherically symmetric. That is, even when the hypothesis of rotational invariance of the solid is lifted, the cation itself is still assumed to be rotationally invariant. For high spin Fe^{2+}, this is not the case, and Fe^{2+} has a large valence electron contribution to the total EFG. As a result, as we shall demonstrate, Fe^{2+} QS distributions look nothing like those of the Gaussian Isotropic Model, even in very disordered systems, except under certain special symmetry conditions.

Domes et al. (1986) calculated EFG distributions from an ensemble of randomly distorted $[Fe(H_2O)_6]_{aq}^{2+}$ octahedra using ligand field theory. Octahedral distortions were analysed in terms of the octahedron's normal modes of vibration, and restricted to certain symmetries. The crystal field Hamiltonian is a function of a limited number of variables describing the normal modes of distortion; Domes et al. generated an ensemble of crystal field Hamiltonians assuming that each of the allowed distortion variables had a Gaussian distribution. An EFG was then calculated from each crystal field Hamiltonian using ligand field theory. The calculated QS distribution is not shown by Domes et al. (1986), but rather a scatter plot of V_{ZZ} and η based on polar coordinates introduced in Czjzek (1983) is given. A QS distribution from these results appears in Nagy and Rölich (1991), which has the characteristic shape of measured Fe^{2+} QS distributions. Dengler et al. (1991) applied the Domes et al. (1986) method to Fe^{2+} in an amorphous alloy, also calculating HF and IS distributions. Again, no actual distributions were shown, although a (V_{ZZ}, η) contour plot in Czjzek coordinates is shown along with simulated Mössbauer spectra.

Like the method of Domes et al. (1986) and Dengler et al. (1991), the method presented in this paper uses ensembles of randomly distorted octahedra to calculate hyperfine parameter distributions. However, there are significant differences:

- in the Domes et al./Dengler et al. (D/D) method, distortions to the octahedral cluster are restricted to have particular point-group symmetries (C_{2h} in Domes et al. (1986), trigonal in Dengler et al. (1991)). In the current method, there are no symmetry restrictions on possible distortions.
- in the D/D method, the crystal field Hamiltonian is a function of a limited number of variables

describing the allowed normal distortion modes; these variables are assumed to be Gaussian-distributed. Thus a particular member of the ensemble is specified by 2 random variables in Domes et al. (1986) and 5 random variables in Dengler et al. (1991). In the current method, random perturbations are added to the atomic coordinates of the $Fe(OH)_6^{4-}$ cluster; thus a particular member of the ensemble is specified by a total of 30 random variables (3 for each oxygen atom, 2 for each hydrogen atom).

- in the D/D method, the EFG is calculated from crystal field Hamiltonians, generated from random values of the allowed distortion variables, using ligand field theory. In the current method, the EFG is calculated from the randomly perturbed clusters with a full electronic structure calculation.
- in the D/D method, specific couplings are assumed between the QS, IS and HF via the crystal field Hamiltonian. In the current method, QS, IS and SP are calculated independently from the electronic configurations.

Although the D/D method is the only method in the literature of simulating hyperfine parameter distributions specific to Fe^{2+} systems, it has not had as great an impact as hard sphere model/point charge calculations (Pustówka et al. 1973, Lines 1979 and 1981) or analytical derivations based on statistics (Cohen and Reif 1957, Stöckmann 1981, Czjzek et al. 1982). Nor has the method suggested until now the plausible next step of replacing the approximate ligand field calculations with rapid electronic structure calculations.

Method of Calculation

We simulated hyperfine parameter generations by a random statistical process. We began with a chosen $Fe(OH)_6^{4-}$ octahedron, which we will refer to as the starting cluster. A large ensemble of octahedra was then generated by adding small random distortions to the starting cluster such that the average geometry corresponds to the starting cluster (see below). Electronic structure calculations were performed on each perturbed cluster and the hyperfine parameters calculated. Probability distributions were then calculated for each hyperfine parameter by sorting the data into bins and then normalizing the total curve with respect to area.

All electronic structure calculations were performed in the local density approximation with the spin-polarized self-consistent charge Xα (SCC Xα) method (Grodzicki 1980, Grodzicki et al. 1987). In this

treatment, the molecular potential is factored into a radial function and a series of spherical harmonics (allowing analytical integration of the angular parts of all Hamiltonian matrix elements), and separated into one-, two- and three-centre integrals. One-centre integrals require high accuracy, and are derived numerically from all-electron, relativistic atomic calculations with semi-local (gradient corrected) exchange correlation functionals. The two- and three-centre integrals are evaluated with small basis sets (2s and 2p for O and F; 3s and 3p for Mg and Al; 3d, 4s and 4p for Fe) and the Slater Xα potential with $\alpha = 0.7$ for the valence electrons (Grodzicki 1980, Baerends and Ros 1973); core electrons are treated with simple pseudopotentials that are also derived from relativistic atomic calculations and are kept frozen during the iteration process.

The one-centre integrals are calculated beforehand and entered as atom-specific parameters in subsequent calculations. Thus only the small, fast calculations need to be done anew each time, so that calculations on a large number of small $Fe(OH)_6$ clusters is very efficient, while still being ab initio in that there are no adjustable parameters.

The EFG is calculated by integrating the electron charge density multiplied by the tensor operator

$$V_{ij}(r) = \left(\frac{1-\gamma(r)}{r^3}\right)\left(\frac{3x_i x_j - r^2\delta_{ij}}{r^2}\right), \tag{18}$$

where $\delta_{ij} = 1$ when $i = j$ and 0 otherwise, and $\gamma(r)$ is the Sternheimer shielding function which arises from the polarization of the core Fe electrons by charges outside the core. It is derived from atomic self-consistent first order perturbation calculations (Lauer et al. 1979). The EFG can be broken up into valence, covalence and ligand contributions. For high-spin Fe^{2+}, the total EFG is dominated by the valence contribution, which is roughly proportional to the Fe(3d) and Fe(4p) shell anisotropies,

$$\Delta n_{3d} = n_{3d(x^2-y^2)} - n_{3d(z^2)} + n_{3d(xy)} - \tfrac{1}{2}\left(n_{3d(xz)} + n_{3d(yz)}\right) \tag{20}$$

$$\Delta n_{4p} = \tfrac{1}{2}\left(n_{4p(x)} + n_{4p(y)}\right) - n_{4p(z)}$$

where $n_{3d(z^2)}, \ldots, n_{3d(yz)}$ and $n_{4p(x)}, n_{4p(y)}, n_{4p(z)}$ are the occupations of the individual 3d and 4p orbitals, respectively. The Fe(3d) anisotropy dominates the valence EFG. The covalence EFG contribution results from anisotropy of the bonding electrons between the iron atom and its surrounding ligands, and the ligand EFG from the ion cores and the valence electrons of the ligands. The covalence and ligand EFGs together are about 5% of the total in the cases considered.

Non-zero temperature EFGs were approximated by first performing zero-temperature calculations to determine the relative orbital energies E_i, and then these energies were used to calculate thermal average populations n_i for each orbital thermodynamically:

$$n_i = \frac{\exp(-E_i/kT)}{\sum_j \exp(-E_j/kT)}, \tag{20}$$

where T is temperature and k is the Boltzmann constant. In practice this was only done for the spin-down t_{2g} Fe(3d) orbitals, the lowest energy of which is the highest fully occupied molecular orbital. Those orbitals below these three remain fully occupied at finite temperatures, and the last two unoccupied spin-down orbitals the e_g anti-bonding orbitals are high enough above the t_{2g} in energy that their occupation at 300 K is negligible (with calculated occupation numbers less than 10^{-7}). The SCC Xα calculation is then repeated with the spin-down t_{2g} orbitals given their thermal average populations. The orbital energies of the second calculation are generally shifted only a few meV from those of the zero-temperature calculations.

Temperature effects other than the thermal population of molecular orbitals were neglected in the 300 K calculations. The time scale of Mössbauer spectroscopy, dictated by the nuclear transition of the ^{57}Fe nucleus (Rancourt 1998), is normally much longer than that of thermal vibration, thus Mössbauer spectroscopy generally sees only the atoms' equilibrium positions. Therefore effects of thermal vibration were not included in the calculation. We have also neglected any changes in bond lengths or flattening angles with temperature.

Randomly perturbed clusters were generated from the starting cluster by adding a small perturbation to each of the Cartesian coordinates of the cluster's six oxygen atoms, drawn from a Gaussian distribution with a mean of zero and a specified standard deviation σ. The mean position of each oxygen atom is thus equal to that of the corresponding atom in the starting cluster. That is, in each randomly generated cluster, each oxygen atom was shifted from its equilibrium position (x, y, z) to a position $(x + \Delta x, y + \Delta y, z + \Delta z)$, where the $(\Delta x, \Delta y, \Delta z)$ are normally distributed with $\langle\Delta x\rangle = \langle\Delta y\rangle = \langle\Delta z\rangle = 0$ and $s(\Delta x) = s(\Delta y) = s(\Delta z) = \sigma$. The Fe^{2+} cation was kept stationary at the origin.

The positions of hydrogen atoms were perturbed in a different way. The O-H bond length was kept at 0.958 Å. The initial O-H bond direction was taken as an axis **n**, and then the O-H bond was tilted by an angle ϕ away from **n**, where ϕ was drawn from a Gaussian distribution with a mean of zero and a

standard deviation σ_H. The bond was then rotated about **n** by an amount θ drawn from a uniform distribution between 0 and 2π. The angular standard deviation σ_H was calculated from σ by assuming σ_H was the angle of a triangle with isosceles sides equal to the O-H bond length and a base equal to σ; in this way we tried to maintain an amount of angular disorder in the OH bond angle commensurate with the amount of positional disorder in the oxygen atoms.

Constraints on the kind of static disorder in real materials are imposed by the global structure and the presence of chemical order, if any. We are ignoring these kinds of constraints as a first approximation, supposing that they have only a negligible effect in the limit of small perturbations to the starting cluster. This may not necessarily be true, and conversely, at large values of σ we may no longer be in the realm of small perturbations. It has been also been shown (Lougear et al. 2000) that accurate calculations of hyperfine parameters in real materials require more than just the first nearest neighbours atoms of ^{57}Fe. We have found (Evans et al. 2005a), however, that EFG response to distortion is qualitatively similar in single octahedra and larger, more realistic clusters, and it is mostly the qualitative link between local distortion environments and hyperfine parameter distributions that we want to simulate here. This will allows us to extract general trends and features of the relationship between local structural disorder and the hyperfine parameter distributions.

The static disorder parameter σ

Let $\mathbf{r}_i^{init}$ be the position vector of the ith oxygen atom (i = 1...6) in the starting cluster, which we may suppose represents the atom's ideal position, i.e. in some refined unit cell. Let $\mathbf{r}_i$ be the corresponding position vector in a randomly perturbed octahedron. While

$$\left\langle \mathbf{r}_i - \mathbf{r}_i^{init} \right\rangle = \mathbf{0}, \tag{21}$$

(where **0** is the zero vector), we also find that

$$\left\langle \left| \mathbf{r}_i - \mathbf{r}_i^{init} \right| \right\rangle = \sqrt{\frac{8}{\pi}}\sigma \approx 1.6\sigma, \tag{22}$$

that is, each atom has been displaced from its ideal position by an average distance of 1.6σ in some direction. The mean square displacement (MSD) is

$$\left\langle \left(\mathbf{r}_i - \mathbf{r}_i^{init}\right)^2 \right\rangle = 3\sigma^2 \tag{23}$$

which follows from the definition of σ.

The coordinate perturbation parameter σ, then, is a measure of static disorder in the solid, and provides a parameter that we should be able to take from experimental measurements. In an X-ray diffraction structure refinement, in addition to obtaining mean atomic positions, one also obtains atomic MSD parameters, generally expressed as U, B or β parameters (Downs 2000). These parameters are usually treated as being due entirely to thermal vibration of the atoms, but they also contain a contribution from static disorder proportional to σ^2. By comparing MSD parameters for a given sample over a range of temperatures, it should be possible to extrapolate the static disorder contribution. We did this for published x-ray diffraction refinements of micas done at multiple temperatures, plotting the U parameter versus temperature and then taking the intercept at $T = 0$ K as the static component of U, which is equal to $3\sigma^2$ from equation 23. For micas with the 2M1 stacking polytype, this procedure gives $\sigma = 0.030$ to 0.070 Å (using Comodi and Zanazzi (2000), Catti et al. (1989), Guggenheim et al. (1987)), and for those with the 1M polytype, $\sigma = 0.010$ to 0.040 Å (using Comodi et al (1999) and Takeda and Morosin (1975)).

A related method of estimating σ is given by Kunz and Armbruster (1990), who modelled atomic MSDs due to chemical disorder as follows. Suppose cation sites M in a structure may be occupied by either A or B cations, where p is the fraction of sites occupied by A cations. Then the MSD along the M-O bond, with length d, is,

$$\langle \Delta_{M-O} \rangle = p\left\{\langle \Delta_{A-O} \rangle + (d - d_{A-O})^2\right\} + (1-p)\left\{\langle \Delta_{B-O} \rangle + (d - d_{B-O})^2\right\}. \tag{24}$$

Here $\Delta_{M\text{-}O}$ is the MSD (in Å^2) along the bond, and angular brackets indicate an average over the polyhedral site; $d_{A\text{-}O}$ and $d_{B\text{-}O}$ are the typical A-O and B-O bond lengths, respectively, and $\Delta_{A\text{-}O}$ and $\Delta_{B\text{-}O}$ are the MSDs in the two end-member compositions. The average M-O bond length in the material can be calculated as

$$d = pd_{A-O} + (1-p)d_{B-O}. \tag{25}$$

Combining equations 24 and 25, we find that $\Delta_{M\text{-}O}$ reaches a maximum of

$$\Delta_{\max} = \left(\frac{\Delta d}{2}\right)^2 + \left(\frac{\Delta_{A-O} + \Delta_{B-O}}{2}\right) + \left(\frac{\Delta_{A-O} - \Delta_{B-O}}{2\Delta d}\right)^2, \tag{26}$$

where $\Delta d = d_{A\text{-}O} - d_{B\text{-}O}$. The first term of equation 26 dominates the others by at least an order of

magnitude; using figures from Kunz and Armbruster (1990) for Si and Al in feldspar, $(\Delta_{max})^{1/2} = 0.068$ Å while $\Delta d/2 = 0.065$ Å. So to a good first approximation, σ in a chemically disordered mineral is no greater than

$$\sigma = \frac{\Delta d}{2\sqrt{3}} \tag{27}$$

where Δd is the difference in M-O bond lengths between the largest and smallest cations in the structure. Calculated values of σ using different estimates of M-O bond lengths of octahedral cations common in micas are given in table 1; they range from 0.052 to 0.085 Å. Both methods of obtaining a physical of estimate of σ are of the order 0.010 to 0.100 Å.

Results and Discussion

We will denote individual simulations by the geometry of their starting clusters with the notation $\{C, \psi, d\}$, where ψ is the octahedral flattening angle, d is the Fe-O bond length, and C indicates the orientation of the O-H bonds. $C = \perp$ denotes OH bonds perpendicular to the upper and lower faces of the FeO_6 octahedron, as in an octahedral sheet, and $C = \parallel$ denotes OH bonds pointing outwards along the Fe-O bonds (see figure 1). Define the octahedron $[C, \psi, d]$ as the *unique* $Fe(OH)_6^{4-}$ octahedron with OH positions denoted by C, as above, flattening angle ψ and all six Fe-O bond lengths equal to d; i.e., $[C, \psi, d]$ is the starting octahedron of the simulation $\{C, \psi, d\}$. This notation is also summarized in table 4. The octahedron $[C, \psi, d]$ will have trigonal symmetry (point group D_{3d}), and is only distorted from pure O_h symmetry by flattening ($\psi >$ 54.74°). An arbitrary member of the ensemble $\{C, \psi, d\}$ will be much more distorted.

Each simulation generated ensembles of $N = 1000$ octahedra for static disorder parameters $\sigma =$ 0.025, 0.050, 0.075, 0.100, 0.125, 0.150 and 0.175 Å. Errors involved in estimating statistical parameters (means, standard deviations, histogram bins) are on the order of $N^{-1/2} \sim 3\%$. Multiple trials were performed for the {⊥, 58°, 2.11 Å} simulation with no significant difference between the resulting hyperfine parameter distributions for each trial, nor did a larger simulation of $N = 6000$ show any significant difference from the results of the smaller simulations.

{⊥, 58°, *d*} simulations - distributions at different bond lengths

The $Fe(OH)_6^{4-}$ cluster denoted [⊥, 58°, 2.11 Å], i.e. with perpendicular OH groups, flattening angle $\psi = 58°$ and equal Fe-O bond lengths $d = 2.11$ Å, is similar to the Fe^{2+} sites in annite (Hazen and Burnham 1973) and is typical of the values found in trioctahedral micas (Mercier 2003). The resulting distributions of hyperfine parameters for the simulations {⊥, 58°, 2.11 Å} are shown in figures 2 to 6.

Figure 2 shows the QS distributions at 0 K for simulations with $\sigma = 0.025$, 0.100 and 0.175 Å. In this and subsequent figures, we show different normalizations for the distributions, to highlight different characteristics. Part A shows the distributions normalized with respect to height. The width of the distributions increase as σ increases. This is not surprising, as we expect to get a wider variety of hyperfine parameter values with a wider range of distortions. The peak value of the distribution decreases as σ increases. As the distribution expands, the low edge moves to the right and the high edge moves to the left; the expansion of the low edge is much greater than that of the high edge. Part B shows the distributions plotted against $(QS - \langle QS \rangle)/s(QS)$, the deviation from the mean normalized with respect to width. This allows the shape of distributions with different means and standard deviations to be directly compared. The distributions have nearly the same shape regardless of the amount of static disorder, a function similar to a Gaussian but skewed slightly to the left. The skew increases only slightly with σ. The shape is exactly that which is characteristic of experimentally extracted Fe^{2+} distributions (e.g. Rancourt et al. 1994), which was also found in the simulation of Domes et al. (1986) presented in Nagy and Rölich (1991).

This skewed shape is intensified in the QS distribution at 300 K, shown in figure 3. In part A, the high edge is relatively constant at around 3.15 mm/s, regardless of σ, while the low edge tail extends to increasingly lower QS as σ increases. The peak value also shifts to lower QS values as σ increases. As QS is generally lower at finite temperatures than at 0 K, due to thermal population of valence orbitals, the QS distribution at 300 K is shifted towards lower values compared to the distribution at 0 K. In part B of figure 3, the relative shapes of the distributions at various σ are again very similar, but the increase in skew with increasing disorder is more pronounced at 300 K than at 0 K. The 300 K distributions in general have a more pronounced skew than at 0 K.

The IS distribution, shown in figure 4, is the same at 0 K and 300 K, as the IS is independent of temperature (Brady et al. 1965, Bancroft 1973). From part A of figure 4, the peak value of the distribution

changes only slightly with increasing disorder. In part B the skew of the IS distribution increases significantly as σ increases. A Gaussian curve is shown for comparison. At σ = 0.025 Å, the IS distribution is very close to Gaussian, deviations from which are small enough to attribute to statistical fluctuations. As σ increases, the IS distribution becomes increasingly skewed to the left, similar to the QS distribution. Figure 5 compares IS and QS distribution shapes at low and high disorder. While the two parameters have significantly different distributions at σ = 0.025 Å (solid lines), at 0.175 Å (dashed lines) the shapes are nearly identical (dashed lines). This is a result of increasing correlation between QS and IS as disorder increases, as discussed below.

Like the IS, the SP is a linear combination of the spin-up and spin-down electron densities, and is independent of temperature. Figure 6 shows the SP distributions with different normalizations. The dominant sign of the SP is positive, i.e. the majority of net spins are pointing up. The SP peak value is nearly constant with disorder, and from part B of figure 6, all distributions are very close to Gaussian. There is no systematic skew in the SP distributions.

Figure 7 shows distributions of the EFG asymmetry parameter η, for simulations with σ = 0.025, 0.050, 0.100 and 0.175 Å. Also shown is the Czjzek η-distribution (equation 15). All curves in this figure are normalized with respect to area. Although the QS distributions differ at 0 and 300 K, the η distribution is the same at both temperatures. The flattened starting cluster possesses trigonal symmetry and therefore has η = 0. For a randomly distorted octahedron, this will not generally be the case, as the probability of creating an axially symmetric octahedron from an axially symmetric octahedron through random distortions is exceedingly low. At low σ, the η distribution is strongly peaked at low values of η. As the degree of disorder increases, the distribution becomes broader and the peak becomes less distinct as the distribution appears to approach the Czjzek η-distribution. The distribution also becomes noisier, an artefact of the binning related to the width of the distribution. There is little apparent change in the distribution above σ = 0.100 Å.

Thus far we have discussed the shape and other features of hyperfine parameter distributions qualitatively. Figures 8-12 quantify the changes in mean and standard deviation or width of the hyperfine parameters in the simulations {⊥, 58°, d} for d = 2.08 Å, 2.11 Å and 2.14 Å, a range of bond lengths chosen to reflect the diverse Fe^{2+}-O bond lengths in minerals. In these and subsequent plots, the hyperfine

parameter calculated for the unperturbed starting cluster is plotted as the value of the mean at $\sigma = 0$ Å, while the standard deviation is taken as zero at $\sigma = 0$ Å.

Part A of figure 8 shows the mean QS as a function of σ at 0 and 300 K. At both temperatures, <QS> decreases significantly as disorder increases. This is consistent with the observation that as σ increases, the high edge of the distribution remains stationary while the width increases. Higher QS is often incorrectly associated with greater distortion from octahedral symmetry in both Fe^{3+} and Fe^{2+} sites, but this is in general not true for Fe^{2+} sites, as has been previously shown both theoretically (e.g. Evans et al. 2005a, Evans et al. 2005b) and experimentally (e.g. Rancourt et al. 1994, Rancourt et al. 1996, Zhe and De Grave 1998).

At 0 K, the <QS> curves at different bond lengths are nearly parallel to one another; there is a constant change in <QS> with bond length for all values of σ, and this change is small compared to the total change in <QS> over the range of σ with constant bond length. The change of <QS> with bond length at 300 K is considerably smaller than at 0 K. This is because at 300 K, QS at $\psi = 58°$ as a function of d reaches a maximum reaches a maximum around 2.11 Å, and changes vary little over the range 2.08-2.14 Å (Evans et al. 2005a).

Part B of figure 8 shows that the standard deviation s(QS) of the QS distribution at 0 and 300 K increases with σ. The standard deviation is slightly smaller at 300 K than at 0 K (hence distributions are narrower at 300 K) and does not appear to be greatly affected by Fe-O bond length.

Parts A and B of figure 9 show the mean and standard deviation of the IS distributions, respectively, as functions of σ. The mean has a maximum in the region 0.050-0.075 Å, which shifts to slightly higher σ as bond length increases. The standard deviation increases with disorder. Unlike the QS, changing the bond length significantly affects the IS distribution parameters; <IS> increases with an increase in bond length, while s(IS) decreases.

Figure 10 shows the mean and standard deviation of SP as functions of σ. The decrease of <SP> with increasing disorder is small compared to the relative change in other hyperfine parameters, and small in comparison with the increase with increasing bond length. The standard deviation s(SP) increases linearly with σ, as opposed to s(IS) and s(QS) which seem to have higher than linear dependences on σ.

Figure 11 shows the evolution of the mean and standard deviation of the EFG asymmetry

parameter, η, at 300 K. The behaviour does not change significantly with bond length. Both $<\eta>$ and $s(\eta)$ show an initial linear increase with σ and then saturate around $\sigma = 0.125$ Å near the values of the Czjzek η distribution, shown on the graph for comparison. (For the Czjzek η distribution, $<\eta> = 0.609$ and $s(\eta) = 0.242$ (Le Caer and Brand 1998).) A similar result is found by Le Caer and Brand (1998) (see their figure 13) for the theoretical model of an EFG tensor with a constant non-zero component and a Gaussian isotropic component, as the latter fraction increases. The Gaussian isotropic EFG tensor is associated with a random amorphous material.

In figure 12, the mean $<\eta>$ peaks just short of the Czjzek value, and then decreases, while $s(\eta)$ shows a slight increase above the Czjzek value. This behaviour indicates that the η distribution converges towards a Czjzek-like distribution at high disorder, but not necessarily the exact Czjzek η-distribution.

The distribution of η is the same at 0 and 300 K, although for any one particular cluster of the ensemble used to construct the distribution, it is not necessarily true that $\eta(0\text{ K}) = \eta(300\text{ K})$. Define

$$\Delta_T\eta = \eta(0\text{ K}) - \eta(300\text{ K}). \qquad (28)$$

Figure 12 shows $<\Delta_T\eta>$ and $s(\Delta_T\eta)$ (for the $d = 2.11$ Å starting cluster only) as functions of σ, quantifying the degree to which η may change from 0 to 300 K. We see that $<\Delta_T\eta>$ and $s(\Delta_T\eta)$ are equal at low σ, but while $s(\Delta T\eta)$ continues to increase monotonically with σ, $<\Delta_T\eta>$ drops to zero at high σ.

{⊥, 54.74°, 2.11 Å} simulations - distributions at different flattening angles

The distribution means and widths of the EFG-related parameters, QS and η, do not change significantly when we alter the cluster's bond length within the normal Fe-O range. In this section we will compare $\psi = 58°$ (flattened) and 54.74° (unflattened) starting clusters.

Figure 13 shows the QS distributions at 0 and 300 K for {⊥, 54.74°, 2.11 Å}, at different values of the static disorder parameter, normalized with respect to height. The distributions are similar to those in figures 2 and 3. Figure 14 shows the mean and standard deviation of the QS as functions of σ in the {⊥, ψ, 2.11 Å} simulations for $\psi = 54.74°$ and 58°. At 0 K the unflattened cluster behaves qualitatively much like the flattened cluster, but at 300 K the behaviour is quite different. For the unflattened starting cluster, <QS> changes little compared to the flattened starting cluster, with a shallow minimum around $\sigma =$

0.050 Å; the width s(QS) initially increases with σ more quickly than for $\psi = 58°$, but reaches a maximum around $\sigma = 0.125$ Å. Both mean and standard deviation are nearly equal at $\sigma = 0.100$ Å and 0.175 Å, so the distributions for these values of σ in figure 15 are nearly the same.

Figure 15 shows IS distributions for {⊥, 54.74°, 2.11 Å}, which are nearly identical to the $\psi = 58°$ case (figure 3B). Figure 16 shows <IS> and s(IS) as functions of disorder for the two flattening angles. Previously, we saw that bond length has a large effect on IS and only a small effect on the QS distribution (figures 8 and 9); from figures 14 and 16, we see the converse, that flattening has a large effect on QS and only a small effect on IS.

Figure 17 shows SP distributions for {⊥, 54.74°, 2.11 Å}, which are similar to those for {⊥, 58°, 2.11 Å}. Figure 18 shows the change in mean and standard deviation of SP with static disorder at $\psi = 58°$ and 54.74°. The trends at each flattening angle are again very similar, as for IS, showing that SP also depends less on flattening than on bond length. A curious feature of <SP> (part A) is the crook in the curves at $\sigma = 0.100$ Å. The <SP> curves in figure 10 also show this feature at larger scales. The presence of the crook all curves indicates that it is most likely not exclusively a statistical fluctuation, but we do not know its origin.

The η distributions of {⊥, 54.74°, 2.11 Å} are shown in figure 19. As disorder increases from $\sigma =$ 0.025 Å to 0.100 Å, the distribution changes from a peak at $\eta = 0.2$ to a broad distribution similar to the Czjzek η-distribution. This is similar behaviour to the {⊥, 58°, 2.11 Å} simulation (figure 7). However, the reverse trend occurs from $\sigma = 0.100$ Å to 0.175 Å, and the peak reappears. Figure 20 shows the mean and standard deviation of η for both {⊥, ψ, 2.11 Å} simulations. The {⊥, 54.74°, 2.11 Å} simulation shows similar saturation of <η> and $s(\eta)$ as the{⊥, 58°, 2.11 Å} simulation; <η> and $s(\eta)$ reach their saturation values at lower σ than in {⊥, 58°, 2.11 Å}, and <η> decreases again at higher σ.

If the {⊥, 58°, 2.11 Å} points (circles) in figure 20 are scaled on the σ-axis by a factor of 0.55 (diamonds), then they coincide with the {⊥, 54.74°, 2.11 Å} curves. That is, if each point (σ, <η>) in part A and (σ, $s(\eta)$) in part B from the {⊥, 58°, 2.11 Å} simulations are replotted at (0.55σ, <η>) and (0.55σ, $s(\eta)$), respectively, then the new points appear to fall on the same curves as those for the {⊥, 54.74°, 2.11 Å} simulations. This phenomenon illustrates the how flattening can change the effect of disorder on the

EFG asymmetry. The η distribution evolves the same way for both starting clusters, but in the flattened cluster, a larger amount of disorder is required for the same effect due to the strong anisotropy of the flattened cluster.

{||, 58°, 2.11 Å} simulations and the similarity of distributions

In the starting cluster {||, ψ, *d*}, the OH bonds point outwards from the centre of the cluster along the Fe-O bonds, and both oxygen and hydrogen atoms form congruent octahedra centred on the Fe atom. When ψ = 54.74°, the starting cluster has perfect octahedral symmetry. This has a dramatic effect on the QS distribution at 300 K. Flattened clusters (ψ > 54.74°) have many similarities with the {⊥, ψ, *d*} clusters.

In figure 21 we show IS distributions (first column), QS distributions at 0 K (second column) and 300 K (third column), and SP distributions (fourth column) normalized with respect to height, for the simulations {⊥, 58°, 2.11 Å}, {⊥, 54.74°, 2.11 Å}, {||, 54.74°, 2.11 Å} and {||, 58°, *d* }. The QS distributions at 300 K are not shown for {||, 54.74°, 2.11 Å} at σ = 0.025 Å and 0.100 Å, as they will be treated separately below.

From figure 21, one can see that despite the different starting cluster geometries, the distributions for a given parameter are similar in shape, if not position, at a particular value of σ, and become more similar as σ increases. The QS at 300 K is an exception for σ = 0.025 Å and 0.100 Å, where the {⊥, 58°, *d*} distribution is significantly narrower than the others. In general the hyperfine parameter distributions of the {||, ψ, *d* } simulations do not behave very differently from those of the previously examined {⊥, ψ, *d*} simulations. While the hyperfine parameter distributions of each geometry are quite distinct at σ = 0.025 Å (top row), they converge at high disorder (σ = 0.175 Å, bottom row). This occurs as the average differences between individual clusters in one ensemble becomes comparable to the difference between the starting clusters of each ensemble. The hyperfine parameter distributions exhibit a nearly universal behaviour in the presence of disorder, irrespective of the crystallographic site symmetry.

Figure 22 shows η distributions and their properties for {||, 58°, 2.11 Å}. The η distributions of {||, 54.74°, 2.11 Å} will be discussed below. Part A shows the η distributions at various values of the static disorder parameter. The ensemble's behaviour is quite similar to that of {⊥, 54.74°, 2.11 Å} (figure 23). Starting at σ = 0.025 Å with a broad peak at low η (< 0.4), the distribution approaches the Czjzek η-

distribution (dashed curve) as σ increases, then reverses this trend as σ continues to increase. This is reflected also in the mean (part B) which increases to the Czjzek value and then decreases. The standard deviation (part C) increases steeply to the Czjzek value, then increases only slowly. These curves are compared with those for {⊥, 54.74°, 2.11 Å}, with which they are quite similar. The two curves cannot be made to coincide with a simple horizontal scaling as in figure 20.

{||, 54.74°, 2.11 Å} simulations and the Gaussian Isotropic Model

While the flattened {||, 58°, 2.11 Å} and {⊥, ψ, 2.11 Å} simulations are very similar, the EFG properties of the unflattened {||, 54.74°, 2.11 Å} simulation at 300 K are unlike the other clusters examined. The starting cluster has ideal O_h symmetry, which has a significant effect on the QS distribution.

The evolution of the QS distribution at 300 K with increasing σ is shown in figure 23 for {||, 54.74°, 2.11 Å}. The low disorder QS distributions are completely unlike those of previous simulations, and unlike most Fe^{2+} QS distributions. At low values of σ, the high temperature QS distribution is skewed strongly towards low QS values, with a low edge at 0 mm/s, a peak value < 1 mm/s, and a high QS tail. These are QS values that would normally be assigned to Fe^{3+} sites. The Fe^{2+} cation is still in its high spin configuration; if this effect was due to a transition to a low spin configuration, there would also be a change in the IS, but as we shall demonstrate below the IS distribution is still that characteristic of high spin Fe^{2+} (see the first column of figure 21).

As σ increases, the low-QS peak shifts to higher values, while a small secondary peak appears around 3 mm/s (σ = 0.075 Å in figure 23). The low-QS peak broadens into a plateau, and eventually shrinks into a broad shoulder on the side of the high-QS peak, which continues to increase in height. At the highest value of σ, the distribution resembles the high disorder distributions of previous starting clusters with a single high-QS peak and a broad low-QS tail. The σ = 0.175 Å QS distribution is shown in comparison to those of the other ensembles in the third column, bottom row panel of figure 21. The distributions clearly have the same shape, although a small low-QS hump is still visible in the {||, 54.74°, 2.11 Å} distribution.

At 0 K, the QS distribution still has the characteristic shape and position of Fe^{2+} (see second column of figure 21), with a sharp high edge around 3.2 mm/s, and a low-QS tail. The difference in the

distributions at low and high temperatures is explainable in terms of the electronic structure of the cluster and the Gaussian Isotropic Model of amorphous EFGs, as follows.

The starting cluster {||, 54.74°, 2.11 Å} has undistorted octahedral symmetry, therefore the EFG of the starting cluster is exactly zero. The highest occupied and four lowest unoccupied spin-down molecular orbitals in an octahedral $Fe(OH)_6^{4-}$ cluster are almost entirely of Fe(3d) character. The three t_{2g} orbitals (conventionally labelled *xy*, *xz* and *yz*) are degenerate and share the single spin-down 3d electron between them. The electronic structure is spherically symmetric and the total EFG tensor is

$$\mathbf{V} = \tfrac{1}{3}\langle xy|\hat{\mathbf{V}}|xy\rangle + \tfrac{1}{3}\langle xz|\hat{\mathbf{V}}|xz\rangle + \tfrac{1}{3}\langle yz|\hat{\mathbf{V}}|yz\rangle = \mathbf{0} \tag{29}$$

where $\hat{\mathbf{V}}$ is the EFG tensor operator and $\mathbf{0}$ is the identically zero 3 × 3 tensor. When a distortion is applied to the starting cluster, the degeneracy between the three t_{2g} orbitals is lifted and, at 0 K, the spin-down 3d electron occupies the lowest orbital (assuming the most general case, where all three orbitals are now non-degenerate). Letting the three t_{2g} orbitals be $|1\rangle$, $|2\rangle$, and $|3\rangle$ with energies $E_1 < E_2 < E_3$, respectively, then at 0 K the EFG tensor is now $\mathbf{V} = \langle 1|\hat{\mathbf{V}}|1\rangle$. The QS in this case is generally of the order of 3 mm/s; the sign of V_{ZZ} depends on the character of the $|1\rangle$ orbital. Even a small distortion will change the QS from 0 to 3 mm/s, because the distorted cluster no longer has octahedral symmetry. Thus at 0 K, even though the starting cluster has QS = 0 mm/s, a small distribution of distorted octahedra will give rise to a distribution whose bulk lies in the neighbourhood of 3 mm/s. The probability that a random series of distortions will leave the cluster with O_h symmetry is exactly zero, thus the value of the QS distribution at 0 mm/s will be zero, regardless of the QS of the starting cluster.

At a finite temperature *T*, the t_{2g} orbitals acquire average effective thermal occupations:

$$n_1 = 1/Z,$$

$$n_2 = \exp[-\Delta_1/k_BT]/Z, \text{ and} \tag{30}$$

$$n_3 = \exp[-\Delta_2/k_BT]/Z,$$

where n_i is the effective occupation of the orbital $|i\rangle$, $\Delta_1 = E_2 - E_1$, $\Delta_2 = E_3 - E_1$, and $Z = 1 + \exp[-\Delta_1/k_BT] + \exp[-\Delta_1/k_BT]$. We assume that the t_{2g}-e_g splitting of the Fe(3d) orbitals is significantly larger than k_BT, so the thermal population of the e_g orbitals is zero. Since Δ_1 and Δ_2 are functions of the distortion, so are the n_i. If the applied distortion from O_h symmetry is small, then Δ_1 and Δ_2

are small with respect to k_BT, and so for each orbital $|i\rangle$, $n_i \sim 1/3$ and

$$\langle i|\hat{\mathbf{V}}|i\rangle \sim \langle i|\hat{\mathbf{V}}|i\rangle_{(\text{undistorted})}. \tag{31}$$

The Fe(3d) orbitals will be approximately spherical, as in the Fe^{3+} electronic structure, and so the EFG tensor

$$\mathbf{V} = n_1\langle 1|\hat{\mathbf{V}}|1\rangle + n_2\langle 2|\hat{\mathbf{V}}|2\rangle + n_3\langle 3|\hat{\mathbf{V}}|3\rangle \tag{32}$$

will be close to **0**, and the QS will be small. Therefore, we see that a distribution of small distortions from octahedral symmetry gives rise at finite temperatures to a QS distribution whose bulk lies in the region of low QS normally associated with Fe^{3+} clusters.

When the average size of the distortions increases - that is, as the static disorder parameter increases - the splittings Δ_1 and Δ_2 increase, n_1 approaches one and n_2 and n_3 approach zero. Thus the EFG tensor **V** in equation 32 approaches the (non-population-averaged) 0 K case, and the distribution shifts its bulk towards the neighbourhood of 3 mm/s.

If the distortion applied to the {||, 54.74°, 2.11 Å} starting cluster is small, then at finite T the means of each of the five linearly independent components of the EFG, U_i, will be approximately zero, and the electronic structure of the Fe atom will approximately spherical. Furthermore, if the distribution of distortions is Gaussian, then the distributions of the U_i will be nearly Gaussian as well. The two hypotheses of the Gaussian Isotropic Model (GIM) are then approximately satisfied, and so the Czjzek QS distribution should be a good approximation for the ensemble when σ is small. In figure 23, we show least-square fits of the Czjzek QS distribution (equation 16) to the QS distribution at σ = 0.025 Å (width parameter w = 0.310(6) mm/s, χ^2 = 0.04) and 0.050 Å (w = 0.577(8) mm/s, χ^2 = 0.011). The reasonable success in fitting the low-σ QS distributions demonstrates that the GIM is a good approximation to the actual EFG distribution in this specialized case.

The changes of mean and standard deviation of the QS at 0 and 300 K for both {||, 58°, 2.11 Å} and {||, 54.74°, 2.11 Å} simulations are shown in figure 24. At 0 K, (solid symbols) both simulations show trends similar to those in the {⊥, ψ, 2.11 Å} simulations (figure 14). At 300 K, the {||, 58°, 2.11 Å} simulation shows trends very similar to the {⊥, 54.74°, 2.11 Å} simulation, with a relatively flat variation of <QS> with disorder, and s(QS) increasing rapidly to a maximum before decreasing. A similar trend is seen in the s(QS) of the {||, 54.74°, 2.11 Å} simulation at 300 K, despite the very different evolution of the

{||, 54.74°, 2.11 Å} QS distribution. The mean QS of the {||, 54.74°, 2.11 Å} simulation at 300 K increases with σ, reflecting the evolution of the distribution shown in figure 21.

Figure 25 shows the η distributions of the {||, 54.74°, 2.11 Å} ensemble, at 0 and 300 K. Unlike in other simulations, the distribution differs significantly at the two temperatures. For small σ, the 0 K distribution (squares) has a single sharp peak around η = 0.1, while at 300 K the distribution is a broad, flat curve (circles) that is very close to the Czjzek η-distribution (dashed line). This latter result is in agreement with our observation that the EFG approximately follows the GIM at low σ. As the disorder increases, the 0 K peak broadens and the 300 K distributions forms a peak at low η, so that by σ = 0.150-0.175 Å, the distributions are almost the same at both temperatures. The high σ distributions are quite similar to those seen in the other simulations (figures 5, 23, and 26).

Figure 26 shows the mean and standard deviation of the η distributions at 0 and 300 K. The curves for {||, 58°, 2.11 Å} at 300 K were previously shown in figure 22, and are qualitatively similar to those of the {⊥, ψ, 2.11 Å} simulations. The 0 K and 300 K behaviour is the same for this ensemble. As observed from the distributions, the curves at 0 and 300 K for {||, 54.74°, 2.11 Å} are quite different, although the values of <η> at the two temperatures are clearly approaching one another as σ increases. Both <η> and $s(\eta)$ curves are discontinuous at σ = 0 Å; the limit as σ goes to zero is non-zero, while η = 0 for the O_h-symmetric starting cluster.

The IS and SP distributions for the {||, 54.74°, 2.11 Å} simulations are shown in comparison with those of the other simulations in figure 21. The IS and SP distributions are unaffected by the spherical symmetry of the Fe(3d) orbitals at 300 K in the {||, 54.74°, 2.11 Å}. The spin-up and spin-down electron densities at the nucleus are due only to the Fe *s*-orbitals, which are spherically symmetric to begin with, and only weakly affected by the total Fe(3d) orbital occupation and not by its symmetry. Figure 27 shows the mean and standard deviation of the IS for the {||, ψ, 2.11 Å} simulations, and figure 28 shows the corresponding mean and standard deviation of SP. There is very little difference between results for both flattening angles, and the <IS>, <SP>, s(IS) and s(SP) vary with σ in ways that are very similar to the corresponding results in the {⊥, ψ, 2.11 Å} simulations.

Simulated spectra and comparison with experiment

Having generated an ensemble of sets of hyperfine parameters, it is straight-forward to calculate a simulated quadrupole doublet from the (QS, IS) pairs. The simulated doublet is given by

$$Y(v) = Y_0 - Y_{peak} \sum_{i=1}^{N} \Gamma^2 \left[\frac{1}{\left(v - \delta_i + \frac{1}{2}V_i^*\right)^2 + \Gamma^2} + \frac{1}{\left(v - \delta_i - \frac{1}{2}V_i^*\right)^2 + \Gamma^2} \right] \tag{33}$$

where $Y(v)$ is the total spectrum, v is Doppler velocity, Y_0 is the background value, Y_{peak} is a peak scaling value, N is the total number of points in the ensemble (N = 1000), V_i^* and δ_i are the ith QS and IS, respectively, and Γ is the elemental Lorentzian line-width, equal to 0.097 mm/s.

Simulating the spectrum of a magnetic material is somewhat more complicated. The total spectrum can be still be calculated as the sum of elemental multiplets,

$$Y(v) = Y_0 - Y_{peak} \sum_{i=1}^{N} B\left(v \mid V_{zz,i}, \eta_i, \theta_i, \phi_i, H_i, \Gamma\right) \tag{34}$$

where, for a powder-averaged sample, $V_{zz,i}$ and η_i are the EFG principal value and asymmetry parameter, respectively, θ_i and ϕ_i are Euler angles describing the HF orientation with respect to the EFG principal axes, δ_i is the IS and H_i is the HF. The elemental Lorentzian multiplet $B\left(v \mid V_{zz,i}, \eta_i, \theta_i, \phi_i, H_i, \Gamma\right)$ can be calculated analytically (see Appendix, and Blaes et al. 1985), although there is no convenient short form.

The structure of the Fe^{2+} site in the mica annite is approximately that of cluster [⊥, 58°, 2.11 Å]; at the M1 site, the mean cluster bond length d = 2.1205 Å and ψ = 58.63°, and at the M2 site, d = 2.1005 Å and ψ = 58.30°, with a small counter-rotation of 0.43° (Mercier 2003, Hazen and Burnam 1973). To calculate hyperfine parameters with quantitative accuracy, however, requires at least the second nearest neighbour octahedra (Lougear et al. 2000), that is, a seven-octahedra section of the octahedral sheet. The computation time on such a large cluster is too long for a simulation of 1000 randomly perturbed seven-octahedra clusters to be practical. However, we observe that the QS vs. flattening curve at 300 K for the cluster [||, 58°, 2.11 Å] is much closer to that of a sample seven-octahedra cluster (described in Evans et al. 2005a) than that of [⊥, 58°, 2.11 Å] (figure 29) for ψ > 54.74°. Pointing the O-H bonds along the Fe-O bonds helps to redistribute the valence electron density along the xy-plane, ameliorating the lack of the second nearest neighbour sites. Therefore, while the {⊥, 58°, 2.11 Å} simulations may not reproduce the

spectrum of annite at room temperature, one of the {||, 58°, 2.11 Å} simulations may.

Figure 30 compares calculated spectra from {⊥, 58°, 2.11 Å} (parts A and B) and {||, 58°, 2.11 Å} (parts C and D) simulations with experimental powder Mössbauer spectra of synthetic (Rancourt et al. 1994b and 1994c). We compared the doublets (parts A and C of figure 30) calculated from each simulation with the annite spectrum taken at room temperature. For {⊥, 58°, 2.11 Å} (part A of figure 30), $\sigma = 0.150$ Å gave the best match in terms of line-width, although there is a clear mismatch in mean QS. The {||, 58°, 2.11 Å} simulations gave better results (part C of figure 30), with satisfactory agreement for σ from 0.075 Å to 0.125 Å (compare the plot of s(QS) vs. σ, figure 24); $\sigma = 0.125$ Å is shown in figure 30.

Annite becomes magnetic at low temperature. In parts B and D of figure 30, the magnetic spectra computed from the chosen simulations at 0 K is compared with an experimental powder spectrum of synthetic annite taken at 7 K (Rancourt et al. 1994c). Additional lines in the experimental spectrum beyond ±6 mm/s, due to small amounts of Fe^{3+} in the sample, are ignored and not shown in the figure. The experimental and simulated spectra are quite different, although there is an overall similarity in individual line widths and positions, and in the total width of the spectra. These similarities imply that local structural disorder is an important effect in the broadening of magnetic Mössbauer spectra, and may be enough alone to explain the widths of spectral lines without resorting to elaborate coupling between moments, such as the effects usually attributed to speromagnetism.

Simulated spectra and correlations between hyperfine parameters

For each simulation, the distributions of each hyperfine parameter have been discussed separately. Next we discuss the joint distributions of the hyperfine parameters, two parameters at a time, as well as correlations between the parameters, and the resulting calculated multiplet spectra. We observe significant correlations between QS and IS, and between IS and SP, whose nature changes with disorder.

Figure 31 shows scatter graphs of QS versus IS and SP versus IS, as well as simulated doublets and magnetic multiplets, for the {⊥, 58°, 2.11 Å} simulations. The first column shows scatter plots of QS versus IS at 300 K for the ensemble (1000 clusters), illustrating the joint distribution of the two parameters, for $\sigma = 0.025$ Å (part A), 0.100 Å (part E) and 0.175 Å (part I). From the shape of the scatter, the correlation between QS and IS increases with disorder. The scatter changes from a near-circular distribution that dies off gradually in all directions at $\sigma = 0.025$ Å (part A), to a comet-shaped distribution

with abrupt edges in the upper-right corner of the graph at $\sigma = 0.175$ Å (part I).

The joint QS-IS distributions in the first column of figure 31 produce the simulated doublets in the second column (parts B, F and J), calculated with equation 33. The increasing positive correlation between QS and IS with disorder manifests as an increasing asymmetry between the low and high velocity peaks of the doublet. The high velocity peak decreases relative to the low velocity peak as σ increases. The doublet with elemental Lorentzian line-width $\Gamma = 0.097$ mm/s for cluster [⊥, 58°, 2.11 Å] is also shown for comparison (dashed line). At $\sigma = 0.025$ Å, the {⊥, 58°, 2.11 Å} simulation doublet is very close to the elemental doublet, but as σ increases, the widths of the doublet lines increase and the asymmetry increases.

The origin of the correlation between QS and IS can be understood in terms of the electronic structure of the Fe(3d) and Fe(4p) valence orbitals. The IS is a linear function of the total electron density at the ^{57}Fe nucleus (see equation 5), such that an increase in density corresponds to a decrease in IS. Only those orbitals of primarily Fe *s* character have non-zero probability at the nucleus; if we consider the 1*s*-3*s* orbitals as Fe core orbitals, relatively unchanged by local environment, then the IS is strcitly a function of n_{4s}, the total valence Fe(4*s*) occupation. The Fe(4s) occupation, however, is dependent on the occupation of the other valence orbitals, as an increase in Fe(3d) or Fe(4p) orbital occupation leads to a decrease in Fe(4s) occupation through screening effects (Brady 1965, Axtmann et al. 1968). Thus IS has a weak dependence on the total Fe(3d) ($n_{3d(z^2)} + n_{3d(x^2-y^2)} + n_{3d(xy)} + n_{3d(xz)} + n_{3d(yz)}$) and Fe(4p) ($n_{4p(x)} + n_{4p(y)} + n_{4p(z)}$) valence orbital occupations. In the Townes-Dailey approximation (Townes and Dailey 1948, Bancroft 1973), the QS is a function of the Fe(3d) and Fe(4p) orbital anisotropies, as given in equation 19, which are themselves linear combinations of the individual Fe(3d) and Fe(4p) orbital occupations. Thus QS and IS are coupled through linear dependence on the valence orbital occupations $n_{3d(z^2)}, \ldots, n_{3d(yz)}$ and $n_{4p(x)}$, $n_{4p(y)}$, and $n_{4p(z)}$. De Vries et al. (1975) proposed similar empirical formulas for QS and IS in isolated atoms.

The third column of figure 31 shows scatter plots of SP versus IS for the ensemble (1000 clusters), for $\sigma = 0.025$ Å (part C), 0.100 Å (part G) and 0.175 Å (part K). There is a very strong positive correlation between IS and SP, which becomes more non-linear as disorder increases. The fourth column of figure 31 shows magnetic multiplets for each simulation at 0 K, calculated with equation 34 and the results of Blaes et al. (1985) for a powder sample (see Appendix). Also shown in each graph is the sextet with elemental

Lorentzian line-width Γ = 0.097 mm/s for cluster [⊥, 58°, 2.11 Å] at 0 K for comparison (dashed line). The evolution of the spectrum as σ increases is considerably more complex than the simple broadening of the elemental lines. Even at σ = 0.025 Å, the {⊥, 58°, 2.11 Å} simulation spectrum is significantly different than the elemental [⊥, 58°, 2.11 Å] sextet. The main lines are noticeably broader, and the lines near 1.5 mm/s and 2.0 mm/s have each split into two. The lines continue to broaden, shift position and in some cases split as σ increases, and it is difficult at σ = 0.175 Å (part L) to identify which features correspond to the lines in the elemental spectrum.

Figure 32 shows the same set of graphs (QS vs. IS, doublet spectra, SP vs. IS, magnetic spectra) for the {⊥, 54.74°, 2.11 Å} simulations. The QS-IS scatter plots (first column) show the same change in shape, from circular to comet-shaped, as the {⊥, 58°, 2.11 Å} scatter plots do in figure 31, although the {⊥, 54.74°, 2.11 Å} simulations have a thicker tail running parallel to the QS axis at high IS (parts E and I), with correspondingly fewer points in the low QS/low IS corner of the graph. In the doublet spectra, this difference manifests as a less pronounced increase in peak height asymmetry as disorder increases. At σ = 0.100 Å there is a slight asymmetry opposite to that in figure 31, with the low velocity (left) peak slightly shorter than the high velocity (right) peak. The line shapes themselves are more asymmetric than in the {⊥, 58°, 2.11 Å} simulations. The SP vs. IS scatter plots (third column) of the {⊥, 54.74°, 2.11 Å} simulations are very similar to those of the {⊥, 58°, 2.11 Å} simulations, and the magnetic spectra (fourth column) show the same kind of evolution with increasing disorder as in the {⊥, 58°, 2.11 Å} simulations.

Figure 33 shows QS vs. IS, SP vs. IS and simulated spectra for the {||, 58°, 2.11 Å} simulations. They are similar to both previous clusters. The correlation between QS and IS increases with disorder, as in the {⊥, 54.74°, 2.11 Å}. The doublet line height asymmetry at high σ is more pronounced than in the {⊥, 54.74°, 2.11 Å} simulations, and the asymmetry is of the tall low-velocity peak type found in the other simulations.

Finally, figure 34 shows QS vs. IS, SP vs. IS and simulated spectra for the {||, 54.74°, 2.11 Å} simulations. While the SP vs. IS scatter plots (third column) are the same as the previous three cases, the spectra and QS vs. IS plots are considerably different. The evolution of the QS vs. IS scatter plots (first column) reflects the changes in the QS distribution shown in figure 21. At high σ (part I), the plot is essentially similar to that of the {||, 58°, 2.11 Å} simulation.

Since the QS of the starting cluster is zero, the elemental non-magnetic spectrum of cluster [||, 54.74°, 2.11 Å] is a single Lorentzian line, while the elemental magnetic spectrum is a Lorentzian sextet with line intensity ratios of 3:2:1:1:2:3. The spectra of the {||, 54.74°, 2.11 Å} simulations, however, are quite different, even at low disorder.

The non-magnetic spectra (second column) are highly broadened doublets that change shape as σ increases. At σ = 0.100 Å, the spectrum appears to be a combination of two doublets, corresponding to high and low QS populations. These populations are visible in the QS distributions of figure 21.

The magnetic spectrum (fourth column) is a broadened sextet at σ = 0.025 Å (part D), with line positions and intensities similar to the elemental [||, 54.74°, 2.11 Å] sextet. The magnetic spectrum broadens with σ in a similar way to the other simulations (figures 31-33). At σ = 0.100 and 0.175 Å (parts H and L), the most intense peak in the magnetic spectrum is at the same position (~ 1 mm/s) as the singlet peak of the non-magnetic [||, 54.74°, 2.11 Å] spectrum (parts B, F and J).

Universal features of the hyperfine parameter distributions

We have already observed that the hyperfine parameter distributions share certain characteristics regardless of the particular geometry of the ensemble's average (i.e. starting) cluster. Many distributions have a common shape regardless of width or peak position: the SP distribution is Gaussian, and the QS distribution, aside from the special case of an O_h symmetric starting cluster, has the right-skewed shape with a constant high QS edge and a variable low QS tail. The IS distribution is Gaussian for small amounts of disorder, and evolves towards the QS distribution shape (figure 5) as disorder and the QS-IS correlation increase. Moreover, we have seen that as disorder increases, the distributions of a given hyperfine parameter (QS, IS, SP) have the same width and position regardless of starting cluster geometry. In this section we shall examine other universal features of the hyperfine parameter distributions, relationships between distribution widths and means, and between the widths of different parameter distributions. These relationships can be used as constraints, to aide in the simultaneous fitting with QS, IS and HF distributions.

In figure 35, we plot the width-to-mean ratios s(QS)/<QS>, s(IS)/<IS> and s(SP)/<SP> for all simulations. Part A shows {⊥, 58°, d} simulations for d = 2.08 Å, 2.11 Å and 2.14 Å; part B shows {⊥, ψ, 2.11 Å} simulations for ψ = 54.74° and 58°; and part C shows {||, ψ, 2.11 Å} simulations for ψ = 54.74°

and 58°. As with other distribution parameters, s(IS)/<IS> and s(SP)/<SP> are sensitive to bond length and relatively insensitive to flattening angle, while s(QS)/<QS> at 0 and 200 K is very sensitive to flattening angle and less sensitive to bond length. With the exception of s(QS)/<QS> at 300 K for the {⊥, 54.74°, 2.11 Å} and {∥, ψ, 2.11 Å} simulations, the width-to-mean ration increases with σ for all parameters and starting clusters, due to the increasing width of the distributions.

The width-to-mean ratio of the SP is much greater than those of the other hyperfine parameters. This contradicts the common assumption that the HF is insensitive to the structure of the local environment; actually, we see that the opposite is true, that the variation in the HF due solely to local disorder is large compared to the HF's absolute value.

The s(QS)/<QS> at 0 K and the s(IS)/<IS>, on the other hand, are of similar magnitudes, with the s(QS)/<QS> being greater by about a factor of two. (The SP width-to-mean ratio, by contrast, is a factor of 4 to 7 greater than that of the QS at 0 K.) Although the IS distribution is significantly narrower than the QS distribution (see the QS scatter graphs in figures 31-34), the IS distribution's width is not negligible. Mössbauer spectra are often fit with the assumption that the relative width of the IS distribution is negligible compared to that of the QS, but in general this is not a valid assumption.

The width to mean ratio of QS at 300 K is nearly the same as that at 0 K in the {⊥, 58°, d} simulations. This is not true for the {⊥, 54.74°, 2.11 Å} and {∥, 58°, 2.11 Å} simulations, however, where s(QS)/<QS> at 300 K reaches a maximum in the region 0.100-0.125 Å and then starts to decrease; the magnitude of the ratio, moreover, is about twice that of the QS at 0 K. Unsurprisingly, at this point, s(QS)/<QS> at 300 K for the {∥, 54.74°, 2.11 Å} simulations behaves contrary to all the others, decreasing with increasing disorder from a magnitude similar to that of s(SP)/<SP>. Given the Fe^{3+}-like symmetry of the electronic structure in this cluster at low σ, this behaviour may be what one might expect of Fe^{3+} clusters.

In figure 36, we show plots of s(QS) versus s(IS) for 0 K and 300 K (parts A and B), and s(SP) versus s(IS) (part C), for all simulations. In parts A, the s(QS) versus s(IS) curves at 0 K all fall within a relatively narrow range. At low temperatures, the proper widths of the QS and IS distributions have a nearly universal relationship that can be used to inform how a joint (QS, IS) is fit to an Fe^{2+} spectra. Part C shows a similar result for the temperature-independent s(SP) versus s(IS) curves. In this case, the {⊥, 58°, 2.14 Å} and {⊥, 58°, 2.08 Å} curves provide upper and lower limits, respectively, to the SP width as a

function of s(IS), with all of the curves between having an Fe-O bond length of 2.11 Å. This is a consequence of the strong dependence of the IS and SP on Fe-O bond length, as observed above (figures 9 and 10).

The relationship between s(IS) and s(QS) at 300 K, shown in part B, is less consistent. The three {⊥, 58°, d} simulations, for d = 2.08, 2.11 and 2.14 Å, follow similar curves to the 0 K simulations, but the remaining three ensembles are quite different. The {⊥, 54.74°, 2.11 Å} and {∥, 58°, 2.11 Å}simulations show similar behaviour, while the high-symmetry {∥, 58°, 2.11 Å} simulation follows its own separate curve. The relationship between QS and IS distribution widths at high temperatures is less universal than at 0 K, and is more dependent on site geometry.

Sign of the EFG principal value

The QS is proportional to the absolute value of the EFG principal eigenvalue, V_{ZZ} (equation 4), therefore the sign of the principal value has no effect on the zero-HF Mössbauer spectra. The sign depends on the character of the lowest energy Fe(3d) orbital, occupied by the lone spin-down electron. For a trigonally-symmetric, flattened $Fe(OH)_6$ octahedron, this is the z^2 orbital in our system of coordinates, which produces a negative V_{ZZ} . Thus in a perfectly ordered crystalline octahedral sheet, V_{ZZ} will be negative at every Fe^{2+} site. For other distortions, the lowest energy Fe(3d) orbital may give a positive V_{ZZ}, therefore if the static disorder in the octahedral sheet is increased, a population with $V_{ZZ} > 0$ appears. In the limit of a perfectly amorphous, isotropic solid, the Fe^{2+} electronic structure will have spherical symmetry *on average*, and thus one might expect equal proportions of positive and negative V_{ZZ}. This is the prediction of the Gaussian Isotropic Model (Czjzek et al. 1981, Le Caer and Brand 1998). Thus when increasing the static disorder in an octahedral sheet from zero, the proportion of positive V_{ZZ} increase from zero to 50% in the amorphous limit. However, our simulations show a more complex situation.

Figure 37 shows the probability density distribution of V_{ZZ} at 0 K and 300 K in the {⊥, 58°, 2.11 Å} simulations. Starting with low static disorder (bottom), the distribution at both temperatures consists of a single peak at negative values, indicating that all clusters in the ensemble have $V_{ZZ} < 0$. A peak of positive V_{ZZ} values appears at σ = 0.075 Å , and increases in relative area as σ increases. At the largest values of σ investigated (σ = 0.150 Å and 0.175 Å, top), the positive and negative peaks are of roughly equal size. Figure 38 shows QS distributions of {⊥, 58°, 2.11 Å} simulations, at 0 and 300 K, decomposed into

contributions from the $V_{ZZ} < 0$ and $V_{ZZ} > 0$ populations. At low disorder, where the positive V_{ZZ} population first appears, the positive partial QS distribution is located in the low QS tail of the total distribution. At high disorder, however, the positive and negative partial QS distributions are similar in both shape and position, although the negative partial QS distributions is entirely responsible for the high QS edge of the total distribution.

Figures 39 and 41 show the V_{ZZ} distributions for the simulations {⊥, 54.74°, 2.11 Å} and {∥, 58°, 2.11 Å}, respectively. As for other hyperfine parameter distributions examined, the V_{ZZ} distributions of these two simulations are very similar. In both simulations, and at both 0 and 300 K, the negative peak shrinks and the positive peak grows as σ increases, and at σ = 0.175 Å, almost all clusters in the ensemble have positive V_{ZZ}. Instead of equal proportions of positive and negative signs at high disorder, we find that positive signs for V_{ZZ} dominate, even though the geometry of the average cluster implies a negative V_{ZZ}. This is a strong reminder that the average site in a chemically disordered material does *not* always predict the average EFG tensor (Evans et al. 2005b), contrary to naive expectations.

The partial QS distributions for the negative and positive V_{ZZ} populations in simulations {⊥, 54.74°, 2.11 Å} and {∥, 58°, 2.11 Å} are shown in figures 40 and 42, respectively. Compared to the {⊥, 58°, 2.11 Å} simulation, the positive V_{ZZ} contribution to the total QS distributions become large at smaller values of σ. When the positive contribution is sufficiently large, it shares the same high QS edge as the total distribution. The high QS edge is therefore determined by neither the positive or negative VZZ contributions alone, but by whichever is the largest.

Figure 43 shows the V_{ZZ} distributions for the {∥, 54.74°, 2.11 Å} simulations at 0 and 300 K. The 0 K simulations (left) show a single peak at $V_{ZZ} > 0$, which increases in width as disorder increases. The $V_{ZZ} <$ 0 population is negligible. The 300 K simulations (right) start with nearly equal positive and negative V_{ZZ} peaks positioned near zero at low disorder (bottom, σ = 0.025 Å). The positive peak is slightly wider than the negative peak. As also seen in the QS and the η distributions, the V_{ZZ} distribution in this case is very close to the predictions of the Gaussian Isotropic Model. Several things happen as the static disorder σ increases: (1) the positive peak increases in area while the negative peak decreases, becoming negligible by σ = 0.175 Å; (2) the positive and negative peaks move farther apart, as the magnitude of the peak positions increases from the values typical of spherically symmetric electronic structures (less than 1 mm/s) to those

values typical of Fe^{2+} (2-4 mm/s); and (3) the shape of the positive peak follows the same evolution as the shape of the QS distribution (figure 27), from left-skewed to right-skewed. At $\sigma = 0.175$ Å, the V_{ZZ} distributions at 0 and 300 K are of similar shape.

Figure 44 shows the partial QS distributions for the negative and positive V_{ZZ} populations of the {||, 54.74°, 2.11 Å} simulations at 300 K. Since the negative V_{ZZ} population at 0 K is negligible, only the 300 K partial and total QS distributions are shown. The negative and positive partial distributions are approximately equal at $\sigma = 0.025$ Å, and then the positive partial distribution becomes dominant as σ increases. From figure 21, we have seen that the 300 K {||, 54.74°, 2.11 Å} simulations, the QS distribution is a combination of low Fe^{3+}-like and high Fe^{2+}-like QS populations whose proportions change as disorder increases. But figure 44 shows that these high/low QS populations do not strictly correspond to the positive and negative V_{ZZ} populations. Although at low σ, the negative V_{ZZ} partial QS distribution corresponds to low QS, the positive V_{ZZ} partial QS distribution is equally divided between low and high QS populations.

The common theme of the evolution of the V_{ZZ} distributions for all four starting geometries is that the positive sign of V_{ZZ} comes to dominate at high disorder, regardless of which sign, if either, dominates at low disorder. This trend is quantified in figure 45, which shows the changing fraction of clusters having positive V_{ZZ} for each simulation as σ increases. The exception is the {⊥, 58°, 2.11 Å} starting cluster, which holds more strongly to negative values of V_{ZZ} due to the double strength of the preferred symmetry axis due to a high flattening angle and the O-H bond directions (see discussion of figure 24). The evolution of the V_{ZZ} distributions shows strongly what was less clear in the distributions of other EFG tensor properties – that the EFG tensor distributions do not tend towards the amorphous and isotropic case at high static disorder, as one might suppose, in Fe^{2+} octahedra. The Gaussian Isotropic Model does not describe a highly disordered ensemble of Fe^{2+} octahedra well at all, nor is such an ensemble well described by simple normal distributions based around the EFG tensor properties of its average octahedral site.

Correlations of the principal value sign and other EFG properties

The sign of V_{ZZ} shows a strong correlation with the direction of the eigenvector associated with V_{ZZ}, called the principal axis of the EFG. Defining ϕ as the angle between the z-axis and principal axis of the EFG, $0° \leq \phi \leq 90°$, in general we find that small ϕ (< 20°) correspond to negative V_{ZZ}, while large ϕ (60-90°) correspond to positive V_{ZZ}. This agrees with previous calculations on larger, multi-octahedral

clusters (Evans et al. 2005b), and with oriented single Mössbauer spectroscopy measurements of micas (Hargraves et al. 1990).

Figure 46 shows scatter plots (1000 points) of the angle ϕ versus the EFG asymmetry η , where η is plotted between -1 and 0 if $V_{ZZ} < 0$, and between 0 and +1 if $V_{ZZ} > 0$. The figure thus shows simultaneous correlations between ϕ, η, and the sign of V_{ZZ}. For the simulations {⊥, 58°, 2.11 Å}, {⊥, 54.74°, 2.11 Å} and {||, 58°, 2.11 Å}, shown for $\sigma = 0.100$ Å, there is a clear correlation between η and ϕ for each sign of V_{ZZ}. When $V_{ZZ} < 0$, an $\eta \sim 0$ corresponds approximately to $\phi \sim 0°$, while larger η correspond to slightly higher ϕ. When $V_{ZZ} > 0$, $\eta \sim 1$ corresponds approximately to $\phi \sim 90°$, while smaller η correspond to slightly smaller ϕ. In both cases, ϕ and η are positively correlated. These correlations are only true on average, and the plot of ϕ against η becomes much noisier as σ increases, and on increasing the temperature. A small population of points with $V_{ZZ} < 0$ and $\phi \sim 70$-$80°$ appears at high disorder for these simulations (e.g. $T = 0$ K in part C), but even at $\sigma = 0.175$ Å these clusters are less than 5% of the total ensemble.

At low disorder, there is also a correlation between η and the sign of V_{ZZ}. When the $V_{ZZ} > 0$ population first appears, the average η over that population, $\langle\eta\rangle_+$, tends to be close to 1, while the average η over the $V_{ZZ} < 0$ population, $\langle\eta\rangle_-$, is small (less than 0.4). As disorder increases and the $V_{ZZ} > 0$ population grows, both groups have η distributed from 0 to 1, as in parts A-C of figure 46. Part A of figure 47 shows the evolution of $\langle\eta\rangle_+$ and $\langle\eta\rangle_-$ with σ for the {⊥, 58°, 2.11 Å}, {⊥, 54.74°, 2.11 Å} and {||, 58°, 2.11 Å} simulations, which show this kind of behaviour.

The correlations between the sign of V_{ZZ}, η, and ϕ can be understood as follows. An $\eta = 0$ corresponds to axial symmetry, while $\eta = 1$ corresponds to planar electronic structures. Thus if the highest occupied spin-down orbital is planar, we expect the EFG to have $\eta = 1$ and an in-plane principal axis ($\phi \sim 90°$). Conversely, if the highest occupied spin-down orbital is aligned along the z-axis, like the Fe(3d) z^2 orbital, then we expect $\eta = 0$ and the principal axis normal to the xy-plane ($\phi \sim 0°$). Those clusters whose highest occupied spin-down orbital is primarily of Fe(3d) z^2 character will have a negative V_{ZZ}, while those with highest occupied spin-down orbitals composed primarily of the other Fe(3d) orbitals, which lie mostly in the xy-plane, all have positive V_{ZZ}.

The {||, 54.74°, 2.11 Å} simulations do not show the kind of correlations between ϕ, η and the

sign of V_{ZZ} as the other simulations. Parts D and E of figure 46 shows the scatter plot of ϕ vs. $\eta \times \text{sign}(V_{ZZ})$ at $\sigma = 0.025$ Å and 0.175 Å. There is no correlation between η and ϕ at either 0 or 300 K. The distribution of ϕ with the sign of V_{ZZ} is different for the two temperatures. At $\sigma = 0.025$ Å, where the ensemble behaves approximately like the Gaussian Isotropic Model at 300 K, ϕ is approximately equally distributed for both signs of V_{ZZ}, as the model predicts. The distribution of ϕ itself is not uniform, as in a perfect Gaussian Isotropic Model, but favours values greater than 20°. At 0 K and $\sigma = 0.025$ Å, there is a complicated correlation between ϕ and the sign of V_{ZZ}. At negative V_{ZZ}, there are two small disconnected populations with $\phi < 10°$ and $\phi \sim 60$-80°. The majority of points have positive V_{ZZ}, all of which have $\phi > 30°$. At $\sigma =$ 0.175 Å, the 0 K scatter plot is very similar to the one at 0.025 Å, and the 300 K scatter plot has become similar to the 0 K plot.

Part B of figure 47 shows the evolution of $\langle\eta\rangle_+$ and $\langle\eta\rangle_-$ with σ for the {||, 54.74°, 2.11 Å} simulations at 0 and 300 K. Surprisingly, since most other EFG properties for this simulation are very different at the two temperatures, $\langle\eta\rangle_-$ is nearly the same at 0 and 300 K, approximately constant at about 0.65. The 0 K value of $\langle\eta\rangle_+$ increases very slowly from 0.2 to 0.3 as σ increases, and the 300 K value decreases from 0.55 to 0.3. This is different again from the other simulations, shown in part A of figure 47.

Polar Representation of the EFG Tensor

Additional insight into the evolution of the EFG tensor distribution with static disorder may be gained by a transformation of variables. If V_{ZZ} is plotted against η for a given ensemble, as in part A of figure 48, one obtains a graph with two disconnected sets of points, the positive and negative V_{ZZ} populations discussed in the previous section. In this case the points in each population are distributed over all values of η from 0 to 1.

However, this plot misrepresents the actual topology of the (V_{ZZ}, η) space. For example, in an EFG tensor where $\eta = 1$, the three EFG eigenvalues must be

$$V_1 = +q,\ V_2 = 0 \text{ and } V_3 = -q \tag{35a}$$

for some $q > 0$, since V_1, V_2 and V_3 must sum to zero. Therefore the principal value is $|V_{ZZ}| = q$, although the sign of V_{ZZ} is undefined because V_1 and V_3 are of equal magnitude but opposite sign. Suppose one adds a small perturbation to the EFG, $\iota > 0$, $\iota << q$, in such a way that the eigenvalues become

$$V_1 = q + \iota,\ V_2 = -2\iota,\ \text{and}\ V_3 = -q + \iota. \tag{35b}$$

Now V_1 alone is of the greatest magnitude, and so $V_{ZZ} > 0$ and $\eta < 1$. If instead one subtracts the same perturbation, so that

$$V_1 = q - \iota,\ V_2 = +2\iota,\ V_3 = -q - \iota, \tag{35c}$$

then V_3 has the greatest magnitude, and $V_{ZZ} < 0$ and $\eta < 1$. Graphically, a small perturbation from a point on the $\eta = 1$ line in part A of figure 48, on either size of the $V_{ZZ} = 0$ line, moves into the $V_{ZZ} > 0$ half of the figure in one direction, and into the $V_{ZZ} < 0$ half of the figure in the other direction. The two halves of the (V_{ZZ}, η) graph must be connected not only through the $V_{ZZ} = 0$ line, but also through the two $\eta = 1$ half-lines.

Czjzek (1983) proposed a transformation of variables from (V_{ZZ}, η) into a polar coordinate system (R, Θ), mapping the infinite strip $\{-\infty < V_{ZZ} < +\infty\ ,\ 0 \le \eta \le 1\}$ onto the sector $\{0 \le R < +\infty\ ,\ -\pi/6 < \Theta \le +\pi/6\}$, where $R = V^*$ (the QS, see equation 17), and Θ is a function of η and the sign of the V_{ZZ} only. We shall use an alternate system used by Le Caer and Brand (1998), which maps the (V_{ZZ}, η) strip onto the half plane $\{0 \le R < +\infty\ ,\ 0 < \Theta \le \pi\}$. This is a more natural choice in the sense that the left half of the graph still corresponds to $V_{ZZ} < 0$, and the right half to $V_{ZZ} > 0$. The planar coordinates

$$X = R\cos\Theta = V_{ZZ}\left[\frac{1-\eta^2}{1+\eta^2/3}\right],\ Y = R\sin\Theta = \sqrt{3}\left|V_{ZZ}\right|\left[\frac{\eta\left(1-\eta^2/9\right)}{1+\eta^2/3}\right], \tag{36}$$

are plotted in part B of figure 48 using the same data as in part A. The two apparently disconnected populations are now clearly a single continuous population. Table 2 gives a full list of relations between the EFG tensor elements and the new coordinate system.

Figure 49 shows scatter graphs in these new coordinates for each simulation performed. The polar coordinates make the nature of the EFG tensor's evolution with increasing disorder very clear. For all but the 300 K {||, 54.74°, 2.11 Å} simulation (red points in part D), the ensembles of EFG tensors form near-circular arcs around the origin. As static disorder increases, the width of the arcs increase, corresponding to the increasing width of the QS distribution. At the same time, the arcs shift clockwise from the left to the right half of the plane. Gradually the body of points moves from high to low Θ, as measured from the positive X axis. This is very clearly seen in parts A, B, and C of figure 42. At the high values of σ (top of columns), the tail from low to high Θ becomes increasingly sparse. The upper limit of QS, manifested in

the QS distribution as a constant high edge, is visible in all of the graphs, as all ensembles seem bounded within the half-circle of radius ~3.5 mm/s centred about the origin.

In the {||, 54.74°, 2.11 Å} simulation (part D), the 0 K ensemble lies predominantly in the right half of the graph, and this does not change as σ increases; the arc only becomes wider and more scattered. At 300 K, the σ = 0.025 Å is not a near-circular arc but a blob of points centred approximately on the Y axis. This agrees with the results of Le Caer and Brand (1998) for the Gaussian Isotropic Model (see their figure 9). As σ increases, the blob expands outwards from the origin towards the right half of the plane. At high σ, the 300 K ensemble comes to resembles the 0 K ensemble.

The simple changes in the EFG tensor ensembles in the coordinate system of equation 36 graphically summarizes the more complex changes in the QS, η and V_{ZZ} distributions illustrated previously. The change in the EFG tensor as static disorder increases can been seen as a rotation of the ensemble in the (X, Y) plane, combined with a widening of the distribution in the radial direction, subject to a radial bound (the constant QS high edge). A more detailed description of this evolution may form a basis for an analytical model of the Fe^{2+} EFG tensor distribution in the presence of chemical disorder in minerals, analogous to the Gaussian Isotropic Model for amorphous materials.

Quadrupole splitting and average cluster properties

We next want to connect the properties of the hyperfine parameter distributions to the structural properties of the underlying ensemble of perturbed octahedra. We have compared hyperfine parameter distributions generated from starting clusters of different Fe-O bond lengths and flattening angles, observing the differences in distribution shape, mean and standard deviation which result. This illustrates the dependence of the hyperfine parameter distributions on the geometrical properties of the average $Fe(OH)_6^{4-}$ cluster in an ensemble of randomly perturbed clusters. In a similar way, if we take the unique cluster [C, ψ, d] and apply successive distortions, e.g. by increasing the flattening angle, we can calculate the hyperfine parameters as functions of distortion, as in figure 29 and as was done in Evans et al. (2005a). These distortion curves give the hyperfine parameters of the average of the ensemble {C, ψ, d}. We are interested to what degree the hyperfine parameters of individual members of the ensemble {C, ψ, d}, as opposed to the average, follow the distortion curves obtained for the average cluster [C, ψ, d]. In other

words, can the hyperfine parameters of a randomly distorted $Fe(OH)_6^{4-}$ cluster be predicted given the suitably-defined average flattening angle and Fe-O bond length, or some other combination of parameters describing the average distortion of the cluster? If such geometric structural factors can be found, then an analytic form for the hyperfine parameter distributions could be calculated by assuming appropriate distributions for the structural factors. The relationship between the hyperfine parameter distributions of the ensemble $\{C, \psi, d\}$ and the average structure of the ensemble, via distortion curves for the average $[C, \psi, d]$, could also allow certain features of the hyperfine parameter distributions to be explained and related to the average structure. We will focus on the $C = \perp$ clusters, as $C = \parallel$ results will be similar when $\psi > 54.74°$.

Define the mean cluster bond length as

$$d = \frac{1}{6}\sum_{i=1}^{6} d_i \,, \tag{37}$$

where the d_i are the individual Fe-O bond lengths in the cluster. The mean cluster flattening angle for an arbitrarily distorted octahedron is defined relative to the average structure:

$$\psi = \frac{1}{6}\sum_{i=1}^{6} \cos^{-1}\left(\frac{|\mathbf{d}_i \cdot \mathbf{z}|}{d_i}\right), \tag{38}$$

where $\mathbf{z}$ is the unit vector pointing along the z-axis, and $\mathbf{d}_i$ is the vector pointing from the Fe cation to the ith O anion. It is reasonable to use the $\mathbf{z}$ axis as the reference angle in this case if the clusters are considered sitting in an octahedral sheet, where the direction of flattening is clearly defined by the normal to the sheet.

Part A of figure 43 shows the QS at 0 K plotted against the mean cluster flattening angle for the $\{\perp, 58°, 2.11\ Å\}$ and $\{\perp, 54.74°, 2.11\ Å\}$ simulations at $\sigma = 0.025$ Å and 0.175 Å. Also shown is the QS vs. ψ curve for the $[\perp, \psi, 2.11\ Å]$ clusters. There is a nearly linear relationship between flattening angle and the QS for the $[\perp, \psi, 2.11\ Å]$ clusters, but there is no such relationship for the $\{\perp, \psi, 2.11\ Å\}$ ensembles. When disorder is low, the simulation results cluster along the $[\perp, \psi, 2.11\ Å]$ line, but when disorder is high, the majority of the simulation results are spread below the curve. Only a few points lie above the line. The upper bound of the QS at 0 K appears to run parallel above the $[\perp, \psi, 2.11\ Å]$ QS curve.

Part B of figure 43 shows QS at 300 K plotted against the mean cluster flattening angle. As at 0 K, the low-σ simulations are spread around the $[\perp, \psi, 2.11\ Å]$ curve. The high-σ simulation points are bounded above (with a handful of exceptions) by the 3.1 mm/s maximum in the $[\perp, \psi, 2.11\ Å]$ flattening

curve located near $\psi = 58°$. This agrees with previous results comparing calculated QS vs. ψ curves for various octahedral clusters with the high edge of experimental QS distributions (Evans et al. 2005a). Note that in both part A and part B, there is a partial overlap between the points of the $\sigma = 0.175$ Å {⊥, 58°, 2.11 Å} and {⊥, 54.74°, 2.11 Å} simulations near 56°, but there are also regions of high ψ occupied only by {⊥, 58°, 2.11 Å}, and of low ψ occupied only by {⊥, 54.74°, 2.11 Å}.

The results with scatter plots of QS vs. mean cluster bond length *d* (part C and D of figure 43 at 0 and 300 K, respectively) for the {⊥, 58°, 2.08 Å} and {⊥, 58°, 2.14 Å} simulations are qualitatively similar to the plots versus flattening angle. The curve shown is the QS as a function of bond length *d* for the [⊥, 58°, *d*] clusters. At low σ, the points of the ensemble are spread around the curve, while at high σ the scatter plot and the curve are largely independent of one another.

At 300 K (part D), the QS versus *d* curve of the [⊥, 58°, *d*] clusters has a maximum equal to the maximum of the QS versus ψ curve of the [⊥, ψ, 2.11 Å] clusters in part B, bounding both high-σ simulations from above. The QS of the [⊥, ψ, *d*] cluster as a simultaneous function of bond length and flattening angle reaches a maximum at $\psi = 58°$ and $d = 2.11$ Å. These are approximately the values of ψ and *d* in the structure of the Fe^{2+} mica annite (see the section above on comparison of simulated spectra with experiment).

Geometric structural factor for quadrupole splitting

The mean cluster bond length and flattening angles as defined in equations 37 and 38 are clearly not enough to determine the QS of any general $Fe(OH)_6^{4-}$ octahedron alone. It would be advantageous to have a parameter that is entirely a function of the cluster's geometry that allows one to predict the value of the QS. Such a parameter would also allow calculation of a QS distribution from a supposed distribution of that parameter (which itself could be calculated from a supposed distribution of local environments).

Define the geometric structural factor *S* as

$$S = \sum_{i=1}^{6} \frac{1}{d_i^6} + \sum_{i=1}^{6} \sum_{j<i} \frac{3\cos^2 \theta_{ij} - 1}{d_i^3 d_j^3}, \tag{39}$$

where d_i are the six Fe-O bond lengths of equation 37, and θ_{ij} is the angle between Fe-O bonds *i* and *j* (i.e.,

$\left|\mathbf{d}_i \cdot \mathbf{d}_j\right| = d_i d_j \cos\theta_{ij}$). For a flattened octahedron with bond length equal to d and flattening angle ψ, this gives

$$S = 9\left(\frac{3\cos^2\psi - 1}{d^3}\right)^2 \quad \text{or} \quad S^{1/2} = 3\left|\frac{3\cos^2\psi - 1}{d^3}\right|. \tag{40}$$

We define the square root $S^{1/2}$ with the absolute value because while the term $3\cos^2\psi - 1$ may be negative, the QS is positive by definition.

If each anion in the octahedron has a charge of eq, then

$$e^2q^2S = \sum_{i=1}^{5} U_i^2 = \tfrac{1}{4}\left(V_{lat}^*\right)^2 \tag{41}$$

(Czjzek et al. 1981), where the U_i are the EFG tensor components defined in equation 12 and V_{lat}^* is the lattice contribution to the QS (see below). For the general case of an octahedron where each anion has a different charge, eq_i, then equation 40 still holds if q and S are defined such that

$$q^2S \equiv \sum_{i=1}^{6}\frac{q_i^2}{d_i^6} + \sum_{i=1}^{6}\sum_{j<i}\frac{q_iq_j}{d_i^3d_j^3}\left(3\cos^2\theta_{ij} - 1\right). \tag{39'}$$

We will assume that all anions have the same charge and use the first equation 39.

The QS may be divided into contributions from the anisotropy of the Fe valence electrons (see equation 19), V_{val}^*, and the lattice of neighbouring charges, V_{lat}^*. From Ingalls (1964),

$$V^* = (1-R)V_{val}^* + (1-\gamma_\infty)V_{lat}^* \tag{42}$$

where R and γ_∞ are Sternheimer shielding factors (Lauer et al. 1979). From equations 41 and 42,

$$V^* = V_0^* + aS^{1/2} \tag{43}$$

where $a = 2(1-\gamma_\infty)e|q|$, and $V_0^* = (1-R)V_{val}^*$.

In figure 51 we plot QS versus $S^{1/2}$ for the {⊥, ψ, 2.11 Å} simulations and [⊥, ψ, d] curves in figure 50. The factor $S^{1/2}$ is calculated from equation 39, in mm/s. Part A of figure shows the QS at 0 K. There is strong correlation between the two parameters, much stronger than with the mean cluster bond length or flattening angle. There is complete overlap between the {⊥, 58°, 2.11 Å} and {⊥, 54.74°, 2.11 Å} simulations at σ = 0.175 Å (black circles and crosses, respectively). Linear fits of the two σ = 0.175 Å

simulations with equation 43 give a = –0.86(1), V_0^* = 3.87(1) mm/s for {⊥, 58°, 2.11 Å}, and a = –0.90(2), V_0^* = 3.93(1) mm/s for {⊥, 54.74°, 2.11 Å}.

Using equation 40 for S as a function of ψ and d, the QS versus ψ curve for the [⊥, ψ, 2.11 Å] clusters (solid yellow line) and the QS versus d for the [⊥, 58°, d] clusters (dashed yellow line) are also shown in figure 51. Since equation 40 gives S = 0 for an unflattened octahedron regardless of d, the QS versus d curve for the [⊥, 58°, d] cluster would be the vertical line through $S^{1/2}$ = 0. The [⊥, ψ, 2.11 Å] curve has a kink at ψ = 0, and the curve changes direction due to the absolute value taken in equation 40. The σ = 0.025 Å {⊥, 58°, 2.11 Å} simulation is centred at the intersection of the [⊥, ψ, 2.11 Å] and [⊥, 58°, d] curves, as expected, but the points tend to follow the former more than the latter. The σ = 0.025 Å {⊥, 54.74°, 2.11 Å} simulation is bound within the kink formed by the [⊥, ψ, 2.11 Å] curve.

Part B of figure 51 shows the 300 K QS data corresponding to part A. All {⊥, ψ, 2.11 Å} simulations are bound both above and on the left by the QS versus ψ curve for the [⊥, ψ, 2.11 Å] clusters. The correlation between QS and $S^{1/2}$ is less clear at 300 K, although the combined σ = 0.175 Å scatter plots do appear to follow a similar shape as the [⊥, ψ, 2.11 Å] curve.

Temperature factor for quadrupole splitting

In figures 50 and 51, the maximum QS value of 3.2 mm/s for the flattened octahedron [⊥, ψ, d] at 300 K is an overall QS maximum for all clusters randomly distorted from O_h symmetry. This maximum is responsible for the high edge of the QS distributions at 300 K (c.f. figures 3, 13, and 21). This agrees with previous results on QS as a function of flattening in octahedral clusters (Evans et al. 2005a), where it was found that a maximum in the QS curve is a general feature for $Fe^{2+}O_6$-centred octahedral clusters of all sizes (figure 29), and that the magnitude of this maximum for larger, more realistic clusters (around 2.9 mm/s) agrees well with the QS high edges in experimental QS distributions at room temperature.

The origin of the 300 K maximum lies in the thermal population of the Fe(3d) t_{2g} orbitals (see equations 30 and 32). At T > 0 equation 42 becomes (Ingalls 1964),

$$V^*(T) = F(T)(1-R)V_{val}^* + (1-\gamma_\infty)V_{lat}^* \qquad (44)$$

where

$$F(T)=\frac{\sqrt{(1-C_\Delta)^2+3S_\Delta^2}}{1+2C_\Delta}, \tag{45a}$$

$$C_\Delta=\tfrac{1}{2}[\exp(-\Delta_1/k_BT)+\exp(-\Delta_2/k_BT)], \tag{45b}$$

$$S_\Delta=\tfrac{1}{2}[\exp(-\Delta_1/k_BT)-\exp(-\Delta_2/k_BT)], \tag{45c}$$

and Δ_1 and Δ_2 (see equation 30) are the energy differences between the t_{2g} levels. We shall refer to $F(T)$ as the thermal factor. Subtracting equations 42 and 44, and assuming that the terms $(1-R)V_{val}^*$ and $(1-\gamma_\infty)V_{lat}^*$ themselves are temperature independent,

$$V^*(0)-V^*(T)=[1-F(T)]\times V_0^* \tag{46}$$

using the notation of equation 43. Thus the difference between the QS at 0 and 300 K should be a linear function of F with slope $-V_0^*$ and intercept V_0^*. Figure 44 plots QS(0 K) – QS(300 K) versus F as calculated for various {⊥, ψ, 2.11 Å} simulations and the [⊥, ψ, 2.11 Å] series of flattened octahedra. As predicted, there is a strong linear relation; linear fits to equation 46 are given in table 3. The [⊥, ψ, 2.11 Å] series curve is not quite linear, which could demonstrate a slight dependence of V_0^* on flattening.

It is straight-forward to demonstrate that the maximum in the QS at $T>0$ K is a result of the temperature factor, $F(T)$. We start by making the simplifying assumption that Δ_1 and Δ_2 are both equal to Δ, as is the case for a trigonally distorted octahedron. The temperature factor F is then

$$F(T)=\frac{1-\exp(-\Delta/k_BT)}{1+2\exp(-\Delta/k_BT)}. \tag{47}$$

Ingalls (1964) approximates the lattice component of the QS, $(1-\gamma_\infty)V_{lat}^*$, as proportional to Δ. Since $(1-\gamma_\infty)V_{lat}^*$ is proportional to $S^{1/2}$ (equation 43) and both Δ and S go to zero for an undistorted octahedron, this seems like a reasonable first-order approximation. Equation 44 can then be written

$$V^*=-B\Delta+V_0^*\left(\frac{1-\exp(-\Delta/k_BT)}{1+2\exp(-\Delta/k_BT)}\right) \tag{48}$$

for constants V_0^* (see equation 43) and B, independent of both structure and temperature. The curve described in equation 48 as a function of Δ (see figure 1 in Burbridge et al. 1967) is the same curve which describes the QS as a function of flattening angle (figure 29; see also Evans et al. 2005a and 2005b).

Differentiating equation 48 with respect to Δ and setting the result equal to zero, yields the maximum:

$$\frac{V^*_{max}}{V^*_0} \doteq 1 - \left[1 - \ln\left(\frac{Bk_BT}{3V^*_0}\right)\right]\left(\frac{Bk_BT}{V^*_0}\right) + \frac{2}{3}\left(\frac{Bk_BT}{V^*_0}\right)^2 \qquad (49)$$

As T approaches zero, V^*_{max}/V^*_0 approaches to 1, and $V^*_{max}/V^*_0 < 1$ for $T > 0$. Ingalls (1964) estimates the ratio $V^*_0/B \doteq 1$ eV, whereas at 300 K, $k_BT = 0.025$ eV, giving $V^*_{max}/V^*_0 = 0.86$. This derivation shows that the temperature factor F produces a maximum QS value at finite T, which decreases as T increases. Further, this maximum is of the right magnitude to be that which globally bounds the QS and produces the high edge in the QS distributions at 300 K - since linear fits to figures 51 and 52 give V^*_0 in the range 3.7 to 4.1 mm/s, V^*_{max} is in the range 3.2 to 3.4 mm/s. This is in satisfactory agreement with the observed QS maximum of 3.2 mm/s.

Taking the limit as T goes to zero, the above derivation predicts that $V^*_{max} = V^*_0$ at 0 K. The same result is implied by equation 43 alone. The constant a must be negative, since the lattice and valence components of the QS are always of opposite sign (Ingalls 1964), and V^* and $S^{1/2}$ are both greater than or equal to zero by definition. Therefore for constant V^*_0, the maximum possible value of V^* must occur when $S = 0$ (i.e. when $\psi = 54.74°$) and be equal to $V^*_0 > 0$. The range of estimated V^*_0 from linear fits in figures 51 and 52, 3.7 to 4.1 mm/s, is in good agreement with the observed upper bound to QS at 0 K around 3.9 mm/s.

The above argument breaks down for the QS of the trigonally-symmetric [⊥, ψ, 2.11 Å] cluster as a function of flattening, however. In part A of figure 51, there are values of QS on the [⊥, ψ, 2.11 Å] curve (solid line), for clusters with $\psi < 54.74°$, greater than the QS at the $S^{1/2} = 0$ point corresponding to the cluster [⊥, 54.74°, 2.11 Å]. The reason is that the S calculated (equation 40) does not take into account the positions of the H atoms in the $Fe(OH)_6^{4-}$ cluster. Equation 43, with a and V^*_0 independent of structure, does not really apply, because there are structural contributions to the lattice QS that are not accounted for by the S calculated. Equation 43 applies on average for a general $Fe(OH)_6^{4-}$ octahedron, not a specific restricted subset of $Fe(OH)_6^{4-}$ octahedra, and its assumptions made about the QS and geometric structure of the general octahedron allows the maxima at 0 and 300 K to be understood.

The temperature factor *F(T)* can also be used to understand why some simulations had QS distribution widths that increase monotonically with disorder at 300 K, and others do not. The width of the QS distribution at 300 K behaves differently than that of the other hyperfine parameters. The widths *s*(QS) always increase monotonically with disorder at 0 K, thus we might consider this the "normal" behaviour. However, for other simulations, s(QS) at 300 K increases rapidly to a maximum and then decreases slowly at high σ (see figures 14 and 24). Of the simulations that show this behaviour, we must consider the {∥, 54.74°, 2.11 Å} simulation as unique because of its starting cluster's O_h symmetry. The other simulations that show this behaviour are the {⊥, 54.74°, 2.11 Å} and {∥, 58°, 2.11 Å} simulations, which share the same point group symmetry as the {⊥, 58°, *d*} simulations, whose *s*(QS) at 300 K behave "normally" (see figure 8). The difference is not therefore due to symmetry. However, if we examine QS versus ψ curves for the [⊥, ψ, 2.11 Å] and [∥, ψ, 2.11 Å] clusters in figure 29, we see that the starting clusters of the two "abnormal" simulations correspond to points on their respective flattening curves before the maximum, where the QS is considerably reduced from its 0 K value (i.e. the temperature factor *F(T)* is significantly less than 1). The [⊥, 58°, *d*] cluster, however, lies very close to the maximum of the [⊥, ψ, 2.11 Å] curve, where the curve behaves similarly to the QS versus ψ curve at 0 K (see Evans et al. 2005a). This means that, before one can be sure that the width of the QS distribution for a particular average structure behaves "normally", allowing it to be coupled to the static disorder parameter σ and the widths of the other hyperfine parameter distributions, one should have an idea of how much the QS of the average structure is reduced from the QS at 0 K, an estimate of *F(T)*. This requires electronic structure calculations be performed to interpret the spectrum. If *F(T)* is small, then either the IS or HF width must be used to estimate σ and the QS width cannot be coupled simply to the others, or the spectrum must be measured at a lower temperature.

Dependence of IS and SP on structural parameters

Figure 53 shows scatter plots of the IS versus structural parameters for the{⊥, 58°, 2.11 Å} simulations. Part A shows IS versus average bond length *d*. The σ = 0.175 Å simulation shows a very sharp upper boundary to IS, which increases with *d*. This upper bound does not correspond to the IS versus *d* curve for the series of trigonal octahedra [⊥, 58°, *d*] (yellow line). The σ = 0.025 Å {⊥, 58°, 2.11 Å}

simulation follows the [⊥, 58°, *d*] curve to some extent, and shares the same upper bound as the high disorder simulation.

Part B shows that IS versus flattening angle for the {⊥, 58°, 2.11 Å} simulations and the series of clusters [⊥, ψ, 2.11 Å] with varying ψ. There is no apparent correlation between ψ and IS for either low (σ = 0.025 Å) or high (0.175 Å) static disorder. Part C shows IS versus the square root of the geometric structural factor $S^{1/2}$. There is a slight negative correlation between IS and $S^{1/2}$, but the relation is not as strong as between the QS and $S^{1/2}$, or between IS and the bond length. The {⊥, 58°, 2.11 Å} simulations follow neither the [⊥, ψ, 2.11 Å] or [⊥, 58°, *d*] curves.

Let us define a bond-length-only structural factor,

$$S_{BL} = \sum_{i=1}^{6} \frac{1}{d_i^6}, \tag{50}$$

which is the first term of the overall QS structural factor defined in equation 39. The IS for {⊥, 58°, 2.11 Å} simulations is plotted versus S_{BL} in part D of figure 53, and there is a very strong correlation between the two parameters. Points fall in a narrow band following a well-defined curve even at high disorder, which distinct from the IS versus *d* curve of the [⊥, 58°, *d*] clusters (solid line). The dependence of IS on S_{BL} and of QS on $S^{1/2}$, and the strong connection between the two structural factors, is possibly a structural origin for the correlation between QS and IS.

Figure 54 shows SP for the {⊥, 58°, 2.11 Å} simulations plotted against the same four structural parameters (*d*, ψ, $S^{1/2}$ and S_{BL}) as in figure 53 for the IS. As with the IS, there is little or no correlation between the SP and either the mean cluster flattening angle ψ (part B) or the EFG structure factor $S^{1/2}$ (part C). There is a significant positive linear correlation between SP and the mean cluster bond length *d* (part A). The {⊥, 58°, 2.11 Å} simulations follow the SP versus *d* curve of the [⊥, 58°, *d*] clusters (solid line) closely. There is also a strong negative non-linear correlation between SP and S_{BL} (part D). There is a sharp lower bound to the scatter of the σ = 0.175 Å simulation, different from the [⊥, 58°, *d*] curve. The correlation between SP and S_{BL} is not as dramatic as between IS and S_{BL}. The SP versus S_{BL} scatter graph for the σ = 0.175 Å simulation has a very similar shape, including the sharp lower bound, to the SP versus IS scatter graphs at σ = 0.175 Å (see figures 32-34), which is a natural consequence of the strong correlation between IS and S_{BL}.

Fitting simulated spectra

Fitting Mössbauer spectra is very difficult, even when the underlying distributions are known. This is because of the uniqueness problem in inverting the integral in equation 8; relying only on a goodness of fit may result in a set of hyperfine parameter distributions that fit the spectrum as well as desired, but are quite different from the actual distributions in the sample. The non-linear nature of the fitting problem makes the situation even worse, as it is often difficult to coax a fitting routine, however advanced, away from a local minimum in goodness-of-fit which gives clearly unphysical results.

The shapes of the hyperfine parameter distributions shown here (summarized in figures 21 and 23) are in general easily represented as the sums of small numbers of Gaussian components. The IS and QS distributions generally require two or three Gaussian components, while the SP can be represented by just one.

We attempted to fit several simulated spectra with the VBF (Rancourt and Ping 1991) and xVBF (Lagarec and Rancourt 1998, 1999) methods as implemented in the software Recoil. The spectra were modified from those calculated using equation 33 by adding simulated noise:

$$Y_{noise}(v) = Y(v) + \lambda(Y(v)) \tag{51}$$

where $\lambda(Y(v))$ is a random number drawn from a Gaussian distribution with a mean of zero and a standard deviation of $[Y(v)]^{1/2}$.

The most successful fits were obtained for the {⊥, 58°, 2.11 Å} simulation with $\sigma = 0.100$ Å at 300 K. The resulting QS and IS distributions are shown in figure 55. In the VBF method, the QS distribution is represented as a sum of Gaussian components, with the IS linearly dependent on the QS as in equation 9. The best fit was obtained using three Gaussian components for the QS distribution (solid line, part A). The fitted distribution approximates the low QS tail and the high QS edge well, but not the peak itself. The IS distribution (solid line, part B) is too narrow compared with the actual distribution. This is a common feature of IS distributions in the VBF method. Adding additional Gaussian components to the QS distribution did not improve the fit.

The xVBF method represents both QS and IS distributions independently with sums of Gaussians, with a correlation between the two parameter distributions (equation 11). There was a considerably degree of trade-off between the QS and IS distributions in fitting. The distributions due to two fits, both with

equally good fits (reduced $\chi^2 < 1$), are shown in figure 55, representing the IS distribution with one Gaussian and the QS distribution with two. The first (dashed line) approximates both distributions well, but the second (dotted line) has an IS distribution that is far too wide, and a QS distribution that is too narrow except for a very wide foot. Adding more components to either distribution does not improve the fit, but increases the chance of very unphysical distributions (e.g. a single extremely tall, narrow peak superimposed on a wider distribution).

One way to narrow down the number of possible fits would be to restrict distribution parameters to follow one of the curves relating widths of QS and IS distributions in figure 36, or ratios of width to mean as in figure 35. Such constraints could eliminate many unphysical distributions.

Conclusions

We have simulated hyperfine parameter distributions in materials with structural disorder by generating ensembles of $Fe(OH)_6^{4-}$ octahedra perturbed from the average structure by adding Gaussian-distributed random distortions and performing electronic structure calculations on each perturbed cluster to calculate the hyperfine parameters.

The quadrupole splitting distribution of octahedral Fe^{2+} has a characteristic shape. It is skewed prominently to the right, with a tail at low QS and a sharp high QS edge. The high edge is a relatively constant feature, occurring around 3.0 mm/s in room temperature measurements. Our simulated QS distributions have exactly this shape, also with a high edge that occurs around 3.2 mm/s regardless of the initial cluster geometry. We have shown that this high edge is due to the existence of an upper bound to the quadrupole splitting, which at 300 K corresponds to the maximum in the curve of the QS of a flattened octahedron as a function of the flattening angle (Evans et al. 2005a), which is an effect caused by the thermal population of the Fe(3d) orbitals. We find this is a universal feature of all Fe^{2+} QS distributions that are wide enough to extend to 3.2 mm/s.

We have found that for most hyperfine parameters – i.e. the IS, SP and the QS at 0 K – the distribution width increases as a function of the static disorder parameter σ. We obtained curves of distribution width as functions of σ by first choosing σ and performing the simulation to obtain the distribution width; but these same relations can be used to estimate the amount of static disorder in a mineral when the width of one or more of the hyperfine distributions is accurately known. This turns

Mössbauer spectroscopy into a powerful tool for measuring the static disorder present in a mineral. X-ray diffraction can also measure the disorder in a sample, but because of the characteristic time-scale of the measurement, it cannot distinguish between static and thermal disorder. The characteristic time-scale of a Mössbauer spectroscopy measurement, however, is such that the measurement sees the thermally averaged position of atoms in the sample, and so the disorder reflected in the width of hyperfine parameter distributions is static disorder only.

Additionally, we have found that the widths of these distributions (IS, SP and QS at 0 K) are relatively universal functions of one another so that, knowing the width of one distribution, the widths of the others are constrained.

Correlations between the hyperfine parameters are very complex (figures 31-34 and 46). No simple functional relationships exist between them. Even simple correlations like that between multi-component Gaussians as in the xVBF method in equation 11 are not adequate descriptions. The correlations predicted by equation 11 give QS versus IS scatter plots in the shape of ellipses. But in figures 31-34 we see that the QS versus IS scatter plot at high σ has a comet-like shape, which is probably a significant factor in the difficulty of fitting the simulated spectra with the xVBF method, while the SP versus IS scatter plot is a non-linear shape with a sharply defined lower edge. No current fitting models of hyperfine parameter correlations can adequately explain these graphs. It is possible to fit experimental spectra with current fitting models and obtain a good fit, but goodness of fit is necessary but not sufficient condition for accurate hyperfine parameter distributions.

We observe, however, that at low σ, the correlation between QS and IS is small, and between IS and SP is elliptical. The IS distribution at low σ is approximately Gaussian. In the limit of low disorder, the xVBF method provides a good approximation. The QS-IS correlation increases with σ, however, and the IS distribution begins to take on a shape similar to that of the QS. The SP distribution, we find, has a near-Gaussian shape at all values of σ.

The SP has been shown to have a very wide distribution. The width to mean ratio for the SP distribution is very large compared to that of the QS and IS. The SP distribution, due entirely to local structural disorder, is sufficient to explain the line widths in the magnetic Mössbauer spectrum, without resorting to inter-moment coupling. This is assuming that the HF is due entirely to the SP. Of course, as we have emphasised, different distributions may give rise to the same Mössbauer spectrum, but our results

imply that the role of local structural disorder in magnetic Mössbauer spectra must be reconsidered.

A disordered material, regardless of the point group symmetry of the average Fe^{2+} site, will in general have populations of EFG tensors with both positive and negative V_{zz}, and as disorder increases, the positive sign begins to dominate. The sign of the principal value V_{zz} is correlated to both the asymmetry parameter η and the angle between the principal axis and the z-axis, ϕ. As with correlations between other hyperfine parameters, these correlations are very complex, but in general we find that the negative V_{zz} populations have a low η and the principal axis nearly normal to the xy-plane, while positive V_{zz} populations have a high η and a principal axis within the xy-plane. These EFG tensor parameters can be measured using oriented singled crystal Mössbauer spectroscopy.

We have shown that the Gaussian Isotropic Model and its extensions (Czjzek et al. 1981, Le Caer and Brand 1998), the most mathematically rigorous and most common statistical model of EFG tensor distributions in disordered materials, does not apply to EFG tensor distributions in Fe^{2+}-bearing disordered minerals. Le Caer and Brand (1998) showed that if one assumes that the EFG in a material is the sum of a Gaussian Isotropic component, and a constant anisotropic component, then as disorder increases the Gaussian Isotropic component begins to dominate; the QS and η distributions become the Czjzek QS and η distributions (equations 16 and 15) and the $V_{zz} > 0$ and $V_{zz} < 0$ populations become equal. This is not what happens in our Fe^{2+} EFG distributions; the QS distribution maintains its characteristic shape, and as stated above, the positive V_{zz} population overwhelms the negative population. The η distribution likewise does not evolve into the Czjzek η-distribution, however, the mean and standard deviation of η at sufficiently high σ is close to that for the Czjzek η-distribution. The Czjzek η-distribution is a fair approximation to an unknown η distribution, since the Mössbauer spectrum is fairly insensitive to η. The problem with the Gaussian Isotropic model is that it assumes an isotropic electronic structure for the Fe atom. The lattice component of the EFG, which is dominant for high-spin Fe^{3+} and low-spin Fe^{2+}, may be well described by the Gaussian Isotropic Model, but clearly a different model is needed for the valence component of the EFG, which dominates in high-spin Fe^{2+}.

An exception is when the $Fe(OH)_6^{4-}$ cluster has O_h symmetry, as in the simulation {||, 54.74°, 2.11 Å} (see table 4 for notation). At high temperature, e.g. 300 K, the distribution of the EFG-derived parameters at low σ are described approximately by the Gaussian Isotropic Model. However, as σ

increases, the distributions becomes more characteristic of Fe^{2+}.

In summary, we have found that when atomic positions in an ensemble of $Fe(OH)_6^{4-}$ octahedra are allowed to vary such that their displacements from the average follow a Gaussian distribution with mean-square displacement $3\sigma^2$, the resulting joint hyperfine parameter distribution of (IS, SP, V_{ZZ}, η, ϕ) is considerably more complex than any current theoretical crystal chemical models can account for. We have found important correlations exist between distribution widths and the static disorder parameter, and that the role of local structural disorder in the hyperfine field distribution is more significant than is often believed. Crystal chemical models of disorder and electronic structure calculations need to become more prominent in the process of fitting of Mössbauer spectra, in order to obtain valid fits.

Furthermore, we have investigated some possibilities for improved physical models of hyperfine parameter distributions. The strong correlations between the QS and geometric structural factor S (equation 39), and between the IS and S_{BL} (equation 50), suggest that these geometrical structural factors can be used to construct models of these hyperfine parameter distributions from models of local structural disorder. Secondly, the distinctive patterns that the joint (V_{ZZ}, η) distributions form when plotted in the polar coordinates (R, Θ) (figure 49 and table 2), and the systematic way that they change with disorder, imply an underlying order to the EFG tensor.

There are many possible directions for future work. Tetrahedral and octahedral Fe^{3+} sites occur in many disordered materials, including micas (Bailey 1984), iron oxides and spinels (Cornell and Schwertmann 1997). Simulations of hyperfine parameter distributions using randomly distorted Fe^{3+} octahedra and tetrahedra may help in distinguishing $^{[6]}Fe^{3+}$ and $^{[4]}Fe^{3+}$ sites, which is relevant to questions of whether $^{[4]}Fe^{3+}$ sites occur in nanoparticle hydrous ferric oxide (Cornell and Schwertmann 1997). New algorithms for fitting spectra could be developed which incorporate the observed relationships between the widths of different hyperfine parameter distributions, as well as more realistic correlations between hyperfine parameters. New theoretical models of hyperfine parameter distributions could also be derived from the correlations between the hyperfine parameters and the geometric structural factors S and S_{BL}, and the evolution of the (V_{ZZ}, η) polar plots with increasing disorder (figure 49). Finally, simulations of hyperfine parameter distributions for specific materials where the random distortions applied to the starting cluster are constrained using more realistic crystal chemical models (e.g. for iron oxide nanoparticles, or octahedral sheets in micas that are bound between two tetrahedral sheets) may reveal additional

information about properties of hyperfine parameter distributions and correlations between hyperfine parameters specific to those minerals.

Appendix: Analytic Line-shape for Magnetic Spectra

The analytic line-shape for arbitrary values of the HF and QS was derived by Blaes et al. (1985). These results are summarized here for the case of a powder sample.

Let U_i for i from 1 to 5 be the five linearly independent components of the EFG tensor given in equation 12,

$$U_1 = \tfrac{1}{2}V_{zz},\quad U_2 = \tfrac{1}{\sqrt{3}}V_{xz},\quad U_3 = \tfrac{1}{\sqrt{3}}V_{yz},$$
$$U_4 = \tfrac{1}{\sqrt{3}}V_{xy},\ \text{and}\ U_5 = \tfrac{1}{2\sqrt{3}}\left(V_{xx} - V_{yy}\right), \tag{A1}$$

and define

$$W = U_1^2 - \frac{3}{5}\left(U_5^2 + U_4^2 - U_3^2 - U_2^2\right). \tag{A2}$$

Let V^* be the QS as defined in equation 4. The HF splitting due to field H is given by

$$z = -g_{3/2}\mu_N H\ , \tag{A3}$$

where μ_N is the nuclear magneton and $g_{3/2}$ is the nuclear g-factor of the I = 3/2 excited state of ^{57}Fe. Letting Γ be the Heisenberg elemental Lorentzian line-width (equal to 0.097 mm/s), define the parameters v_{+z} and v_{-z} as

$$v_{\pm z} = v - \delta \pm \frac{1}{2}\left(\frac{g_{1/2}}{g_{3/2}}\right)z\ , \tag{A4}$$

where v is the Doppler velocity, δ is the centre shift (including the IS and the second-order Doppler shift due to thermal atomic vibrations), and $g_{1/2}$ is the nuclear g-factor of the I = 1/2 ground state of ^{57}Fe. (The subscript on $v_{\pm z}$ emphasizes the dependence on z.)

The general magnetic spectrum is given by

$$Y(v) = \left\{\frac{R(v_{+z},z)D_1(v_{+z},z) + I(v_{+z},z)D_2(v_{+z},z)}{[D_1(v_{+z},z)]^2 + [D_2(v_{+z},z)]^2}\right\} + \left\{\frac{R(v_{-z},-z)D_1(v_{-z},-z) + I(v_{-z},-z)D_2(v_{-z},-z)}{[D_1(v_{-z},-z)]^2 + [D_2(v_{-z},-z)]^2}\right\}, \tag{A5}$$

where

$$R(v,z) = -4\Gamma\left[4v^2 + \tfrac{20}{9}zv + A(z) - \tfrac{1}{3}\Gamma^2\right], \tag{A6}$$

$$I(v_{\pm z},z) = \tfrac{32}{3}v^3 + \tfrac{80}{9}zv^2 + 8\left[A(z) - \Gamma^2\right]v + B(z) - \tfrac{20}{9}\Gamma^2 z\ , \tag{A7}$$

$$D_1(v,z) = 8v\left[2v^3 - \left(5z^2 + V^{*2} + 3\Gamma^2\right)v - 8U_1 z^2\right] + C(z), \tag{A8}$$

$$D_2(v,z)=8\Gamma\left[4v^3-\left(5z^2+V^{*2}+\Gamma^2\right)v-4U_1z^2\right], \tag{A9}$$

$$A(z)=-\tfrac{5}{3}z^2+\tfrac{16}{9}U_1z-\tfrac{1}{3}V^{*2}, \tag{A10}$$

$$B(z)=-4z^3-\tfrac{32}{3}U_1z^2+\tfrac{80}{9}W^2z\text{, and} \tag{A11}$$

$$C(z)=9z^4+10\left(\Gamma^2-4W^2\right)z^2+\left(V^{*2}+\Gamma^2\right)^2. \tag{A12}$$

The most general full expansion of equation A5 is a sum of eight Lorentzian lines. For $z = 0$ mm/s, equation A5 reduces to a doublet with quadrupole splitting $\Delta=\frac{1}{2}eQV^*$ (equation 33), and for an identically zero EFG, it reduces to a sextet with line height ratios 3:2:1:1:2:3. In the limit of low V^*, the spectrum is a sextet with a quadrupole shift given by $\varepsilon = eQU_1$.

Table 1. Estimation of the parameter σ from published [6]M-O bond lengths; largest and smallest values are taken from among those cations common in the octahedral sheet of micas, with and without considering vacancies (Vac.). See table 6.6 of Mercier (2003).

	Largest (Å)	Smallest (Å)	σ (Å)
Shannon (1976)	2.197 (Mn^{2+})	1.902 (Al^{3+})	0.085
Weiss et al. (1992)	2.140 (Mn^{2+})	1.919 (Al^{3+})	0.064
	2.210 (Vac.)		0.084
Mercier (2003)	2.126 (Fe^{2+})	1.945 (Al^{3+})	0.052
	2.210 (Vac.)		0.076

Table 2. Relations between EFG tensor elements and the polar coordinate representation of Le Caer and Brand (1998).

	$V_{ZZ} > 0$ $0 \leq \Theta < \pi/2$	$V_{ZZ} < 0$ $\pi/2 \leq \Theta < \pi$
V_{ZZ}	$R\cos\frac{1}{3}\Theta$	$-R\cos\frac{1}{3}(\pi-\Theta)$
V_{YY}	$-R\cos\frac{1}{3}(\pi-\Theta)$	$R\cos\frac{1}{3}\Theta$
V_{XX}	$-R\cos\frac{1}{3}(\pi+\Theta)$	$-R\cos\frac{1}{3}(\pi+\Theta)$
η	$\sqrt{3}\tan\frac{1}{3}\Theta$	$\sqrt{3}\tan\frac{1}{3}(\pi-\Theta)$
$V^* = \lvert V_{ZZ}\rvert\sqrt{1+\eta^2/3}$	R	R
$\cos^{-1}\left[\frac{(1-\eta^2)\times\mathrm{sign}(V_{ZZ})}{(1+\eta^2/3)^{3/2}}\right]$	Θ	Θ
$V_{ZZ}\left[\frac{1-\eta^2}{1+\eta^2/3}\right]$	$X = R\cos\Theta$	$X = R\cos\Theta$
$\sqrt{3}\lvert V_{ZZ}\rvert\left[\frac{\eta(1-\eta^2/9)}{1+\eta^2/3}\right]$	$Y = R\sin\Theta$	$Y = R\sin\Theta$

Table 3. Linear fits of QS(300 K) – QS(0 K) vs. temperature factor *F* in figure 44.

Simulation/Curve	Slope (mm/s)	Intercept (mm/s)	Difference in Magnitude† (%)
{⊥, 54.74°, 2.11 Å} σ = 0.025 Å	- 4.019(3)	3.968(2)	0.11 ± 0.60
{⊥, 54.74°, 2.11 Å} σ = 0.175 Å	- 3.837(13)	3.832(10)	0.25 ± 0.59
{⊥, 58°, 2.11 Å} σ = 0.025 Å	- 3.729(3)	3.719(2)	1.27 ± 0.12
{⊥, 58°, 2.11 Å} σ = 0.175 Å	- 3.767(12)	3.757(11)	0.26 ± 0.14
[⊥, ψ, 2.11 Å] flattening series	- 4.040(21)	4.013(18)	0.68 ± 0.96

†Difference = | Intercept + Slope | / [(Intercept – Slope)/2]

Table 4. List of common symbols and abbreviations

e	electron charge
T	temperature
k_B	Boltzmann constant
g_e	electron g-factor
μ_B	Bohr magneton
Q	^{57}Fe quadrupole moment, 0.16 barns (Dufek et al. 1995)
$\{C, \psi, d\}$	simulation of 1000 octahedra, perturbed from a starting cluster with bond length d, flattening angle ψ, and OH bond angles described by C ($\perp$ or $\parallel$)
$[C, \psi, d]$	unique cluster with bond length d, flattening angle ψ, and OH bond angles described by C ($\perp$ or $\parallel$)
$\langle X \rangle$	ensemble mean of X
$s(X)$	ensemble standard deviation of X
N	number of points in simulation (1000)
$P(X, Y, ...)$	probability density function or distribution of $(X, Y, ...)$
IS, δ	isomer shift
QS, V^*	quadrupole splitting
HF	hyperfine magnetic field
SP, $\Delta\rho$	nuclear electron spin polarization
EFG	electric field gradient
V_{ZZ}	principal value of the electric field gradient (mm/s)
V_{XX}, V_{YY}, V_{ZZ}	electric field gradient eigenvalues, ordered (mm/s)
V_1, V_2, V_3	electric field gradient eigenvalues, unordered (mm/s)
V_{xx}, V_{yy}, V_{zz}, V_{xy}, V_{xz}, V_{yz}	electric field gradient components in $\{x, y, z\}$ coordinates (mm/s)
$\mathbf{V}$	electric field gradient tensor
$U_1, ..., U_5$	linearly independent components of the electric field gradient

	(equation 12)
η	electric field gradient asymmetry parameter
ϕ, θ, ζ	Euler angles of the electric field gradient principal axes; $0° < \phi < 90°$ is the angle between the EFG eigenvector associated with V_{ZZ} and the z-axis
ε	quadrupole shift
$\rho^a_\uparrow(0),\ \rho^a_\downarrow(0)$	spin-up and spin-down electron density at the ^{57}Fe nucleus
H_{ext} , H_{SP}, H_L, H_D, H_{demag}	components of the hyperfine field (equation 6)
v	Doppler velocity
$Y(v)$	Mössbauer spectrum
$L(v \mid \mathbf{h}, \Gamma)$	elemental Mössbauer spectrum
Γ	elemental Lorentzian line-width
$\mathbf{h}$	general set of hyperfine parameters
$n_{3d(x^2-y^2)}, n_{3d(z^2)}, n_{3d(xy)}, n_{3d(xz)}, n_{3d(yz)}$	populations of Fe(3d) orbitals
$n_{4p(x)}, n_{4p(y)}, n_{4p(z)}$	populations of Fe(4p) orbitals
$\lvert i \rangle$	spin-down orbital i, where $i = 1$ is the lowest energy spin-down t_{2g} orbital
n_i	population of spin-down orbital i
E_i	energy of spin-down orbital i
Δ_1, Δ_2	spin-down t_{2g} orbital splittings
Δ	spin-down t_{2g} orbital splitting under trigonal symmetry
σ	static disorder parameter (Å)
σ_H	O-H bond angle disorder parameter (degrees or radians)
MSD	atomic mean-square displacement (Å^2)
d	mean cluster bond-length (Å)
d_i, $i = 1...6$	bond length from Fe to ith O anion (Å)

$\mathbf{d}_i$, $i = 1...6$	vector pointing from Fe to ith O anion
ψ	flattening angle (degrees or radians)
θ_{ij}	angle between bonds $\mathbf{d}_i$ and $\mathbf{d}_j$ (degrees or radians)
q_i	charge of ith anion
q	mean cluster anion charge
$\Delta_T\eta$	$\eta(0\ \mathrm{K}) - \eta(300\ \mathrm{K})$
R	radial variable in EFG polar coordinates (mm/s)
Θ	angular variable in EFG polar coordinates (degrees or radians)
V^*_{val}, V^*_{lat}	valence and lattice EFGs
$(1-R), (1-\gamma_\infty)$	Sternheimer factors
V^*_0	$(1-R)V^*_{val}$ at $T = 0$ K
$F(T)$	QS temperature factor (equation 45)
V^*_{max}	maximum value of the QS
S	QS geometric structural factor (equation 39)
S_{BL}	IS geometric structural factor (equation 50)
a	linear coupling between V^* and $S^{1/2}$ (equation 43)
B	first-order coupling between lattice EFG and the t_{2g} orbital splitting (equation 48)

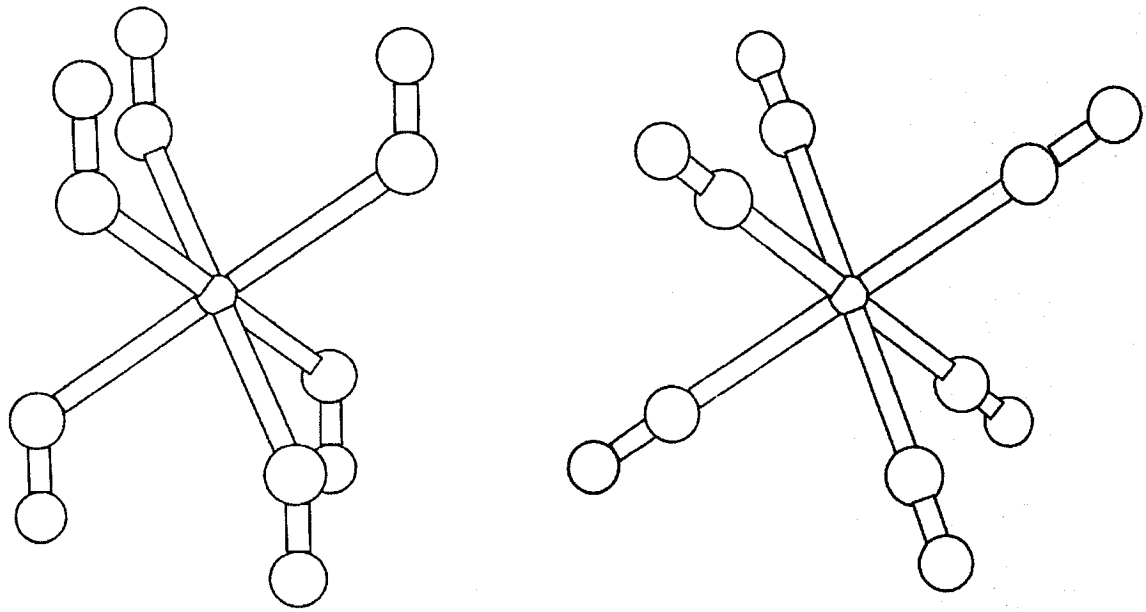

Figure 1. Types of $Fe(OH)_6^{4-}$ clusters. The unique cluster [C, ψ, d] is the starting cluster for the simulation denoted {C, ψ, d}, where $C = \perp$ or ||, ψ is the flattening angle and d is the Fe-O bond length.

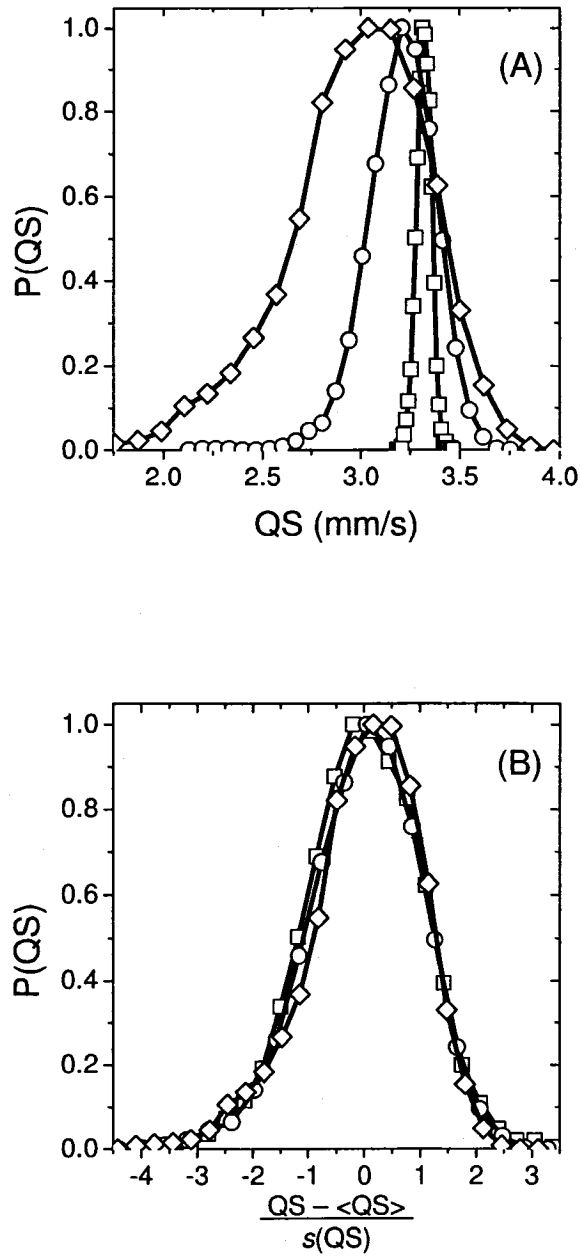

Figure 2. Simulated QS distributions for simulation {⊥, 58°, 2.11 Å} at 0 K, (A) normalized with respect to height, and (B) relative to the mean and normalized with respect to height and width. Squares - $\sigma = 0.025$ Å; circles - $\sigma = 0.100$ Å; diamonds - $\sigma = 0.175$ Å.

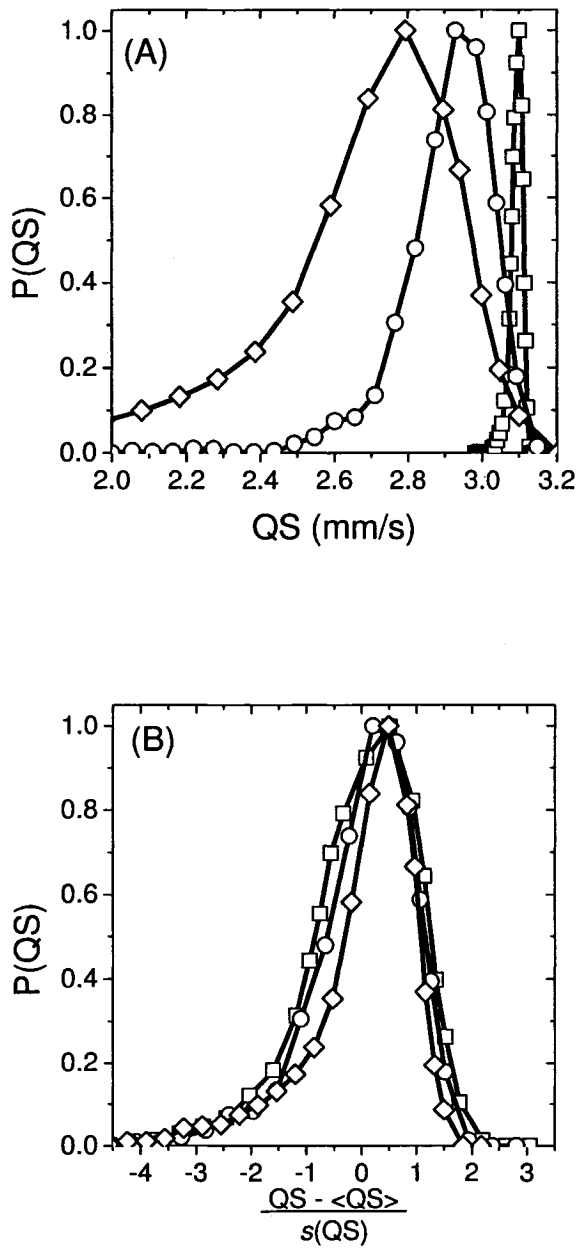

Figure 3. Simulated QS distributions for simulation {⊥, 58°, 2.11 Å} at 300 K, (A) normalized with respect to height, and (B) relative to the mean and normalized with respect to height and width. Squares - σ = 0.025 Å; circles - σ = 0.100 Å; diamonds - σ = 0.175 Å.

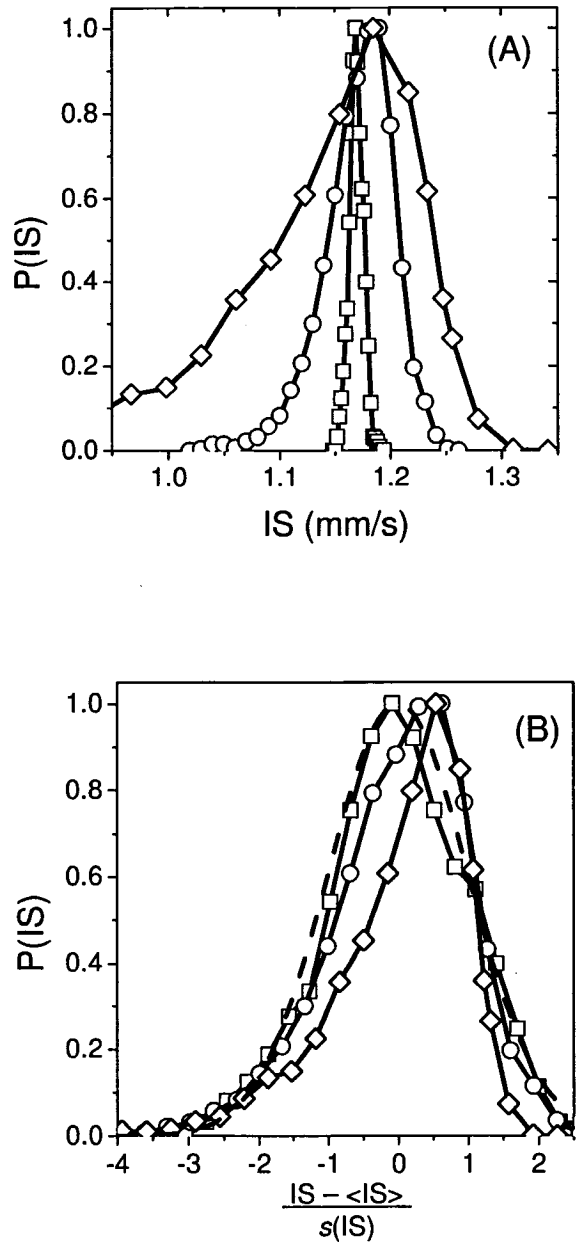

Figure 4. Simulated IS distributions for simulation {⊥, 58°, 2.11 Å}, (A) normalized with respect to height, and (B) relative to the mean and normalized with respect to height and width. Squares - σ = 0.025 Å; circles - σ = 0.100 Å; diamonds - σ = 0.175 Å. A Gaussian curve (dashed line) is shown for comparison in part B.

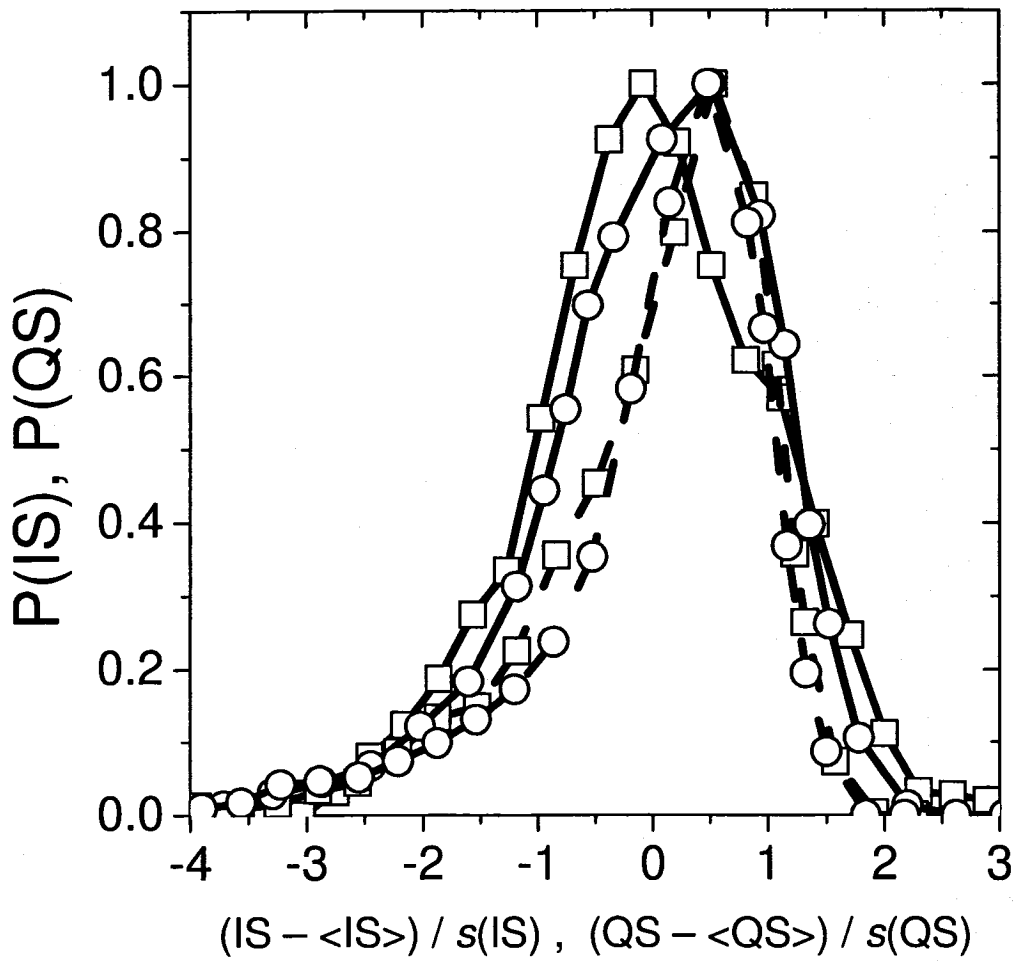

Figure 5. A direct comparison of the shapes of QS and IS distributions, relative to the mean and normalized with respect to height and width, for {⊥, 58°, 2.11 Å}. Squares - IS; circles - QS at 300 K; solid lines - $\sigma = 0.025$ Å; dashed lines - $\sigma = 0.175$ Å.

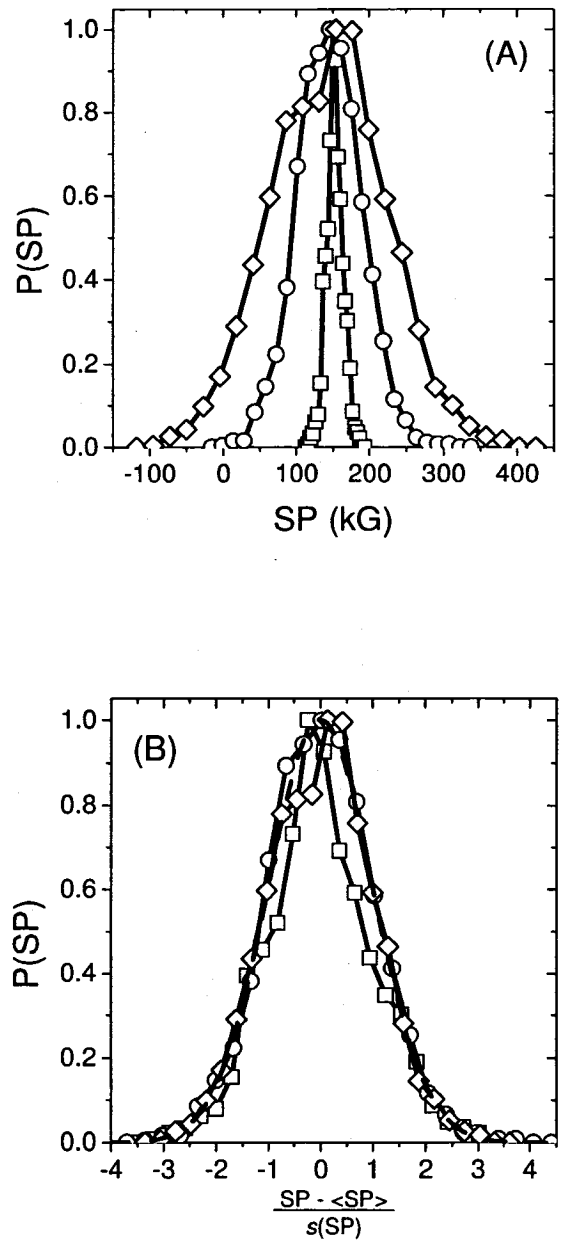

Figure 6. Simulated SP distributions for simulation {⊥, 58°, 2.11 Å}, (A) normalized with respect to height, and (B) relative to the mean and normalized with respect to height and width. Squares - $\sigma = 0.025$ Å; circles - $\sigma = 0.100$ Å; diamonds - $\sigma = 0.175$ Å. A Gaussian curve (dashed line) is shown for comparison in part B.

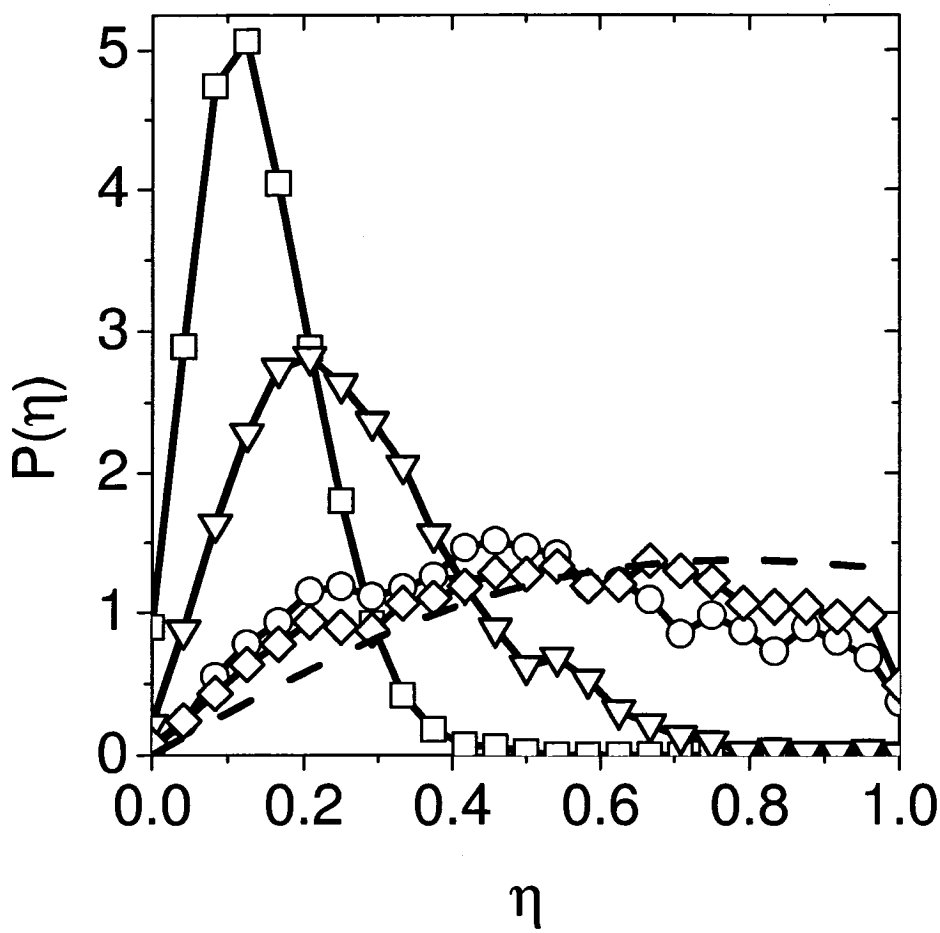

Figure 7. Simulated η distributions normalized with respect to area for {⊥, 58°, 2.11 Å}. Squares - σ = 0.025 Å; downward triangles - σ = 0.050 Å; circles - σ = 0.100 Å; diamonds - σ = 0.175 Å; dashed line - Czjzek η-distribution.

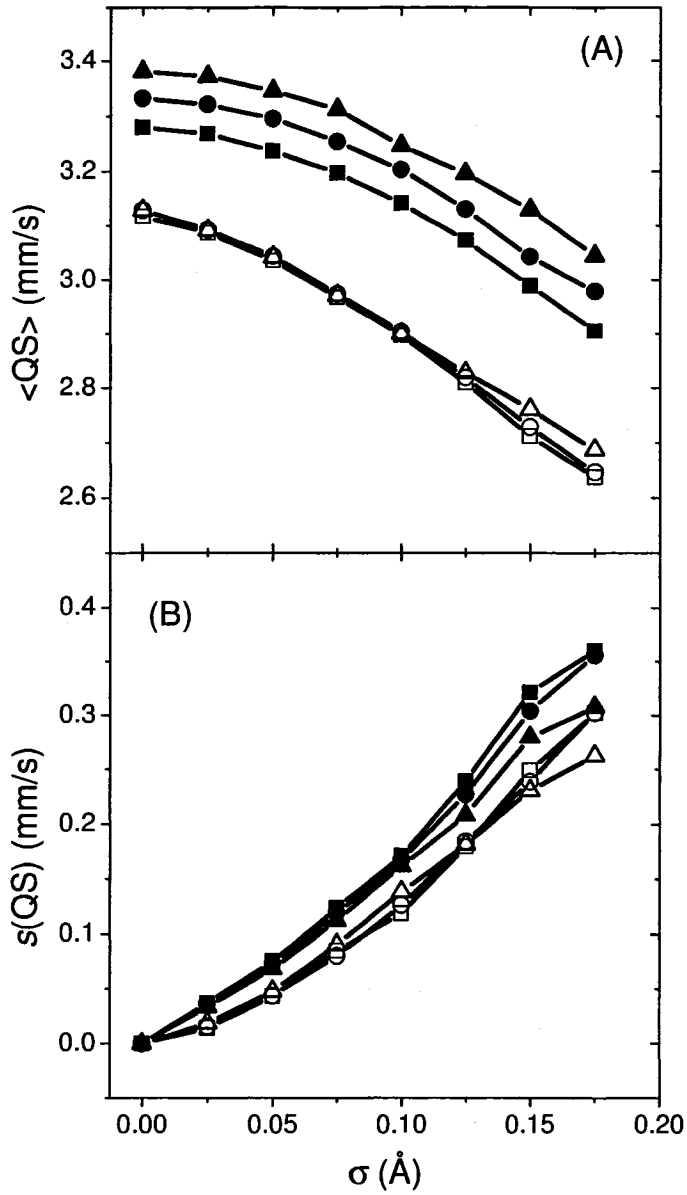

Figure 8. Distribution parameters of QS at 0 K (solid symbols) and 300 K (open symbols) as a function of static disorder for {⊥, 58°, *d*}. (A) Mean <QS> and (B) standard deviation *s*(QS). Squares - *d* = 2.08 Å; circles - *d* = 2.11 Å; triangles - *d* = 2.14 Å.

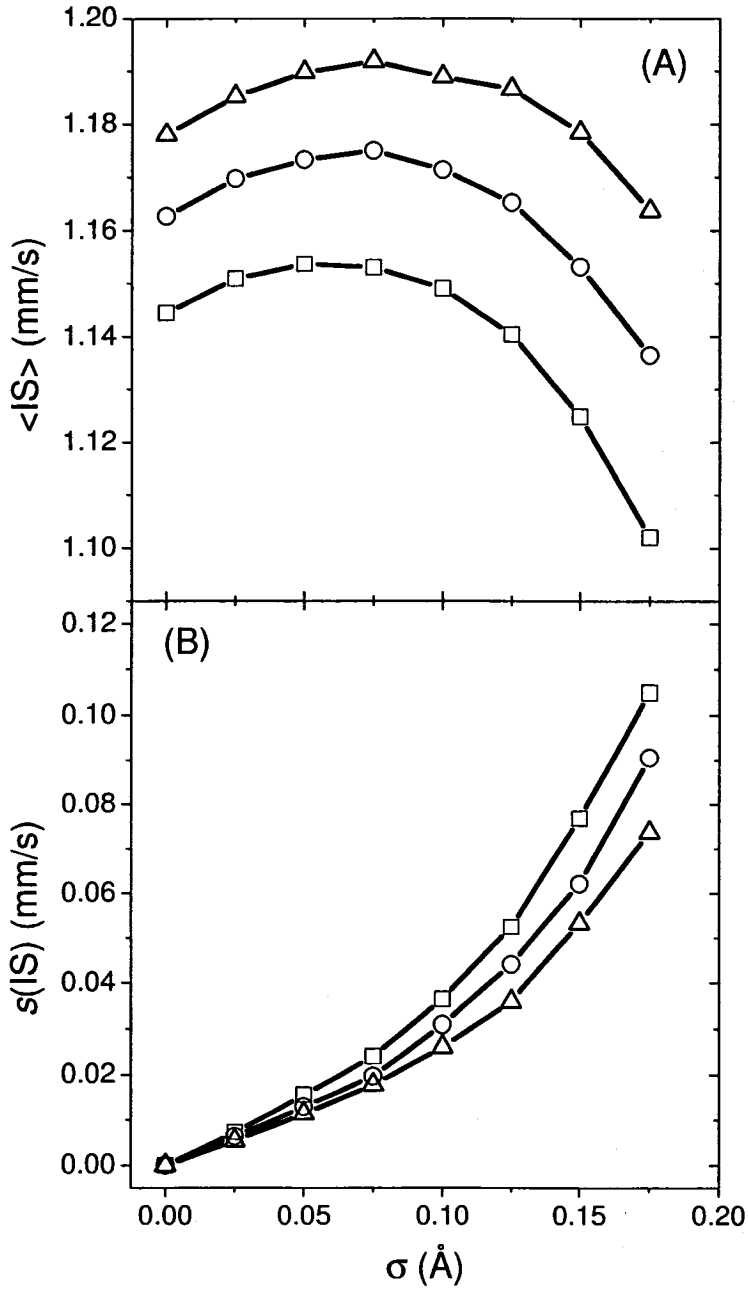

Figure 9. Distribution parameters of IS as a function of static disorder for {⊥, 58°, *d*}. (A) Mean <IS>. (B) Standard deviation *s*(IS). Squares - *d* = 2.08 Å; circles - *d* = 2.11 Å; triangles - *d* = 2.14 Å.

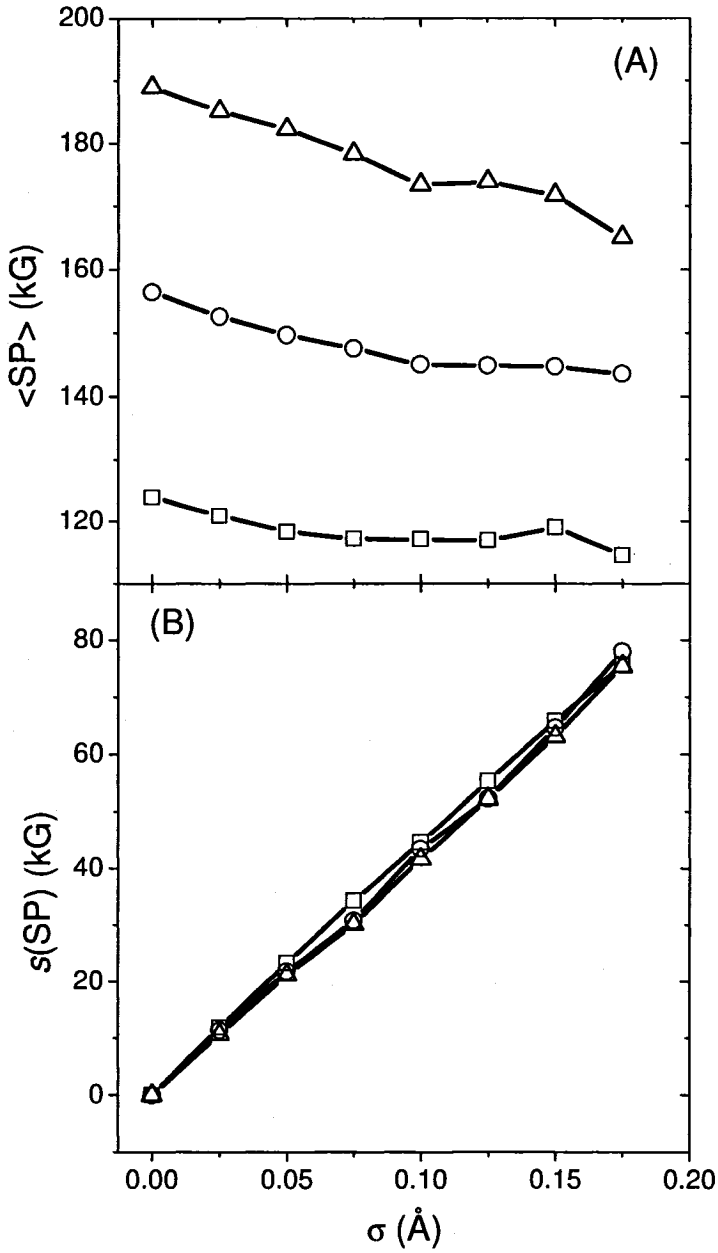

Figure 10. Distribution parameters of SP as a function of static disorder for {⊥, 58°, *d*}. (A) Mean <SP>. (B) Standard deviation *s*(SP). Squares - *d* = 2.08 Å; circles - *d* = 2.11 Å; triangles - *d* = 2.14 Å.

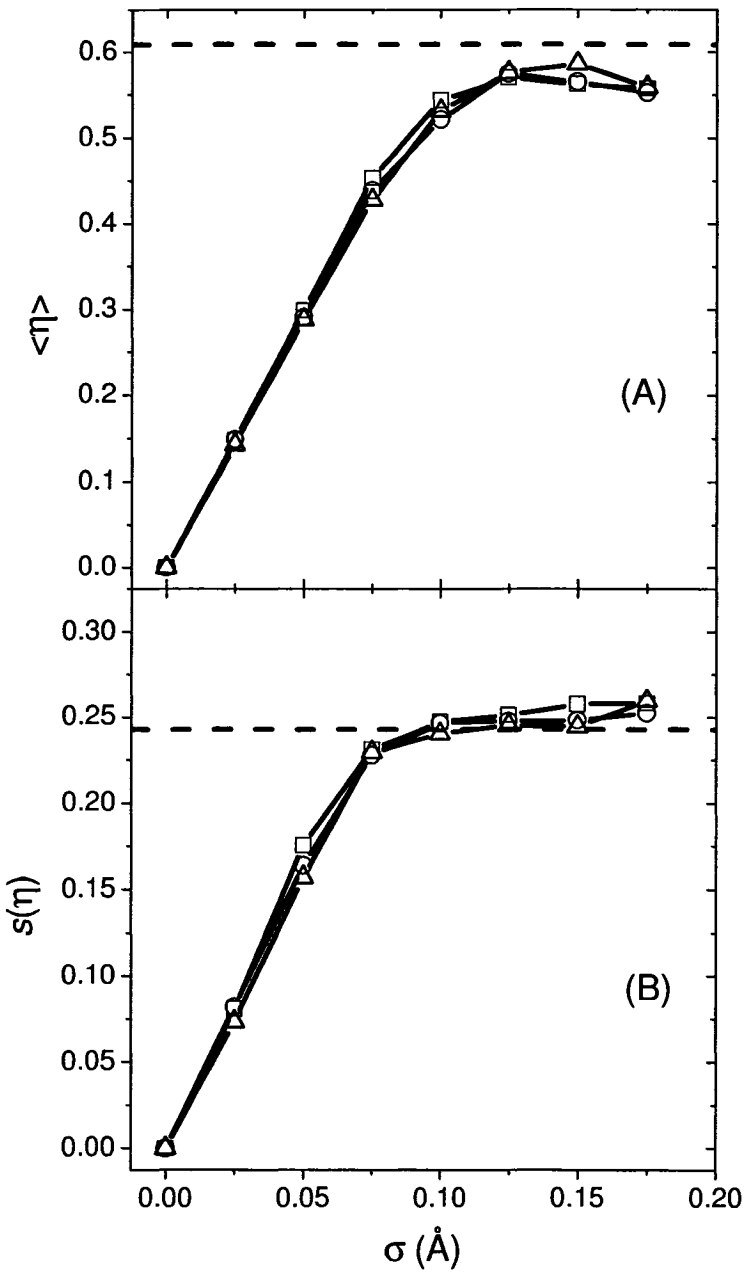

Figure 11. Distribution parameters of η at 300 K as a function of static disorder for {⊥, 58°, *d*}. (A) Mean <η>. (B) Standard deviation *s*(η). Squares - *d* = 2.08 Å; circles - *d* = 2.11 Å; triangles - *d* = 2.14 Å; dashed line - values for the Czjzek η-distribution (equation 15).

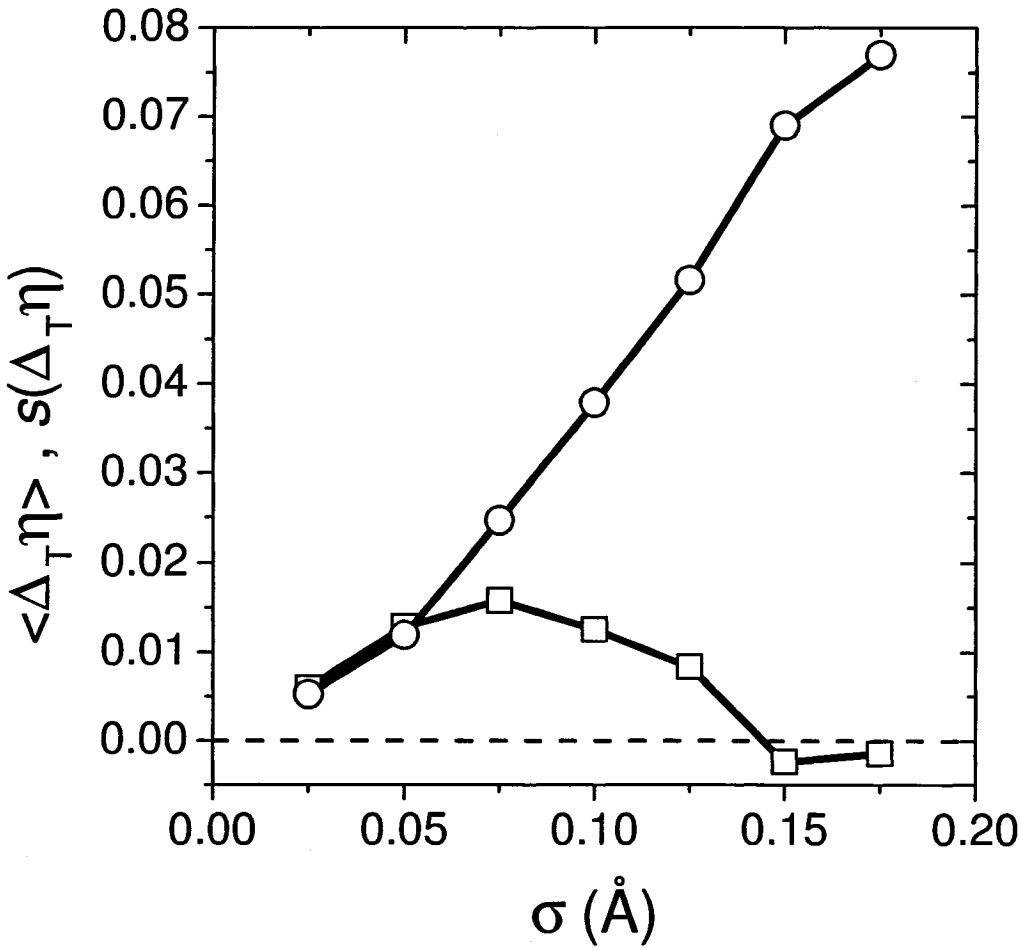

Figure 12. Mean (<$\Delta_T\eta$>, squares) and standard deviation ($s(\Delta_T\eta)$, circles) of the difference between η at 0 K and 300 K, as a function of static disorder, for starting cluster {⊥, 58°, 2.11 Å}. Dashed line - zero.

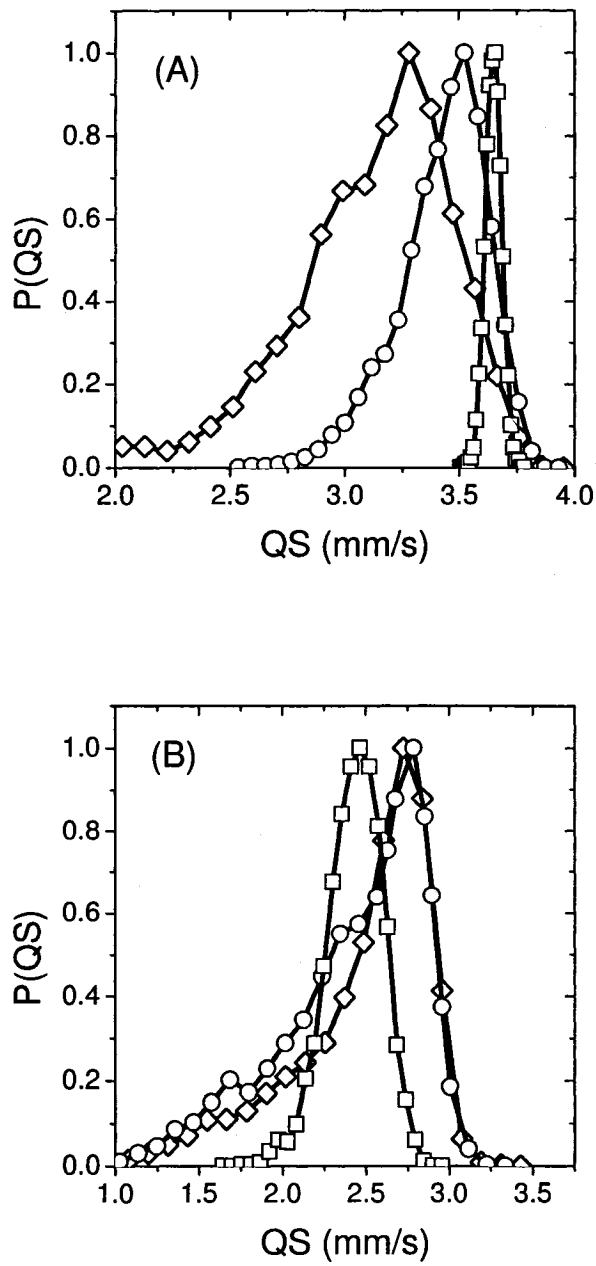

Figure 13. QS distributions at (A) 0 K and (B) 300 K for {⊥, 54.74°, 2.11 Å}, normalized with respect to height. Squares, $\sigma = 0.025$ Å; circles, $\sigma = 0.100$ Å; diamonds, $\sigma = 0.175$ Å.

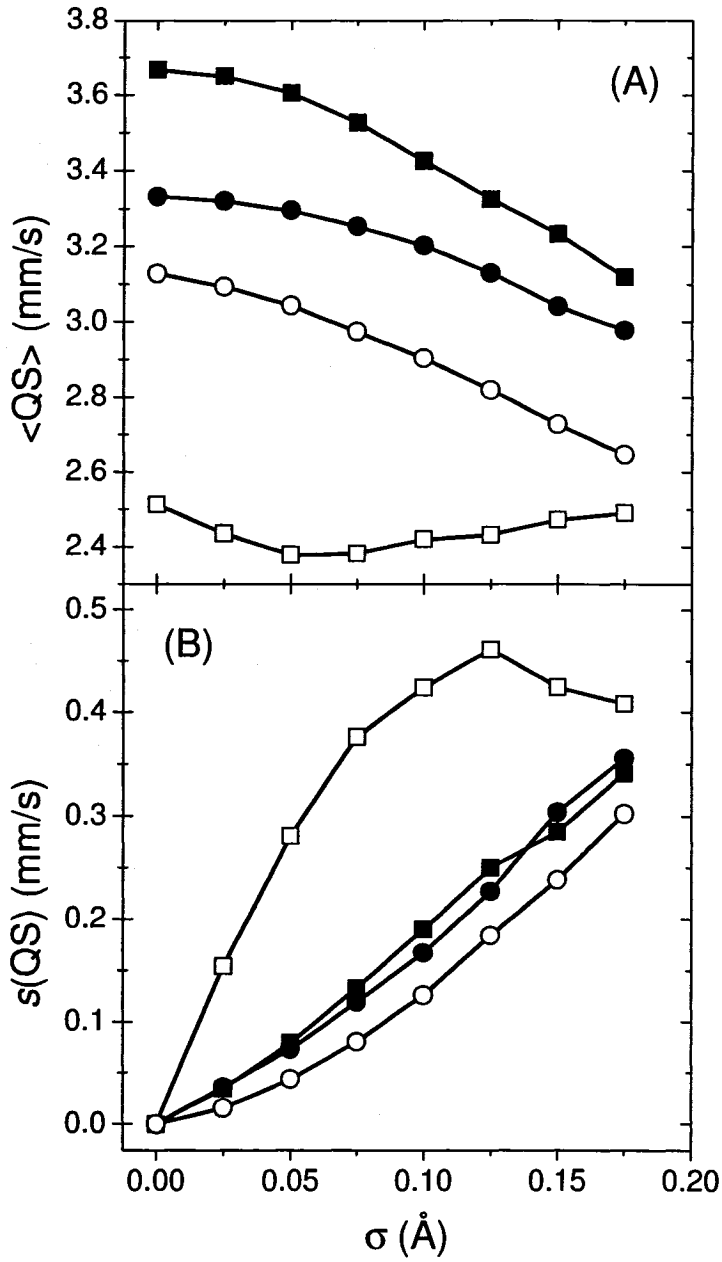

Figure 14. Distribution parameters of QS at 0 K (solid symbols) and 300 K (open symbols) as a function of static disorder for {⊥, ψ, 2.11 Å}. (A) Mean <QS> and (B) standard deviation *s*(QS). Squares, ψ = 54.74°; circles, ψ = 58°.

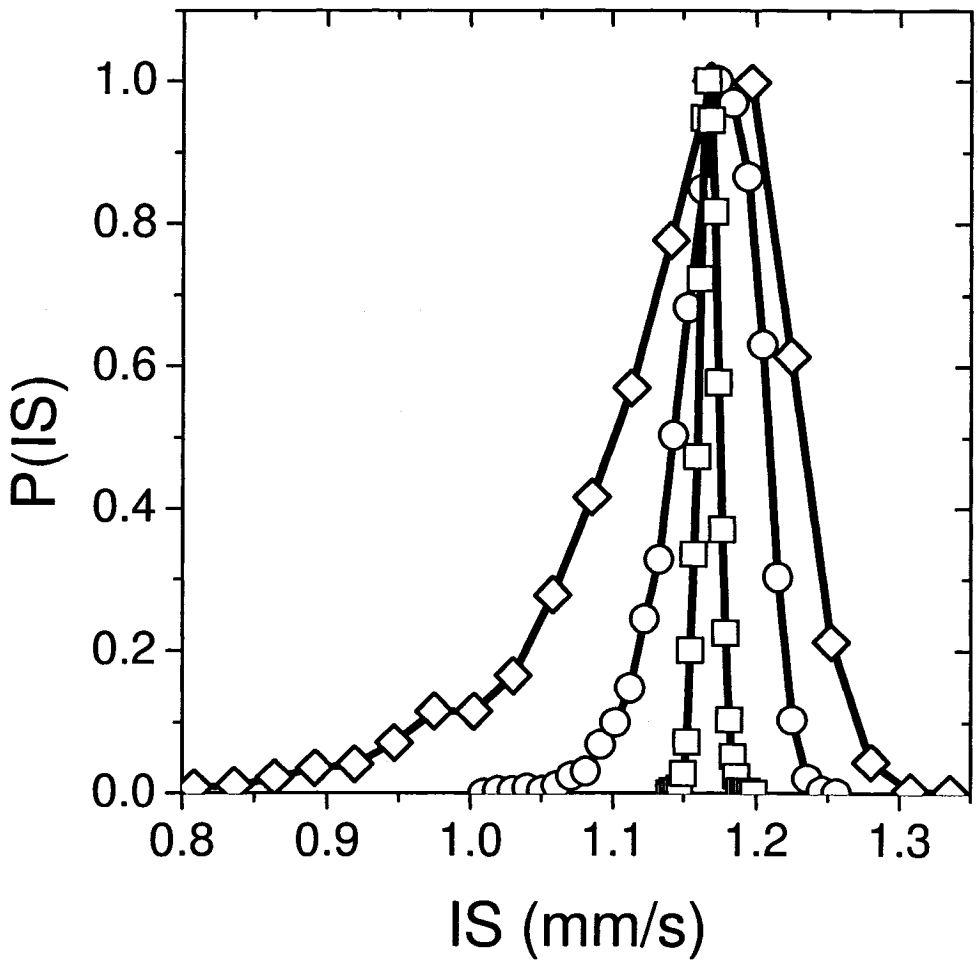

Figure 15. IS distributions for {⊥, 54.74°, 2.11 Å}, normalized with respect to height. Squares, $\sigma = 0.025$ Å; circles, $\sigma = 0.100$ Å; diamonds, $\sigma = 0.175$ Å.

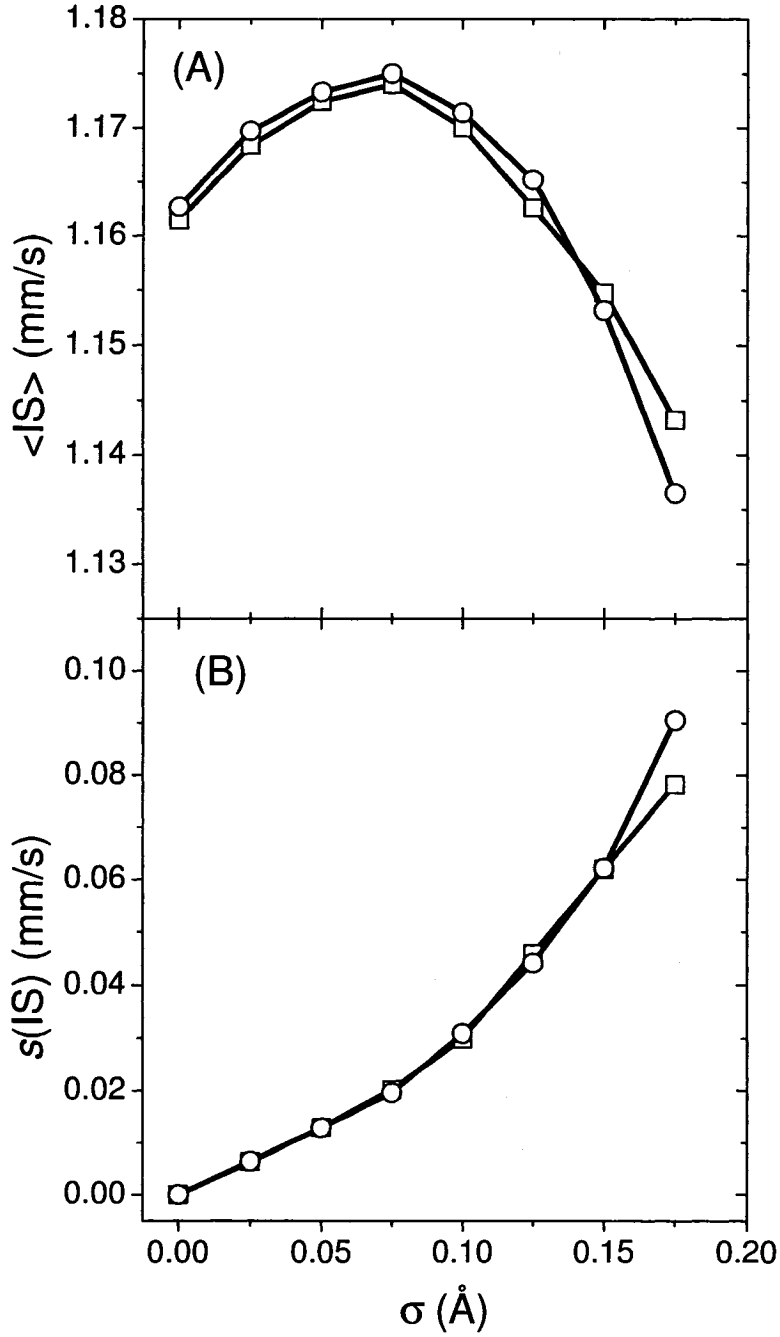

Figure 16. Distribution parameters of IS as a function of static disorder for {⊥, ψ, 2.11 Å}. (A) Mean <IS>. (B) Standard deviation *s*(IS). Squares, ψ = 54.74°; circles, ψ = 58°.

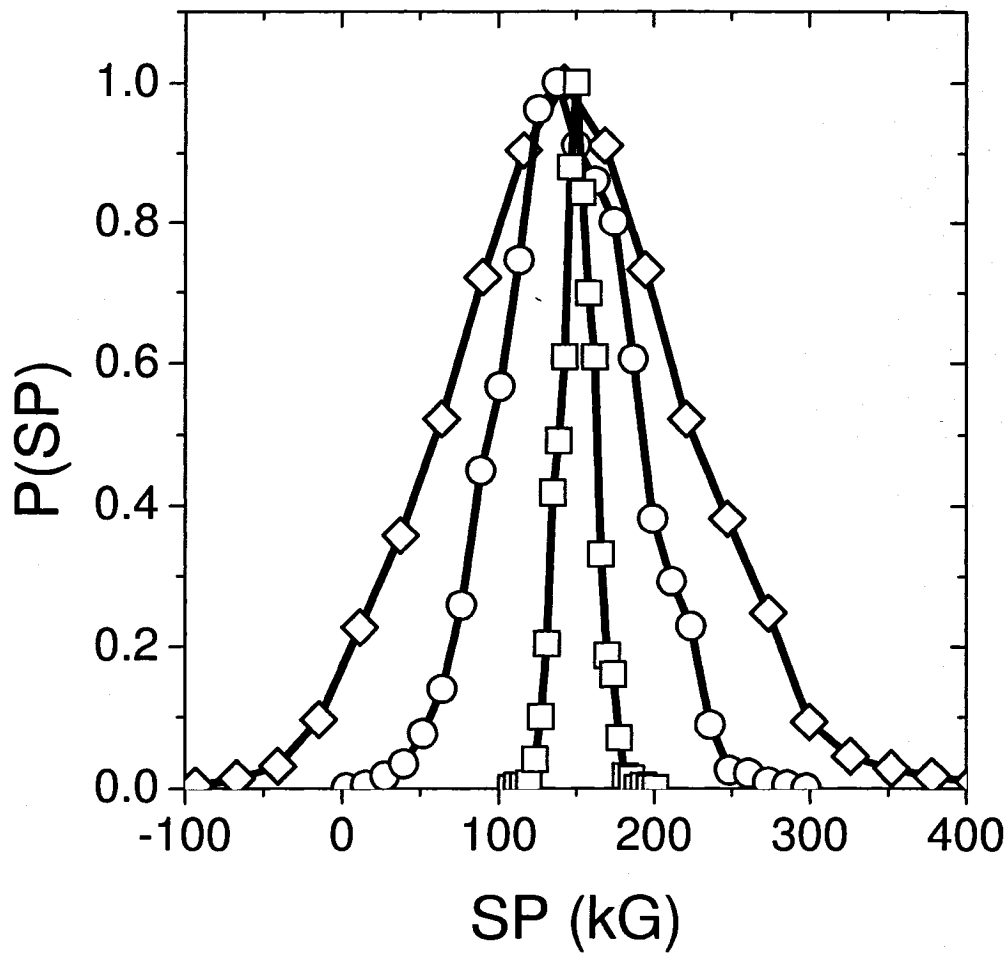

Figure 17. SP distributions for {⊥, 54.74°, 2.11 Å}, normalized with respect to height. Squares, $\sigma = 0.025$ Å; circles, $\sigma = 0.100$ Å; diamonds, $\sigma = 0.175$ Å.

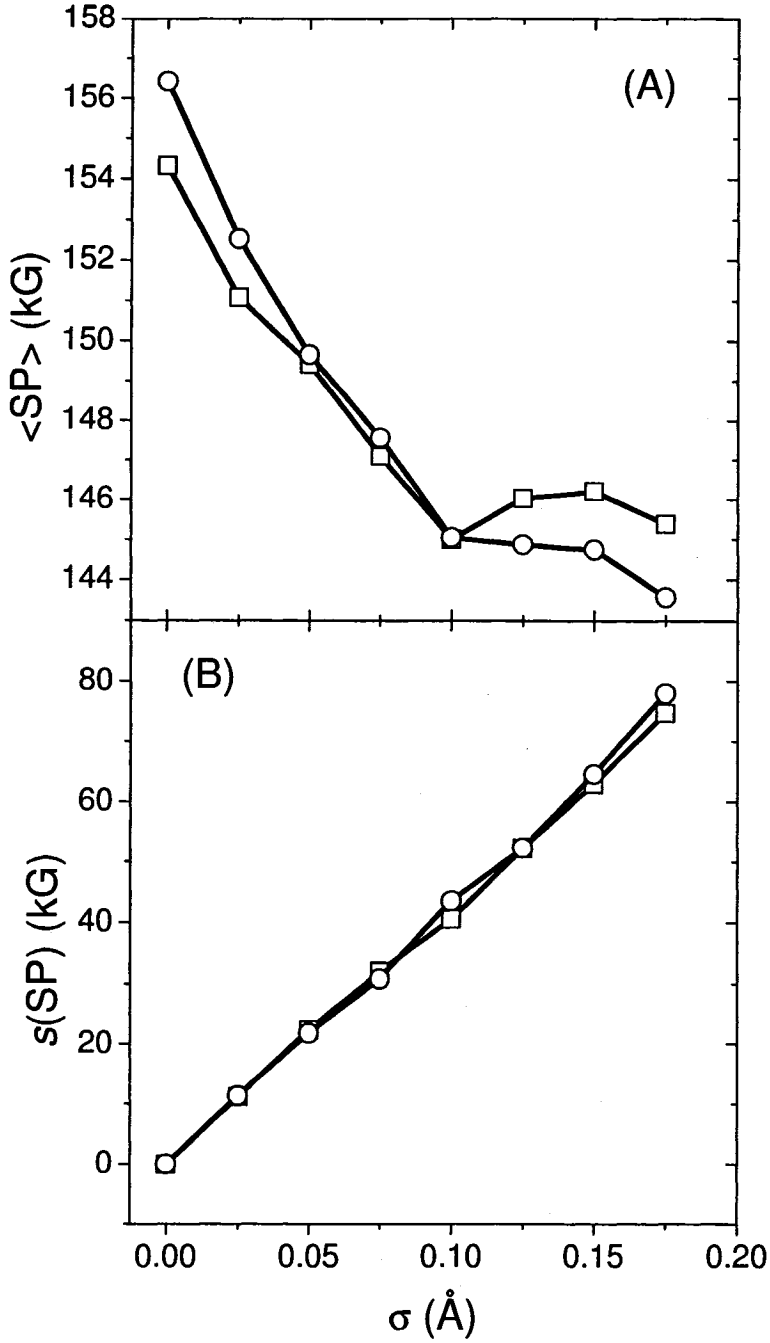

Figure 18. Distribution parameters of SP as a function of static disorder for {⊥, ψ, 2.11 Å}. (A) Mean <SP>. (B) Standard deviation *s*(SP). Squares, ψ = 54.74°; circles, ψ = 58°.

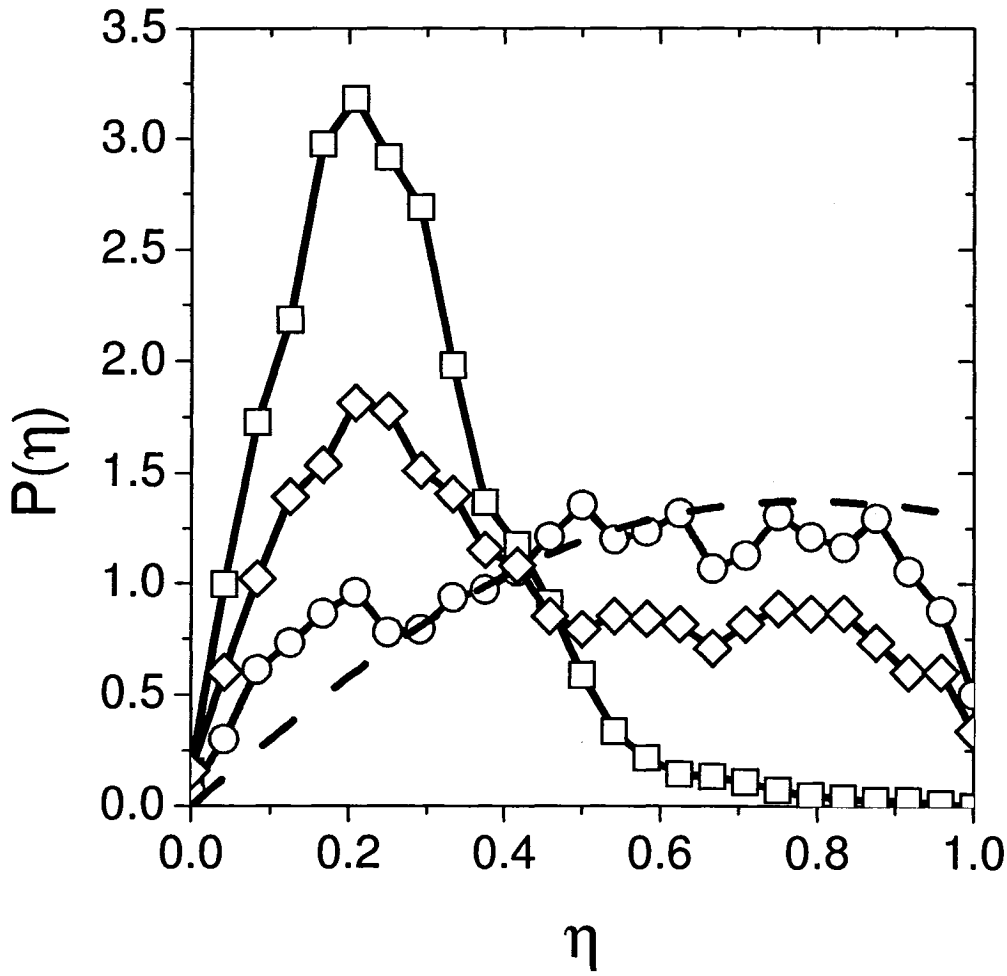

Figure 19. Simulated η distributions normalized with respect to area for {⊥, 54.74°, 2.11 Å}. Squares, σ = 0.025 Å; circles, σ = 0.100 Å; diamonds, σ = 0.175 Å; dashed line - Czjzek η-distribution.

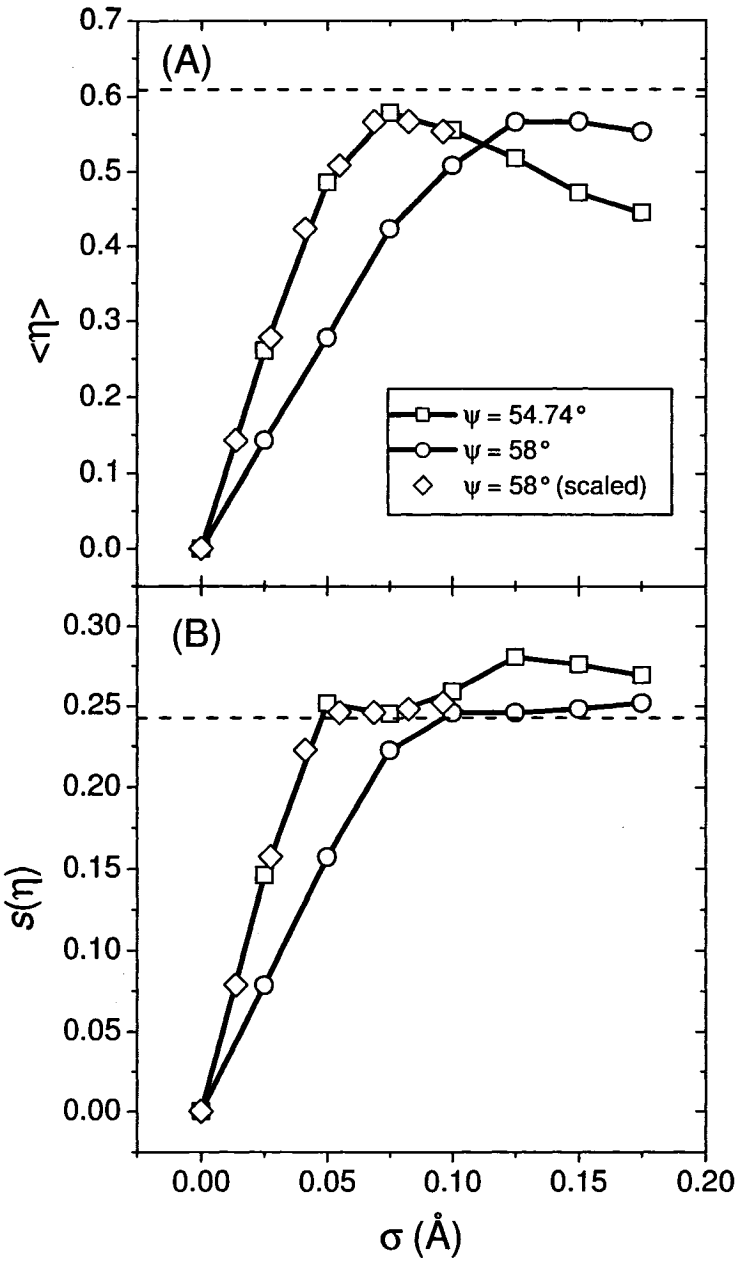

Figure 20. Distribution parameters of η for {⊥, ψ, 2.11 Å} simulations. (A) Mean <η>. (B) Standard deviation $s(\eta)$. Squares, ψ = 54.74° points plotted vs. σ; circles, ψ = 58° points plotted vs. 0.55σ; diamonds, ψ = 58° points plotted vs. 0.55σ; dashed line - values for the Czjzek η-distribution.

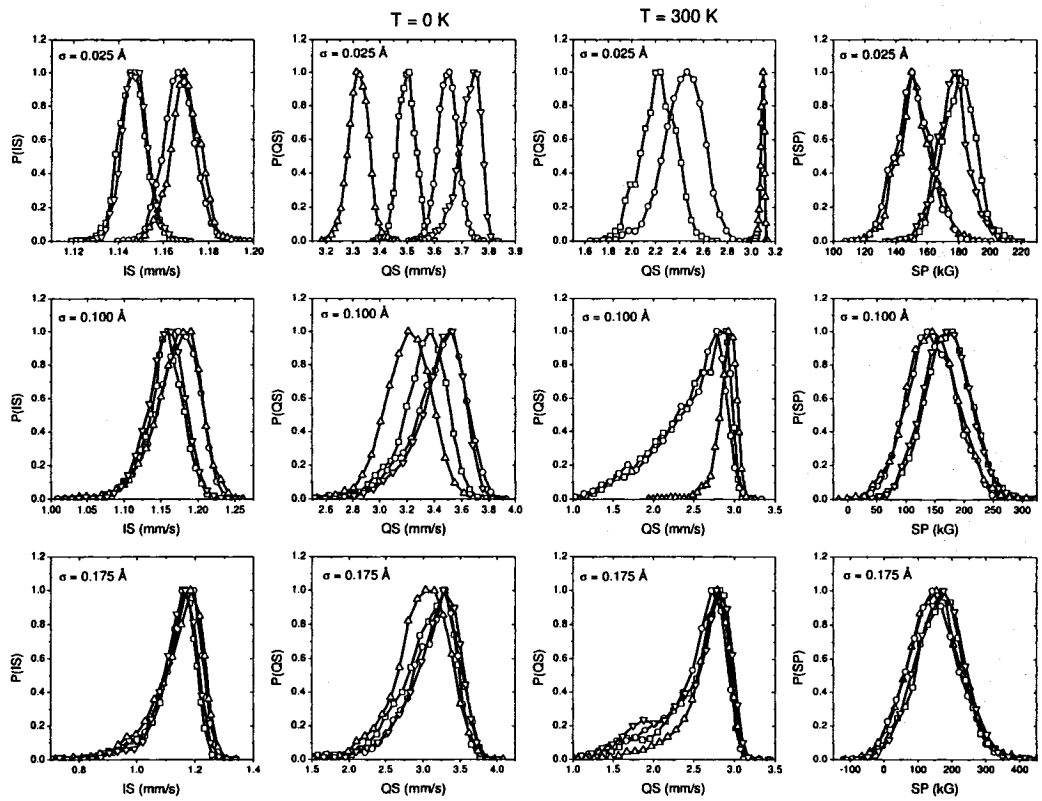

Figure 21. IS, QS (0 K), QS(300K) and SP distributions, normalized with respect to height, for {∥, 54.74°, 2.11 Å} (downward triangles), {∥, ψ = 58°, 2.11 Å} (squares), {⊥, 54.74°, 2.11 Å} (circles), and {⊥, 58°, 2.11 Å} (upward triangles).

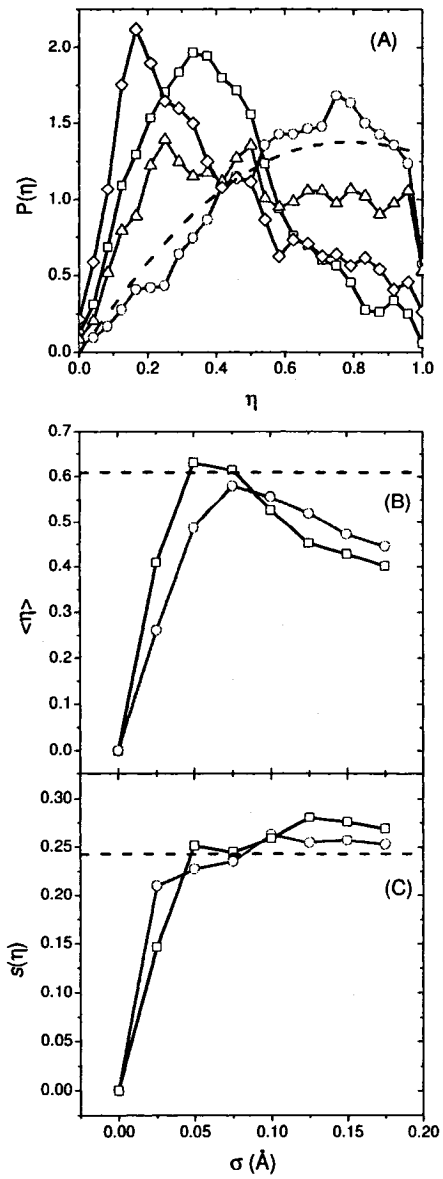

Figure 22. (A) Simulated η distributions normalized with respect to area for {||, 58°, 2.11 Å}. Squares, σ = 0.025 Å; circles, σ = 0.050 Å; diamonds, σ = 0.100 Å; triangles, σ = 0.175 Å; dashed line - Czjzek η-distribution. (B) and (C), mean and standard deviation of η as a function of σ. Squares, {||, 58°, 2.11 Å}; circles, {⊥, 54.74°, 2.11 Å}.

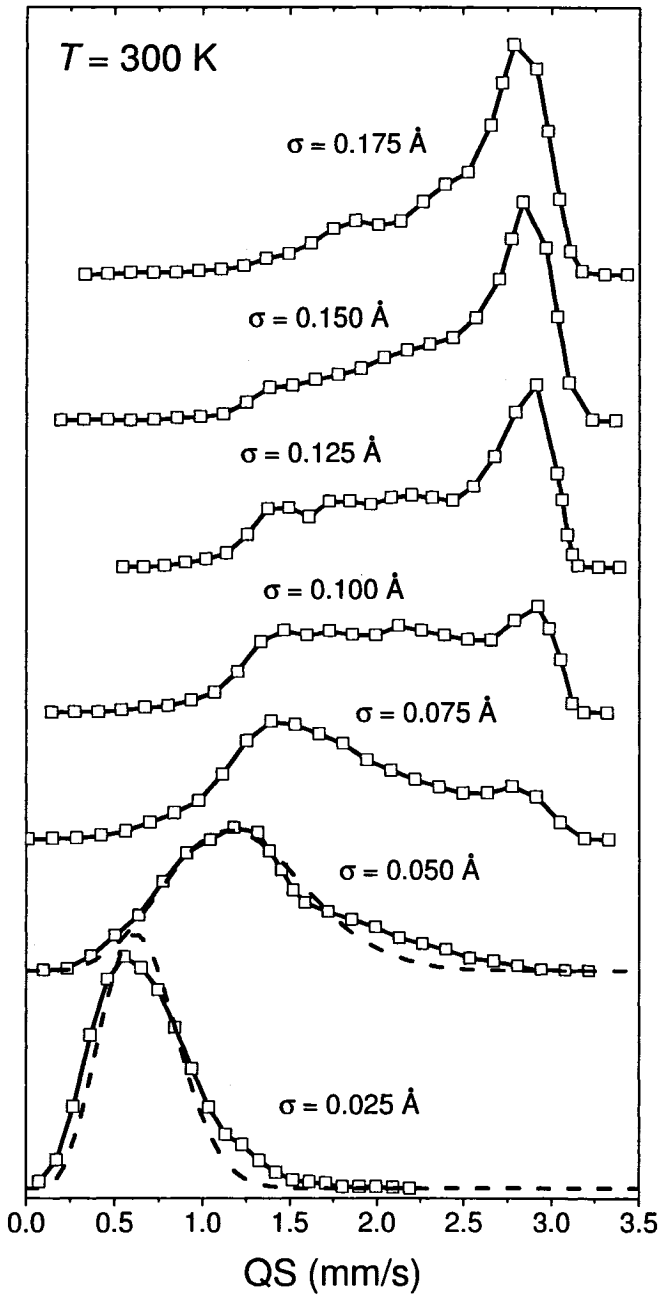

Figure 23. QS distributions normalized with respect to area for cluster {||, 54.74°, 2.11 Å} at 300 K. All distributions are shown to the same vertical scale. Fits with the Czjzek QS distribution are shown for σ = 0.025 Å and 0.050 Å (dashed line).

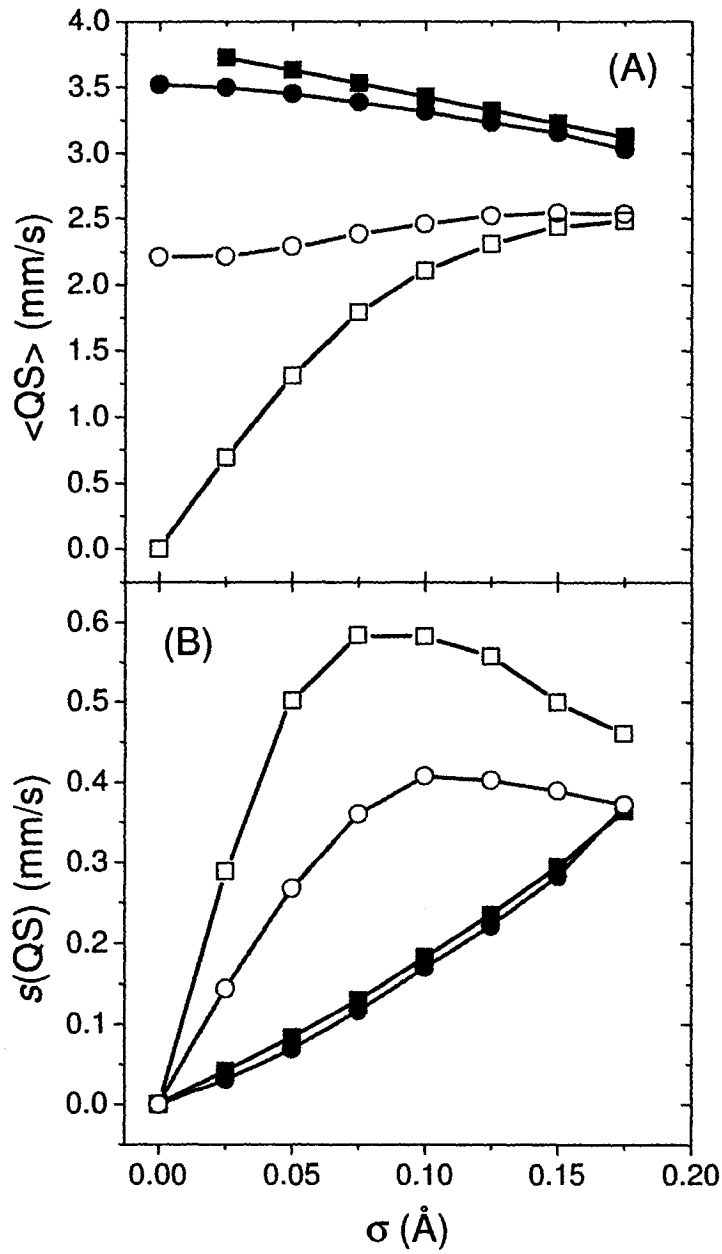

Figure 24. Distribution parameters of QS at 0 K (solid symbols) and 300 K (open symbols) as a function of static disorder for {||, ψ, 2.11 Å}. (A) Mean <QS> and (B) standard deviation *s*(QS). Squares, ψ = 54.74°; circles, ψ = 58°. In (A) the discontinuity point QS = 0 at σ = 0 Å for {||, 54.74°, 2.11 Å} at 0 K is not shown.

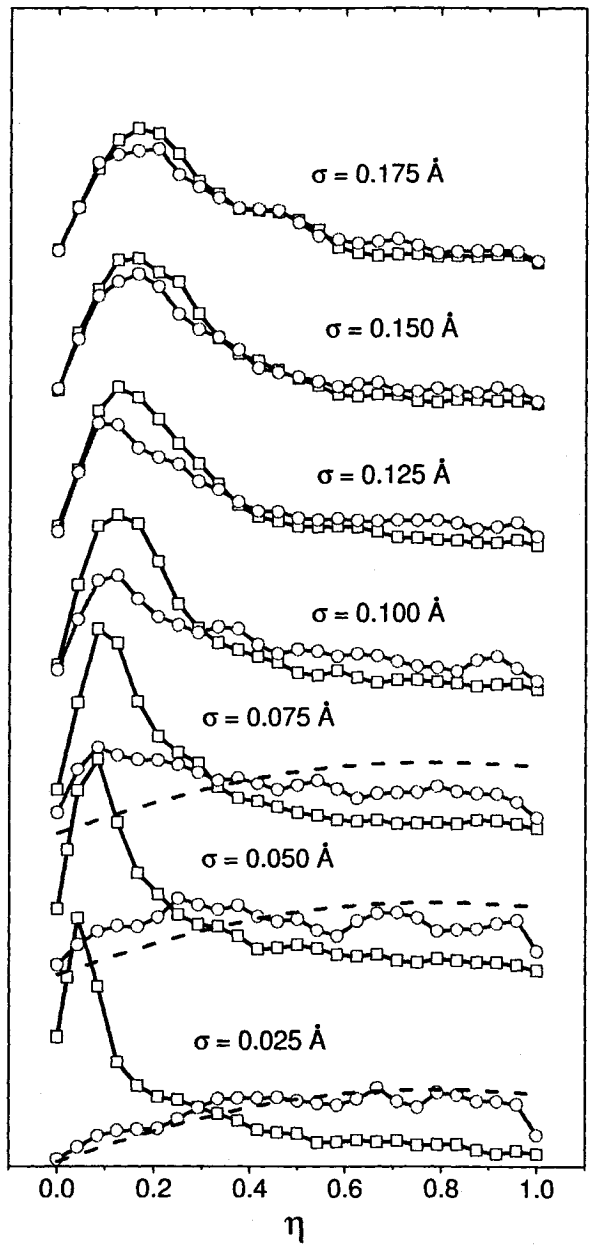

Figure 25. EFG asymmetry parameter distributions, normalized with respect to area, for cluster {||, 54.74°, 2.11 Å}, at 0 K (squares) and 300 K (circles). All distributions are show to the same vertical scale. The Czjzek η-distribution is shown with the σ = 0.025 Å, 0.050 Å and 0.075 Å graphs (dashed line).

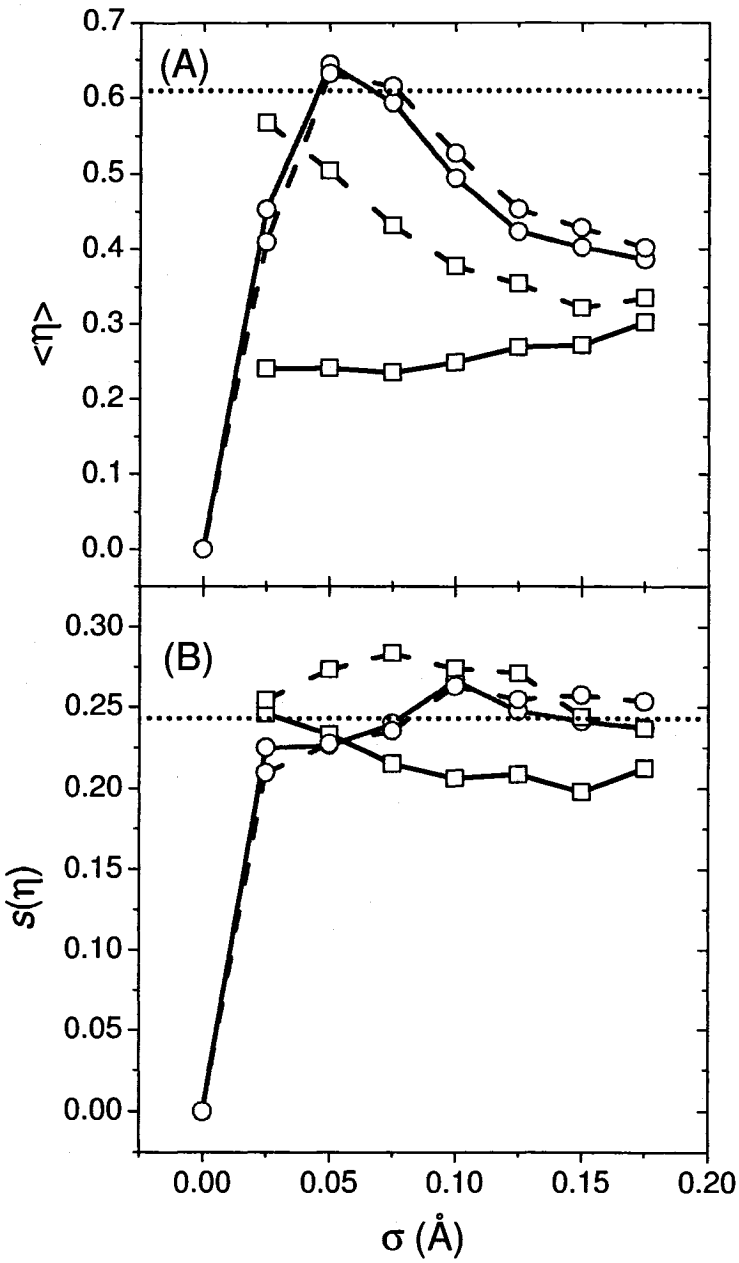

Figure 26. Distribution parameters of η as a function of static disorder for {||, ψ, 2.11 Å}. (A) Mean <η>. (B) Standard deviation $s(\eta)$. Squares - ψ = 54.74°; circles - ψ = 58°; solid lines - 0 K; dashed lines - 300 K; dotted lines, values for the Czjzek η-distribution.

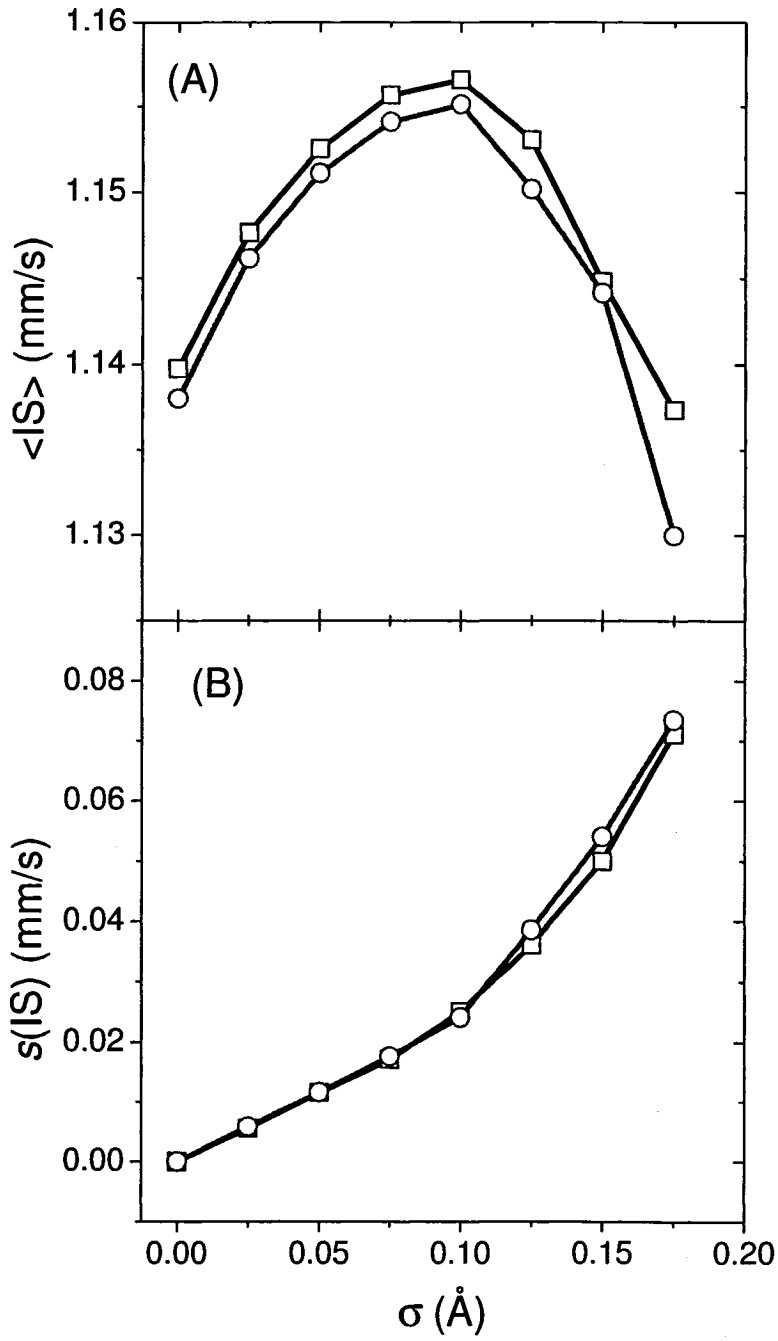

Figure 27. Distribution parameters of IS as a function of static disorder for {||, ψ, 2.11 Å}. (A) Mean <IS>. (B) Standard deviation *s*(IS). Squares, ψ = 54.74°; circles, ψ = 58°.

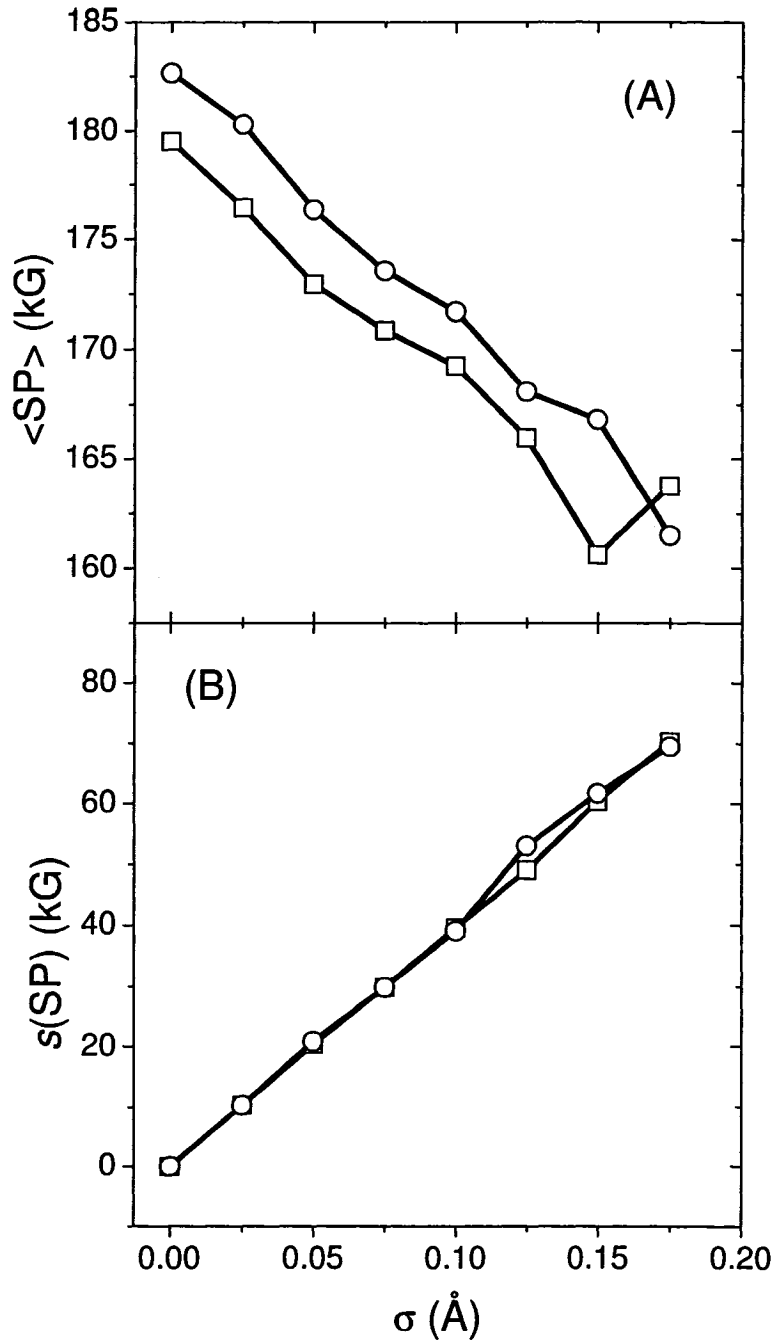

Figure 28. Distribution parameters of SP as a function of static disorder for {||, ψ, 2.11 Å}. (A) Mean <SP>. (B) Standard deviation *s*(SP). Squares, ψ = 54.74°; circles, ψ = 58°.

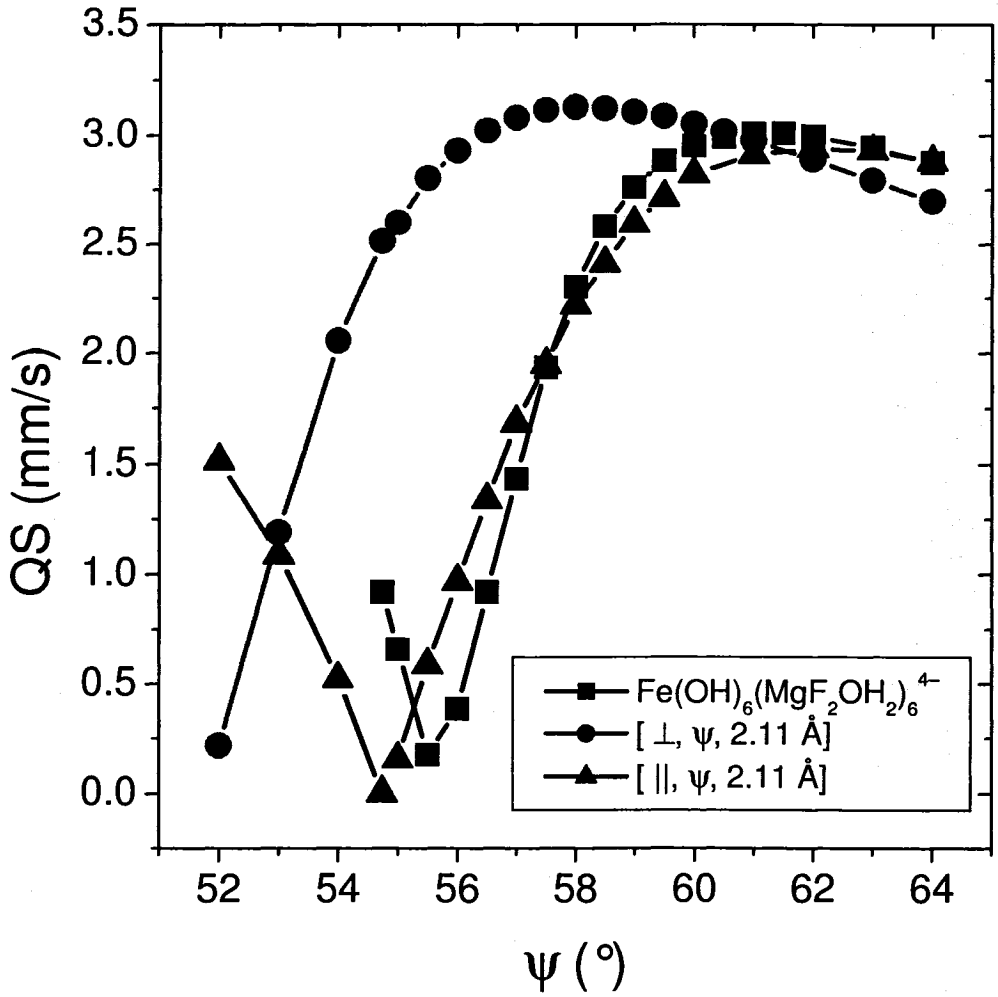

Figure 29. QS at 300 K as a function of flattening angle ψ for [⊥, y, 2.11 Å] (circles), [||, y, 2.11 Å] (triangles), and the seven-octahedra cluster $Fe(OH)_6(MgF_2OH_2)_6^{4-}$ (squares). The seven-octahedra cluster has Fe-O and Mg-O bond lengths equal to 2.11 Å, and OH groups normal to the plane (Evans et al. 2005a).

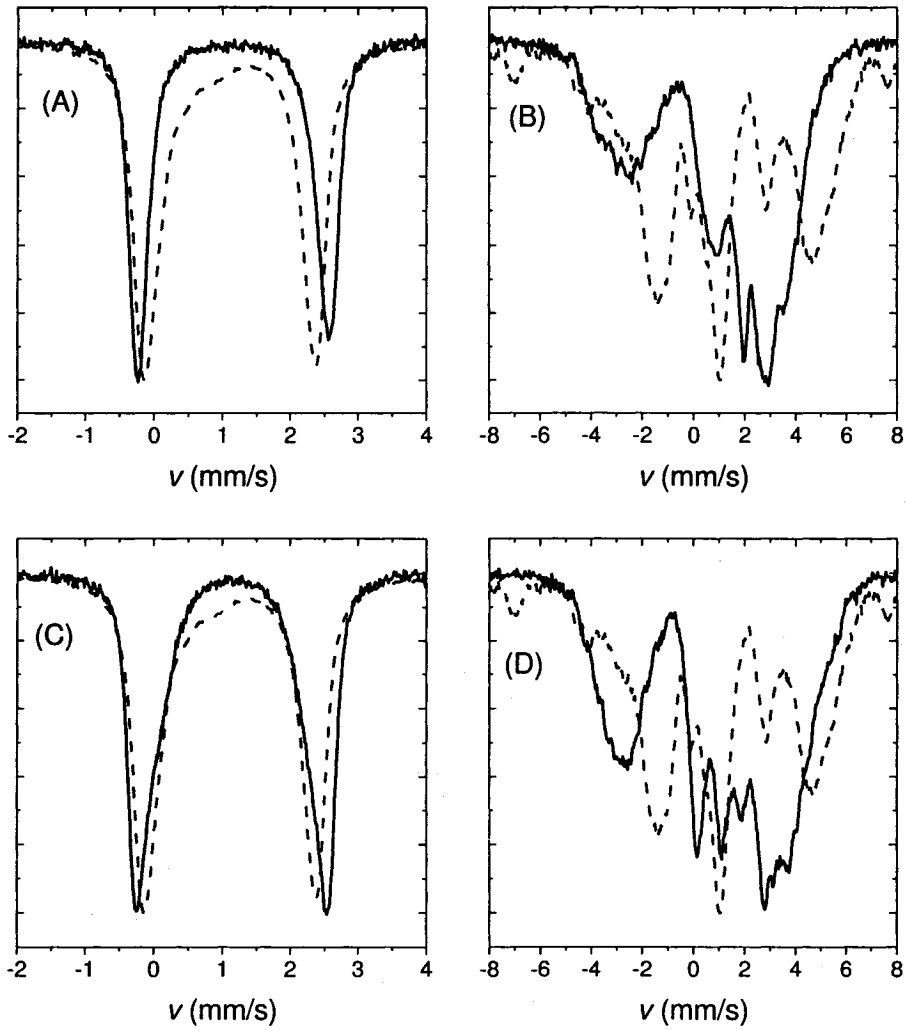

Figure 30. Comparison of simulated and experimental spectra (data from Rancourt et al. 1994b and 1994c). (A) Solid line - doublet from simulation {⊥, 58°, 2.11 Å}, σ = 0.150 Å at 300 K; dashed line - synthetic annite measured at 300 K. (B) Solid line - magnetic multiplet from simulation {⊥, 58°, 2.11 Å}, σ = 0.150 Å at 0 K; dashed line - synthetic annite measured at 7 K. (C) Solid line - doublet from simulation {||, 58°, 2.11 Å}, σ = 0.125 Å at 300 K; dashed line - synthetic annite measured at 300 K. (D) Solid line - magnetic multiplet from simulation {||, 58°, 2.11 Å}, σ = 0.125 Å at 0 K; dashed line - synthetic annite measured at 7 K.

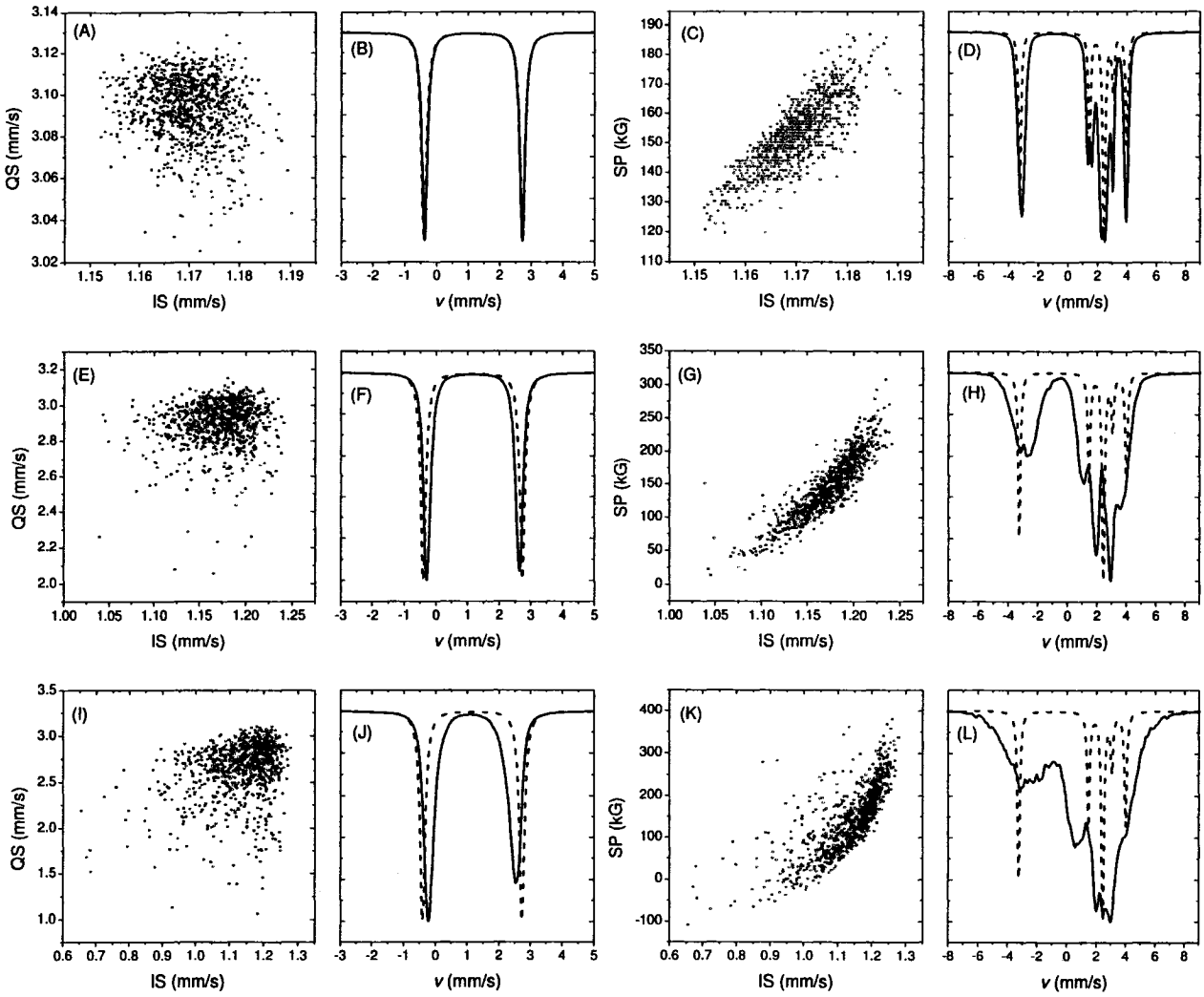

Figure 31. Correlations between hyperfine parameters and simulated spectra for {⊥, 58°, 2.11 Å} at σ = 0.025 Å (top row), 0.100 Å (centre row), and 0.175 (bottom row). First column: scatter plot of QS vs. IS at 300 K (1000 points). Second column: simulated doublets for the simulation (solid line) and cluster [⊥, 58°, 2.11 Å] with elemental Lorentzian line-width (dashed line) at 300 K. Third column: scatter plot of SP vs. IS (1000 points). Fourth column: simulated magnetic multiplets for the simulation (solid line) and cluster [⊥, 58°, 2.11 Å] elemental Lorentzian line-width (dashed line) at 0 K.

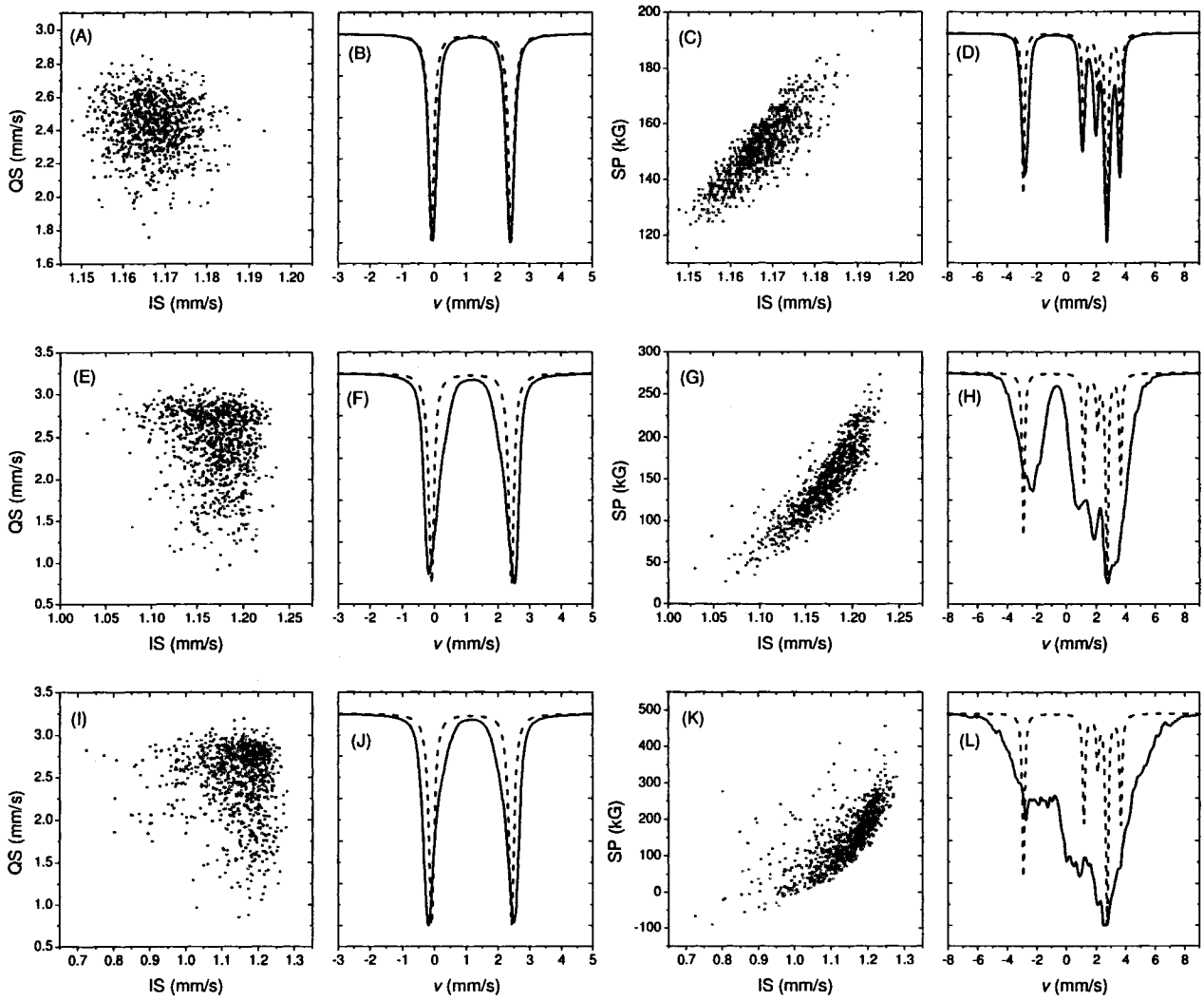

Figure 32. Correlations between hyperfine parameters and simulated spectra for {⊥, 54.74°, 2.11 Å} at σ = 0.025 Å (top row), 0.100 Å (centre row), and 0.175 (bottom row). First column: scatter plot of QS vs. IS at 300 K (1000 points). Second column: simulated doublets for the simulation (solid line) and cluster [⊥, 54.74°, 2.11 Å] with elemental Lorentzian line-width (dashed line) at 300 K. Third column: scatter plot of SP vs. IS (1000 points). Fourth column: simulated magnetic multiplets for the simulation (solid line) and cluster [⊥, 54.74°, 2.11 Å] elemental Lorentzian line-width (dashed line) at 0 K.

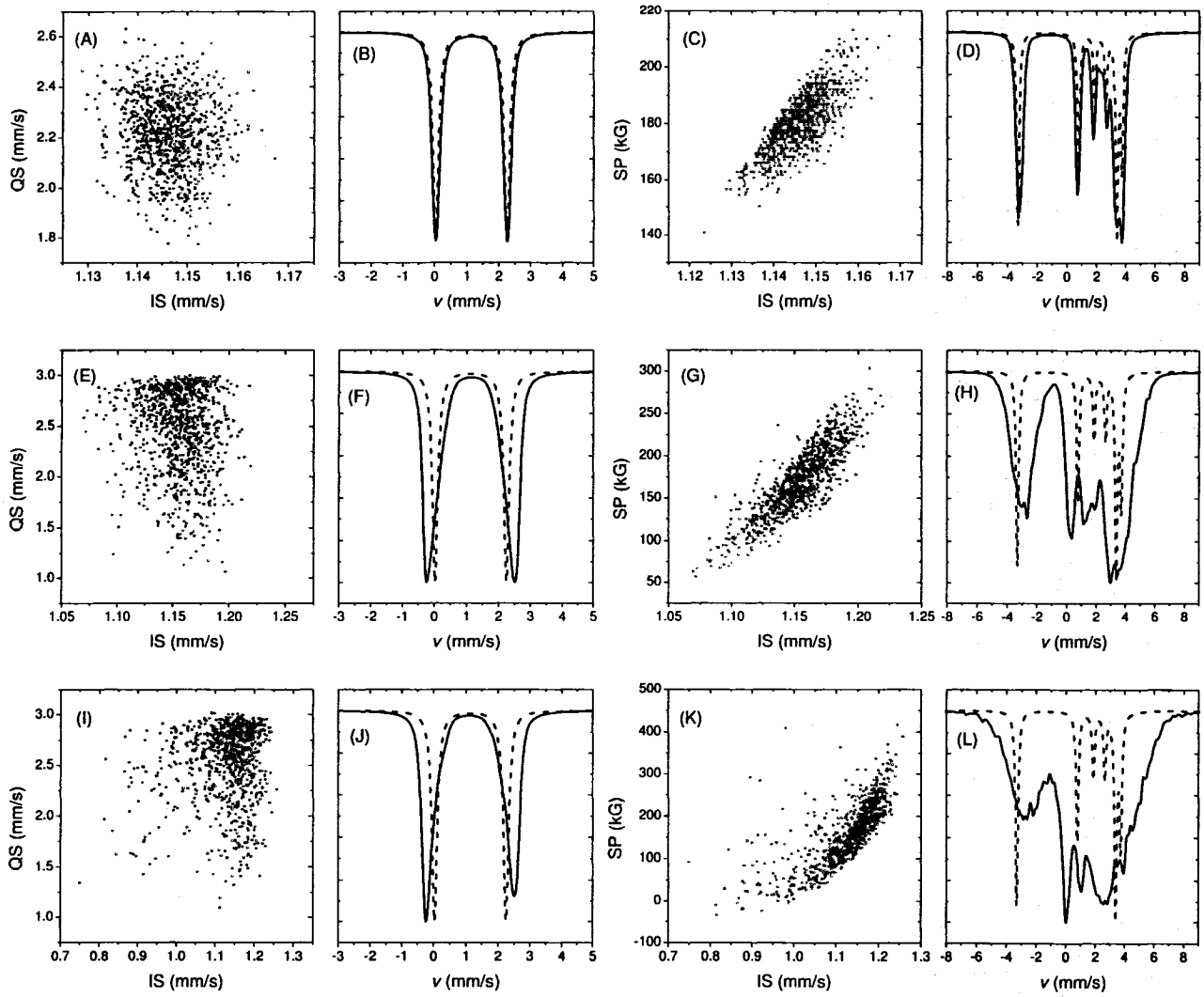

Figure 33. Correlations between hyperfine parameters and simulated spectra for {||, 58°, 2.11 Å} at σ = 0.025 Å (top row), 0.100 Å (centre row), and 0.175 (bottom row). First column: scatter plot of QS vs. IS at 300 K (1000 points). Second column: simulated doublets for the simulation (solid line) and cluster [||, 58°, 2.11 Å] with elemental Lorentzian line-width (dashed line) at 300 K. Third column: scatter plot of SP vs. IS (1000 points). Fourth column: simulated magnetic multiplets for the simulation (solid line) and cluster [||, 58°, 2.11 Å] elemental Lorentzian line-width (dashed line) at 0 K.

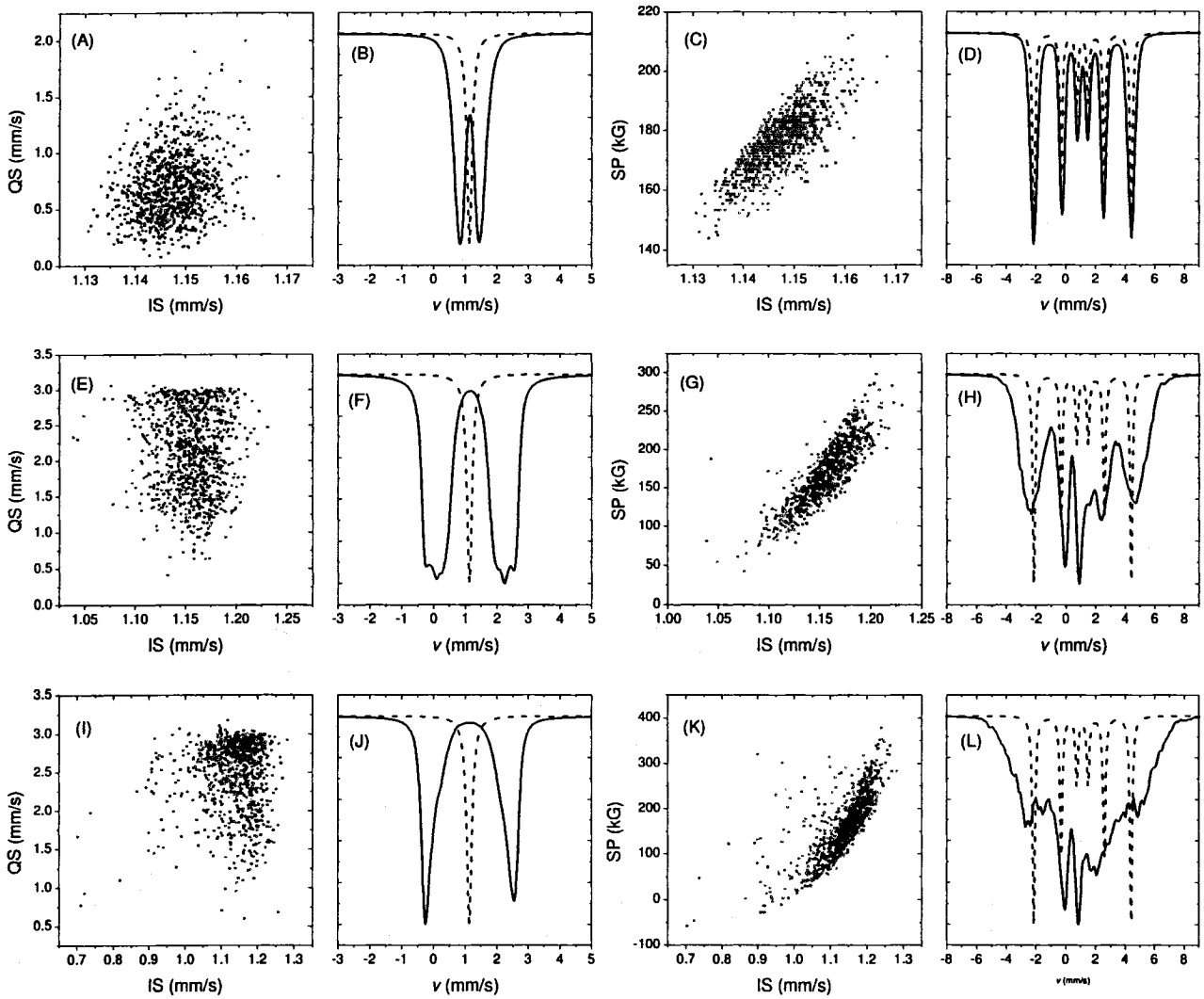

Figure 34. Correlations between hyperfine parameters and simulated spectra for {||, 54.74°, 2.11 Å} at σ = 0.025 Å (top row), 0.100 Å (centre row), and 0.175 (bottom row). First column: scatter plot of QS vs. IS at 300 K (1000 points). Second column: simulated doublets for the simulation (solid line) and cluster [||, 54.74°, 2.11 Å] with elemental Lorentzian line-width (dashed line) at 300 K. Third column: scatter plot of SP vs. IS (1000 points). Fourth column: simulated magnetic multiplets for the simulation (solid line) and cluster [||, 54.74°, 2.11 Å] elemental Lorentzian line-width (dashed line) at 0 K.

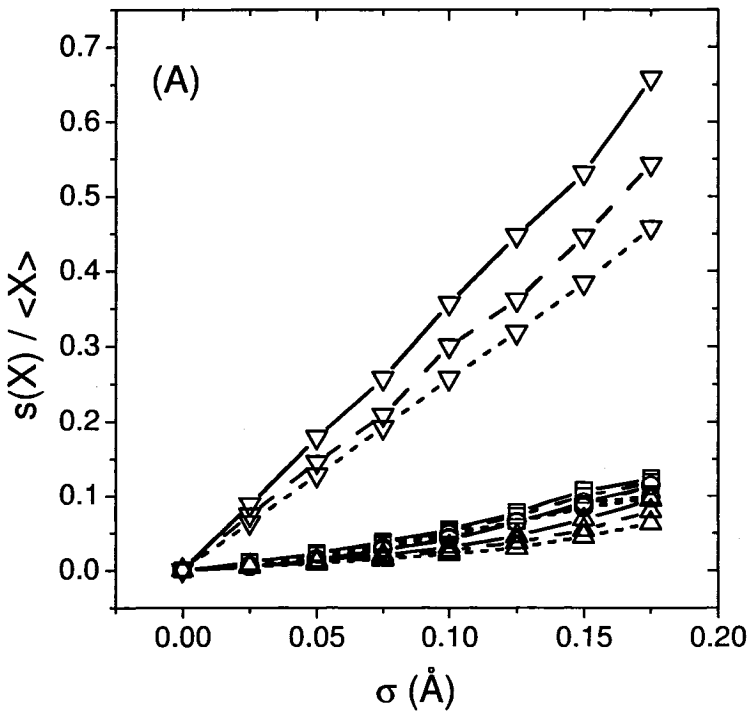
(A)
s(X) / <X>
σ (Å)
0.0
0.1
0.2
0.3
0.4
0.5
0.6
0.7
0.00
0.05
0.10
0.15
0.20

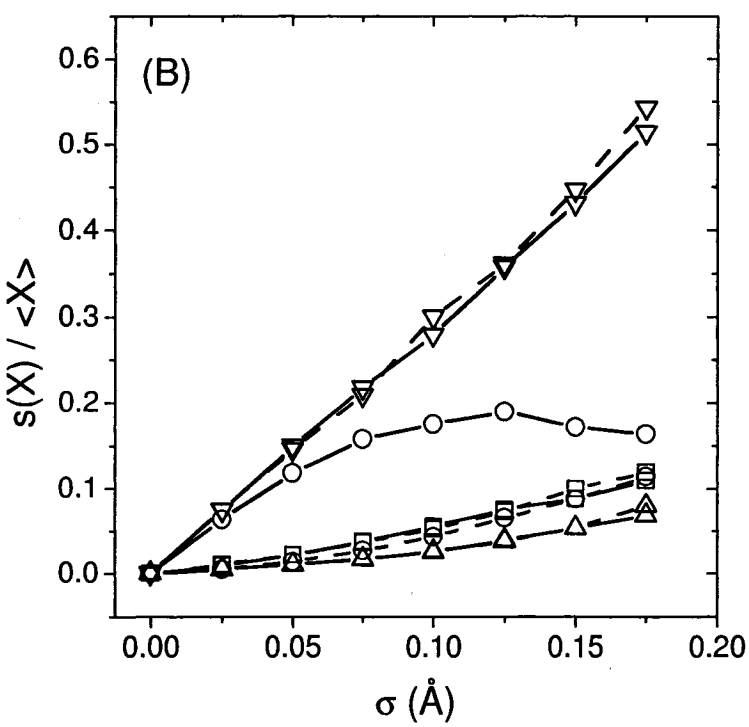
(B)
s(X) / <X>
σ (Å)
0.0
0.1
0.2
0.3
0.4
0.5
0.6
0.00
0.05
0.10
0.15
0.20

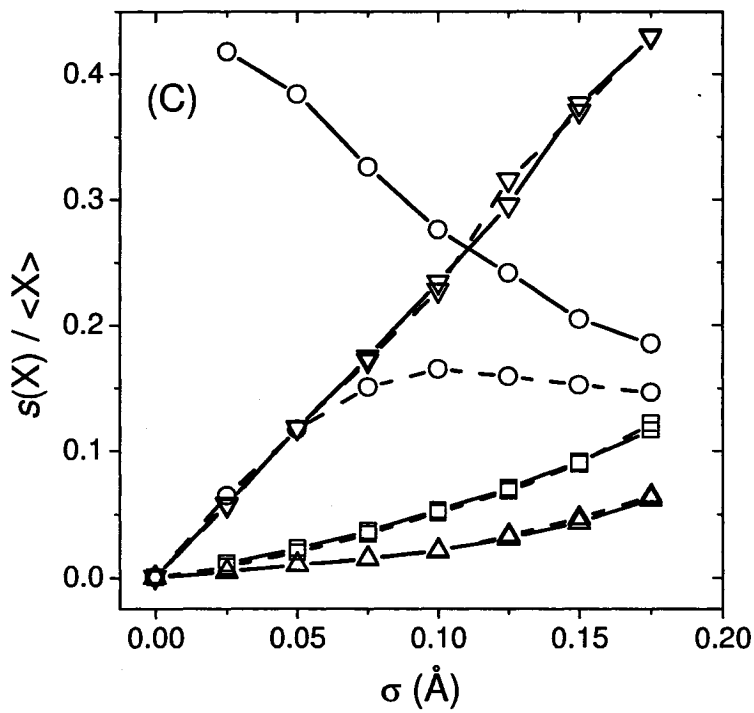

Figure 35. Width to mean ratios s(*X*)/<*X*> (*X* = IS, SP, QS), versus the static disorder parameter, σ. Squares - QS at 0 K; circles - QS at 300 K; upward triangles - IS; downward triangles - SP. (A) {⊥, 58°, *d*} simulations. Solid line - *d* = 2.08 Å; dashed line - *d* = 2.11 Å; dotted line - *d* = 2.14 Å. (B) {⊥, ψ, 2.11 Å} simulations. Solid line - ψ = 54.17°; dashed line - ψ = 58°. (C) {∥, ψ, 2.11 Å} simulations. Solid line - ψ = 54.17°; dashed line - ψ = 58°.

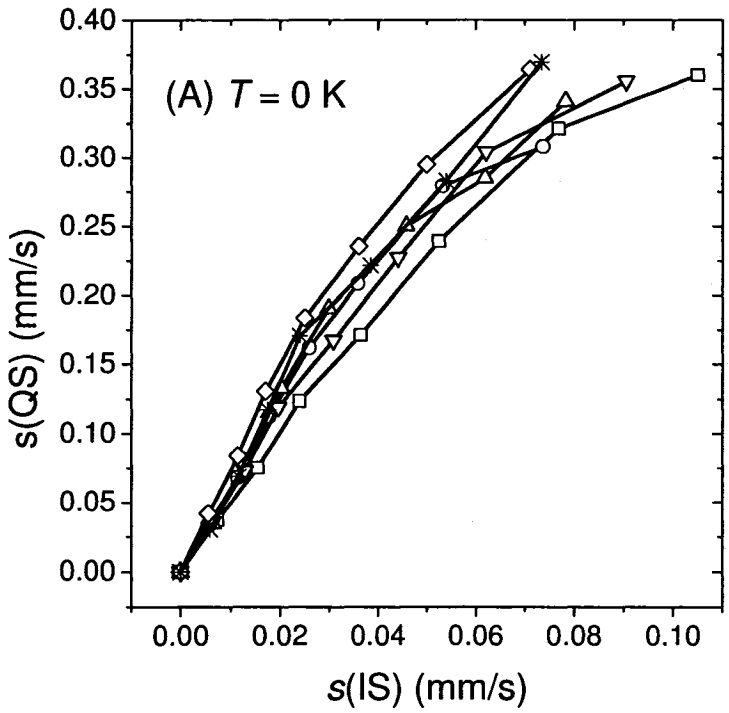
(A) T = 0 K
s(QS) (mm/s)
s(IS) (mm/s)
0.00
0.05
0.10
0.15
0.20
0.25
0.30
0.35
0.40
0.00
0.02
0.04
0.06
0.08
0.10

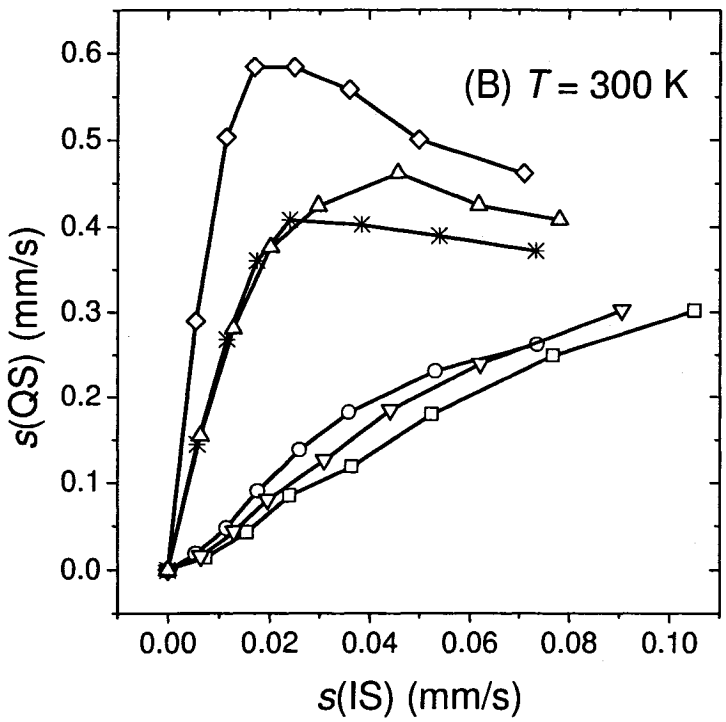
(B) T = 300 K
s(QS) (mm/s)
s(IS) (mm/s)
0.0
0.1
0.2
0.3
0.4
0.5
0.6
0.00
0.02
0.04
0.06
0.08
0.10

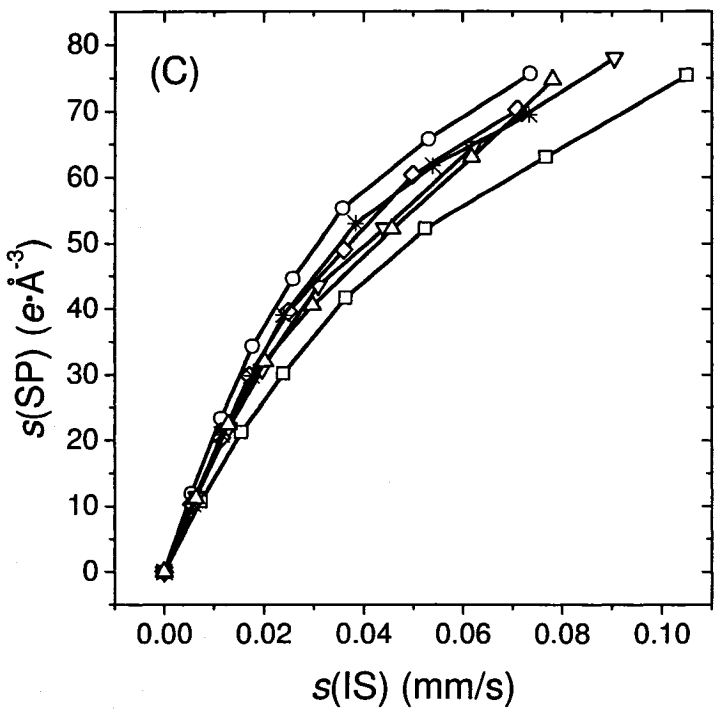

Figure 36. *s*(QS) vs. *s*(IS) at (A) 0 K and (B) 300 K, and (C) *s*(SP) vs. *s*(IS) for all ensembles calculated. Squares, {⊥, 58°, 2.08 Å}; circles, {⊥, 58°, 2.14 Å}; upward triangles, {⊥, 54.74°, 2.11 Å}; downward triangles, {⊥, 58°, 2.11 Å}; diamonds, {∥, 54.74°, 2.11 Å}; left triangles, {∥, 58°, 2.11 Å}.

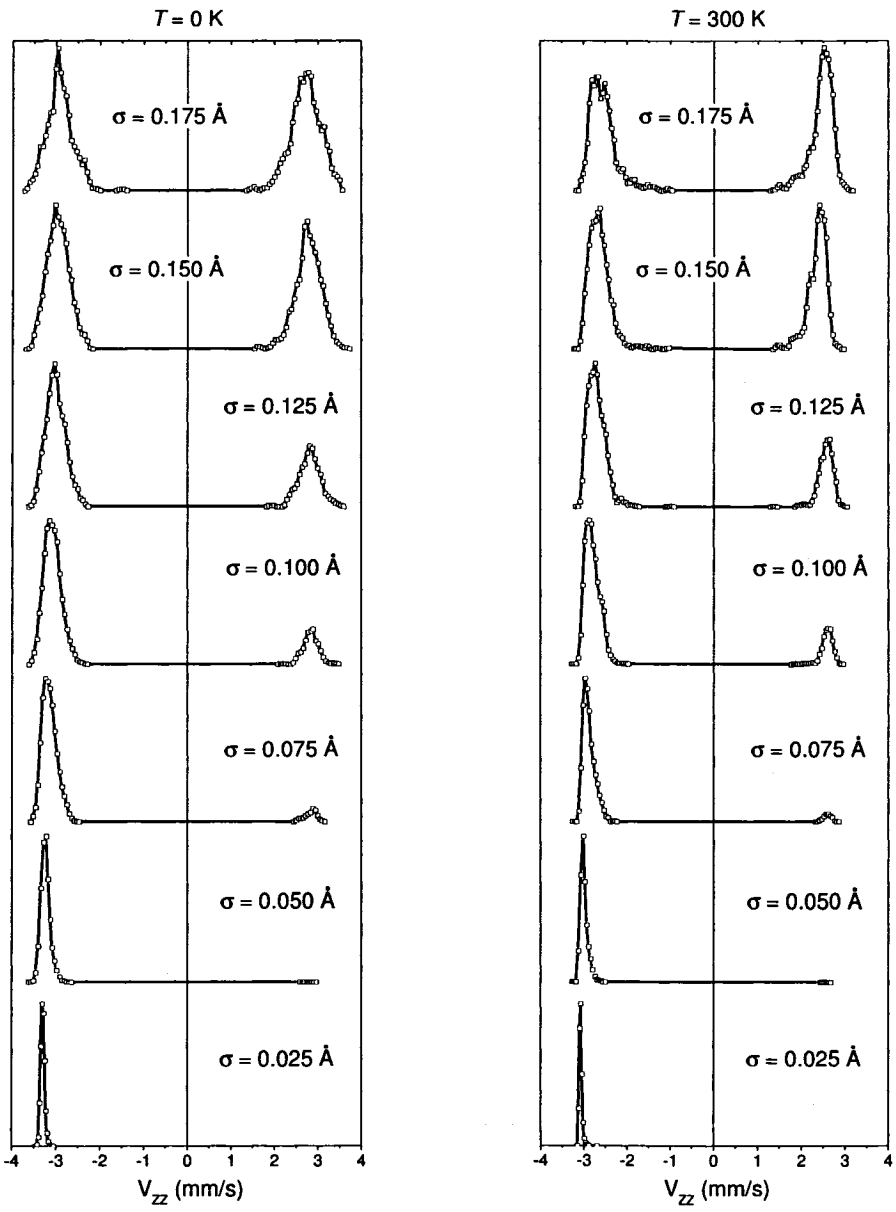

Figure 37. V_{ZZ} distributions of {⊥, 58°, 2.11 Å}. Left, 0 K; right, 300 K.

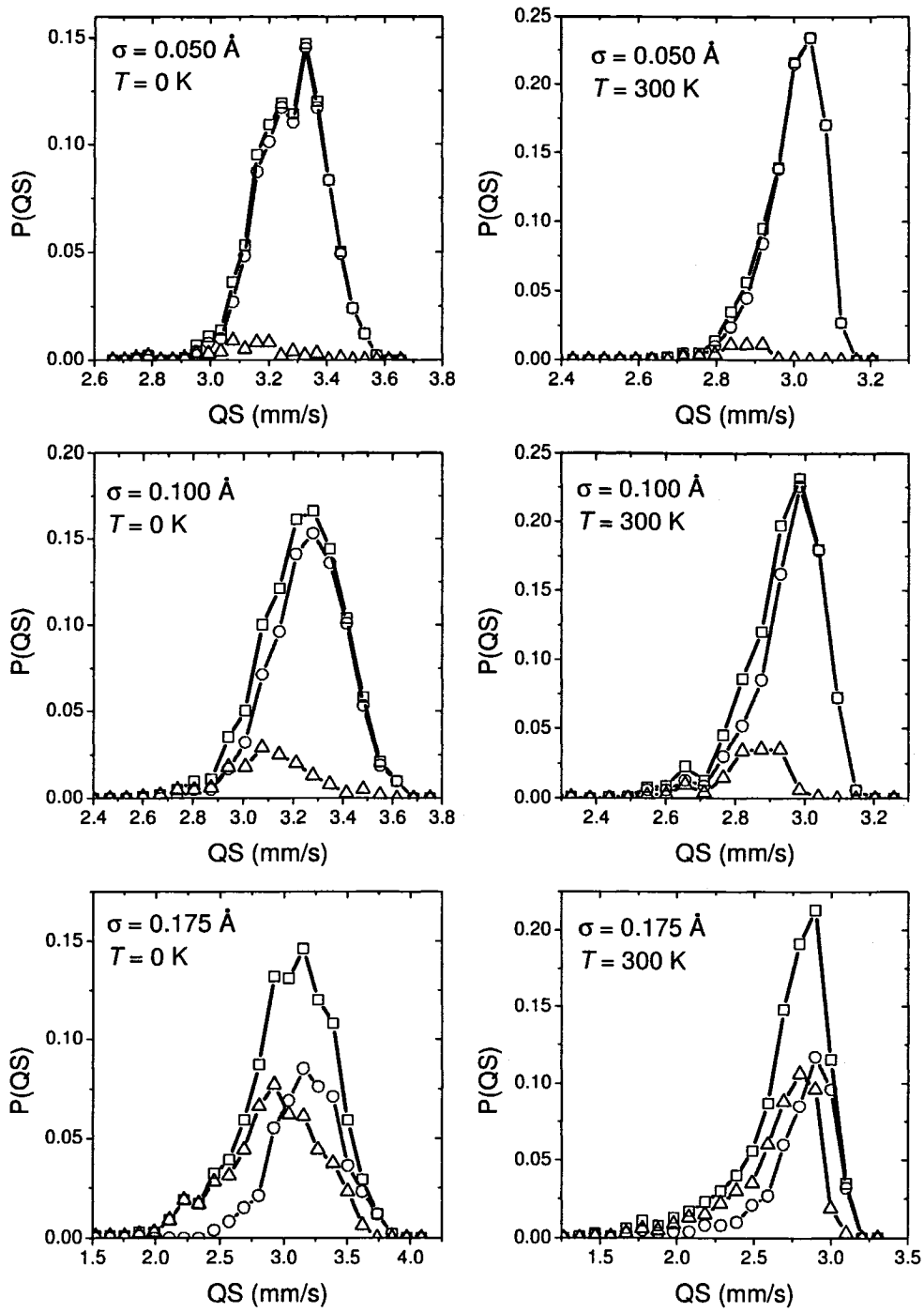

Figure 38. Partial QS distributions for {⊥, 58°, 2.11 Å}. Squares - total QS distribution; circles - QS distribution with $V_{ZZ} < 0$; triangles - QS distribution with $V_{ZZ} > 0$.

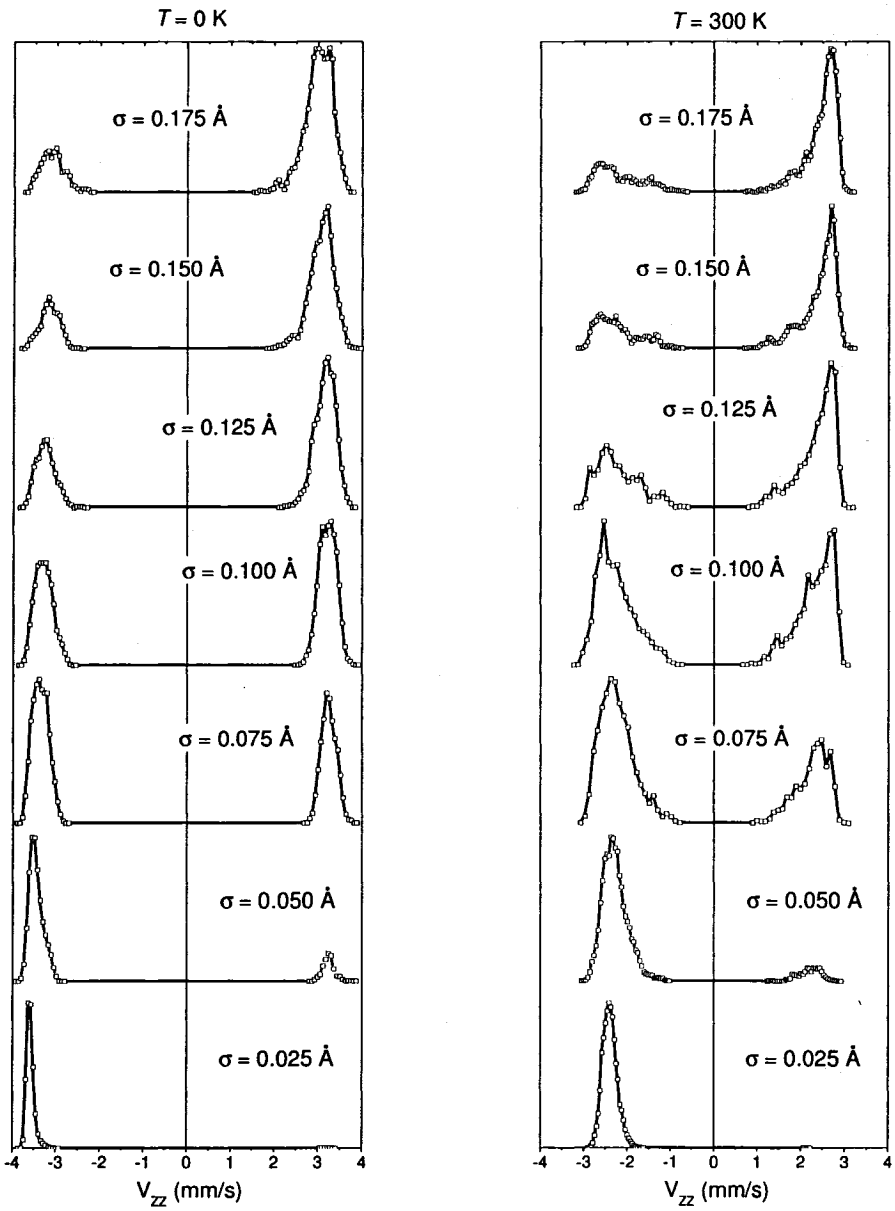

Figure 39. V_{ZZ} distributions of {⊥, 54.74°, 2.11 Å}. Left, 0 K; right, 300 K.

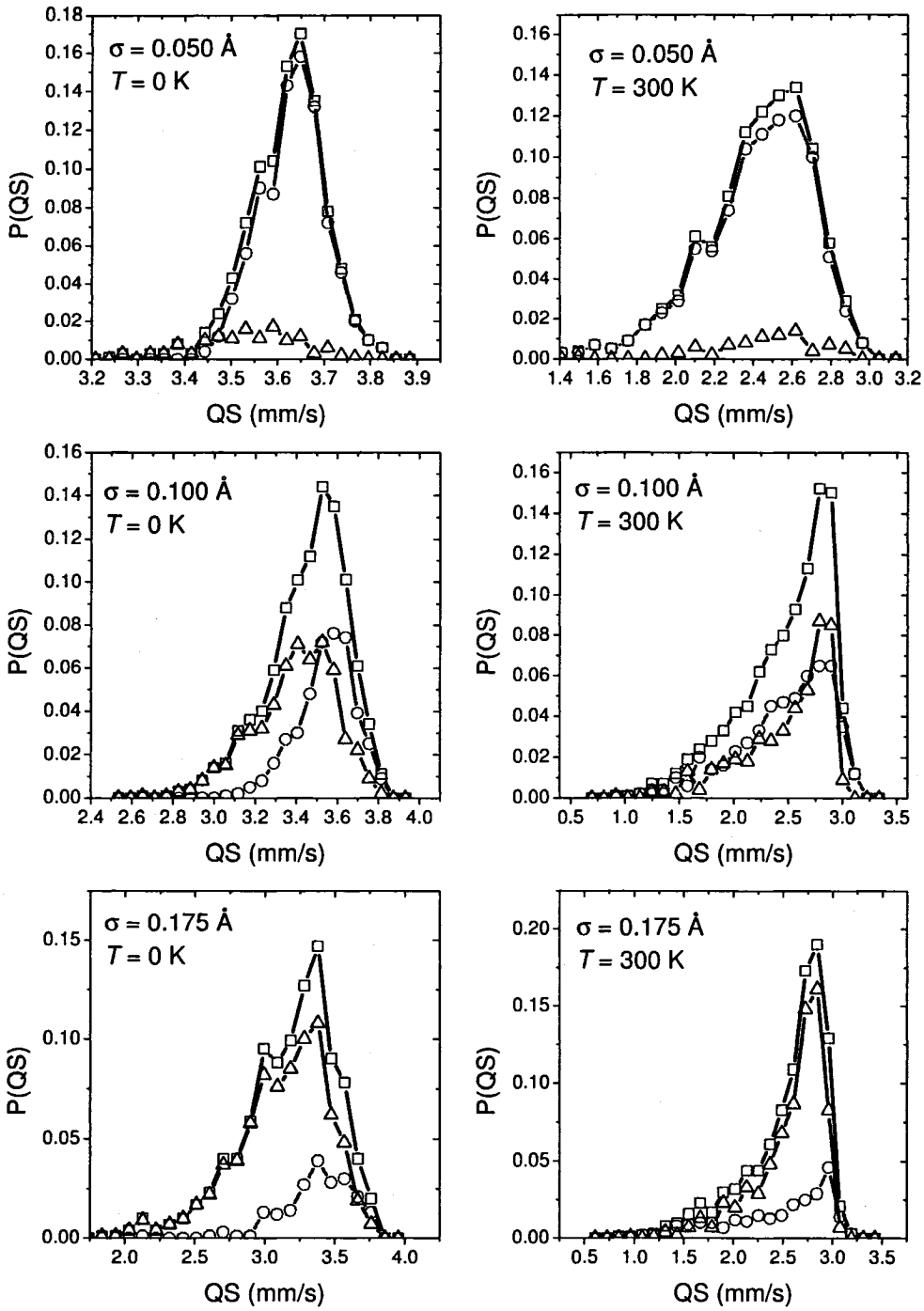

Figure 40. Partial QS distributions for {⊥, 54.74°, 2.11 Å}. Squares - total QS distribution; circles - QS distribution with $V_{ZZ} < 0$; triangles - QS distribution with $V_{ZZ} > 0$.

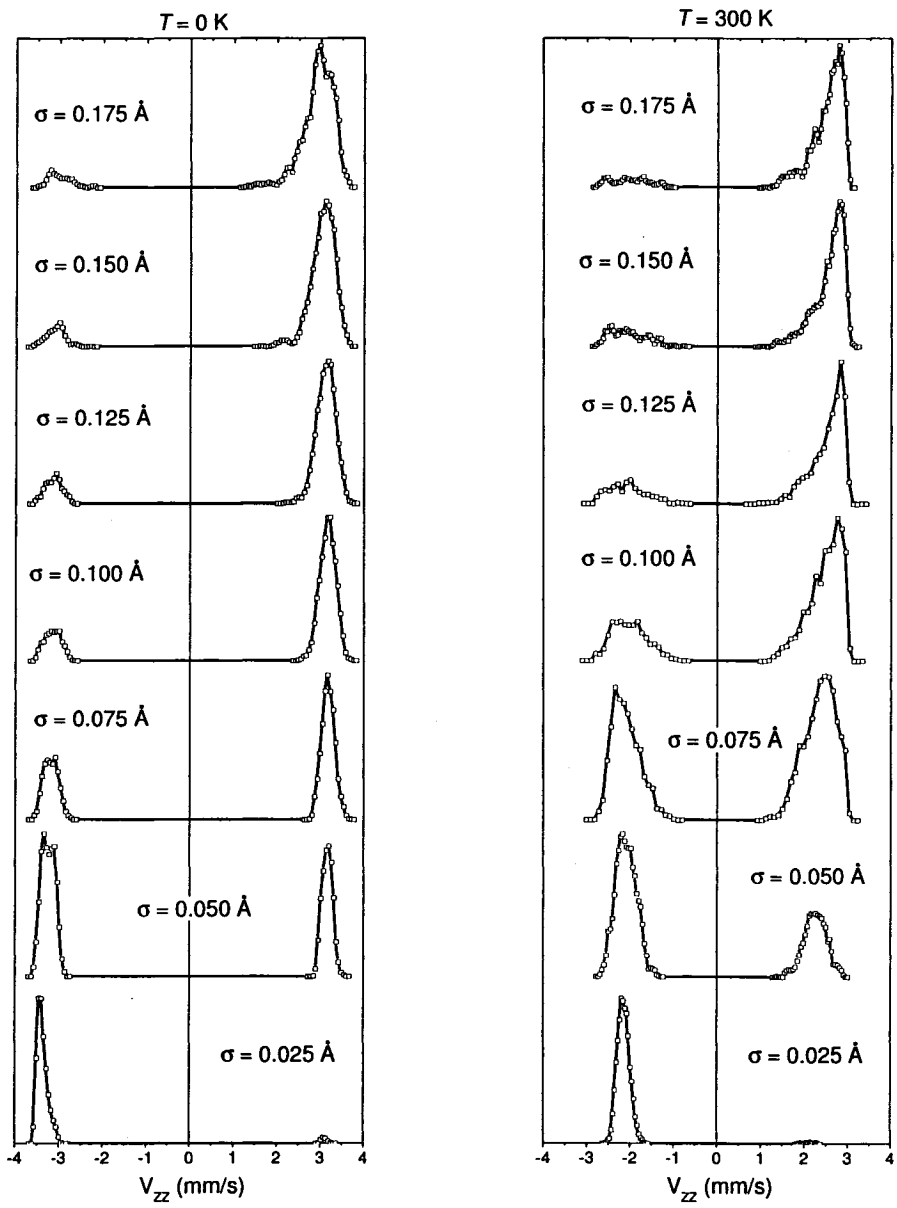

Figure 41. V_{ZZ} distributions of {||, 58°, 2.11 Å}. Left, 0 K; right, 300 K.

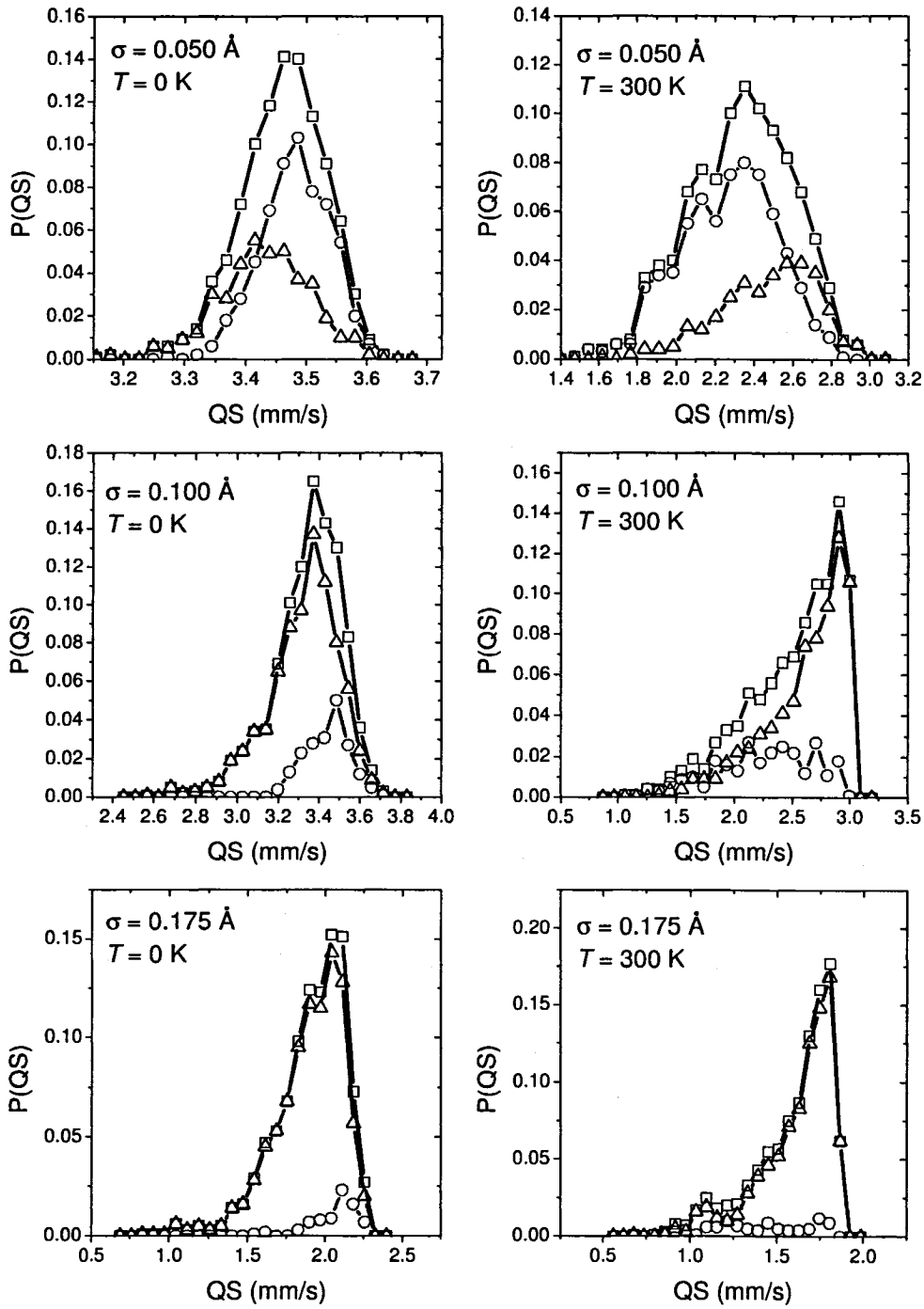

Figure 42. Partial QS distributions for {||, 58°, 2.11 Å}. Squares - total QS distribution; circles - QS distribution with $V_{ZZ} < 0$; triangles - QS distribution with $V_{ZZ} > 0$.

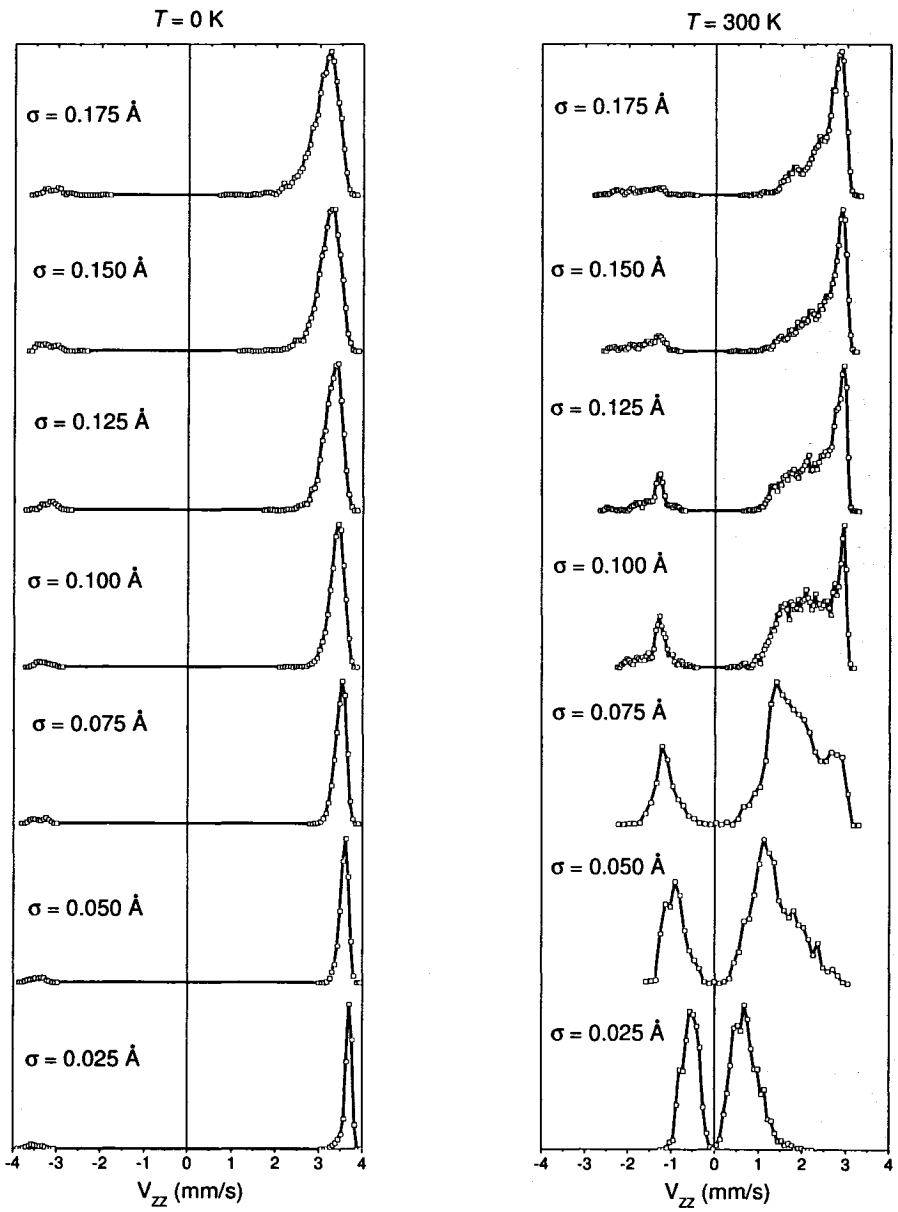

Figure 43. V_{ZZ} distributions of {||, 54.74°, 2.11 Å}. Left, 0 K; right, 300 K.

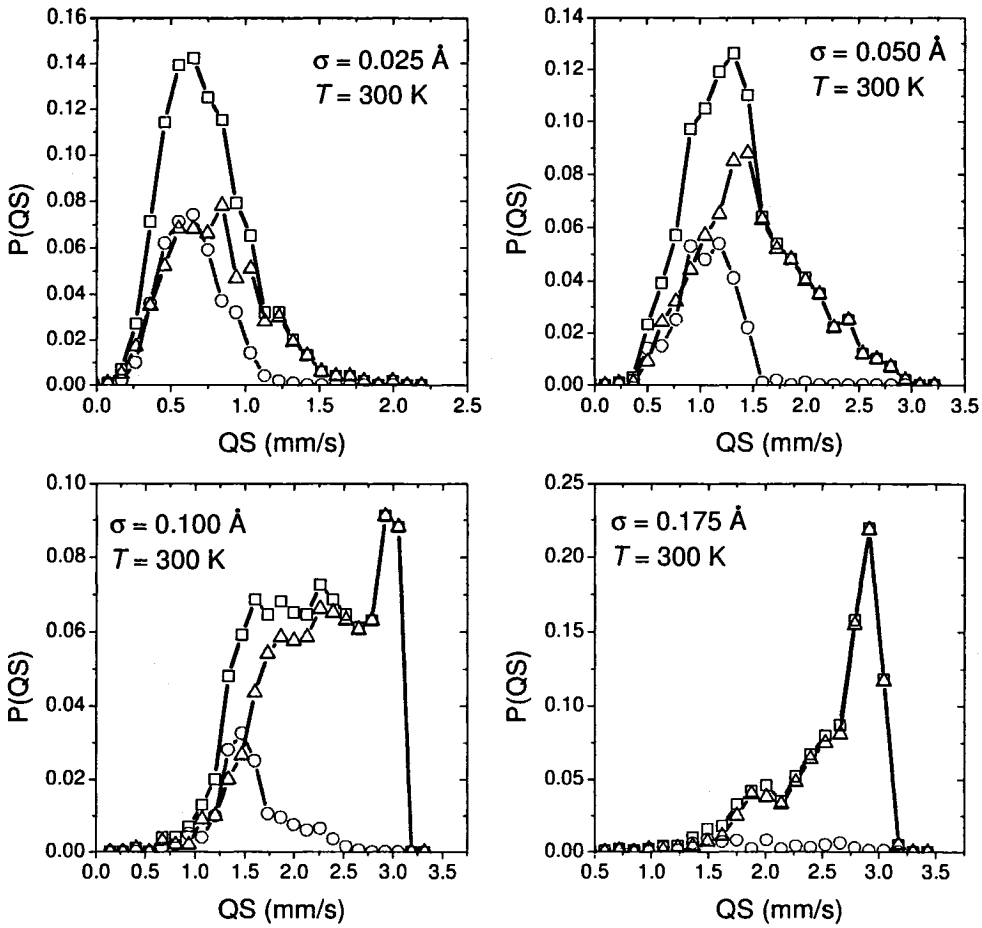

Figure 44. Partial QS distributions for {⊥, 58°, 2.11 Å} at 300 K. Squares - total QS distribution; circles - QS distribution with $V_{ZZ} < 0$; triangles - QS distribution with $V_{ZZ} > 0$. At 0 K, almost all EFGs have $V_{ZZ} > 0$.

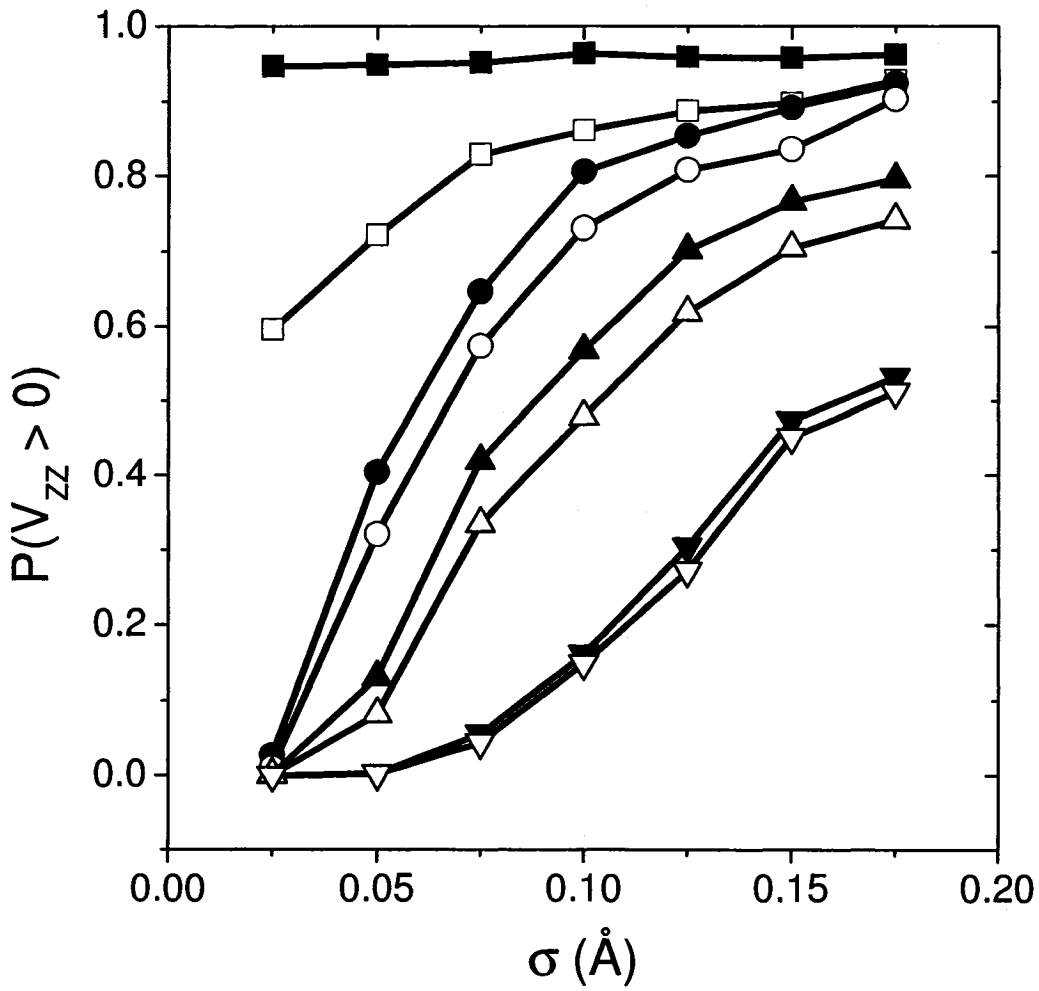

Figure 45. The fraction of clusters with positive V_{ZZ} in each ensemble, $P(V_{ZZ} > 0)$, as a function of σ. Open symbols, $T = 0$ K; closed symbols, $T = 300$ K; squares, {∥, 54.74°, 2.11 Å}; circles, {∥, 58°, 2.11 Å}; upward triangles, {⊥, 54.74°, 2.11 Å}; downward triangles, {⊥, 58°, 2.11 Å}.

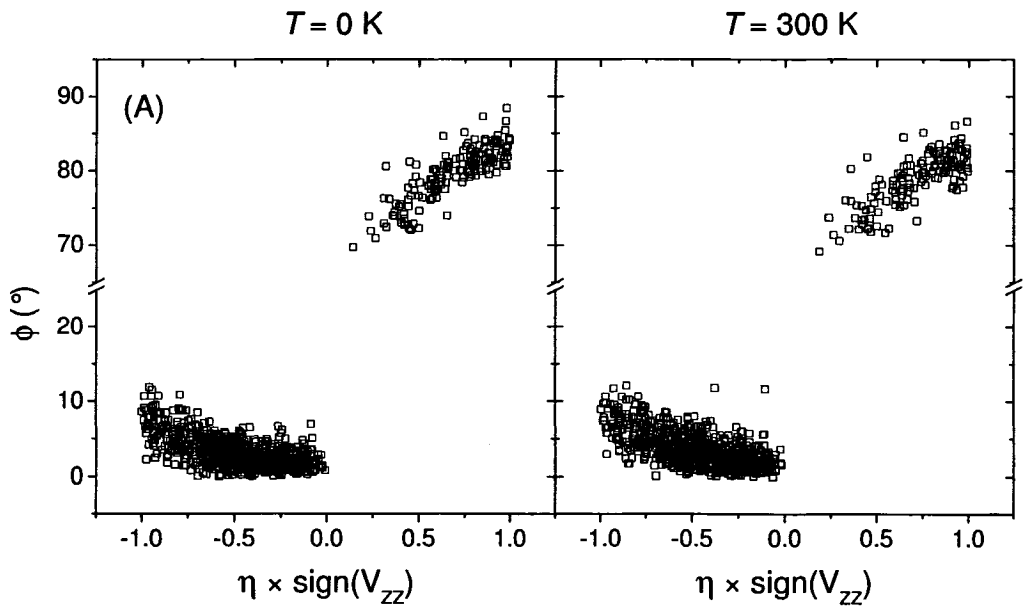
T = 0 K
T = 300 K
(A)
φ (°)
η × sign(V_zz)

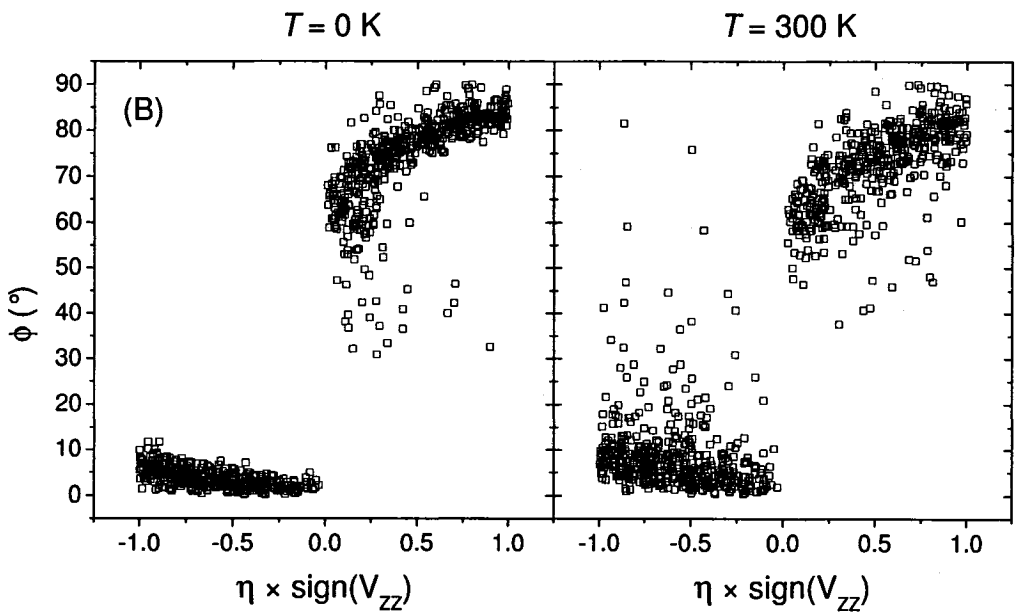
T = 0 K
T = 300 K
(B)
φ (°)
η × sign(V_zz)

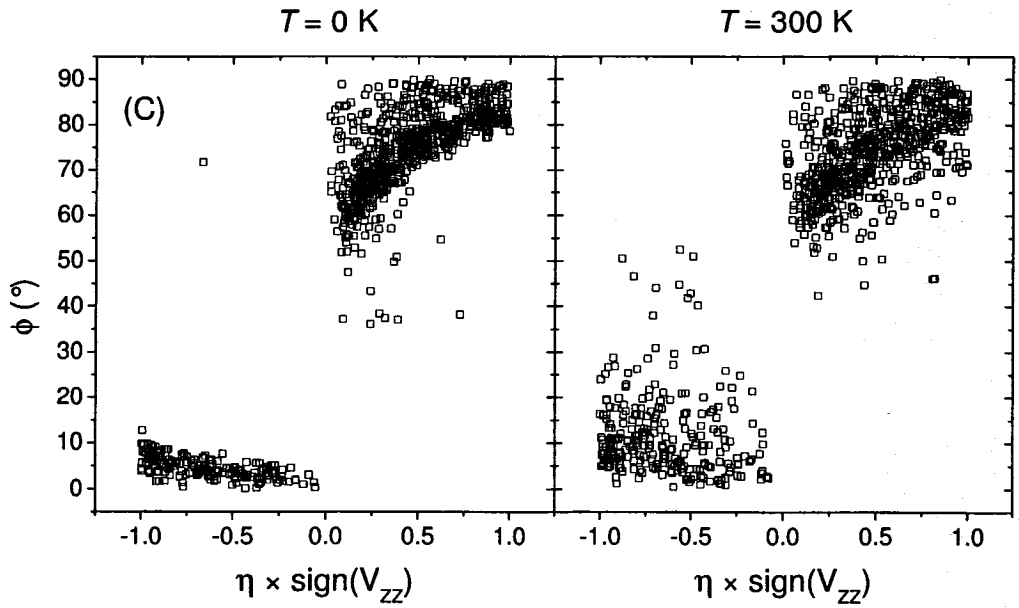
T = 0 K
T = 300 K
(C)
φ (°)
η × sign(V_zz)
η × sign(V_zz)

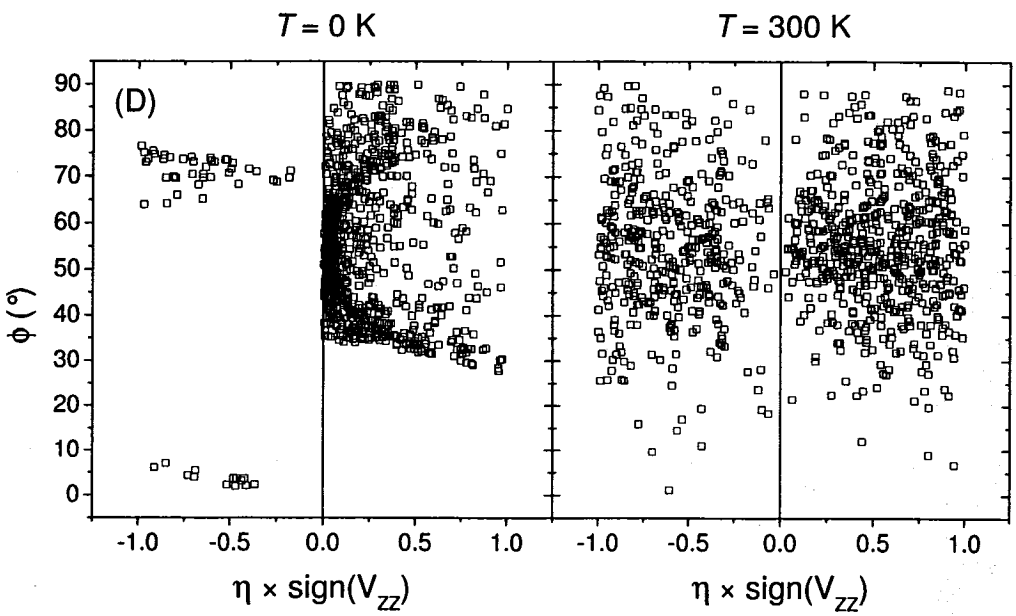
T = 0 K
T = 300 K
(D)
φ (°)
η × sign(V_zz)
η × sign(V_zz)

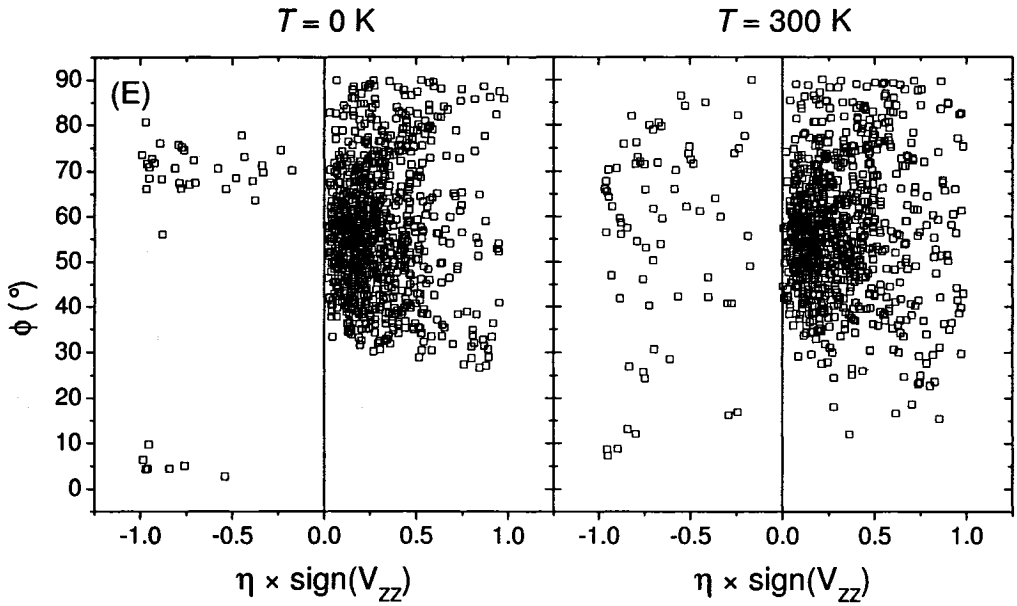

Figure 46. Scatter plot of ϕ vs. $\eta \times \text{sign}(V_{ZZ})$ from different simulations. (A) {$\perp$, 58°, 2.11 Å} at $\sigma = 0.100$ Å, (B) {$\perp$, 54.74°, 2.11 Å}at $\sigma = 0.100$ Å, (C) {$\parallel$, 58°, 2.11 Å} at $\sigma = 0.100$ Å, (D) {$\perp$, 54.74°, 2.11 Å} at $\sigma = 0.025$ Å, (E) {$\perp$, 54.74°, 2.11 Å} at $\sigma = 0.175$ Å.

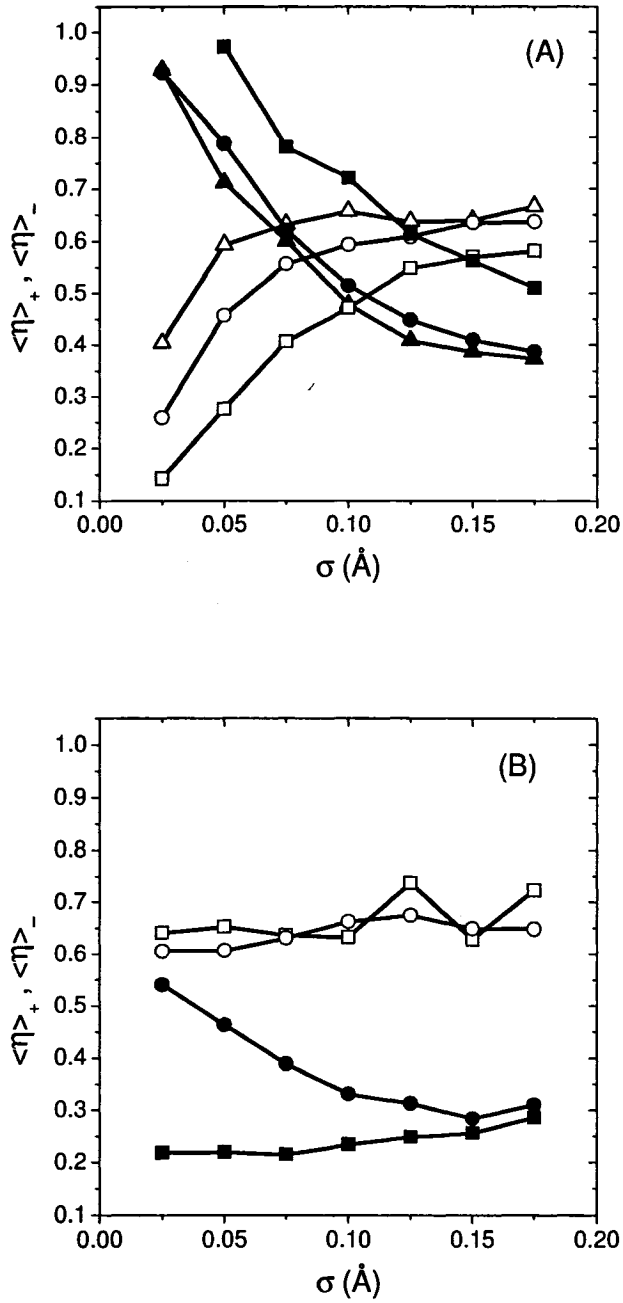

Figure 47. Mean η for $V_{ZZ} > 0$ ($<\eta>_+$, solid symbols) and $V_{ZZ} < 0$ ($<\eta>_-$, open symbols) subpopulations. (A) Squares, {⊥, 58°, 2.11 Å}; circles, {⊥, 54.74°, 2.11 Å}; triangles, {||, 58°, 2.11 Å}. (B) Squares, {||, 54.74°, 2.11 Å} at 0 K; circles, {||, 54.74°, 2.11 Å} at 300 K.

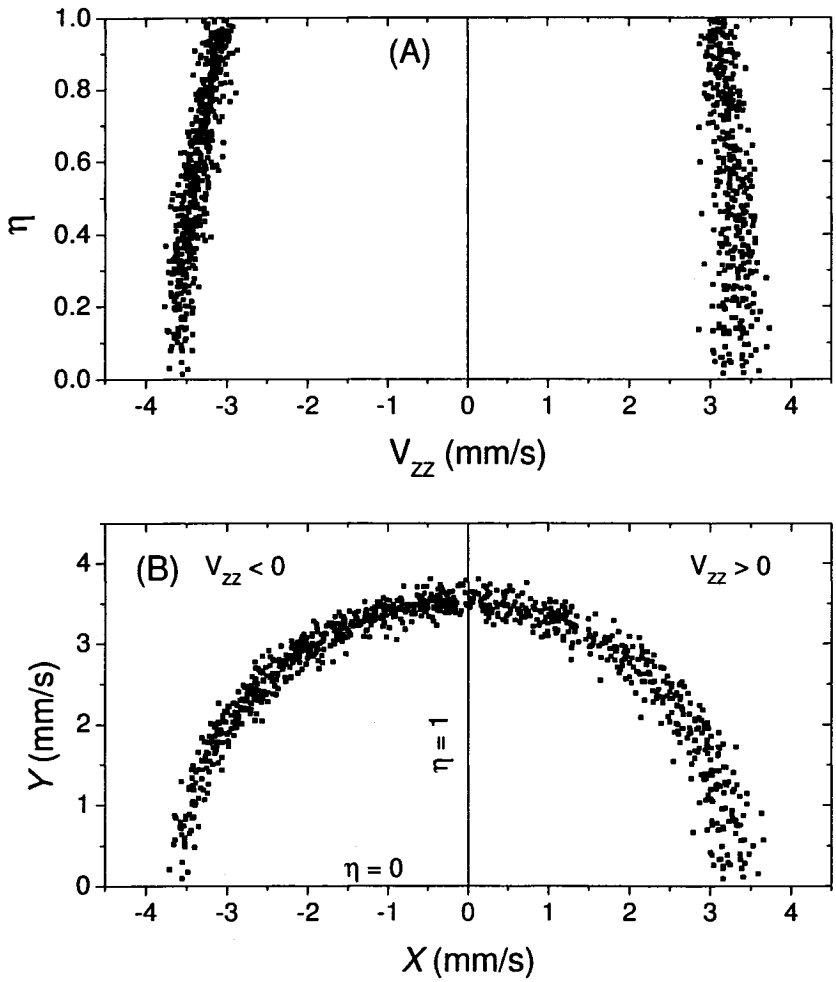

Figure 48. The advantage of displaying EFG tensor properties using polar coordinates. (A) V_{ZZ} vs. η from the σ = 0.075 Å {⊥, 54.74°, 2.11 Å} simulation. In order to accurately represent the (V_{ZZ}, η)-space, the two halves of the graph must be connected both at $V_{ZZ} = 0$ and at $\eta = 1$. (B) The same data displayed using polar coordinates defined by Le Caer and Brand (1998) (see equation 36). The left half of the graph contains $V_{ZZ} < 0$, and the right $V_{ZZ} > 0$; lines through the origin represent constant η, while half-circles centred at the origin represent constant V^* (QS). The connectivity of the (V_{ZZ}, η)-space is accurately depicted.

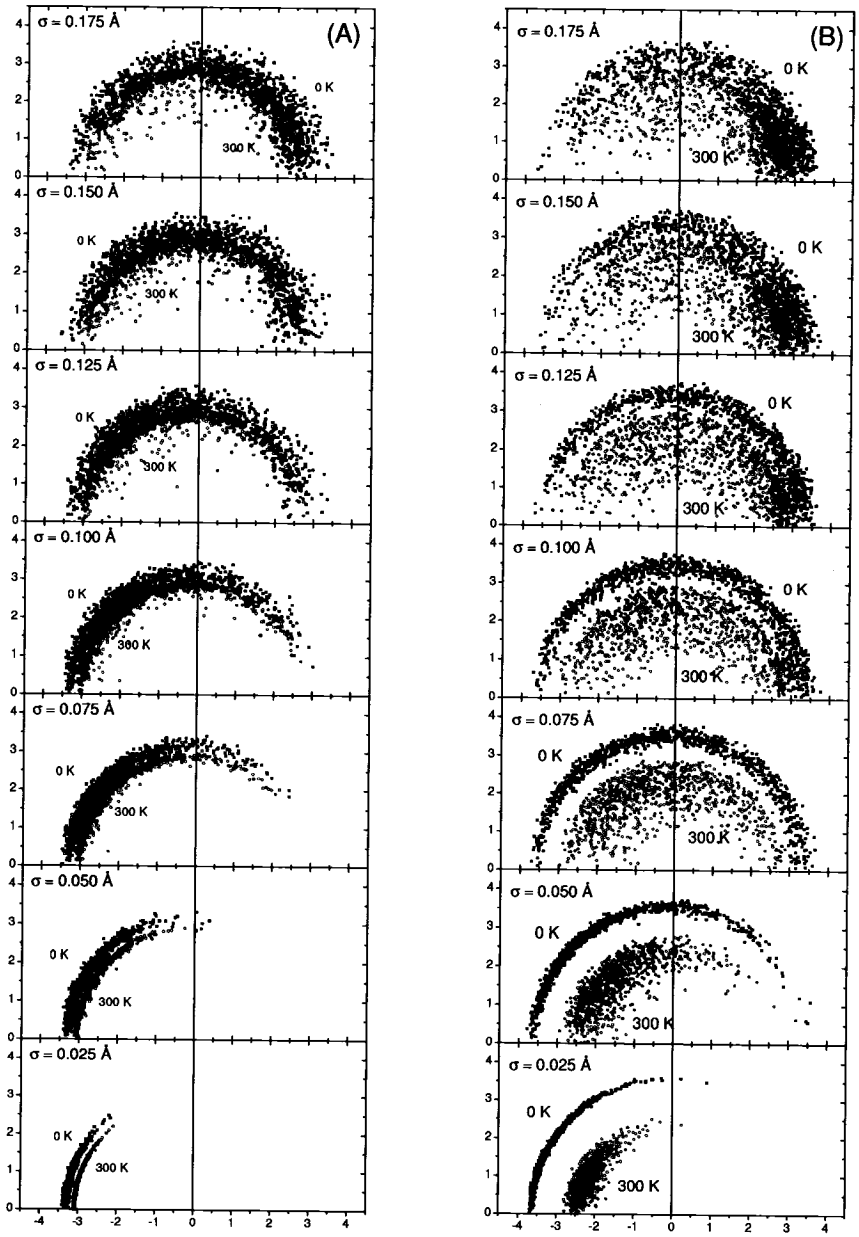
(A)
(B)
σ = 0.175 Å
σ = 0.150 Å
σ = 0.125 Å
σ = 0.100 Å
σ = 0.075 Å
σ = 0.050 Å
σ = 0.025 Å
0 K
300 K

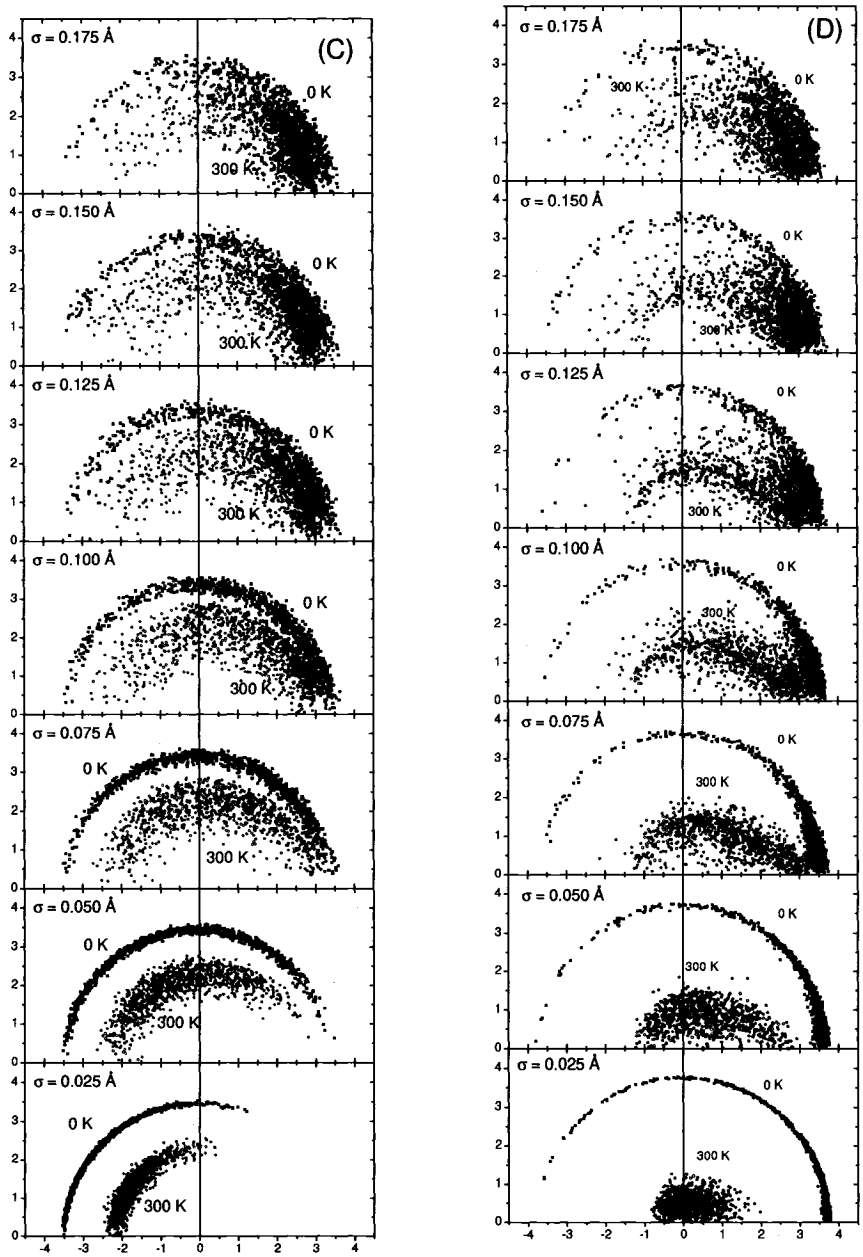

Figure 49. Polar plots of EFG tensor properties using the co-ordinates of Le Caer and Brand (1998). (A) {⊥, 58°, 2.11 Å}, (B) {⊥, 54.74°, 2.11 Å}, (C) {||, 58°, 2.11 Å}, (D) {||, 54.74°, 2.11 Å}. Black points are 0 K, red points are 300 K results. Axes are measured in mm/s.

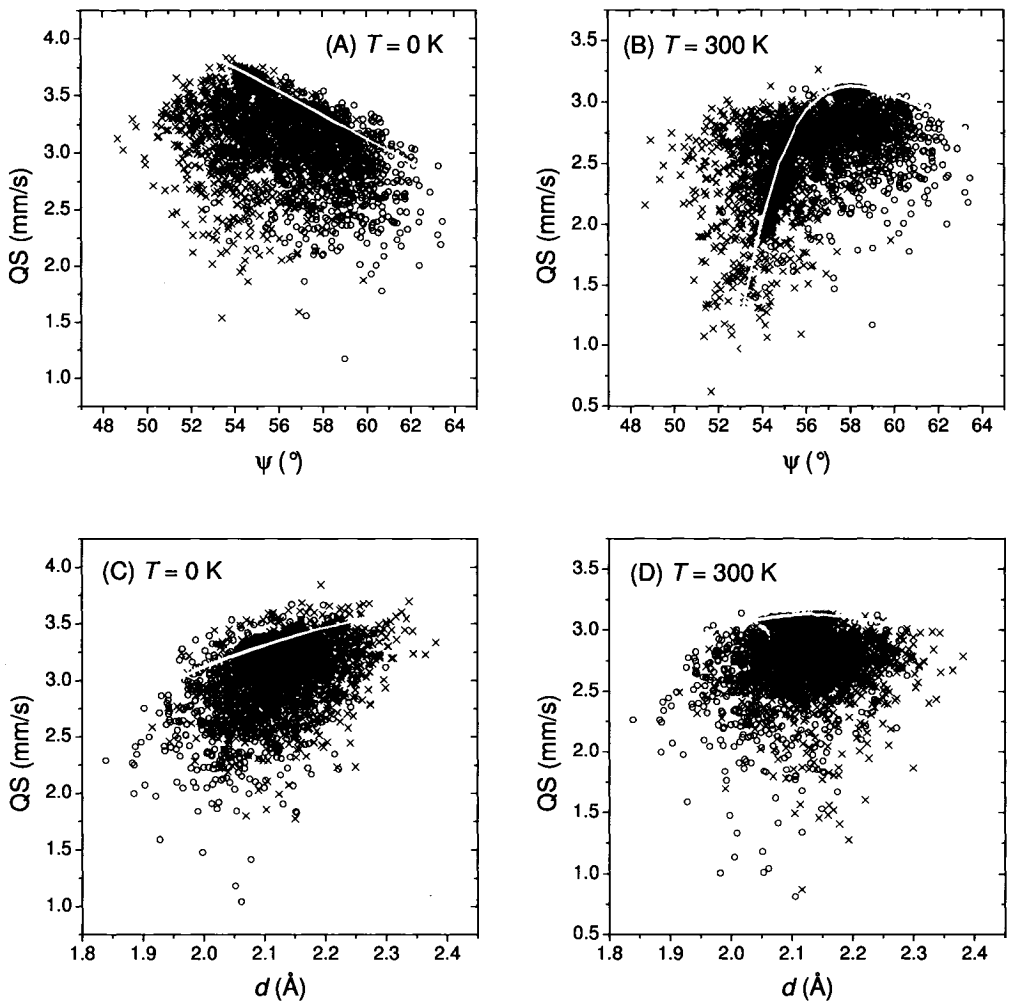

Figure 50. QS as a function of mean cluster bond length d and mean cluster flattening angle ψ. (A), (B) red solid circles - {⊥, 58°, 2.11 Å}, σ = 0.025 Å; black open circles - {⊥, 58°, 2.11 Å}, σ = 0.175 Å; blue crosses - {⊥, 54.74°, 2.11 Å}, σ = 0.025 Å; black crosses - {⊥, 54.74°, 2.11 Å}, σ = 0.175 Å; yellow line - QS vs. ψ , [⊥, ψ, 2.11 Å]. (C), (D) red solid circles - {⊥, 58°, 2.08 Å}, σ = 0.025 Å; black open circles - {⊥, 58°, 2.08 Å}, σ = 0.175 Å; blue crosses - {⊥, 58°, 2.14 Å}, σ = 0.025 Å; black crosses - {⊥, 58°, 2.14 Å}, σ = 0.175 Å; yellow line - QS vs. d, [⊥, 58°, d].

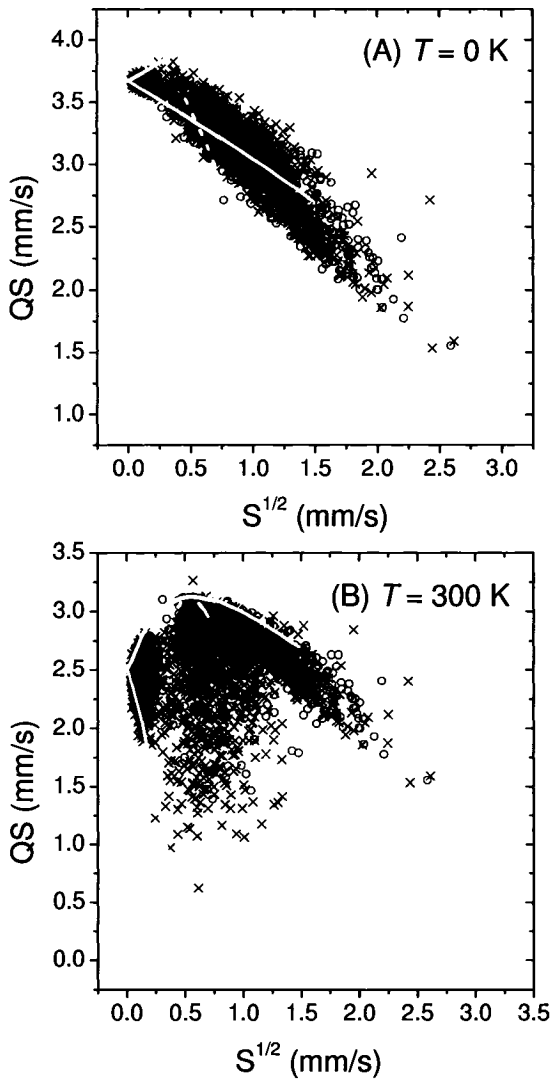

Figure 51. QS as a function of the square root of the total EFG structure factor S at (A) 0 K and (B) 300 K. Red solid circles - {⊥, 58°, 2.11 Å}, σ = 0.025 Å; black open circles - {⊥, 58°, 2.11 Å}, σ = 0.175 Å; blue crosses - {⊥, 54.74°, 2.11 Å}, σ = 0.025 Å; black crosses - {⊥, 54.74°, 2.11 Å}, σ = 0.175 Å; yellow solid line - QS vs. $S^{1/2}$, [⊥, ψ, 2.11 Å]; yellow dashed line - QS vs. $S^{1/2}$, [⊥, 58°, d]; orange dashed line - QS vs. $S^{1/2}$, [⊥, 54.74°, d].

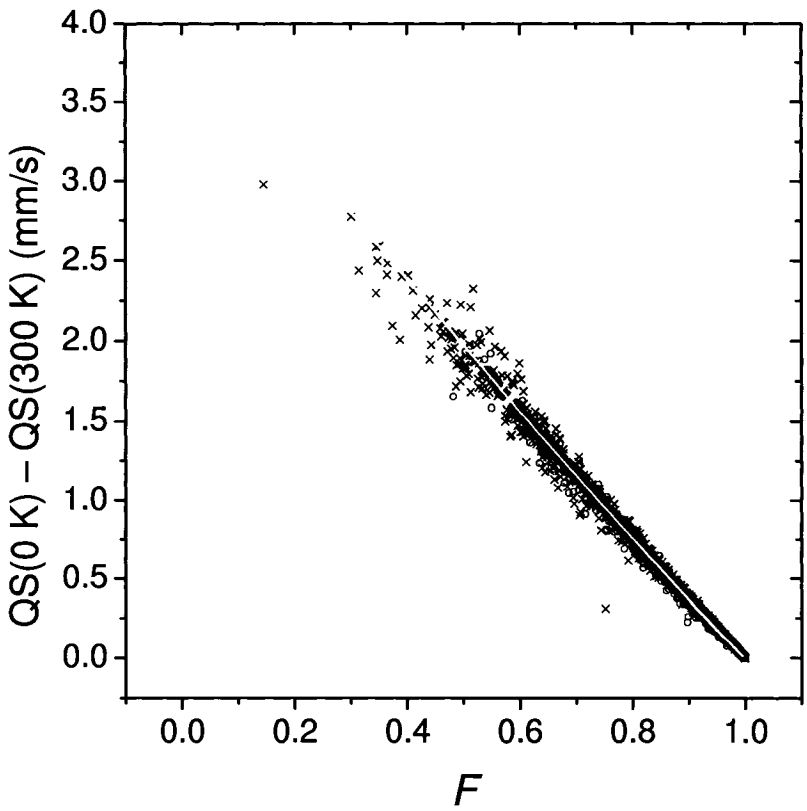

Figure 52. QS(0 K) – QS (300 K) vs. the temperature factor *F*. Red solid circles - {⊥, 58°, 2.11 Å}, σ = 0.025 Å; black open circles - {⊥, 58°, 2.11 Å}, σ = 0.175 Å; blue crosses - {⊥, 54.74°, 2.11 Å}, σ = 0.025 Å; black crosses - {⊥, 54.74°, 2.11 Å}, σ = 0.175 Å; yellow line - [⊥, ψ, 2.11 Å] series.

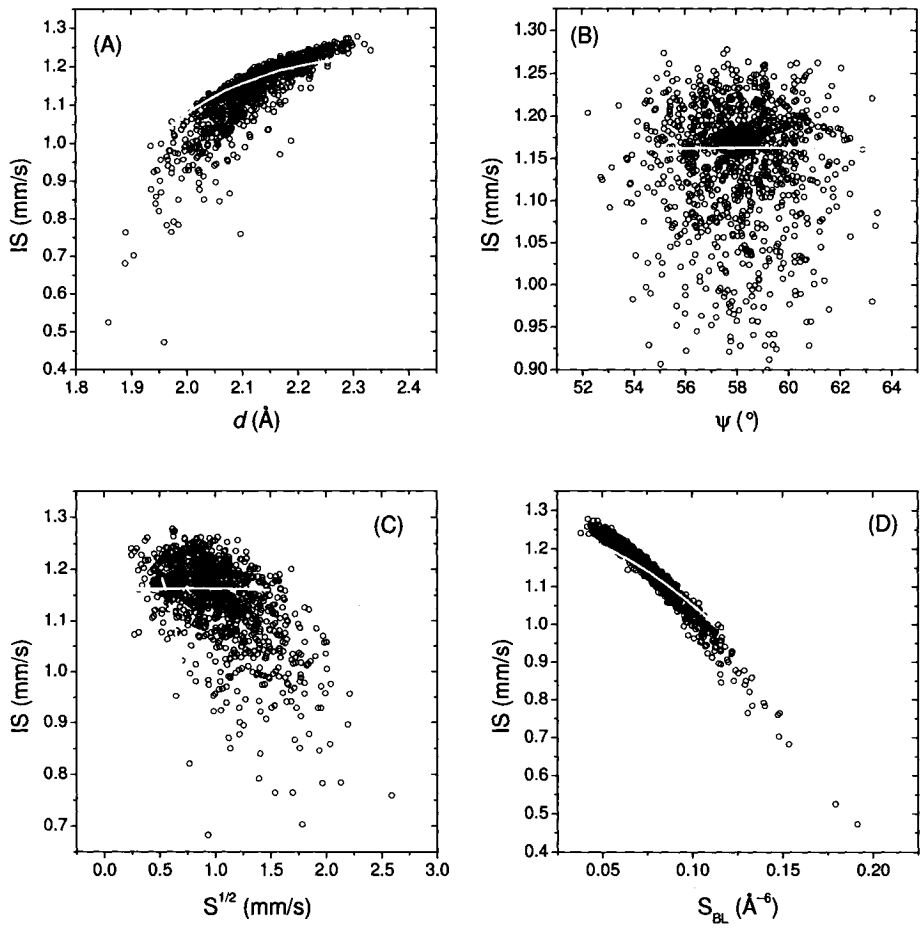

Figure 53. IS vs. various octahedral structural parameters. Red solid circles - {⊥, 58°, 2.11 Å}, σ = 0.025 Å; black open circles - {⊥, 58°, 2.11 Å}, σ = 0.175 Å. (A) IS vs. mean cluster bond length *d*; yellow solid line - [⊥, 58°, *d*] series. (B) IS vs. mean cluster flattening angle ψ; yellow solid line - [⊥, ψ, 2.11 Å] series. (C) IS vs. the square root of the total EFG structure factor *S*; yellow solid line - [⊥, ψ, 2.11 Å] series; yellow dashed line - [⊥, 58°, *d*] series. (D) IS vs. S_{BL} (see equation 50); yellow solid line - [⊥, 58°, *d*] series.

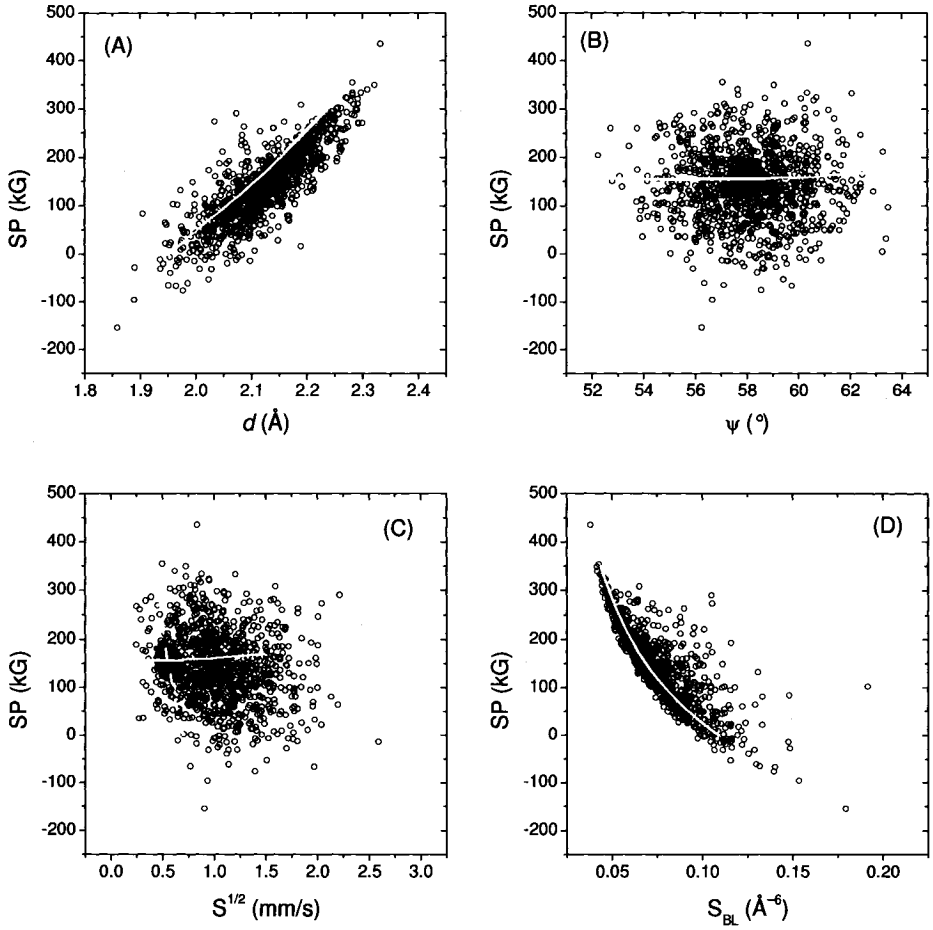

Figure 54. SP vs. various octahedral structural parameters. Red solid circles - {⊥, 58°, 2.11 Å}, σ = 0.025 Å; black open circles - {⊥, 58°, 2.11 Å}, σ = 0.175 Å. (A) SP vs. mean cluster bond length *d*; yellow solid line - [⊥, 58°, *d*] series. (B) SP vs. mean cluster flattening angle ψ; yellow solid line - [⊥, ψ, 2.11 Å] series. (C) SP vs. the square root of the total EFG structure factor *S*; yellow solid line - [⊥, ψ, 2.11 Å] series; yellow dashed line - [⊥, 58°, *d*] series. (D) SP vs. S_{BL} (see equation 50); yellow solid line - [⊥, 58°, *d*] series.

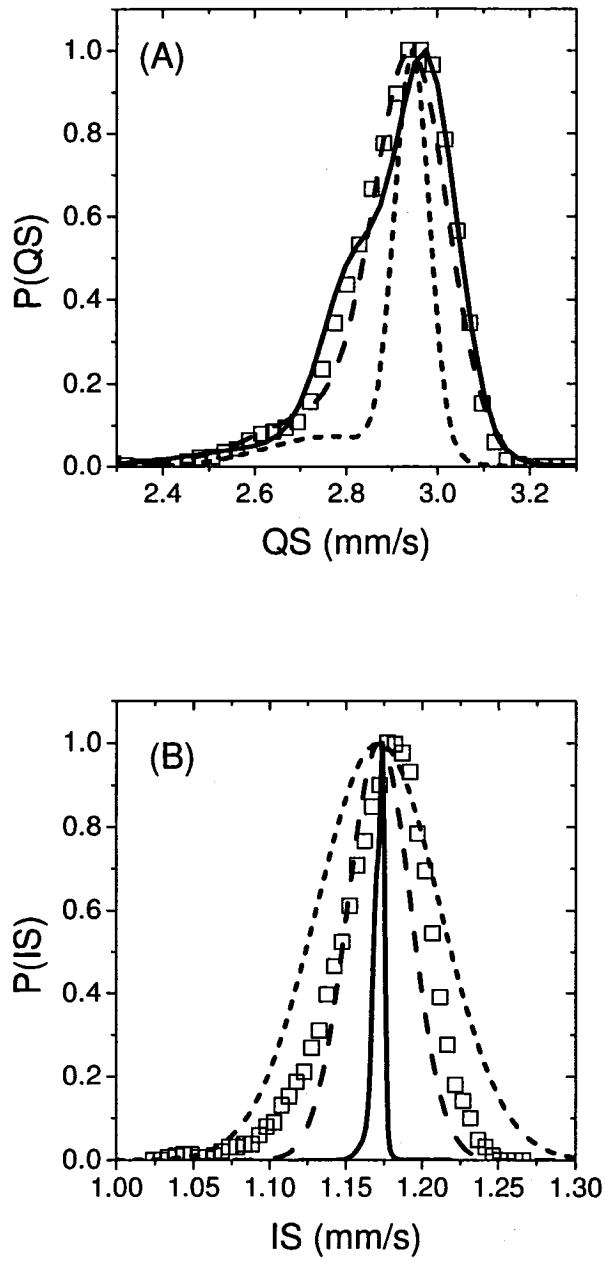

Figure 55. Results of fitting the doublet calculated from the {⊥, 58°, 2.11 Å}, σ = 0.100 Å, simulation (T = 300 K). Squares - distribution calculated from simulation; solid line - distribution from the best fit using VBF method; dashed line, dotted line - distributions from the best fits using the xVBF method.

References

Alberto, H. V., Pinto da Cunha, J. L., Mysen, B. O., Gil, J. M., and Ayres de Campos, N. (1996) Analysis of Mössbauer spectra of silicate glasses using a two-dimensional Gaussian distribution of hyperfine parameters. Journal of Non-Crystalline Solids **194**, 48-57.

Axtmann, R. C., Hazony, Y. A., and Hurley, J. W. Jr. (1968) 3d electron delocalization from Mössbauer measurements on ferrous halides. Chemical Physics Letters **2**, 673-675.

Baerends, E.J., and Ros, P. (1973), Self-consistent molecular Hartree-Fock-Slater calculations II. The effect of exchange scaling in some small molecules. Chemical Physics **2**, 52-59.

Bailey, S., Ed. (1984) Micas. Reviews in Mineralogy & Geochemistry **13**

Bancroft, G.M. (1973) Mössbauer Spectroscopy: An Introduction for Inorganic Chemists and Geochemists. John Wiley and Sons, Ltd., New York.

Billard, L., Lançon, F., Rodmacq, B., and Chamberod, A. (1984) On the Mössbauer effect in metallic glasses. Journal of Physics F: Metal Physics **14**, 555-564.

Blaes, N., Fischer, H. and Gonser, U. (1985) Analytical expression for the Mössbauer line shape of ^{57}Fe in the presence of mixed hyperfine interactions. Nuclear Instruments and Methods in Physics Research B **9**, 201-208.

Brady, P. R., Duncan, J. F., and Mok, K. F. (1965) Chemical aspects of the Mössbauer effect. Proceedings of the Royal Society of London A **287**, 343-362.

Brand, R. A., Le Caer, G., and Dubois, J. M. (1990) Crystalline and quasi-crystalline phases of the Al-Si-Mn system: a comparison of the ^{57}Fe electric field gradient properties. Journal of Physics: Condensed Matter **2**, 6413-6431.

Brand, R. A., Pelloth, J., Hippert, F., and Calvayrac, Y. (1999) Correlations in the electronic properties of AlCuFe quasicrystals and high-order approximants: ^{57}Fe Mössbauer, and ^{27}Al and ^{65}Cu nuclear magnetic resonance studies. Journal of Physics: Condensed Matter **11**, 7523-7543.

Burbridge, C. D., Goodgame, D. M. L., and Goodgame, M. (1967) Orbital splittings for some high-spin tetragonal complexes of iron(II) from Mössbauer and electronic spectra. Journal of the Chemical Society A **349**, 349.

Burns, R. G. (1994) Mineral Mössbauer spectroscopy: correlations between chemical shift and quadrupole splitting parameters. Hyperfine Interactions **91**, 739-745.

Bureau, B., Silly, G., Buzaré, J. Y., Boulard, B., and Legein, C. (2000) Nuclear magnetic resonance quadrupolar parameters and short range order in disordered ionic fluorides. Journal of Physics: Condensed Matter **12**, 5775-5788.

Campbell, S.J. and Aubertin, F. (1989) Evaluation of distributed hyperfine parameters, in Long, G.J. and Grandjean, F. (eds.) Mössbauer spectroscopy applied to inorganic chemistry **3**, 183. Plenum Press, New York.

Cohen, M.H., and Reif, F. (1957) Quadrupole Effects in Nuclear Magnetic Resonance Studies of solids, in Seitz, F. and Turnbull, D. (eds.) Solid State Physics: Advances in Research and Applications **5**, 321-438. Academic Press, New York.

Comodi, P. and Zanazzi, P.F. (2000) Structural thermal behaviour of paragonite and its dehydroxylate: a

high-temperature single-crystal study, Physics and Chemistry of Minerals **27**, 377-385.

Comodi, P., Zanazzi, P.F., Weiss, Z., Rieder, M., and Drabek, M. (1999) "Cs-tetra-ferri-annite": High-pressure and high-temperature behaviour of a potential nuclear waste disposal phase. American Mineralogist **84**, 325-332.

Cornell, R.M. and Schwertmann, U. (1997) The Iron Oxides, John Wiley & Sons Ltd., New York.

Czjzek, G. (1982) Electric field gradients in amorphous materials. Nuclear Instruments and Methods in Physics Research **199**, 37-44.

Czjzek, G. (1983) Distribution of nuclear quadrupole splittings in amorphous materials and the topology of the (VZZ, η)-parameter space. Hyperfine Interactions **14**, 189-194.

Czjzek, G., Fink, J., Götz, F., Schmidt, H., Coey, J. M. D., and Rebouillat, J.-P. (1981) Atomic coordination and the distribution of electric field gradients in amorphous solids. Physical Review B **23**, 2513-2529.

de Vries, J. L. K. F., Trooster, J. M., and Ros, P. (1975) Numerical relativistic self-consistent field calculation of electron density and $\langle r^{-3} \rangle$ for a number of electron configurations of iron and tin. Application to tin Mössbauer spectroscopy. Journal of Chemical Physics **63**, 5256-5262.

Dengler, H., Leupold, O., Nagy, D. L., Ritter, G., Aubertin, F., Limbach, C. T., and Gonser, U. (1991) Distribution of hyperfine fields of $^{57}Fe^{2+}$ in amorphous $LiNbO_3$: Mössbauer study at low temperature in high magnetic fields. Hyperfine Interactions **69**, 667-672.

Devore, J.L. (1991) Probability and Statistics for Engineering and the Sciences, Third Edition. Brooks/Cole Publishing Company, Pacific Grove, California.

Domes, H., Leupold, O., Nagy, D. L., Ritter, G., Spiering, H., Molnár, B., and Szücs, I. S. (1986) Mössbauer study of short range order in frozen aqueous solutions of $Fe(ClO_4)_2$. Journal of Chemical Physics **85**, 7294-7300.

Downs, R.T. (2000) Analysis of Harmonic Displacement Factors. Reviews in Mineralogy and Geochemistry **41**, 61-78.

Dufek, P., Blaha, P., Schwarz, K. (1995) Determination of the nuclear-quadrupole moment of Fe-57. Physical Review Letters **75**, 3545-3548.

Dunitz, J. D., Schomaker, V. and Trueblood, K. N. (1988) Interpretation of Atomic Displacement Parameters from Diffraction Studies of Crystals. Journal of Chemical Physics **92**, 856-867.

Evans, R. J., Rancourt, D. G., and Grodzicki, M. (2005a) Hyperfine electric field gradients and local distortion environments of octahedrally co-coordinated Fe^{2+}. American Mineralogist **90**, 187-198.

Evans, R. J., Rancourt, D. G., and Grodzicki, M. (2005b) Hyperfine electric field gradient tensors at Fe^{2+} sites in octahedral layers: Towards understanding oriented single-crystal Mössbauer spectroscopy measurements of micas. American Mineralogist **90**, in press.

Fermi , E. (1930) Uber die magnetischen Momente der Atomkerne. Zeitschrift für Physiks **60**, 320-333.

Greenwood, N. N. and Gibb, T. C. (1971) Mössbauer Spectroscopy, Chapman and Hall, London, U.K.

Grenèche, J. M., Teillet, J., and Coey, J. M. D. (1987) Simulation of an octahedral random network by computer. Journal de Physique **48**, 1709-1714.

Grodzicki, M. (1980) A self-consistent charge Xα method I. Theory. Journal of Physics B: Atomic and Molecular Physics **13**, 2683-2691.

Grodzicki, M., Männing, V., Trautwein, A.X., and Friedt, J.M. (1987) Calibration of isomer shift and quadrupole coupling for ^{119}Sn, ^{127}I and ^{129}I as derived from self-consistent charge Xα calculations and Mössbauer measurements. Journal of Physics B: Atomic and Molecular Physics **20**, 5595-5625.

Guenzberger, D., Ellis, D.E., and Zeng, Z. (1998) First principles calculations of Mössbauer parameters for solids and large molecules. Hyperfine Interactions **113**, 25-36.

Guggenheim, S., Change, Y.H., and Vangroos, A. F. K., Muscovite dehydroxylation - high temperature studies. American Mineralogist **72**, 537-550.

Hargraves, P., Rancourt, D.G., and Lalonde, A. E. (1990) Single-crystal Mössbauer study of phlogopite mica. Canadian Journal of Physics **68**, 128-144.

Hazen, R. M., and Burnham, C. W. (1973) The crystal structures of one-layer phlogopite and annite. American Mineralogist **58**, 889-900.

Ingalls, R. (1964) Electric-field gradient tensor in ferrous compounds. Physical Review **133**, A737-A795

Kunz, M. and Armbruster, T. (1990) Difference displacement parameters in alkali feldspars: Effects of (Si, Al) order-disorder. American Mineralogist **75**, 141-149.

Lagarec, K. and Rancourt, D. G. (1997) Extended Voigt-based analytic line shape method for determining N-dimensional correlated hyperfine parameter distributions in Mössbauer spectroscopy. Nuclear Instruments and Methods in Physics Research B **129**.

Lagarec, K. and Rancourt, D. G. (1999) A new model for multidimensional distributions of hyperfine parameters in Mössbauer spectroscopy. in Kodama, H., Mermut, A. R., and Torrance, J. K. (eds.) Clays for our future: Proceedings of the 11th International Clay Conference. 215-220, Ottawa, Canada, ICC97 Organizing Committee.

Le Caer, G., Dubois, J.M., and Brand, R.A. (1984) Local parameter distributions in amorphous metals, in von Allmen, M. (ed.) Amorphous Metals and Non-Equilibrium Processing, Les Éditions de Physique, Les Ulis, France.

Le Caer, G., Brand, R. A., and Dehghan, K. (1985) Sign determination of the ^{57}Fe electric field gradient in amorphous $Al_{70}Si_{17}Fe_{13}$. Journal de Physique Colloque **46**, C8-169-C8-173.

Le Caer, G. and Dubois, J. M. (1987) Metallic glass structure by ^{57}Fe Mössbauer spectroscopy. Key Engineering Materials **13-15**, 555-566.

Le Caer, G. and Brand, R. A. (1992) A review of two decades of the analysis of hyperfine parameter distributions in Mössbauer spectroscopy: Difficulties, progress and prospects. Hyperfine Interactions **71**, 1507-1514.

Le Caer, G. and Brand, R. A. (1998) General models for the distributions of electric field gradients in disordered solids. Journal of Physics: Condensed Matter **10**, 10715-10774.

Zhe, L. and De Grave, E. (1998) The Fe^{2+} quadrupole splitting at octahedral sites in chain silicates: correlations with the site-distortion parameters. Hyperfine Interactions **116**, 173-178.

Lines, M. E. (1979) Hard-sphere random-packing model for an ionic glass: Yttrium iron garnet. Physical Review B **20**, 3729-3738.

Lines, M. E. (1981) The electric field gradient in a random packing model of amorphous ionic materials. Journal of Non-Crystalline Solids **46**, 1-12.

Lines, M. E. and Eibschütz, M. (1983) Influence of isomer-shift distribution on Mössbauer quadrupole spectra in amorphous magnetic insulators. Physical Review B **27**, 5308-5312.

Lougear, A., Grodzicki, M., Bertoldi, C., Trautwein, A.X., Steiner, K., and Amthauer, G. (2000) Mössbauer and molecular orbital study of chlorites. Physics and Chemistry of Minerals **27**, 258-269.

Maurer, M. (1986) Electric field gradients of randomly disordered compounds. Physical Review B **34** , 8996-8999.

Mercier, P.H.J. (2003) Crystal chemistry of trioctahedral 2:1 layer silicates: Testing the limits of simple geometrical models, Ph.D. thesis, University of Ottawa, Ottawa, Ontario, Canada.

Mössbauer, R. L. (1958) Gammastrahlung in Ir^{191}, Z. Physik **151**, 124

Nagy, O. L and Röhlich, U. (1991) An overview on model-independent data reduction methods in Mössbauer spectroscopy. Hyperfine Interactions **66**, 105-126.

Odintsov, O. G. and Pushkarev, E. A. (1990) Combined recovery of the quadrupole splitting distribution function and the dependence of the isomer shift using Mössbauer spectral data. USSR Computational Mathematics and Mathematical Physics **30**, 112-115.

Ping, J.Y. and Rancourt, D.G. (1994) Failure of the direct HFD extraction method. Hyperfine Interactions **92**, 1209-1212.

Pustówka, A. J., Sawicka, B. D., and Sawicki, J. A. (1973) Electric field gradients in charge-perturbed lattices. Physica Status Solidi B **57**, 783-791.

Rancourt, D.G. (1994a) Mössbauer spectroscopy of minerals, I. Inadequacy of Lorentzian-line doublets in fitting spectra arising from quadrupole splitting distributions. Physics and Cehmistry of Minerals **21**, 244-249.

Rancourt, D. G. (1994b) Mössbauer spectroscopy of minerals, II. Problem of resolving cis and trans octahedral Fe^{2+} sites. Physics and Chemistry of Minerals **21**, 250-257.

Rancourt, D. G. and Ping, J. Y. (1991) Voigt-based methods for arbitrary-shape static hyperfine parameter distributions in Mössbauer spectroscopy. Nuclear Instruments and Methods in Physics Research B **58**, 85-97.

Rancourt, D. G., Ping, J. Y., and Berman, R. G. (1994a) Mössbauer spectroscopy of minerals, III. Octahedral-site Fe^{2+} quadrupole splitting distributions in the phlogopite-annite series. Physics and Chemistry of Minerals **21**, 258-267.

Rancourt, D.G., Christie, I.A.D., Royer, M., Kodama, H., Robert, J.-L., Loalonde, A.E., and Murad, E. (1994b) Determination of accurate $^{[4]}Fe^{3+}$, $^{[6]}Fe^{3+}$ and $^{[6]}Fe^{2+}$ site populations in syntheic annite by Mössbauer spectrometry. American Mineralogist **79**, 51-62.

Rancourt, D.G., Christie, I.A.D., Lamarche, G., Swainson, I., and Flandrois, S. (1994c) Magnetism of syntheitic and natural annite mica: ground state and nature of excitations in an exchange-wise two-dimensional easy-plane ferromagnet with disorder. Journal of Magnetism and Magnetic Materials **138**, 31-44.

Rancourt, D. G., Ping, J. Y., Boukili, B., and Robert, J.-L. (1996) Octahedral-site Fe^{2+} quadrupole splitting distributions from Mössbauer spectroscopy along the (OH-F)-annite join. Physics and Chemistry of

Minerals **23**, 63-71.

Rancourt, D.G. (1998) Mössbauer spectroscopy in clay science. Hyperfine Interactions **117**, 3-38.

Shannon, R.D. (1976) Revised effective ionic radii and systematic studies of interatomic distances in halides and chalcogenides, Acta Crystalographica A **32**, 751-767.

Stöckmann, H. (1981) Electric field gradients resulting from randomly distributed unscreened point charges. Journal of Magnetic Resonance **44**, 145-158.

Takeda, H. and Morosin, B. (1975) Comparison of observed and predicted structural parameters of mica at high temperature. Acta Crystallographica B **31**, 2444-2452.

Townes, C. H. and Dailey, B. P. (1948) Determination of electronic structure of molecules from nuclear quadrupole effects. Journal of Chemical Physics **17**, 782-796

Trautwein, A. and Zimmermann, R. (1976) Internal magnetic field in α-$FeSO_4$ Physical Review B **13**, 2238-2240.

Turek, I. (1990) Mixed hyperfine interactions in amorphous materials: a model study. Hyperfine Interactions **62**, 343-351.

Vandenberghe, R. E., De Grave, E., and de Bakker, P. M. A. (1994) On the methodology of the analysis of Mössbauer spectra. Hyperfine Interactions **83**, 29-49.

Varret, F. and Henry, M. (1980) Amorphes ioniques: caractères spécifiques d'une étude Mössbauer (isotope ^{57}Fe). Revue de Physique Appliquée **15**, 1057-1061.

Watson, R. E. and Freeman, A. J. (1961) Origin of effective fields in magnetic materials. Physical Review **123**, 2027-2047.

Weiss, Z., Rieder, M., and Chmielová, M. (1992) Deformation of coordination polyhedra and their sheets in phyllosilicates, European Journal of Mineralogy **4**, 665-682.

Conclusions

This thesis presents the most comprehensive exploration of the link between local distortion environments and ^{57}Fe Mössbauer hyperfine parameters, as well as the first simulations of hyperfine parameter distributions using electronic structure calculations.

It has been shown that the correlations between hyperfine parameters in disordered materials are more complicated than are currently accounted for by fitting models. It seems that, while distortion series where hyperfine parameters are calculated as functions of progressive distortion of the iron site, as calculated in paper 1, are useful as a guide, they are unlikely to provide as much insight into experimental Mössbauer spectra as full simulations of hyperfine parameter distributions using ensembles of randomly distorted sites, as in paper 3.

Possible directions for future work include applications of the methods of paper 3 to $^{[6]}Fe^{3+}$ and $^{[4]}Fe^{3+}$ sites; developing new algorithms for fitting spectra which incorporate the observed relationships between the widths of different hyperfine parameter distributions, as well as more realistic correlations between the hyperfine parameters; developing new theoretical models of the EFG tensor distribution at $^{[6]}Fe^{2+}$ sites in disordered materials, analogous to the Gaussian Isotropic Model (Le Caer and Brand 1998) for amorphous Fe^{3+} materials, based on the observed evolution of the (V_{ZZ}, η) polar plots with disorder (figure 50 of paper 3); and simulations of hyperfine parameter distributions with more realistic crystal chemical models for specific materials. I hope to apply the last method in future work on environmental iron oxide nanoparticles.

References

Le Caer, G. and Brand, R. A. (1998) General models for the distributions of electric field gradients in disordered solids. Journal of Physics: Condensed Matter **10**, 10715-10774.